Novel photo-patterning technology for direct writing in resist based systems

David Elfström

Institute of Photonics

University of Strathclyde

A thesis submitted for the degree of

Doctor of Philosophy (PhD)

2010 January

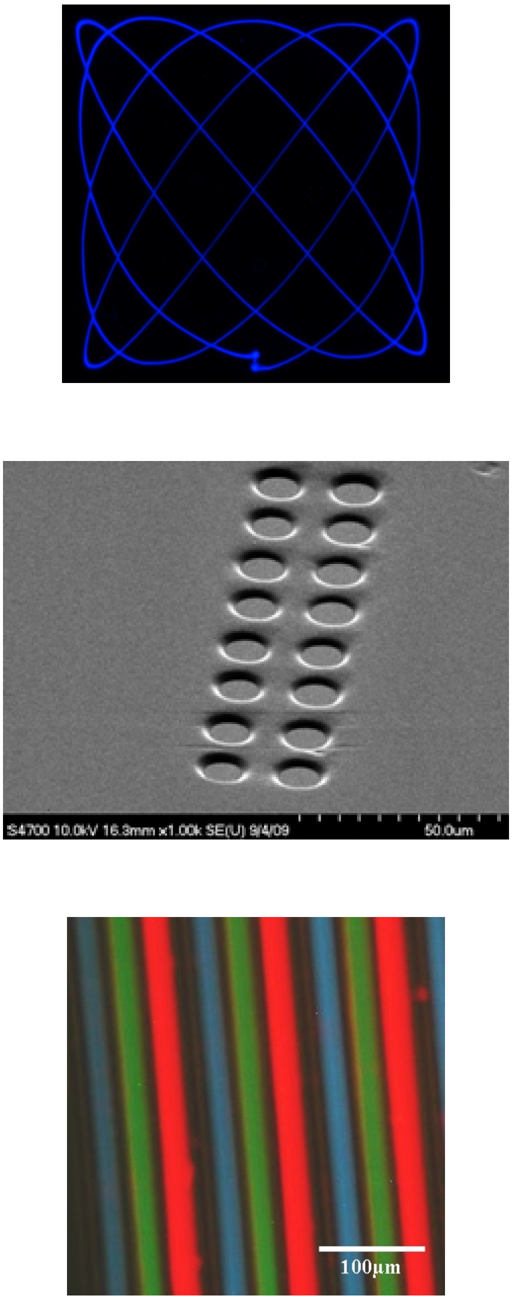

Frontispiece: Upper: Lissajous figure produced in truxene/resist blend by UV laser direct writing. Middle: Exposed dots in S1818 photoresist using a CMOS driven micro-LED array. Lower: Red-green-blue quantum dot nanocomposite stripes aligned onto UV micro-stripe light emitting diodes by UV laser direct writing.

Abstract

This thesis presents studies on micro-patterning techniques and their applications in direct writing of photoresist based systems. Gallium nitride based ultraviolet light sources, micro-pixelated light emitting diodes and laser diodes, are utilised in photolithography systems.

Laser direct writing is used to pattern negative-type photoresist and resist based nanocomposites with an organic light-emitting oligomer, oligofuorene-functionalised truxenes, added. Characteristics of such structures are investigated.

A CMOS-chip-driven micro-LED array is used in an optical projection system for maskless photolithography. The performance of this setup is investigated and the system is used to pattern positive- and negative-type photoresists.

Semiconductor nanocrystals are investigated for the use as colour converters in integrated micro-LED devices. The performance of such devices in terms of colour conversion efficiency is measured.

For Gülis.

Contents

List of Figures

List of Tables

UV - Ultraviolet
PAG - Photoacid generator
DI water - Deionised water
LEP - Light-emitting polymer
PFO - Polyfluorene (Poly(9,9'di-*n*-octylfluorene))
NC - Nanocrystal
QD - Quantum dot
CHDV - 1,4-cyclohexanedimethanol divinyl ether
PET - Photoinduced electron transfer
PL - Photoluminescence
US - Ultrasonic
LDW - Laser direct writing
DMD - Digital micro-mirror device
SLM - Spatial light modulator
FIB - Focused ion beam
EBL - Electron beam lithography
PMMA - Poly(methyl methacrylate)
ZPAL - Zone-plate-array lithography
SPAD - Single-photon avalanche diode
PCB - Printed circuit board
FPGA - Field programmable gate array
VCO - Voltage-controlled oscillator
LFSR - Linear feedback shift register

Chapter 1

Introduction

Photonics is the science of light; its emission, transmission, modulation, amplification, and detection. It is of ever increasing importance, in commercial terms as well as in research. As proof of this importance the 2009 Nobel Prize in physics was awarded for fundamental innovations in the area, namely high transmission optical fibres and the charge-coupled device (CCD).

One deciding factor for the future of photonics is going to be the ability to produce micro- and nano-scale patterns rapidly, accurately, and inexpensively. For certain types of functional, predominately organic, materials standard patterning techniques, involving photolithography and chemical etching, cannot be used because of the environmental sensitivity of these materials. For low volume production and prototyping another limiting factor is the photomask, which is expensive and time consuming to produce. Therefore maskless techniques are of great importance.

This thesis work utilised novel nano-engineered light emitting materials for the production of microscaled structures. The structures were produced with maskless techniques and put to use in, for example, colour conversion for micro-pixellated light emitting diodes.

In this first chapter the concepts and devices that form the basis of this work will be presented. The light emitting diode (LED) will be discussed and some background and current performance characteristics will be given. Micropatterning techniques used for manufacturing of photonic and other microstructured devices will also be introduced and nanoengineered light emitting materials will be presented.

In Chapter 2 a further, more detailed overview of the photoresists and light emitting materials used in the thesis work will be given. The novel nanocomposite materials, consisting of photoresists and light emitting materials, will also be presented.

In Chapter 3 the theory and background of laser direct writing (LDW) as patterning technique for photoresists will given and the experimental results using this technique will be presented.

In Chapter 4 direct micro-patterning with a CMOS driven micro-LED array by projection through back-to-back microscope objectives will be discussed and results presented.

In Chapter 5 the theory and benefits of colour conversion of the ultraviolet emission from a micro-LEDs will be given. Results and characteristics of integrated devices will be presented.

In Chapter 6 the concluding discussions will be given and planned future work briefly mentioned.

1.1 Light Emitting Diodes

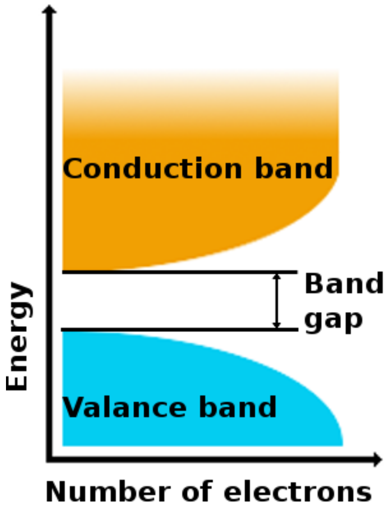

Figure 1.1: Schematic of the bandgap in a semiconductor.

In metals, electrons are delocalised and free to move, because there is overlap in energy between the valence band and the conduction band. In insulators the valence band electrons are strongly bound. Semiconductors are materials with electrical conductivity characteristics intermediate between a conductor and an insulator. They conduct electricity only when exposed to external stimulation, be it an electric field or light. Their use in modern day-to-day life is very widespread as they form the basis of all modern electronic devices. They can be pure elemental materials such as silicon and germanium or compounds such as gallium arsenide and silicon carbide. The energy separation, where there is a lack of electron states, in energy between the valence band and the conduction band in such a material is called the bandgap, see figure 1.1. The bandgap is calculated as the difference between the lowest energy of the conduction band and the highest energy in the valence band ($E_g = E_c - E_v$).

The electrical properties of a semiconductor can be changed by itentionally introducing impurities to the semiconductor material. This is known as doping. By introducing atoms with a higher electron affinity, energy states close to the valance band are created. This is known as P-type (positive-type, “lack” of electrons) doping and the materials used are called 'acceptors', as they accept weakly-bound electrons from the semiconductor. The electron vacancy is known as a 'hole'. In silicon (Group IV element), Group III materials such as boron or aluminium are used as acceptors. Magnesium, being a Group II element, is used for P-type doping in gallium nitride. Introducing atoms with the capability of providing extra electrons to the semiconductor is known as N-type (negative-type, "surplus" of electrons) doping and the material used as 'donors'. In silicon, Group V, such as phosphorus or arsenic, can be used for this purpose. Gallium nitride can be doped with oxygen or silicon to make it N-type.

1.1.1 General introduction

A light emitting diode (LED) is a semiconductor electroluminescent light source. Electroluminescence was first observed in silicon carbide by H. J. Round of Marconi Labs in 1907 [1] and the LED was invented by Oleg Vladimirovich Losev in 1927 [2]. Losev observed the non-thermal light emission from silicon carbide (SiC) crystals and measured the current-voltage dependence of the device. He even proposed his invention's use in communications [3]. However it was not until Rubin Braunstein at the Radio Corporation of America observed emission from several semiconductor materials including gallium arsenide (GaAs) [4] that the true potential for these devices was realised. Blue LEDs were based on SiC until the early 1990s when gallium nitride (GaN) made a dramatic leap in output efficiency possible [5]. Later GaN based material systems have also been developed for LEDs emitting in the UV [6]. LEDs have now been made from many semiconductors and their performance is summerised in figure 1.2.

Nowadays LEDs are found in many applications in daily life, e.g., as indicators (from small power indicators to traffic lights), displays (e.g., huge outdoor displays at sports stadia), and for illumination. The performance of light sources in illumination is commonly measured in luminous flux per electrical input power (lm/W). The Lumen (lm) is a unit that takes into account the eye's sensitivity to light of different wavelengths and hence measures how bright a light is perceived to be. Since the 1990s LEDs have been more efficient light emitters than incandescent bulbs (∼13 lm/W) and in the last decade they have surpassed fluorescent lamps (∼90 lm/W) as white light illumination sources (see figure 1.2). Unlike LEDs, incandescent bulbs and fluorescent lamps have reached their fundamental limit of efficiency [7]. Nichia Corp. has demonstrated white-LEDs with an efficiency of 150 lm/W ([8]) and Cree Inc. have reported even higher figures.

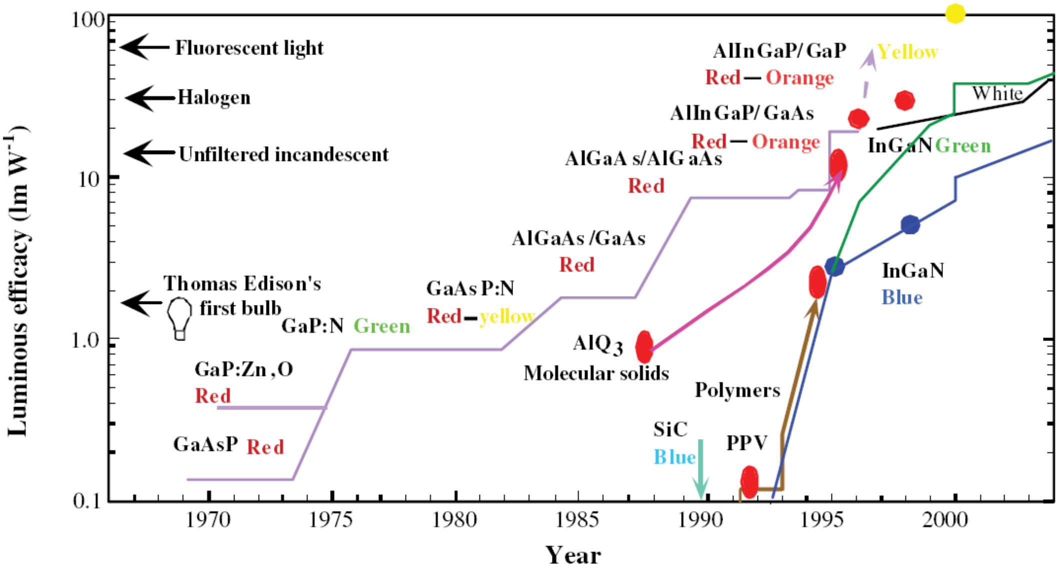

Figure 1.2: Evolution in performance for some relevant light sources. Efficient gallium nitride technology has emerged only since the mid 1990's. After [9]

The basic working principle of all LEDs is the radiative recombination of holes and electrons. A hole is a vacant electron state in the valance band. In figure 1.3

a schematic image of a basic P-N junction LED can be seen. P-type materials are doped with a “hole creating” material (i.e., a material with high electron affinity) creating energy levels within the bandgap close to the valence band. This leads to holes as the majority charge carrier. N-type materials on the other hand are doped with electron donating materials, forming energy states close to the conduction band. By creating a junction between regions of P- and N-doping and by applying an electric field over the junction (positive on the P-side and negative on the N-side), referred to as forward bias, holes and electrons are injected and can recombine in the middle. For a light-emitting device, the recombination preferably occurs radiatively meaning that the energy released, by an electron recombining with a hole, is emitted as a photon, with an energy defined by the bandgap of the material, i.e., conserving the energy of the system. A device with this junction configuration is known as a ’homojunction’ light emitting diode and is the simplest type of LED. The width of the active region in such a device is basically defined by the diffusion length of the respecitve charge carriers.

For any LED to work efficiently, a direct bandgap semiconductor is needed. Figure 1.4 shows a schematic diagram of the energy level and the band gap in such a direct bandgap material. In indirect bandgap materials the crystal momentum of the lowest point of the conduction is not equal to the crystal momentum of the highest point of the valence band. In these materials the direct transition from conduction band to valence band is forbidden due to conservation laws (conservation of crystal momentum) making this transition inefficient as it needs to be aided by interaction with a phonon (crystal vibration). This is why semiconductor light emitting devices almost always are made from direct bandgap materials, such as GaAs and GaN, and not indirect bandgap materials, such as

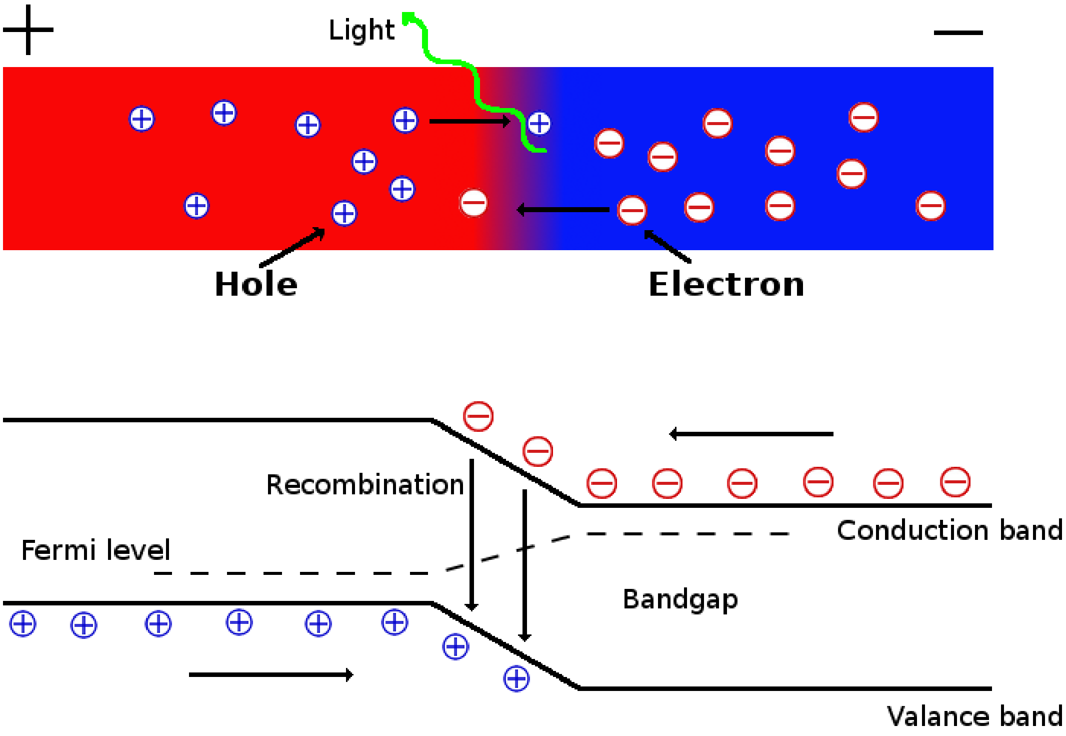

Figure 1.3: Schematic of a PN-junction LED. Electrons and holes recombine in the junction between n-doped and p-doped material.

silicon (Si).

The photon energy emitted when a hole and an electron recombine is given by

$$h\nu \approx E_g \tag{1.1}$$

where h is Planck's constant and ν is the photon frequency [11]. However thermal distribution of the carriers gives a broadening of the spectral emission peak (photon energy), proportional to k_bT, where k_b is the Boltzmann constant (1.38×10^{-23} m^2kg s^{-2} K^{-1}) and T is temperature in Kelvin. Non-radiative recombination also occurs in all real LEDs, and is detrimental to good performance as it "steals" energy from the radiative processes and increases the temperature in the active region, hence exacerbating thermal management problems. Non-radiative recom-

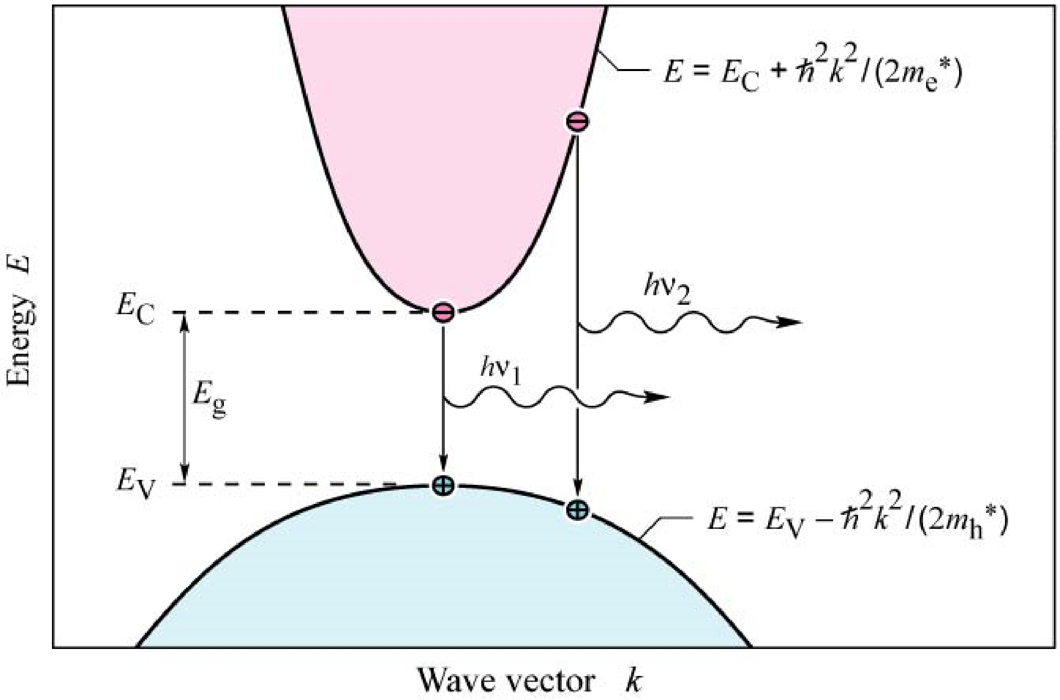

Figure 1.4: Schematic image of the bandgap and the radiative recombination process in a LED. After [10].

bination can occur at e.g., crystal defects, impurities, material interfaces and surfaces.

Problems in homojunction LEDs include difficulty in restricting electrons and holes to a common region in the device, and that photons can get reabsorbed before they can leave the material. Therefore the junction needs to be placed close to the surface of the material, where the probability for non-radiative recombination is higher. A solution to this is a 'heterojunction' configuration where a lower bandgap material is wedged between the p- and the n-type material. This type of junction is named a p-i-n junction ('p-type'-intrinsic-'n-type' junction). A schematic image of such a junction can be seen in figure 1.5. This particular configuration is known as a double heterostructure (DH) since it contains two back-to-back junctions of higher to lower bandgap materials. The recombination occurs in the lower bandgap region while limiting charge diffusion and the higher bandgap regions cannot reabsorb the photons created as they do not have enough energy to lift an electron from the valence band to the conduction band. The fact that the active region is defined by the DH rather than the diffusion length gives a higher carrier concentration at the same injection current and hence the radiative recombination rate is increased.

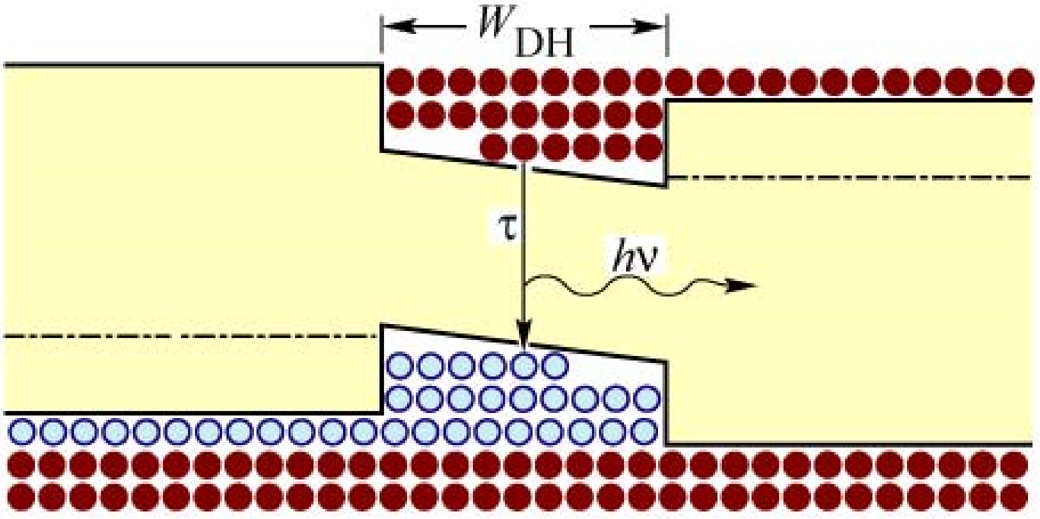

Figure 1.5: Schematic of a hetrojunction under forward bias. Z is the spatial position through the thickness of the material. After [11].

If the lower bandgap region is decreased in thickness enough for quantum size effects to become apparent, i.e., when the dimension becomes comparable with the de Broglie wavelength of an electron in the material, the energy bands can no longer be considered as continuous but become discrete [12]. The DH structure is then called a quantum well (QW). The typical thickness of a quantum well is $\leq$10 nm. Quantum wells show a step-like density of states between discrete energy levels. In this thesis LEDs and laser diodes made using InGaN quantum wells are utilised, of thickness ∼2.5 nm between barriers of gallium nitride.

One problem with making the active region thinner is carrier overflow leading to electrons “leaking” over the barriers and causing a current without recombinations. As a solution to this, active regions with multiple quantum wells (MQW) have been fabricated [13]. An ’electron blocking layer’, i.e., a potential barrier for electron, prevents overflow [14]. A schematic of such a configuration in a GaN based device can be seen in figure 1.6.

One important electrical property of a diode is described by the diagram in figure 1.7. The current is plotted versus the voltage, in what is refered to as an I-V diagram. When the voltage increases over the threshold value (close to the bandgap of the active region) the ideal diode has no resistance. However real diodes do have series resistance, the effect of which can be seen in the image. A shunt can also occur if the device is damaged. This leads to a leaked current below the threshold and is detrimental to device performance.

The current through a diode is expressed by the Shockley ideal diode equation [15]

$$I = I_{\mathrm{S}}(e^{V_{\mathrm{D}}/(nV_{\mathrm{T}})} - 1) \tag{1.2}$$

where I_{S} is the reverse bias saturation current, V_{D} is the voltage over the diode junction, V_{T} is the thermal voltage, and n is the emission coefficient, also known as the ideality factor. The emission coefficient n varies from about 1 to 2 depending on the fabrication process and semiconductor material and can in many practical cases be assumed to be approximately equal to 1. The thermal voltage $V_{\mathrm{T}} = \frac{kT}{q}$ (q is the electron charge (1.6×10^{-19} C)) is approximately 25.85 mV at 300 K,

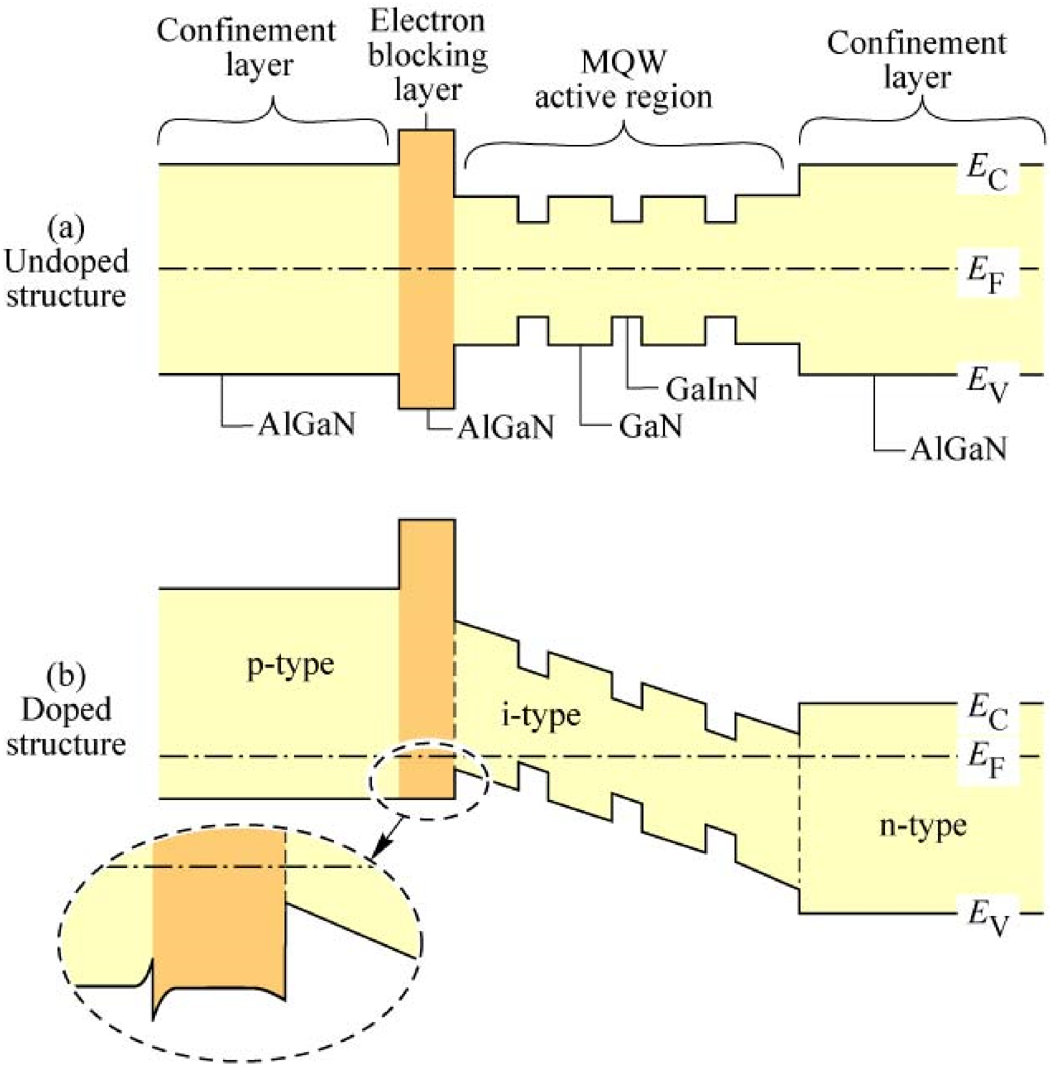

Figure 1.6: Schematic of an AlGaN/GaN/GaInN MQW structure with an AlGaN electron blocking layer. The $In_xGa_{1-x}N$ quantum wells are typically ∼2.5 nm thick with 2% In for near-UV, 30% In for blue (440 nm), and 45% In for green. After [11]

which is often taken as room temperature.

Under forward bias the equation is often approximated to

$$I = I_S \times e^{V_D/(nV_T)} \tag{1.3}$$

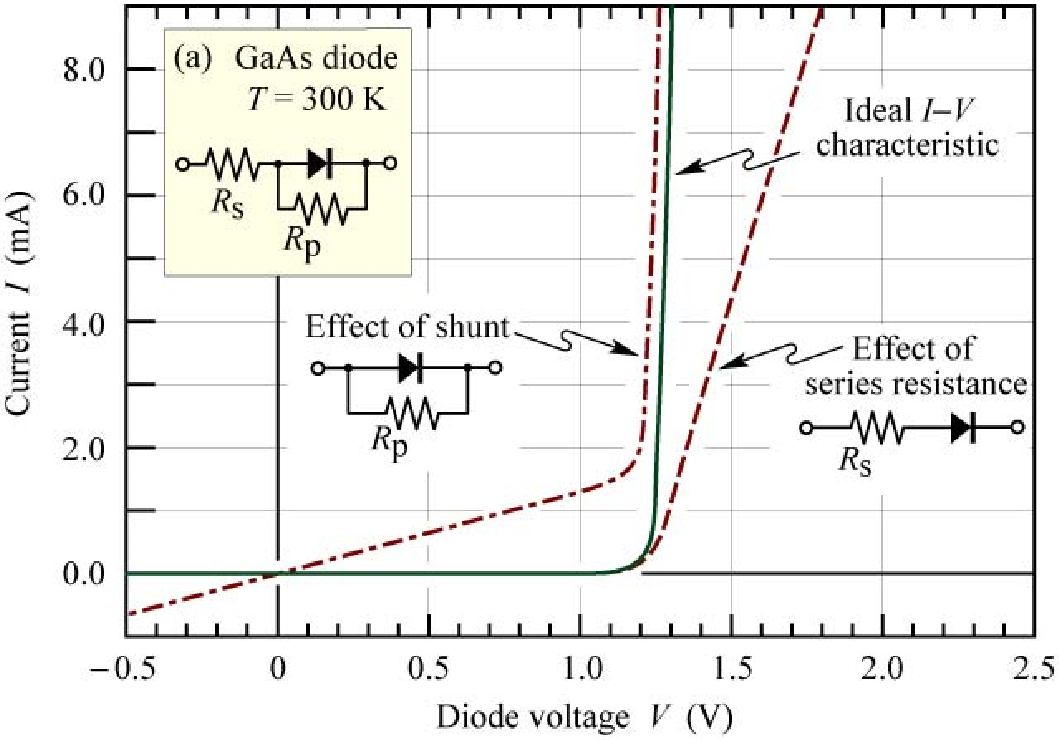

Figure 1.7: I-V characteristics of an ideal diode and the effect of shunt and series resistance. After [11]

The turn on voltage for a LED is in the ideal case decided by the bandgap (the bandgap in eV directly gives the turn on voltage), typically 1.9–3.1 V for diodes emitting in the visible spectrum. The turn-on voltage can also be affected by the quality of the fabrication process.

1.1.2 Gallium nitride based LEDs

The semiconductor material systems that are of special interest for this thesis work are GaN based alloys. The first single crystal GaN was grown in 1969 [16]. The direct energy bandgap was determined to be 3.39 eV, giving a theoretical emission wavelength of 366 nm. The GaN was grown on a sapphire substrate which is to this day the most common substrate for growing GaN based diodes

(SiC is sometimes used). The first report of a GaN based LED was in 1971 [17]. The device was an i-n junction, made by Zn-doping, emitting in the green. However for a long time there was a problem with p-doping the GaN based materials, a problem that was not solved until the late 1980s [18]. In 1995 the group around Shuji Nakamura at Nichia Chemical Industries, Ltd. reported on efficient GaN based LEDs emitting in the blue and violet [19]. This led to developments that have now put GaN based LEDs as among the most efficient light emitters known, cf. figure 1.2.

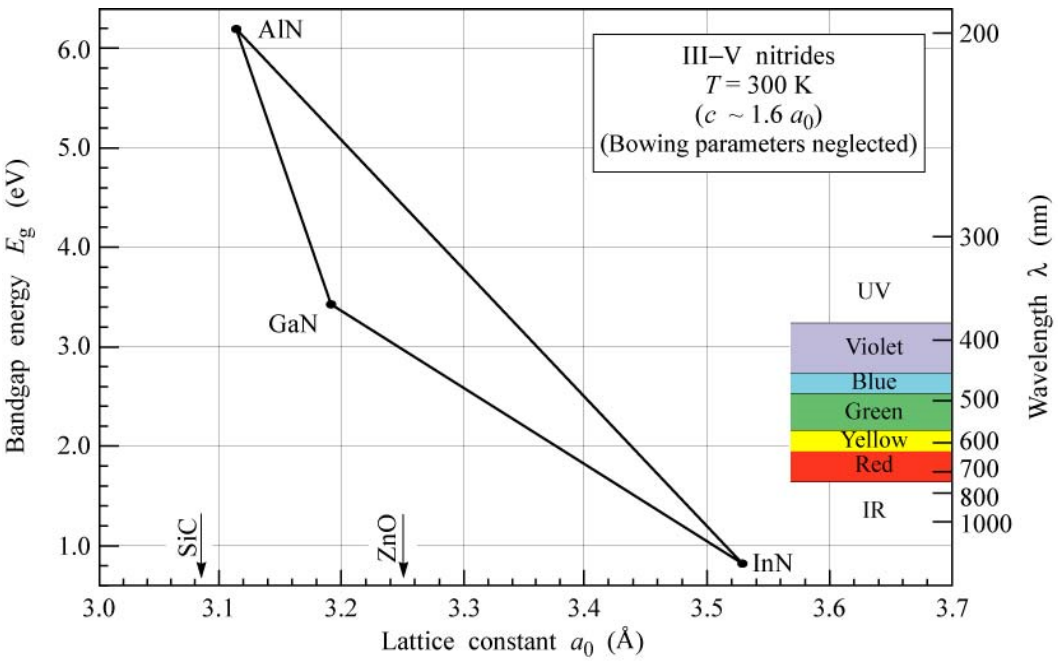

Figure 1.8: Bandgap of III-nitride materials vs. lattice constant. After [10].

Research has shown that in principle alloys of III-nitrides can cover wavelengths from deep UV to infrared, with bandgap energies ranging from 0.7 eV for InN to 6.2 eV for AlN (see figure 1.8). The GaN-based diodes realised so far cover an impressive fraction of this wavelength range. There have been reports of emission wavelengths as short as 229 nm (AlGaN) [20] and as long as 675 nm (InGaN) [21]. In figure 1.8 the bandgap energy of the ternary and quaternary alloys (Al-Ga-In-N) is plotted against the material lattice constant at room temperature. Typical high-performance devices range 370–520 nm.

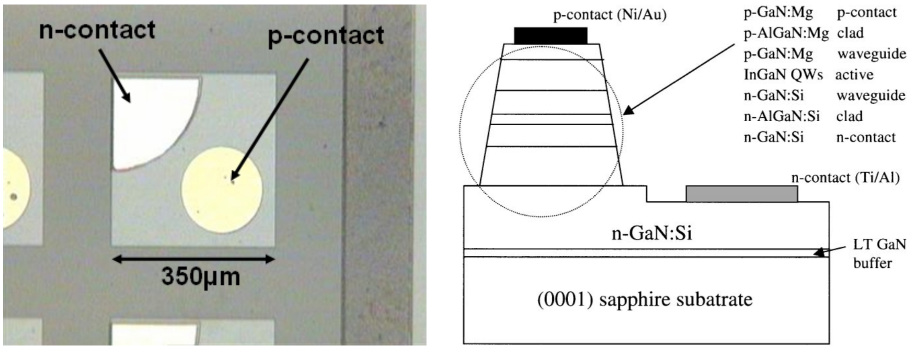

(a) Optical micrograph showing the typical die size of a 'broad area' LED.

(b) Schematic of the cross-sectional structure of a GaN based laser diode, the difference from a LED structure is mainly the waveguide layers. After [22]

Figure 1.9: Images showing the die size and structure of a typical GaN based LED.

In figure 1.9(b) the cross-sectional layer structure typical of a UV or blue emitting LED can be seen. The first layer grown on the sapphire substrate is a buffer layer and is followed by undoped GaN, then by n-type GaN and the active region (quantum wells), finally a p-doped GaN layer is added. There are several methods for growing these layers on the substrate, including molecular beam epitaxy (MBE) [23] and, metal organic chemical vapour deposition (MOCVD) [19] (also known as metal organic vapour phase epitaxy (MOVPE)). Wafers differ depending on the emission wavelength of the quantum wells. Blue/green/yellow/red LEDs have a MQW structure consisting of GaN/InGaN. Near UV LEDs can also utilise InGaN with a small molar fraction of In. For shorter wavelengths QWs of GaN, AlGaN, or AlGaInN are used, with higher Al content for higher energy emission [9].

Because the typically used sapphire substrate is electrically insulating, to contact the n-doped layer the overlayers are selectively removed by dry etching. The metal contacts for p and n are then deposited. Nickel-gold is used for the p-contact and titanium-gold (or titanium-aluminium) for the n-contact. For uniform injection current a "spreading layer" is deposited on the p-type material covering the active area. When the light extraction is on the epitaxial side of the device the spreading layer has to be thin to be semi-transparent or it will adversely affect the performance of the device. Transparent indium tin oxide (ITO) has also been used for the p-contact to avoid the need for a thin spreading layer [24]. Figure 1.9 illustrates such an 'epi-up' format of device, with typical die dimensions indicated.

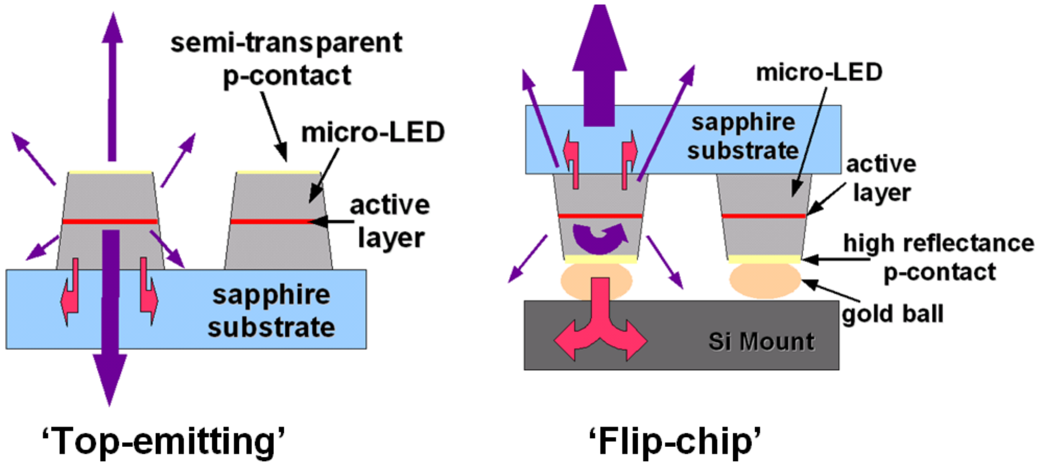

Figure 1.10: Schematic showing the difference between 'top emitting' and 'flip-chip' configurations of GaN LED devices. In the 'top-emitting' format, light is extracted via the p-contact; in 'flip-chip' devices it is extracted via the sapphire substrate.

The alternative to extracting the light on the epitaxial side is to do it through the sapphire substrate. Since sapphire is highly transparent throughout the visible and well in to the UV this is the preferred way for high power LEDs. A schematic image of the differences between normal 'top emission' and such a 'flip-chip' configuration can be seen in figure 1.10. The p-contact can be made thick and reflective, thus doubling the theoretical extraction efficiency. Another advantage of this technique is improved thermal management, as the thick metal bumps conduct heat from the active area of the LED and the silicon mount acts as a heat sink.

1.1.3 Micro-LEDs

As shown in figure 1.9, typical GaN LEDs have active area greater than $350 \times 350\ \mu\text{m}^2$. However, for some specialised applications, having LED devices with a small (10–100 μm sized) emission area can be very beneficial. This type of device can be used in for instance biological applications, e.g., neuron stimulation [25], sectioned imaging [26], and micro-fluidics [27], and also for lithography as we will show [28, 29].

These devices have been fabricated, by the Institute of Photonics (IoP) at Strathclyde University, in several different formats including rings (figure 1.11(a)), disks (figure 1.11(b)), and stripes (figure 1.12) in GaN based materials. The sizes, from below 10 μm to conventional LED sizes of several hundred μm, are defined by conventional photolithography (section 1.2) and etched by inductively coupled plasma (ICP) dry etching (for more information about this technique see [31]). This leaves mesa structures, which function as light emitting pixels, in the epitaxial layers. The device thus formed, consisting of many μm-sized pixels, is referred to as a 'micro-LED array'. One of the first beneficial properties that was

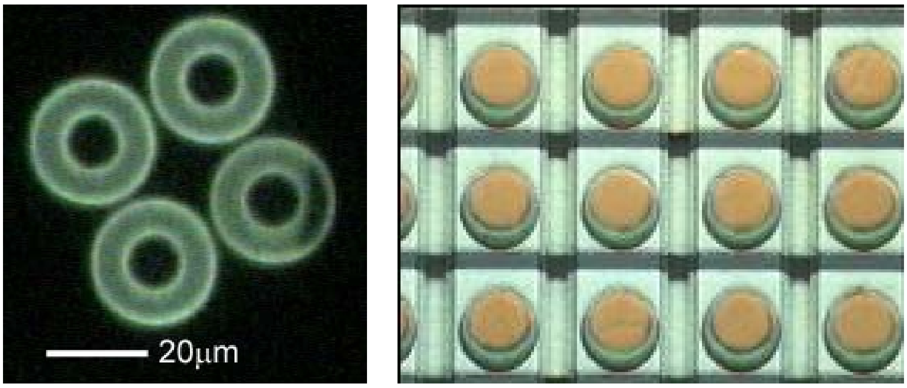

(a) Optical micrograph of device with ring shaped mesa structures. The rings have an outer diameter of 20 μm and inner diameter of 12 μm [30].

(b) Optical micrograph of device with disk shaped mesa structures. The disks have a diameter of 20 μm and the pixel to pixel pitch is 50 μm.

Figure 1.11: Optical micrographs of representative formats of micro-LED devices.

discovered in this micro-pixel format was that the extraction efficiency increases relative to 'broad area' LEDs of the same total active area. This was attributed to the scattering of light, which normally would be trapped by total internal reflection, from the sidewalls.

Several modes of addressing these devices have been developed, including parallel- [32], matrix- [33], and individual-addressing [34]. The n-type GaN has a relatively high conductance and hence a common n-contact can be used to address all pixels. In parallel addressing a common p-contact used as well, i.e., all the pixels of the device will turn on at the same time. The main advantage of this type of device is the increased extraction efficiency, giving higher per light emission area optical output power. A matrix addressing scheme, where a grid electrode arrangement is used, connecting devices in rows and columns, is well suited for high resolution micro-displays with many pixels. The number of contacts required

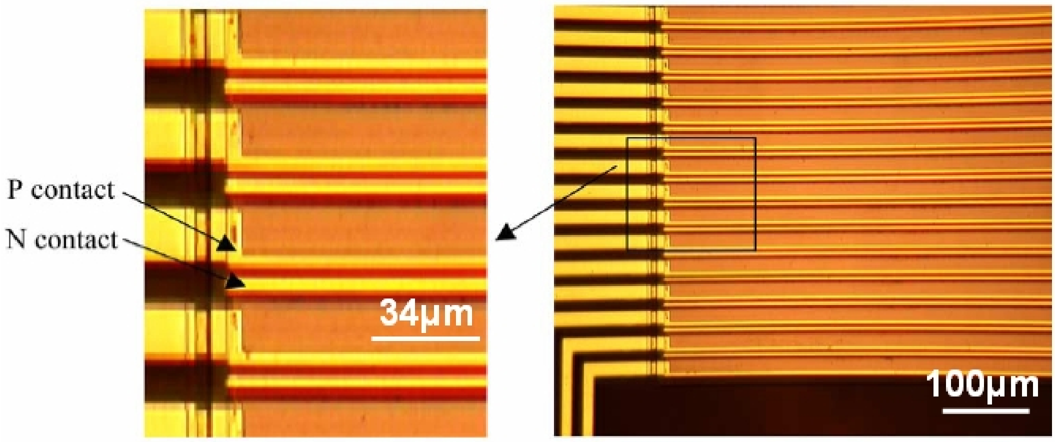

Figure 1.12: Optical micrographs of a micro-stripe device. The emitting area of each stripe measures 20 μm × 3600 μm and the stripe-to-stripe pitch is 34 μm.

to address each pixel is $m + n$ for a device with $m \times n$ pixels, in contrast to the $m \times n + 1$ contacts required for individual addressing (each pixel requires two contacts, but the n-contact can be common to all pixels). One drawback is however that to display patterns of pixels other than row-column symmetrical patterns, a driving scheme is needed where for instance the rows are addressed in sequence, so that each frame or image is divided in time by the number of rows. While one row is being addressed the appropriate columns are also addressed, then moving to the next row and so forth. If this is done fast enough the eye will not register flickering and the image appears stable on the micro-display. However any individual device will be duty cycled and does not operate continuously. This is also the technique used for addressing in modern flat-screen liquid crystal displays (LCDs). For some applications instant addressing access to each pixel can be more important than limitations in the number of contacts, in which case an individual addressing scheme needs to be used. A major leap forward for this type of addressing was the integration of a micro-LED array with a CMOS driver

[35]. This allows not only for individual addressing by bump bonding each pixel individually to the CMOS chip (cf. figure 1.10), but also for unique control of the electrical injection to each pixel. The injection current is regulated by on-chip controls in the CMOS and can, for example, be pulsed down to sub-nanosecond durations or modulated at high frequencies.

Devices fabricated in the IoP have wavelengths spanning from UV (370 nm) to green (∼500 nm), via violet (405 nm) and blue (450 nm and 470 nm). These devices, particularly those emitting in the UV, form the basis of much of the work described in this thesis.

1.1.4 Diode lasers

The first report of the emission of coherent light from a semiconductor emitter was made by Hall et al. in 1962 [36] and the first visible diode laser was reported later the same year by Holonyak et al. [37]. Both used GaAs-based material systems. The first reliable laser diode with blue emission was achieved by Nakamura in 1995 [38], based on an InGaN MQW structure.

Diode lasers (light amplification by stimulated emission of radiation) are semiconductor light emitters, which emit coherent light by the process of stimulated emission using electrical pumping. In contrast to LEDs, stimulated emission is the dominant process rather than spontaneous emission. A simple schematic of this process can be seen in figure 1.13. The probability of this process is dependent on the density of photons with appropriate energy for stimulating the emission of a photon in the active region. Three conditions are generally needed to be fulfilled for laser action:

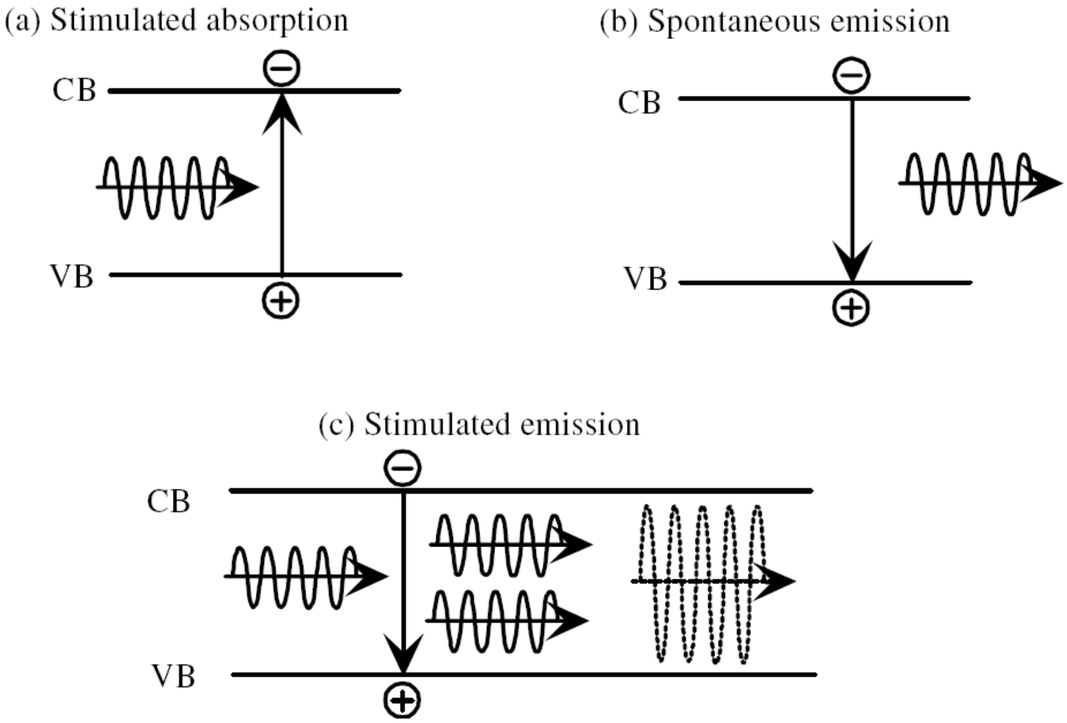

Figure 1.13: Schematic diagram of stimulated emission in a two level system. The photon generated from stimulated emission has the same energy, phase, polarisation and direction as the photon which stimulated the emission. The probability of the stimulated process depends on the density of photons which can stimulate the emission. After [9].

1. Population inversion, i.e., a higher number of atoms, molecules, etc. in excited states than in lower energy states.
2. Losses have to be lower than the gain in one roundtrip of the laser cavity.
3. The active region has to be contained in a cavity with a suitable optical resonance for stimulated emission.

In diode lasers the population inversion required for laser action is produced by electrical injection. The second requirement was the most difficult to fulfil for diode lasers since the active (gain) region is very thin, often a fraction of the light wavelength [36]. For QW diode lasers this is an even more crucial problem and is solved by more effectively guiding the light into the active area by separate confinement layers (cf. figure 1.9(b))[39]. Diode lasers have optical feedback to provide a laser cavity. The feedback can be provided simply by the facets (cleaved edges) of the semiconductor die making a Fabry-Perot cavity (as in [36]), by a grating, e.g., in distributed feedback (DFB) lasers [40], distributed Bragg reflector (DBR) lasers [41], and vertical-cavity surface-emitting laser (VCSEL) [42], or by external mirrors, e.g., in vertical-external-cavity surface-emitting-laser (VECSEL) [43].

Of special interest for this work are ultraviolet-emitting laser diodes. The first report of direct laser diode emission in the UV was in 2001 [44]. The asymmetry in the guided mode (typically much thinner perpendicular to the junction than parallel to it) leads to astigmatic and highly divergent output in a typical Fabry-Perot format laser diode (figure 1.15). Circularising optics are therefore required to produce a symmetric beam.

1.2 Micro-patterning techniques

There are a number of different ways of micro- and nano-patterning organic materials and transferring these patterns to a substrate (usually a subsequent etching step). Micropatterning is not only of interest in semiconductor manufacturing, but also in microelectromechanical systems (MEMS), microfluidic devices, microsensors, and increasingly for organic electronics and organic-LEDs (OLEDs). This section will introduce a few of the relevant techniques.

Of special interest for this work are maskless photolithography techniques. Laser direct writing (LDW) will be described in chapter 3 and section 4.1 will

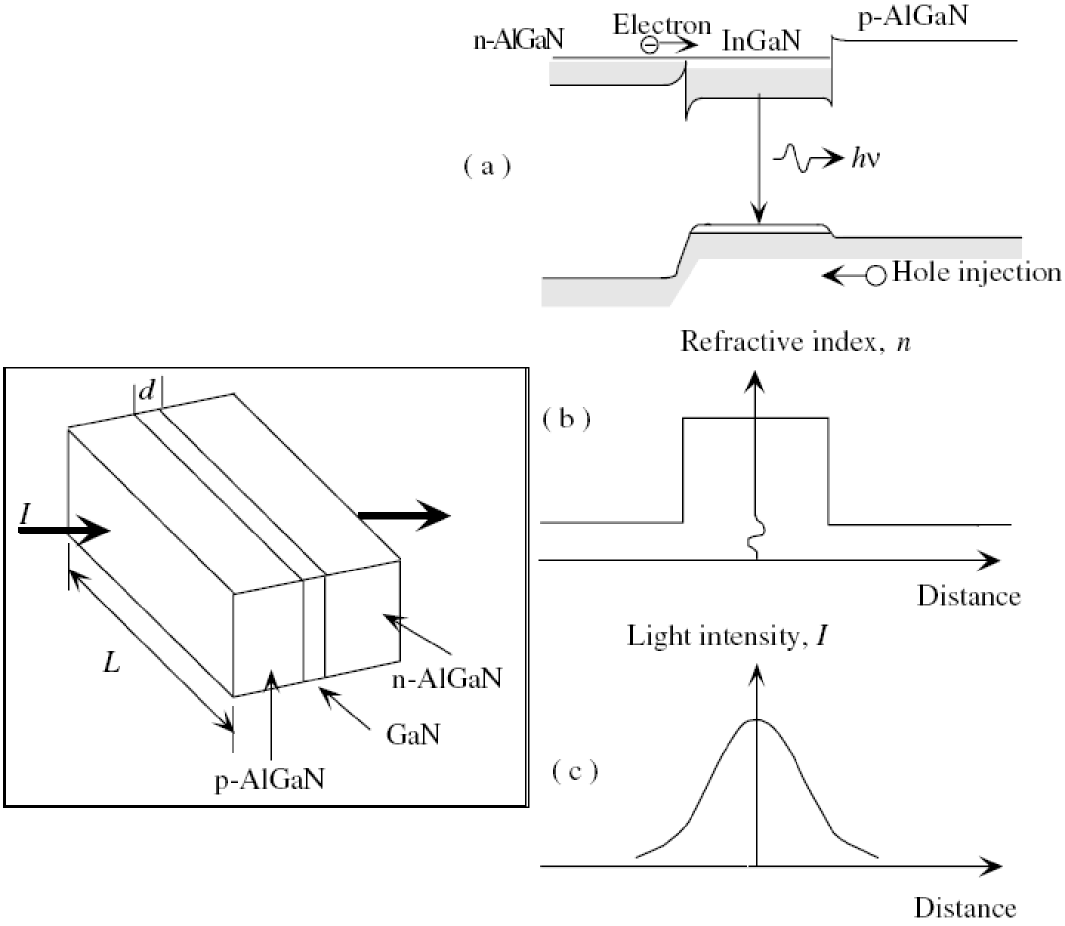

Figure 1.14: Simple schematic of a diode laser. Light is guided in the gain/active region by lower refractive index (cladding layer, AlGaN in the image) regions outside the active region (GaN in the image). In the simplest form, feedback is provided by the facets of the edges. (a) shows the conduction and valence band edge vs. distance through the device structure, (b) shows the corresponding refractive index, and (c) the guided light profile along the junction. After [9].

present a brief review of other maskless patterning techniques, such as electron beam lithography (EBL), focused ion beam (FIB), interference lithography (IL), and zone-plate-array lithography (ZPAL).

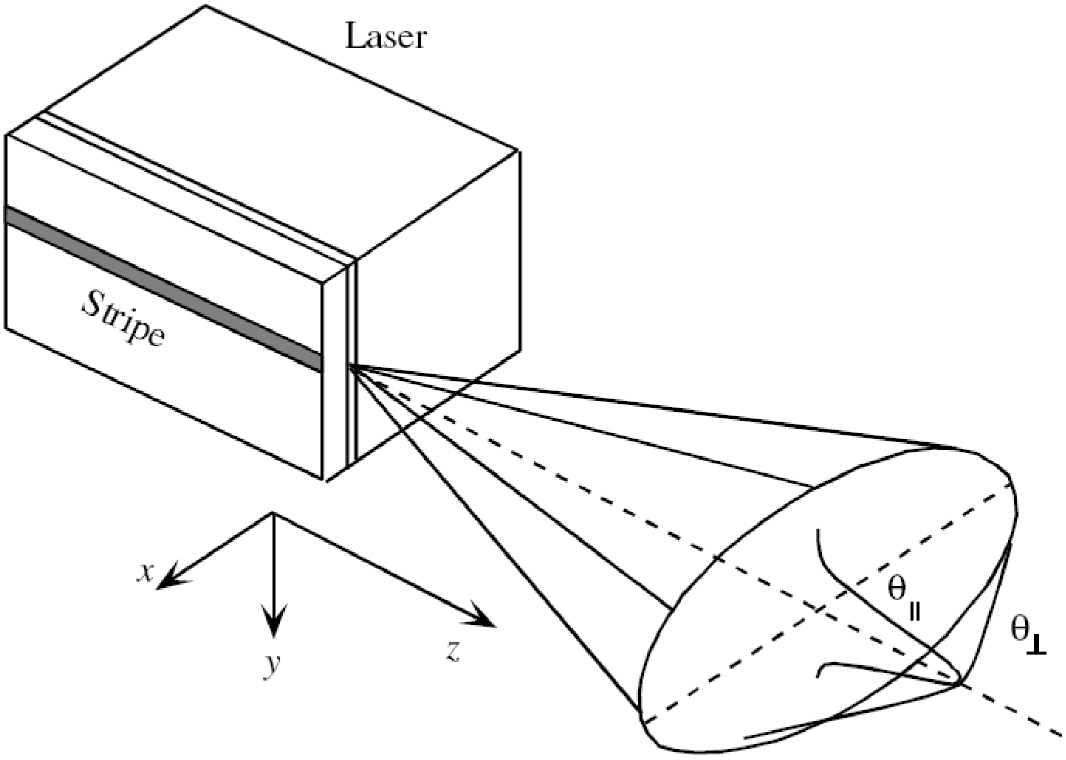

Figure 1.15: Simple schematic representation of an edge emitting diode laser and the far-field characteristics. Such a device typically emits an astigmatic and asymmetric output beam. After [9].

1.2.1 Conventional photolithography

To pattern semiconductor wafers to manufacture devices such as LEDs, the most commonly used technique is photolithography, also known as optical lithography. In this method, the semiconductor wafer is covered with a photosensitive (organic, normally polymer) material, a photoresist. Light is shone through a photomask, which defines the desired exposure pattern. The resist reacts to light of a certain wavelength and decomposes and becomes soluble in the case of a positive resist or cures and becomes insoluble in the case of a negative resist. More details about these materials will be given in section 2.1.

Figure 1.16 shows a schematic image of an exposure in a photolithographic

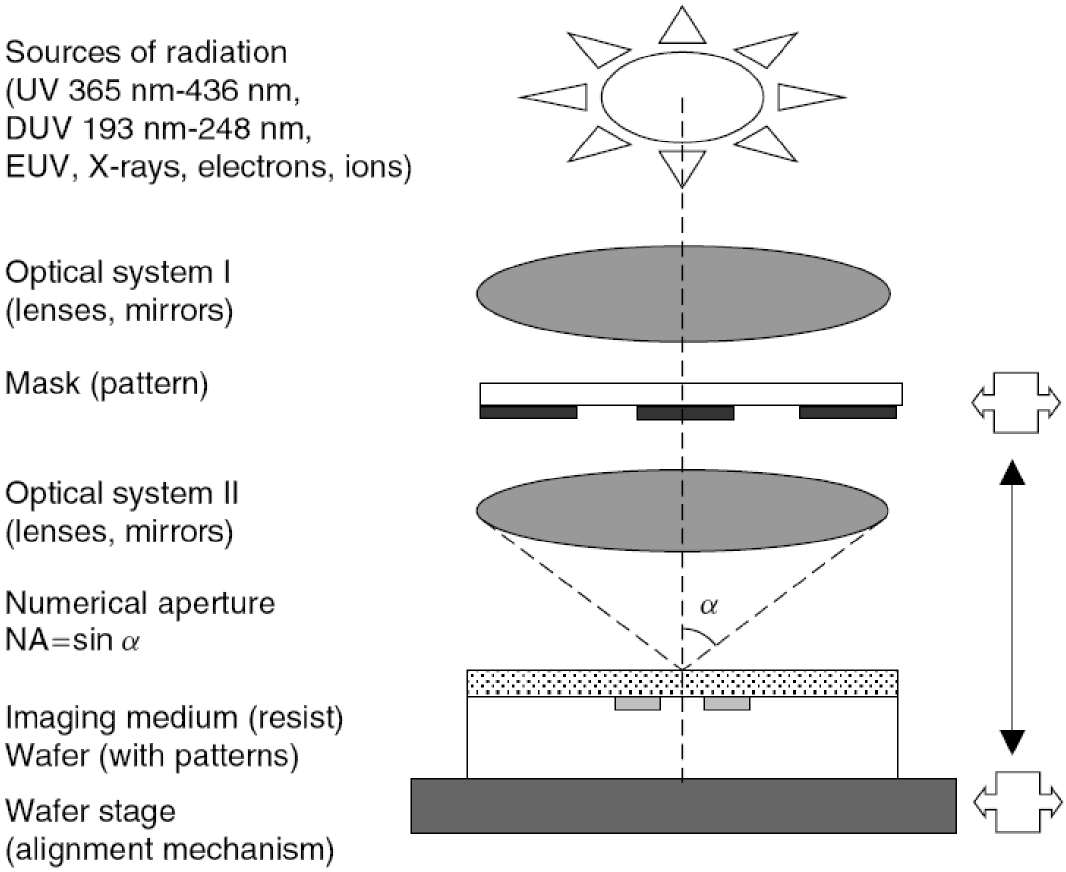

Figure 1.16: Schematic of photolithographic exposure. The wafer is covered with a photosensitive film which is exposed by the pattern defined by the photomask. After [45].

process. By the optical system the pattern on the photomask can be demagnified in principle down to the diffraction limit of the system. The diffraction limit is commonly given by the Rayleigh relations:

$$\text{resolution} = \frac{k_1\lambda}{N.A.} \tag{1.4}$$

and

$$\text{depth of focus} = \frac{k_2\lambda}{N.A.^2} \tag{1.5}$$

where λ is the wavelength of the light used for the exposure, N.A. is the numerical aperture of the system, and k_1 and k_2 are parameters of the system, the mask and the resist [45]. Empirical measurements usually give k_1 of 0.5–1.0.

A major disadvantage of mask-based photolithography is the need of a hard photomask, which is time consuming and expensive to manufacture.

1.2.2 Ink-jet printing

A technique for printing solution processed materials, such as nanoparticles (quantum dots, metal particles, etc.), organic materials (light emitting and conducting polymers etc.), and even biosamples, is inkjet printing. The principle behind inkjet printing in micropatterning is the same as in printing in standard office inkjet printers. By techniques called drop-on-demand (DOD) a small amount of liquid material is propelled onto a substrate in a controlled manner. In figure 1.17 a schematic picture of a typical inkjet printing setup can be seen.

Advantages of this technique is that it does not require a photomask and that it is flexible concerning what materials can be used. Any materials with low enough viscosity can in principle be inkjet printed. One disadvantage is complicated manner in which solvents dry from a spherical surface, often leaving 'coffee stain' patterns after evaporation. The resolution is highly dependent not only on the drop size, but also on the substrate and the material printed (surface interaction between the two materials) and is not usually below 100 μm on untreated surfaces [47] however feature sizes down to 2 μm has been achieved [48], by small volume droplets printed onto appropriately prepared surfaces.

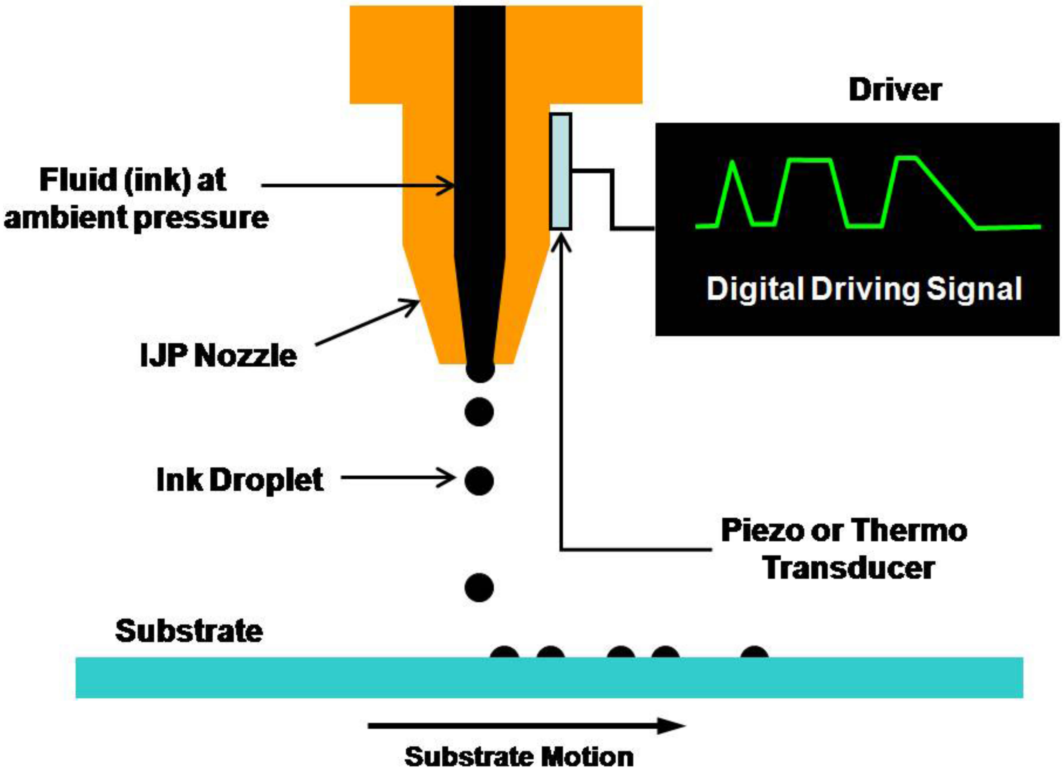

Figure 1.17: A schematic image of a typical setup for inkjet printing. After [46].

1.2.3 Nanoimprint lithography and nanotransfer printing

Nanoimprint lithography (NIL) is a technique for making patterns, of predominately organic material, with a high resolution. In NIL a mould is used to imprint a pattern in a polymer or monomer film on a surface. The film is cured thermally or by UV exposure, the mould is then lifted and the pattern has been imprinted in the cured polymer. In figure 1.18(b) a schematic for the process flow in a special kind of NIL technique called step-and-flash imprint lithography (SFIL) can be seen. A related technique is transfer printing, where a mould is used to lift a layer of molecules from one surface and transfer it to another surface (see figure 1.18(a)). In [49] a commercial optical adhesive (urethane-related photopolymer)

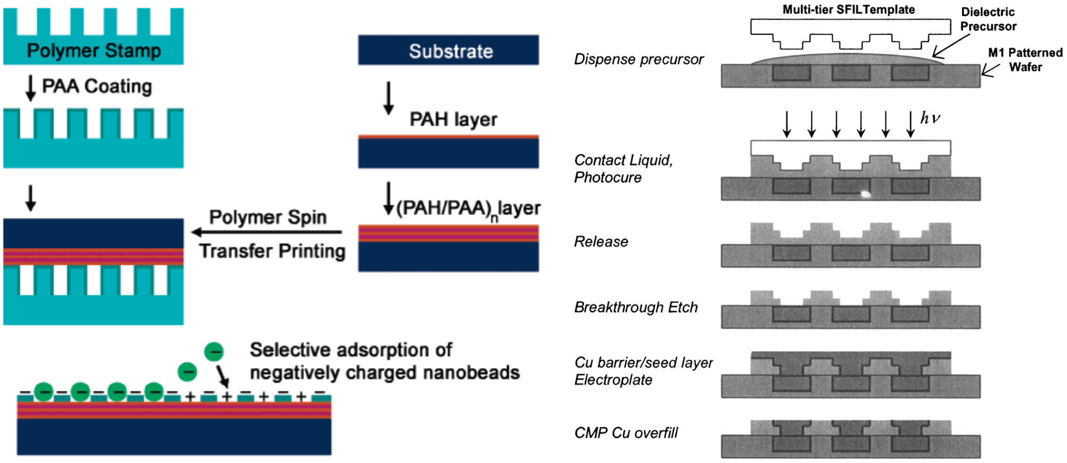

(a) Schematic image of the process flow in polymer spin transfer printing. After [49].

(b) Schematic of the process flow in SFIL. After [51].

Figure 1.18: Process flow in two mould based patterning techniques.

is used for producing the mould and feature sizes down to 80 nm are shown. The resolution is limited by the mould and features down to at least 5 nm have been demonstrated with NIL [50].

While these techniques represent very powerful methods to produce patterns with very high resolution, an obvious disadvantage is the need to produce a very high quality mould.

1.3 Nanoluminophores

’Nanoluminophores’ is the collective name given to luminescent nanoengineered materials. They can be organic or inorganic. For the purpose of the structure of this thesis, conjugated light emitting polymers (LEPs) will also be introduced here.

One important measure of the performance of luminophores is the photoluminescence quantum yield. It is defined as the ratio of absorbed photons to emitted photons:

$$\Phi_{QY} = \frac{\#\text{ photons emitted}}{\#\text{ photons absorbed}} \tag{1.6}$$

1.3.1 Semiconductor nanocrystals

An emerging technology that has found applications in several different fields is semiconductor nanocrystal quantum dots (NQDs). These are very small (normally ≤10 nm) semiconductor crystals normally suspended in a solvent and showing three dimensional quantum confinement. Quantum confinement means that the structure size is smaller than the mean exciton Bohr radius (the spatial separation between hole and electron after excitation). As in the case of quantum wells this will affect the bandgap structure of the material. In fact the bandgap is related to the size of the nanocrystal and can thus be tuned by engineering the size of the quantum dot [52]. This is known as the "quantum size effect". Figure 1.19 shows for comparison a schematic of the bandgap structure in a bulk semiconductor and in a nanocrystal.

Nanocrystal quantum dots have been synthesised with emission covering the visible spectral range [54] and near infrared [55]. These structures are normally produced by chemical means. The inorganic core of the solution processed NQD is covered with organic ligands to avoid aggregation. The NQDs are synthesised by pyrolysis of metalorganic precursors in hot coordinating solvents. Nucleation is started when the precursors are injected into the hot solvents (120-360°C) and is followed by a relatively rapid growth and finally a slower growth [56].

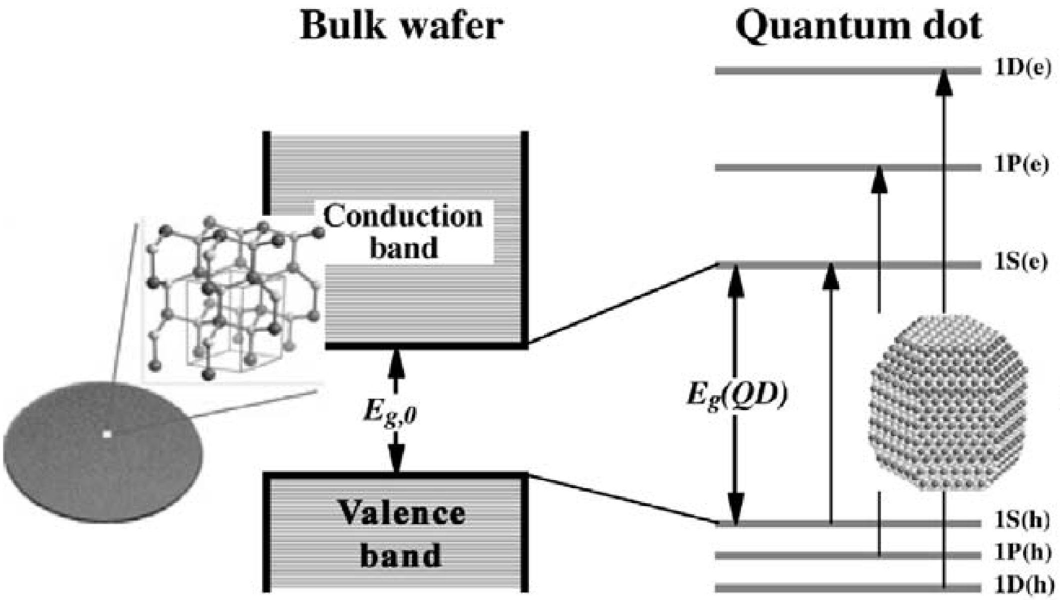

Figure 1.19: In bulk semiconductor the bandgap is fixed and the valance and conduction band are continuous, while QDs have discrete atom-like energy levels and the bandgap is affected by the size of the QD. After [53].

Aliquots (portions of the total amount) can be removed from the reaction chamber during the slow growth, by this method a range of different sized NQDs can be synthesised from the same batch. Figure 1.20 show a schematic of the growth and a representative reaction chamber for small volume synthesis of nanocrystals.

Because of their high quantum yield (typically 30–50%), environmental stability, high bleaching threshold, broadband absorption spectrum, and narrow and tuneable emission wavelength nanocrystals have been put to use in various applications. For instance QDs have been used in selective biological labelling [57], for photovoltaics [58, 59], for LEDs [60], lasers [61], and for colour conversion for white light generation [62, 63].

The nanocrystal quantum dots of special interest for this work have a cadmium selenide (CdSe) core capped with a zinc sulphide (ZnS) shell. More detail about

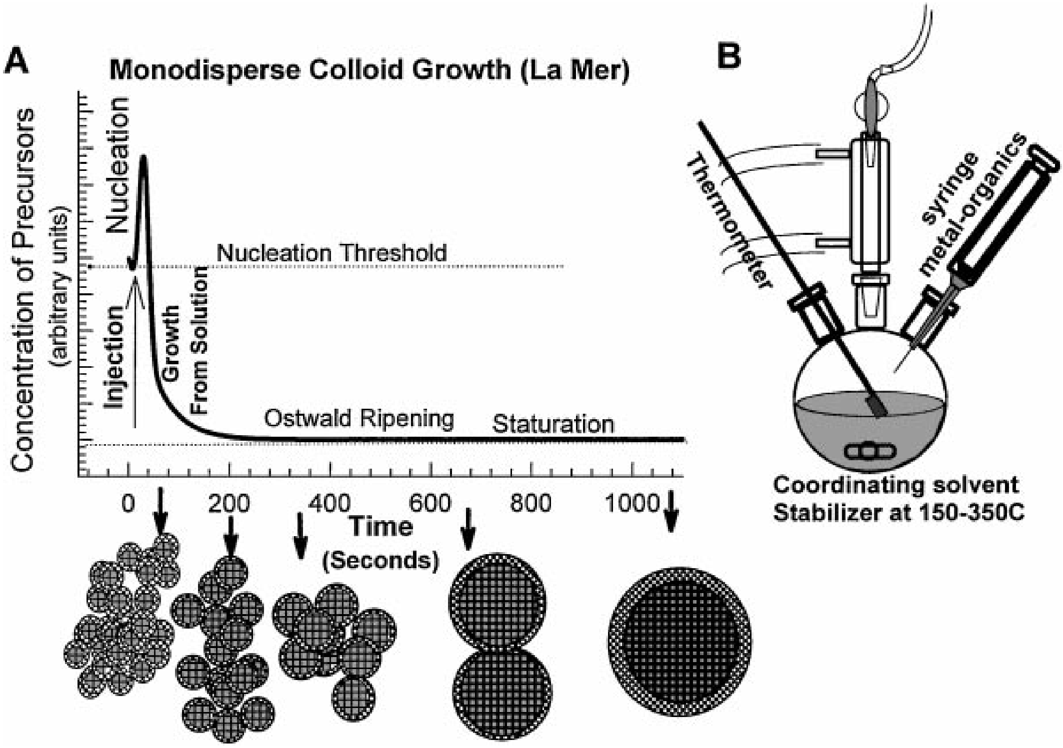

Figure 1.20: Schematic showing the synthesis process of nanocrystal quantum dots. The NQDs grow with time and by removing aliquots periodically from the reaction chamber, different size NQDs can be synthesised from the same batch. After [56].

this type of nanocrystals is given in section 2.2.2.

1.3.2 Organic Light emitters

A category of materials that have generated much interest in recent years is organic materials with semiconductor-like characteristics, i.e., organic semiconductors. Since the first report on the use of these materials for light emitting diodes at the beginning of the 1990s [64], conjugated polymers, which can show such semiconducting properties, have been the focus of much research because of their processability and beneficial optical properties. Their semiconductor-like electrical properties originate from the delocalised π-bonds in the polymer backbone. The bond is delocalised when the organic molecule has alternating single and multiple bonds; this is called conjugation. The “bandgap” of this kind of polymer is defined as the gap between the lowest unoccupied molecular orbital (LUMO) and the highest occupied molecular orbital (HOMO). The process by which one of these molecules absorbs and emits light can be understood with the help of a Jablonski energy diagram (see figure 1.21). A photon is absorbed and an electron in the HOMO (or a lower orbit) gets excited to the LUMO (or a higher orbit). This is a fast process ($\sim 10^{-15}$s) and it is followed by vibrational relaxation and internal conversion to the lowest orbital from which the relaxation requires the emission of a photon, i.e., fluorescence (10^{-9}–10^{-7}s), a non-radiative relaxation, or intersystem crossing to a triplet state. The last process is undesirable for many applications as it has a slow relaxation rate (10^{-3}–10^{2}s). Alternatively, the excitation can be made by electrical injection, giving electrical luminescence (EL) in contrast to photoluminescence (PL).

1.4 Summary

In this chapter some concepts that form the basis of this thesis work have been introduced. The history and theory of light emitting diodes based on direct bandgap materials, in particular GaN, was briefly presented. The benefits of micro-pixellated LEDs for applications in biology, instrumentation, and lithography have been introduced. Laser diodes were also briefly discussed.

Basic techniques of micropatterning were presented and the need for low cost maskless techniques explained.

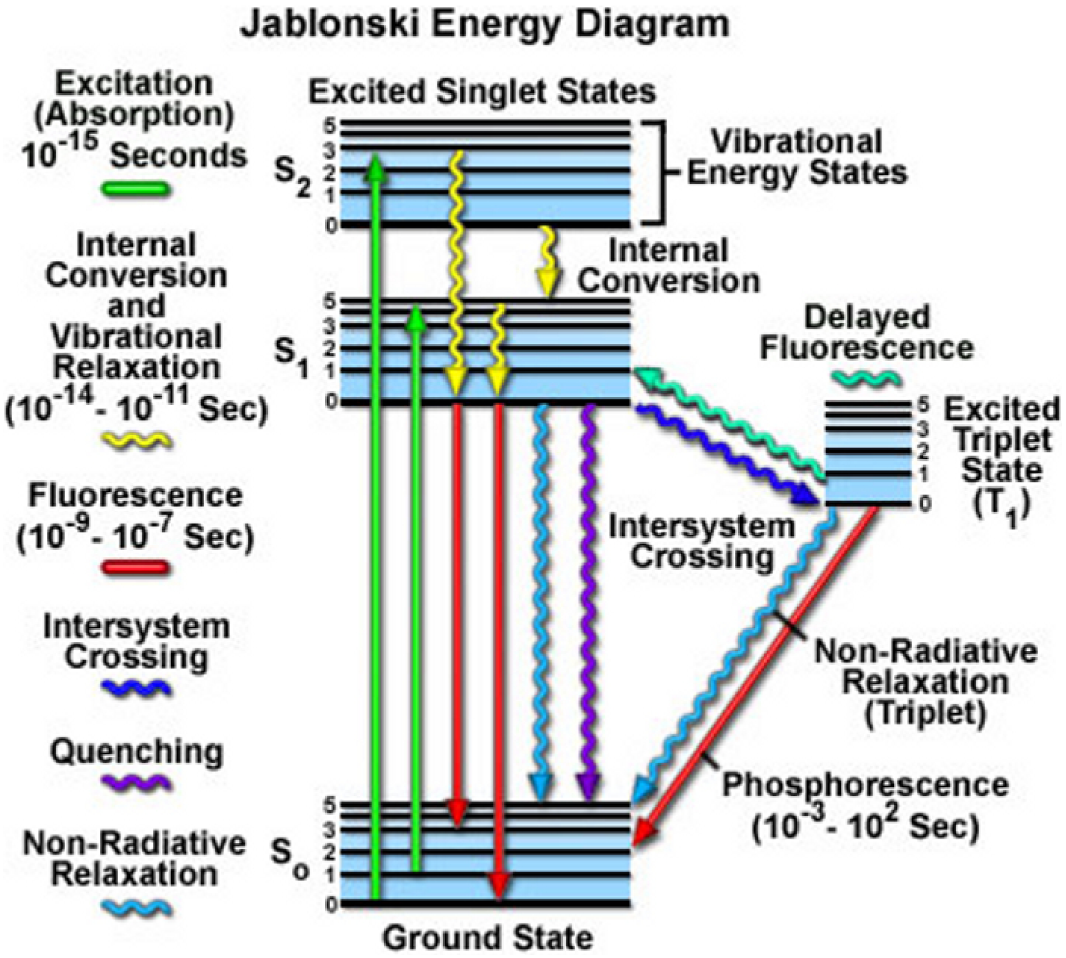

Figure 1.21: Jablonski energy diagram showing the different routes by which energy is converted in an organic molecule. After [65].

The concept of nanoluminophores was introduced and explained. Nanocrystal quantum dots and their beneficial luminescence characteristics were presented. Also organic light emitting materials were introduced and the basis of their light emission processes was schematically given.

References

[1] H. J. Round. A note on carborundum. *Electrical World*, 49:309, 1907. 4

[2] O. V Losev. Luminous carborundum [silicon carbide] detector and detection with crystals. *Telegrafiya i Telefoniya bez Provodov*, 44:485494, 1927. 4

[3] Nikolay Zheludev. The life and times of the LED - a 100-year history. *Nat Photon*, 1(4):189–192, 2007. 10.1038/nphoton.2007.34. 4

[4] R. Braunstein. Radiative transitions in semiconductors. *Phys. Rev.*, 99(6):1892–1893, Sep 1955. 4

[5] Shuji Nakamura, Takashi Mukai, and Masayuki Senoh. High-power GaN p-n junction blue-light-emitting diodes. *Japanese Journal of Applied Physics*, 30(Part 2, No. 12A):L1998–L2001, 1991. 4

[6] Isamu Akasaki and Hiroshi Amano. Widegap column-III nitride semiconductors for uv/blue light emitting devices. *Journal of The Electrochemical Society*, 141(8):2266–2271, 1994. 4

[7] E. Fred Schubert and Jong Kyu Kim. Solid-State Light Sources Getting Smart. *Science*, 308(5726):1274–1278, 2005. 5

[8] `http://techon.nikkeibp.co.jp/english/NEWS_EN/20061221/125713/`. 5

[9] Hadis Morkoc. *Handbook of Nitride Semiconductors and Devices.* WILEY-VCH Verlag GmbH, 2009. v, vi, 5, 15, 20, 22, 23

[10] E. F. Schubert. *Light-Emitting Diodes - 2nd Edition.* Cambridge University Press, June 2006. v, 8, 13

[11] E. F. Schubert. *Light-Emitting Diodes.* Cambridge University Press, June 2003. v, 7, 9, 11, 12

[12] R. Dingle, W. Wiegmann, and C. H. Henry. Quantum states of confined carriers in very thin Al_x Ga_{1-x} As - GaAs - $\mathrm{Al}_x\mathrm{Ga}_{1-x}$ As heterostructures. *Phys. Rev. Lett.*, 33(14):827–830, Sep 1974. 9

[13] E. A. Rezek, Jr. N. Holonyak, B. A. Vojak, and H. Shichijo. Single and multiple thin-layer ($\mathrm{L}_z < \sim$400 å) In_{1-x} Ga_x P_{1-z} As_z - InP heterostructure light emitters and lasers (lambda 1.1 μm, 77K). *Journal of Applied Physics*, 49(1):69–74, 1978. 10

[14] Reiko Soejima, Akito Kuramata, Shin ichi Kubota, Kay Domen, Kazuhiko Horino, and Toshiyuki Tanahashi. Continuous-wave operation at 250 K of InGaN multiple quantum well laser diodes grown on 6H-SiC with vertical conducting structure. *Japanese Journal of Applied Physics*, 37(Part 2, No. 10B):L1205–L1207, 1998. 10

[15] William Shockley. *Electrons and Holes in Semiconductors, With Applications to Transistor Electronics.* D. Van Nostrand Company, 1950. 10

[16] H. P. Maruska and J. J. Tietjen. The preparation and properties of vapor-deposited single-crystalline GaN. *Applied Physics Letters*, 15(10):327–329, 1969. 12

[17] J.I. Pankove, E.A. Miller, and J.E. Berkeyheiser. GaN electroluminescent diodes. In *Electron Devices Meeting, 1971 International*, volume 17, pages 78–78, 1971. 13

[18] Hiroshi Amano, Masahiro Kito, Kazumasa Hiramatsu, and Isamu Akasaki. P-type conduction in Mg-doped GaN treated with low-energy electron beam irradiation (LEEBI). *Japanese Journal of Applied Physics*, 28(Part 2, No. 12):L2112–L2114, 1989. 13

[19] Shuji Nakamura, Masayuki Senoh, Naruhito Iwasa, and Shin ichi Nagahama. High-power InGaN single-quantum-well-structure blue and violet light-emitting diodes. *Applied Physics Letters*, 67(13):1868–1870, 1995. 13, 14

[20] Gregory A. Garrett, Craig G. Moe, Meredith L. Reed, Michael Wraback, Wenhong Sun, Max Shatalov, Xuhong Hu, Jinwei Yang, Yuriy Bilenko, Alex Lunev, Michael S. Shur, and Remis Gaska. Time-resolved photoluminescence studies of AlGaN-based deep UV LED structures emitting down to 229 nm. In *Conference on Lasers and Electro-Optics/International Quantum Electronics Conference*, page CMEE2. Optical Society of America, 2009. 13

[21] Takashi Mukai, Motokazu Yamada, and Shuji Nakamura. Characteristics

of InGaN-based UV/blue/green/amber/red light-emitting diodes. *Japanese Journal of Applied Physics*, 38(Part 1, No. 7A):3976–3981, 1999. 14

[22] S. J. Pearton, F. Ren, A. P. Zhang, and K. P. Lee. Fabrication and performance of GaN electronic devices. *Materials Science and Engineering: R: Reports*, 30(3-6):55 – 212, 2000. 14

[23] J. M. Van Hove, R. Hickman, J. J. Klaassen, P. P. Chow, and P. P. Ruden. Ultraviolet-sensitive, visible-blind GaN photodiodes fabricated by molecular beam epitaxy. *Applied Physics Letters*, 70(17):2282–2284, 1997. 14

[24] T. Margalith, O. Buchinsky, D. A. Cohen, A. C. Abare, M. Hansen, S. P. DenBaars, and L. A. Coldren. Indium tin oxide contacts to gallium nitride optoelectronic devices. *Applied Physics Letters*, 74(26):3930–3932, 1999. 15

[25] V. Poher, N. Grossman, G. T. Kennedy, K. Nikolic, H. X. Zhang, Z. Gong, E. M. Drakakis, E. Gu, M. D. Dawson, P. M. W. French, P. Degenaar, and M. A. A. Neil. Micro-LED arrays: a tool for two-dimensional neuron stimulation. *Journal of Physics D: Applied Physics*, 41(9):094014 (9pp), 2008. 16

[26] V. Poher, H. X. Zhang, G. T. Kennedy, C. Griffin, S. Oddos, E. Gu, D. S. Elson, M. Girkin, P. M. W. French, M. D. Dawson, and M. A. Neil. Optical sectioning microscopes with no moving parts using a micro-stripe array light emitting diode. *Opt. Express*, 15(18):11196–11206, 2007. 16

[27] J. Alex Chediak, Zhongsheng Luo, Jeonggi Seo, Nathan Cheung, Luke P. Lee, and Timothy D. Sands. Heterogeneous integration of CdS filters with

GaN LEDs for fluorescence detection microsystems. *Sensors and Actuators A: Physical*, 111(1):1 – 7, 2004. Micromechanics section of Sensors and Actuators, based on contributions revised from the Technical Digest of the 16th IEEE International conference on Micro Electro mechanical Systems (MEMS 2003). 16

[28] C. W. Jeon, E. Gu, and M. D. Dawson. Mask-free photolithographic exposure using a matrix-addressable micropixellated AlInGaN ultraviolet light-emitting diode. *Applied Physics Letters*, 86(22):221105, 2005. 16

[29] D. Elfström, B. Guilhabert, J. McKendry, S. Poland, Z. Gong, D. Massoubre, E. Richardson, B. R. Rae, G. Valentine, G. Blanco-Gomez, E. Gu, J. M. Cooper, R. K. Henderson, and M. D. Dawson. Mask-less ultraviolet photolithography based on CMOS-driven micro-pixel light emitting diodes. *Opt. Express*, 17(26):23522–23529, 2009. 16

[30] H. W. Choi, M. D. Dawson, P. R. Edwards, and R. W. Martin. High extraction efficiency InGaN micro-ring light-emitting diodes. *Applied Physics Letters*, 83(22):4483–4485, 2003. 17

[31] Jewon Lee, Hyun Cho, D.C. Hays, C.R. Abernathy, S.J. Pearton, R.J. Shul, G.A. Vawter, and J. Han. Dry etching of GaN and related materials: comparison of techniques. *Selected Topics in Quantum Electronics, IEEE Journal of*, 4(3):557–563, May/Jun 1998. 16

[32] H.W. Choi, C.W. Jeon, M.D. Dawson, P.R. Edwards, and R.W. Martin. Fabrication and performance of parallel-addressed InGaN micro-LED arrays. *Photonics Technology Letters, IEEE*, 15(4):510–512, April 2003. 17

[33] C.W. Jeon, H.W. Choi, and M.D. Dawson. Fabrication of matrix-addressable InGaN-based microdisplays of high array density. *Photonics Technology Letters, IEEE*, 15(11):1516–1518, Nov. 2003. 17

[34] H.X. Zhang, E. Gu, C.W. Jeon, Z. Gong, M.D. Dawson, M.A.A. Neil, and P.M.W. French. Microstripe-array InGaN light-emitting diodes with individually addressable elements. *Photonics Technology Letters, IEEE*, 18(15):1681–1683, Aug. 2006. 17

[35] B R Rae, C Griffin, J McKendry, J M Girkin, H X Zhang, E Gu, D Renshaw, E Charbon, M D Dawson, and R K Henderson. CMOS driven micro-pixel LEDs integrated with single photon avalanche diodes for time resolved fluorescence measurements. *Journal of Physics D: Applied Physics*, 41(9):094011 (6pp), 2008. 19

[36] R. N. Hall, G. E. Fenner, J. D. Kingsley, T. J. Soltys, and R. O. Carlson. Coherent light emission from GaAs junctions. *Phys. Rev. Lett.*, 9(9):366–368, Nov 1962. 19, 20, 21

[37] Nick Holonyak Jr. and S. F. Bevacqua. Coherent (visible) light emission from Ga(As_{1-x} P_x) junctions. *Applied Physics Letters*, 1(4):82–83, 1962. 19

[38] Shuji Nakamura, Masayuki Senoh, Shin ichi Nagahama, Naruhito Iwasa, Takao Yamada, Toshio Matsushita, Hiroyuki Kiyoku, and Yasunobu Sugimoto. InGaN-based multi-quantum-well-structure laser diodes. *Japanese Journal of Applied Physics*, 35(Part 2, No. 1B):L74–L76, 1996. 19

[39] W. T. Tsang. Extremely low threshold (AlGa)As graded-index waveguide

separate-confinement heterostructure lasers grown by molecular beam epitaxy. *Applied Physics Letters*, 40(3):217–219, 1982. 21

[40] H. Kogelnik and C. V. Shank. Coupled-wave theory of distributed feedback lasers. *Journal of Applied Physics*, 43(5):2327–2335, 1972. 21

[41] R. D. Dupuis and P. D. Dapkus. Room-temperature operation of distributed-Bragg-confinement Ga_{1-x} Al_x As-GaAs lasers grown by metalorganic chemical vapor deposition. *Applied Physics Letters*, 33(1):68–69, 1978. 21

[42] J.L. Jewell, J.P. Harbison, A. Scherer, Y.H. Lee, and L.T. Florez. Vertical-cavity surface-emitting lasers: Design, growth, fabrication, characterization. *Quantum Electronics, IEEE Journal of*, 27(6):1332–1346, Jun 1991. 21

[43] M. Kuznetsov, F. Hakimi, R. Sprague, and A. Mooradian. High-power (>0.5 W CW) diode-pumped vertical-external-cavity surface-emitting semiconductor lasers with circular TEM00 beams. *Photonics Technology Letters, IEEE*, 9(8):1063–1065, Aug. 1997. 21

[44] Shin ichi Nagahama, Tomoya Yanamoto, Masahiko Sano, and Takashi Mukai. Ultraviolet GaN single quantum well laser diodes. *Japanese Journal of Applied Physics*, 40(Part 2, No. 8A):L785–L787, 2001. 21

[45] Sami Franssila. *Introduction to microfabrication.* John Wiley and Sons, 2004. vi, 24, 25

[46] Jun Xu, Chengmei Zhong, and Chun Fu. Novel method for printing high-quality metal wires. *SPIE Newsroom*, 2007. vi, 26

[47] T. H. J. van Osch, J. Perelaer, A. W. M. de Laat, and U. S. Schubert. Inkjet printing of narrow conductive tracks on untreated polymeric substrates. *Advanced Materials*, 20(2):343–345, 2008. 25

[48] Tsuyoshi Sekitani, Yoshiaki Noguchi, Ute Zschieschang, Hagen Klauk, and Takao Someya. Organic transistors manufactured using inkjet technology with subfemtoliter accuracy. *Proceedings of the National Academy of Sciences of the United States of America*, 105(13):4976–80, 2008. 25

[49] Juhyun Park, Youn Sang Kim, and Paula T. Hammond. Chemically nanopatterned surfaces using polyelectrolytes and ultraviolet-cured hard molds. *Nano Letters*, 5(7):1347–1350, 2005. doi: 10.1021/nl050592p. 26, 27

[50] Michael D. Austin, Haixiong Ge, Wei Wu, Mingtao Li, Zhaoning Yu, D. Wasserman, S. A. Lyon, and Stephen Y. Chou. Fabrication of 5 nm linewidth and 14 nm pitch features by nanoimprint lithography. *Applied Physics Letters*, 84(26):5299–5301, 2004. 27

[51] Gerard M. Schmid, Michael D. Stewart, Jeffrey Wetzel, Frank Palmieri, Jianjun Hao, Yukio Nishimura, Kane Jen, Eui Kyoon Kim, Douglas J. Resnick, J. Alexander Liddle, and C. Grant Willson. Implementation of an imprint damascene process for interconnect fabrication. *Journal of Vacuum Science & Technology B: Microelectronics and Nanometer Structures*, 24(3):1283–1291, 2006. 27

[52] M. A. Reed, J. N. Randall, R. J. Aggarwal, R. J. Matyi, T. M. Moore, and

A. E. Wetsel. Observation of discrete electronic states in a zero-dimensional semiconductor nanostructure. *Phys. Rev. Lett.*, 60(6):535–537, Feb 1988. 28

[53] V. I. Klimov. *Semiconductor and Metal Nanocrystals.* Marcel Dekker, 2004. vi, 29

[54] B. O. Dabbousi, J. Rodriguez-Viejo, F. V. Mikulec, J. R. Heine, H. Mattoussi, R. Ober, K. F. Jensen, and M. G. Bawendi. (CdSe)ZnS coreshell quantum dots: Synthesis and characterization of a size series of highly luminescent nanocrystallites. *The Journal of Physical Chemistry B*, 101(46):9463–9475, 1997. doi: 10.1021/jp971091y. 28

[55] A. A. Lipovskii, E. V. Kolobkova, A. Olkhovets, V. D. Petrikov, and F. Wise. Synthesis of monodisperse PbS quantum dots in phosphate glass. *Physica E: Low-dimensional Systems and Nanostructures*, 5(3):157 – 160, 1999. 28

[56] C. B. Murray, C. R. Kagan, and M. G. Bawendi. Synthesis and characterization of monodisperse nanocrystals and close-packed nanocrystal assemblies. *Annual Review of Materials Science*, 30(1):545–610, 2000. vi, 28, 30

[57] W. J. Parak, T. Pellegrino, and C. Plank. TOPICAL REVIEW: Labelling of cells with quantum dots. *Nanotechnology*, 16:9–+, February 2005. 29

[58] A. J. Nozik. Quantum dot solar cells. *Physica E: Low-dimensional Systems and Nanostructures*, 14(1-2):115 – 120, 2002. 29

[59] Alexi C. Arango, David C. Oertel, Youfeng Xu, Moungi G. Bawendi, and Vladimir Bulovic. Heterojunction photovoltaics using printed colloidal quan-

tum dots as a photosensitive layer. *Nano Letters*, 9(2):860–863, 2009. doi: 10.1021/nl803760j. 29

[60] Jialong Zhao, Julie A. Bardecker, Andrea M. Munro, Michelle S. Liu, Yuhua Niu, I. Kang Ding, Jingdong Luo, Baoquan Chen, Alex K. Y. Jen, and David S. Ginger. Efficient CdSe/CdS quantum dot light-emitting diodes using a thermally polymerized hole transport layer. *Nano Letters*, 6(3):463–467, 2006. doi: 10.1021/nl052417e. 29

[61] Hans-Jürgen Eisler, Vikram C. Sundar, Moungi G. Bawendi, Michael Walsh, Henry I. Smith, and Victor Klimov. Color-selective semiconductor nanocrystal laser. *Applied Physics Letters*, 80(24):4614–4616, 2002. 29

[62] Sedat Nizamoglu, Evren Mutlugun, Tuncay Özel, Hilmi Volkan Demir, Sameer Sapra, Nikolai Gaponik, and Alexander Eychmüller. Dual-color emitting quantum-dot-quantum-well CdSe-ZnS heteronanocrystals hybridized on InGaN/GaN light emitting diodes for high-quality white light generation. *Applied Physics Letters*, 92(11):113110, 2008. 29

[63] Sedat Nizamoglu, Gülis Zengin, and Hilmi Volkan Demir. Color-converting combinations of nanocrystal emitters for warm-white light generation with high color rendering index. *Applied Physics Letters*, 92(3):031102, 2008. 29

[64] J. H. Burroughes, D. D. C. Bradley, A. R. Brown, R. N. Marks, K. Mackay, R. H. Friend, P. L. Burns, and A. B. Holmes. Light-emitting diodes based on conjugated polymers. *Nature*, 347(6293):539–541, 1990. 10.1038/347539a0. 30

[65] Ian D. Johnson and Michael W. Davidson. Olympus microscopy resource center: Fluorescence - jablonski energy diagram - interactive java tutorial. `http://www.olympusmicro.com/primer/java/jablonski/jabintro/index.html`, January 2010. vii, 32

Chapter 2

Materials

This chapter will introduce the different functional materials used in this thesis work. Some of the materials are off-the-shelf standard chemicals, while others are custom-produced by the Pure and Applied Chemistry department of the University of Strathclyde.

First the standard photoresist-type materials will be introduced. In this work, they are not only used as normal photoresists, but also as the matrix in different functional blend systems. As such, they not only provide the ability to pattern these materials by photolithographic methods, but also give environmental protection to the blended active material.

The second section will present the light emitting materials used. They are divided into organic molecules and inorganic semiconductor nanocrystals. The accepted collective name for these nanoengineered materials is ’nanoluminophores’. Applications for these materials will be briefly mentioned.

The last section will deal with nanocomposite materials consisting of the previously presented negative photoresists and nanoluminophores.

2.1 Photoresist materials

Photoresists are materials which react in a controlled manner when exposed to light of certain wavelengths. They are widely used in micro- and nano-manufacturing with photolithographic, also called optical lithographic, techniques (as presented in section 1.2). Most commonly, these techniques are used with a photomask, a transparent plate with opaque areas (e.g., chrome metal areas on transparent fused silica) that block light from shining through and thus create a defined exposure pattern. With this method large areas can be patterned very quickly and high yield is achieved. In small-scale patterning and prototyping, single beam techniques such as laser direct writing (LDW) are also used to define the pattern.

There are two types of photoresists, negative and positive (see figure 2.1). The names derive from photography and they make a positive or a negative image of the photomask on the substrate.

2.1.1 Negative photoresist

Negative type photoresists produce a negative image of a photomask, i.e., they cure and become insoluble when exposed to light of appropriate wavelength, typically in the near UV spectral range (300–400nm) . Negative resists are often used as etch masks, but can also be used directly for applications in e.g., waveguides [2], microfluidics [3], and photonic crystals [4].

In this work, two different types of negative photoresist are used, namely Norland Optical Adhesive (NOA), a commercial optical adhesive, and 1,4-cyclohexanedimethanol divinyl ether (CHDV) with an added photo curing agent, a

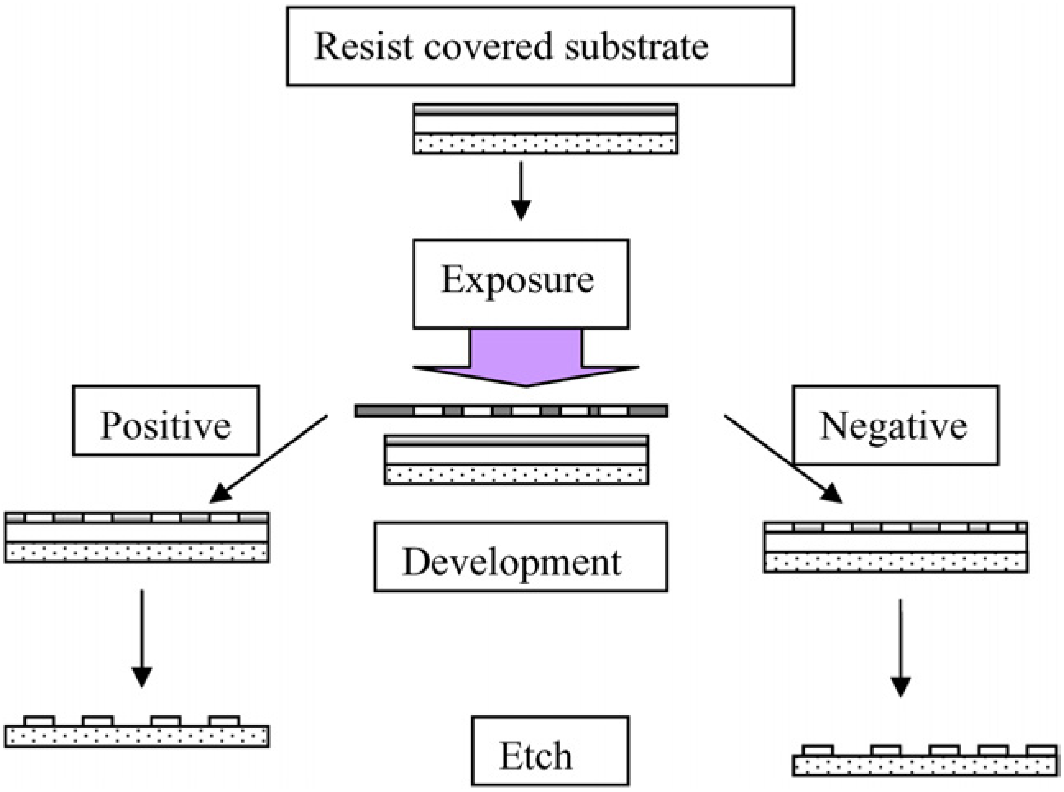

Figure 2.1: Photolithography process flow for positive- and negative-type photoresist. Negative photoresists form a negative image of the photomask after exposure and positive form a positive image. After [1].

photoacid generator (PAG). The second system, which was developed in-house, is referred to as high transparency polymer 3 (HTP3), the third in a series of customised polymers.

Norland optical adhesives: NOA are commercial products mostly used as adhesives in different applications, but as they cure with near UV light and are easy to handle and store, they make ideal candidates for testing UV writing capabilities. They come in several different types each with different characteristics, such as viscosity, adhesion strength to different substrates, and temperature stability. The type most used in this work is NOA81, which is a fast curing (low energy required for curing) polyurethane with excellent adhesion to glass and other substrates. It is photo-sensitive over the near UV range with peak sensitivity at 365 nm (the Hg *i*-line). The recommended dose for full cure is 2 J/cm^2 and maximum bonding strength is reached after one week in room temperature or 12 hours at 50°C. The viscosity at 25°C is 300 centipoise (cP) and spectral transmission is above 90% in the visible range (down to 400 nm) (see figure 2.2) [5]. NOA81 has been used for microfluidic channels [6] among other things.

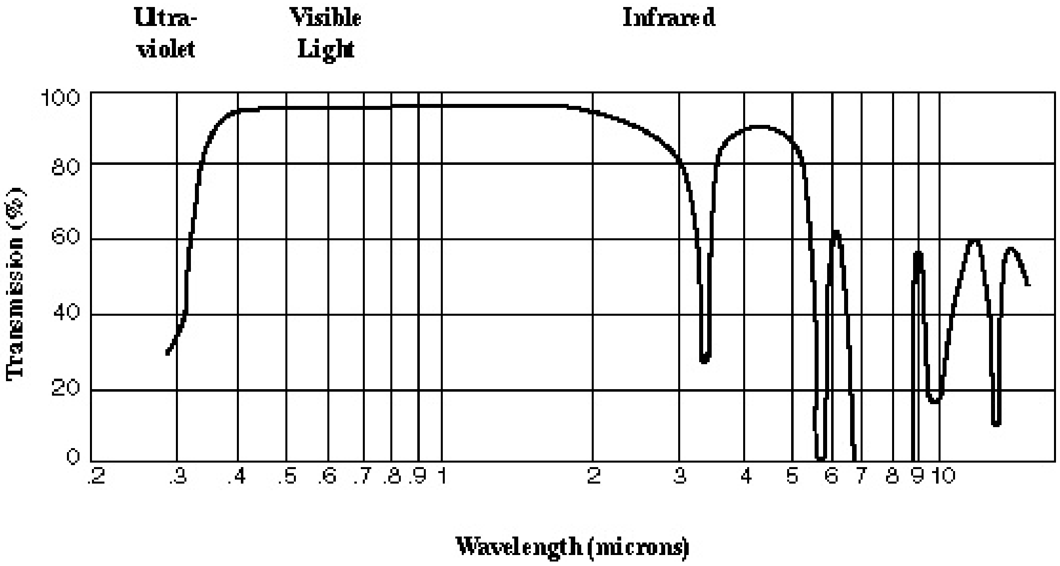

Figure 2.2: The spectral transmission of a thin film of NOA81. After [5].

High transparency polymer 3: 1,4-cyclohexanedimethanol divinyl ether (CHDV) (molecular structure in 2.3(a)) is a clear low viscosity monomeric liquid, which is bought from Sigma Aldrich. To make it light-sensitive, it is mixed with a photosensitizer. In this work a PAG named p-(Octyloxy)diphenyliodonium hexafluoroantimonate (DAI-SbF6) (ABCR, Karlsruhe, Germany), is used for this purpose as it was the only PAG tested that proved miscible in CHDV. The molecular

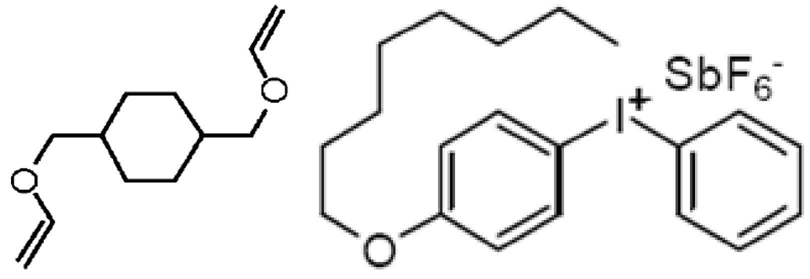

(a) Molecular structure of CHDV.

(b) Molecular structure of DAI-SbF6.

Figure 2.3: HTP3 is composed of 1,4-cyclohexanedimethanol divinyl ether and the PAG DAI-SbF6. After [7].

structure of the PAG can be seen in figure 2.3(b). DAI-SbF6 does not absorb near UV light, but when exposed to UV light with wavelengths below 250 nm the PAG releases an H^+-ion that in turn starts a cationic polymerisation process. This bonds the CHDV monomers together, by cross-linking the vinyl moieties, to form a solid polymer. The process is depicted in figure 2.4. CHDV with added PAG is referred to as HTP3 (high transparency polymer 3), as it was the third material system developed in-house for high UV transparency applications.

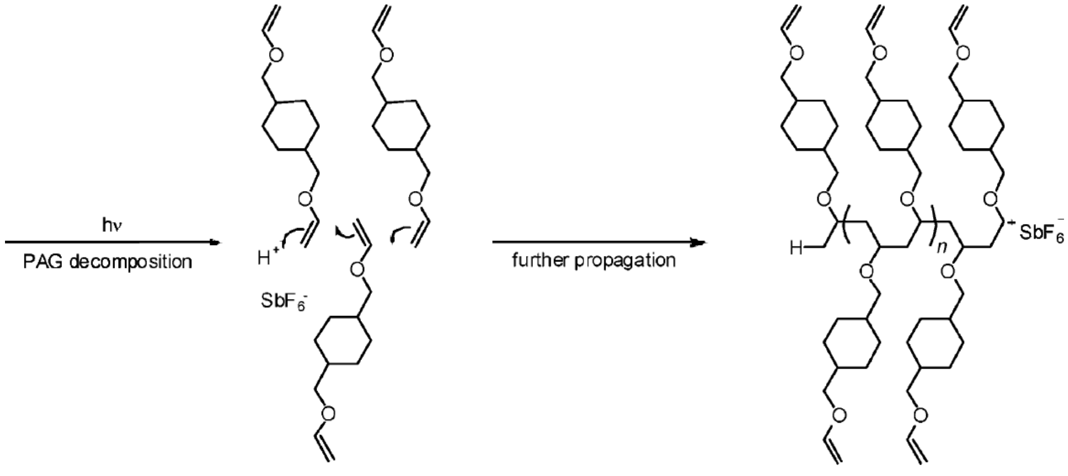

Figure 2.4: The curing route for CHDV as the PAG decomposes. After [7].

The transparency of CHDV is above 90% down to ∼240 nm in a 20 μm cured film and above 99% in the visible to near UV spectral range for the same thickness of film (see figure 2.5). It also has good miscibility properties, but some mechanical properties of CHDV, such as shrinkage during curing are less desirable [7, p.76-78]. The viscosity is low, 15 cps, and due to this its film forming characteristics are poor. The reason for this is the same as the reason for its high transparency, being the lack of aromatic rings in the molecule and hence lack of π to π interactions [8].

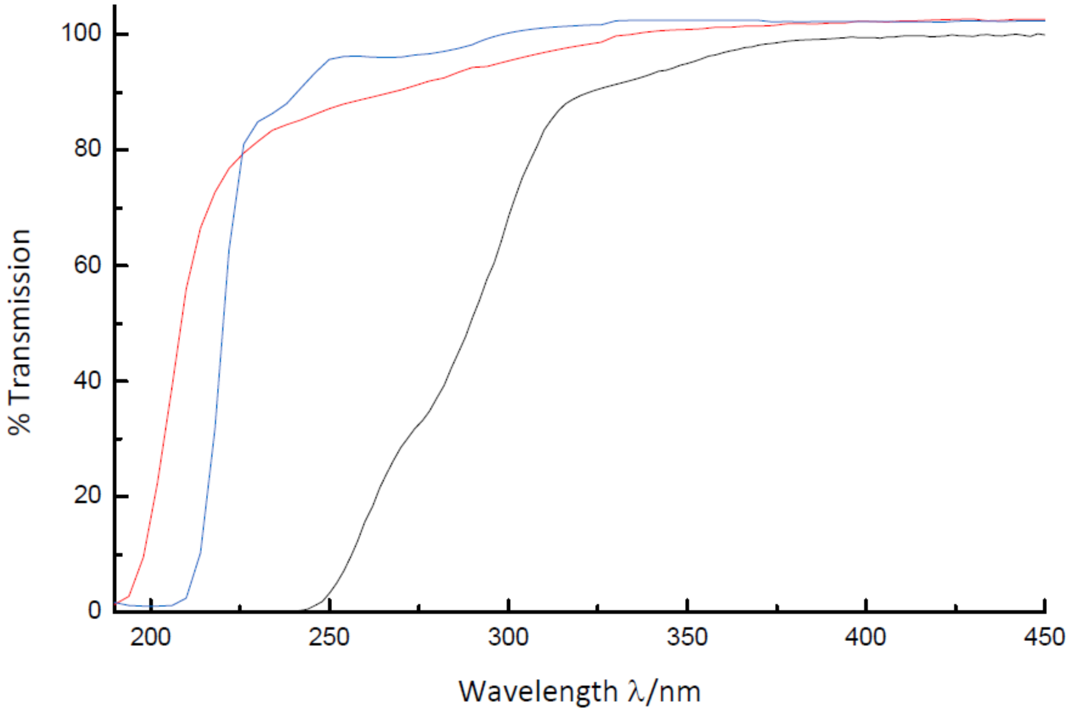

Figure 2.5: Spectral transmission for 20 μm film of NOA63 (black), 20 μm film of 'Prepol' (blue), and 20 μm film of CHDV (red) . After [7].

While curing, CHDV shrinks significantly. This creates tension between the polymer and the underlying substrate, which adversely affects adhesion. Because of this, special measures have to be taken when processing the material, as will be presented in section 3.4.

2.1.2 Positive photoresist

A photoresist of the positive type forms a positive image of the photomask it is exposed through, i.e., the exposed resist material decomposes and becomes soluble in a development solution or can be evaporated by heat treatment.

The positive resists used throughout this work are standard photoresists from the Shipley Microposit S1800-series. They have good film-forming ability and adhesion to most substrates, and are easy to use. They are optimised for Hg g-line exposure (436nm), but work well in a broad spectral interval (350–450 nm) [9]. The resist materials of the S1800-series have slightly different properties, such as different viscosities for the formation of different film thicknesses when spin casting, or with added dye for increased absorption to be used with highly reflective substrates.

The two types used in this work are S1805 and S1818. S1805 forms films of below 1 μm thickness when spin coated on a flat substrate, while the film thickness of S1818 is around 2 μm (see figure 2.6). The recommended dose for g-line exposure is 150 mJ/cm^2, slightly higher than for i-line exposure.

The process used for the positive type Microposit photoresists is as follows:

1. The substrates are thoroughly cleaned in ultrasonicated solvent baths (acetone, methanol, and iso-propanol) and subsequently rinsed in copious amounts of water. Water and solvent residues are evaporated by placing the samples on a hotplate at 110°C for at least 20 minutes.

2. The resist is spun at 2000 rpm for 30 seconds.

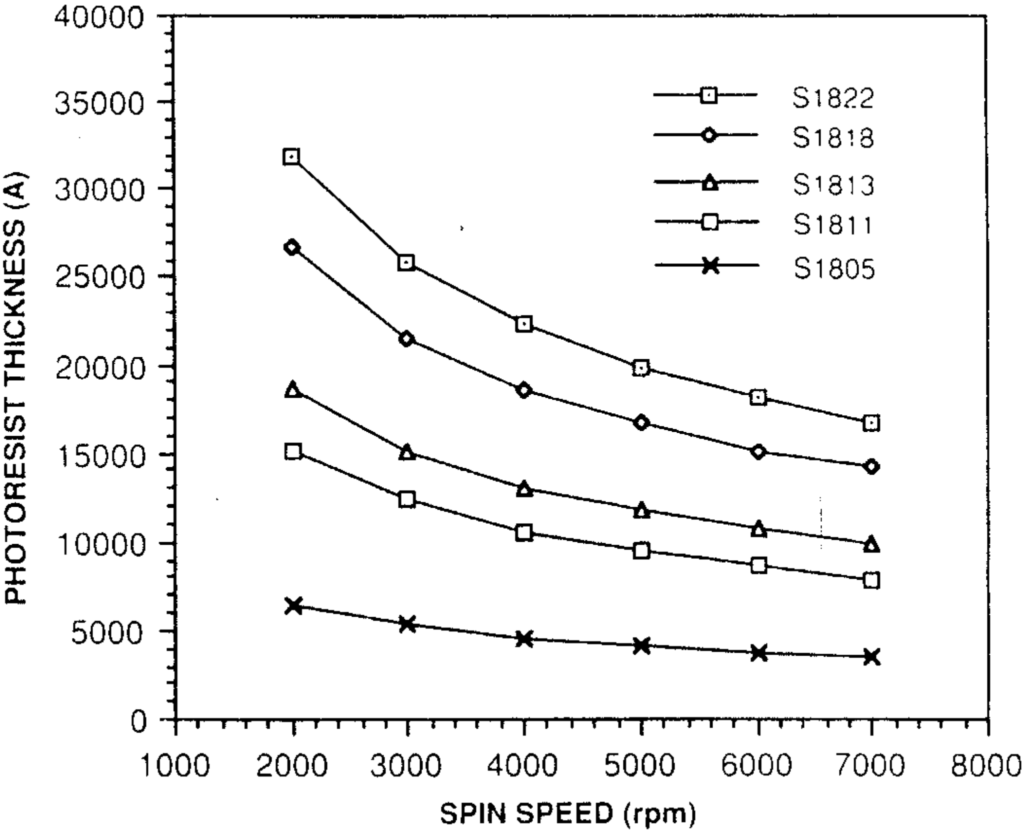

Figure 2.6: Film thickness for different types of S1800-series photoresists plotted against spinning speed. After [9].

3. A softbake is performed on a hotplate at 120°C for 60 seconds.
4. Exposure with an *i*-line source is performed, giving sufficient dose to locally decompose the photoresist layer.
5. The sample is developed in Microposit Micro-Dev solution at 1:1 volume ratio with DI water for 60 seconds while moving it gently at first and then using more vigorous movements.
6. The sample is rinsed in DI water.

All processing steps are performed with low wavelength filtered illumination, i.e., yellow filters are used on the general illumination, to prevent exposure by ambient light.

2.2 Light emitting materials

Light emitting materials are materials which absorb energy and emit it in the form of photons. Photoluminescing materials absorb light in a certain wavelength region and emit light at a wavelength (lower photon energy). The difference between the two bands is known as the Stokes shift. Fluorescence occurs when some of the energy from the absorbed photon is dissipated in the material before a photon is emitted. This is typically a fast process, compared to phophorescence, with a lifetime of 1–100ns. If a so-called triplet state (a state where the total quantum mechanical spin of the system adds up to 1 and not 0 as in the singlet state) is excited when the relaxation from the excited state occurs, the relaxation to the ground state is quantum mechanically forbidden. This process, in which the triplet state is relaxed, is known as phosphorescence and is a slow process. The relaxation typically takes 1ms–100s (cf. figure 1.21). For high performance light emitting organic devices, such as lasers, triplet states presents a problem and effort is made to avoid exciting these.

2.2.1 Organic light emitters

Organic light emitting materials have been studied for a long time and electroluminescence was first reported from these materials in 1955 [10]. More recently the materials have been used to make white light illumination sources [11] and full colour displays [12] which are now commercially available as TV sets and computer monitors.

Poly(9,9'di-*n*-octylfluorene): The type of organic light emitting materials of interest here are polymers and oligomers (small number of repeats of a monomer unit) with conjugated π-bonds, meaning the molecules contain bonds formed by partially delocalised electrons. This makes them have some properties in common with semiconductor materials. The first light emitting material used in this work is a light emitting polymer (LEP), poly(9,9'di-*n*-octylfluorene), more commonly refered to as polyfluorene (PFO). The structure of the molecule can be seen in figure 2.7(a). It has bright blue emission with a high photoluminescence quantum yield, $\sim$55% in thin film [13]. However, a major disadvantage of PFO for practical applications is that the molecule is very sensitive to photo-oxidation. The fluorene oxidises and fluorenone moieties are formed, resulting in the peak of the emission spectrum being shifted from blue to green [14, 15]. The absorption spectrum in figure 2.7(b) shows a distinct peak at 384 nm corresponding to the $\pi \rightarrow \pi^*$ transition. The emission spectrum has the expected peaks from the transitions discussed in section 1.3.2.

Oligofluorene-functionalised truxenes: The star-shaped oligofluorene truxene (simply referred to as 'truxene' from now on) molecule can be said to be an evolution of PFO, as the molecule's building blocks are the same fluorene units. The molecule consists of three arms of fluorene units, with a central truxene core. The molecules are synthesised by adding the oligo-fluorene moities to the core, the approach is called the divergent method (meaning that the syntesis starts from the core and dendrimer is built outwards). The number of repeated fluorene

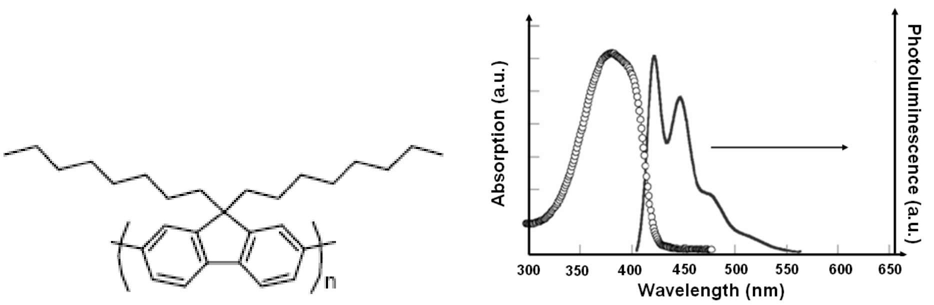

(a) Molecular structure of polyfluorene, with n being the number of repeats.

(b) Absorption (○) and emission (solid line) spectra of PFO.

Figure 2.7: Characteristics of PFO. After [16].

units outside the core is between one and four (denoted T1-T4). In figure 2.8 the molecular structure of truxene can be seen and figure 2.9 shows a "three dimensional" representation of the T3 molecule. With a radius of 3.9 nm, T4 was one of the largest star-shaped conjugated systems known when it was introduced in 2004 [17].

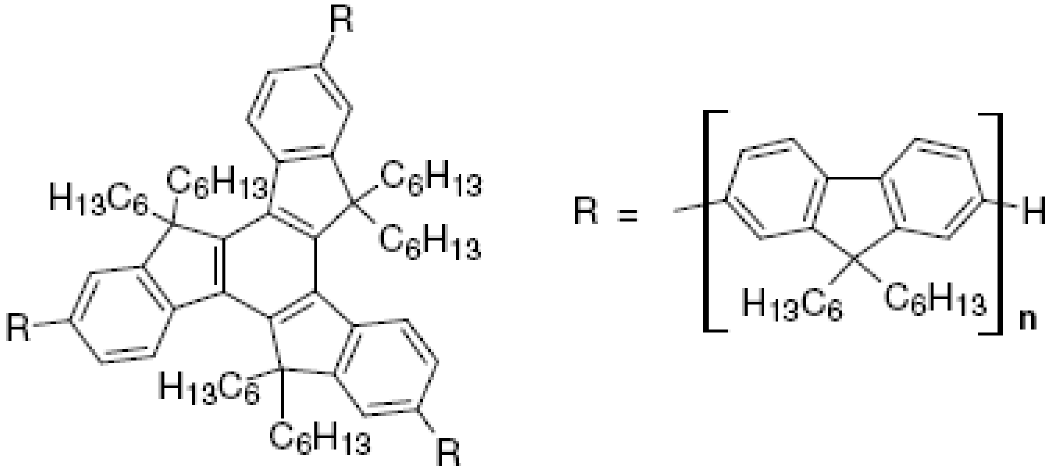

Figure 2.8: Molecular structure of oligofluorene-functionalised truxene. The R oligomer units have n = [1–4] repeats. After [17].

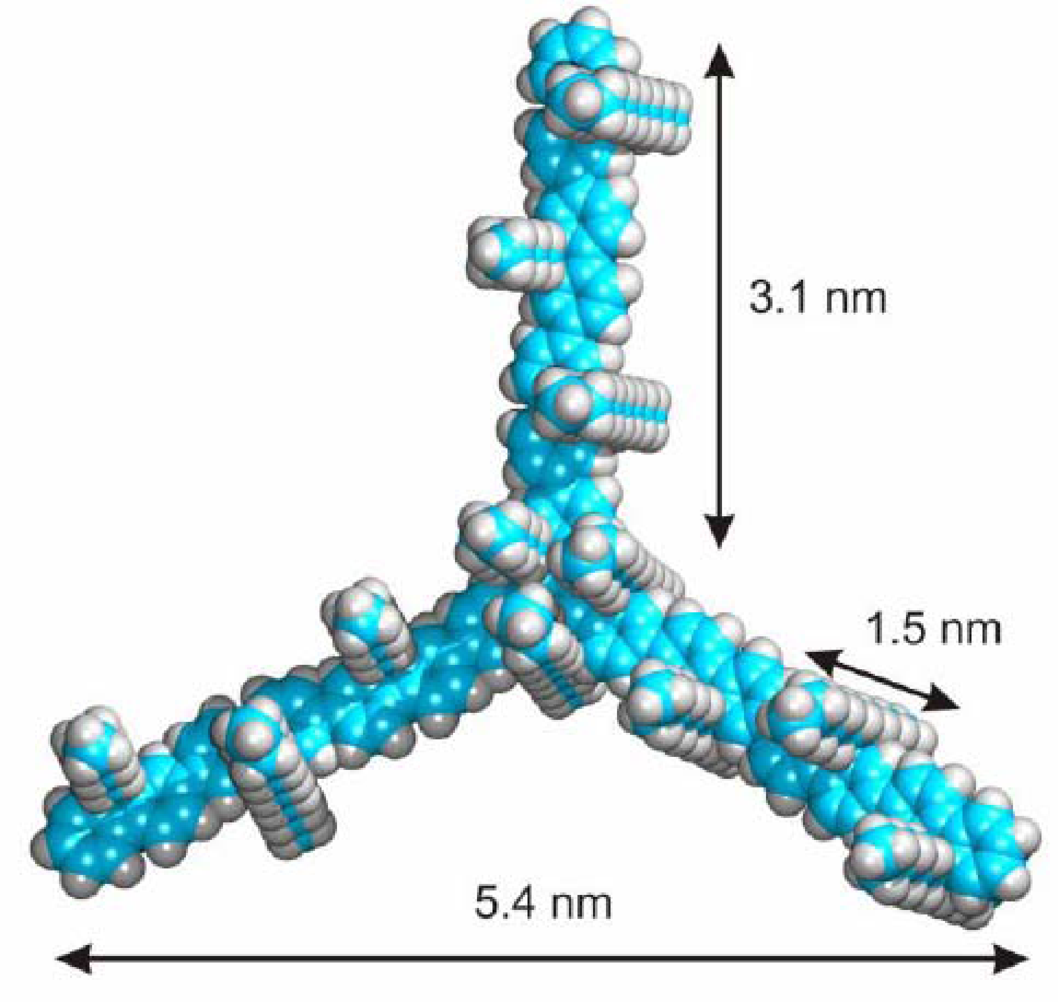

Figure 2.9: "Three dimensional" representation of a truxene molecule with three repeating fluorene units (T3).

Truxene has a very high photoluminescence quantum yield ($\Phi_{QY} = 86\%$ for T4 in toluene solution and $\Phi_{QY} = 59\%$ in a thin film) and bright blue emission [17]. The band gap, i.e., the gap between HOMO and LUMO (as described in section 1.3.2), in T4 is estimated from the red edge of the absorption spectrum to be 3.05 eV. As the arm lengths are increased both the absorption and emission spectra are redshifted as can be seen in table 2.1. This is due to the excited electron being free to move along the fluorene backbone and thus able to minimise its energy before relaxing in a vibrational transition. This can also be understood in the sense of quantum confinement, equivalent to the case quantum dots.

Table 2.1: Absorption and emission wavelengths and photoluminescence quantum efficiencies for truxene derivatives T1-T4 in toluene solution and in films [17].

	λ_{abs}(nm) (toluene)	λ_{abs}(nm) (film)	λ_{PL}(nm) (toluene)	λ_{PL}(nm) (film)	Φ_{PL} (toluene)	Φ_{PL} (film)
T1	343	343	375, 396, 416	380, 398, 419	0.70	0.43
T2	360	359	399, 422, 443	404, 425, 449	0.83	0.51
T3	370	369	408, 431, 460	417, 436, 462	0.83	0.60
T4	374	372	411, 436, 460	422, 442, 467	0.86	0.59

The emission spectra for the compounds T1–T4 (figure 2.10) show the same characteristics, with the three vibration peaks, as PFO. The conjugation between fluorene units is found to increase with increasing number of fluorenes, though there is seemingly a saturation of this conjugation at approximately four repeated units [18].

While PFO often has defects and impurities and has various chain lengths, truxenes are monodisperse with uniform molecular structure and molecular weight. They are also extremely chemically pure. Compared to PFO this makes the truxenes more environmentally stable and hence easier to process. They are also thermally stable, up to 400°C [17]. After heat treatment up to 200°C in air they show the same photoluminescence and quantum efficiency. However, like PFO, they are sensitive to photo-oxidisation, i.e., on excitation they react with oxygen and a fluorenone unit is formed in the place of a fluorene unit.

By spinning a solution of oligofluorene truxene, T4 in this case, onto a grating and pumping it with a optical parametric oscillator at 375 nm, a distributed feedback laser has been realised [19].

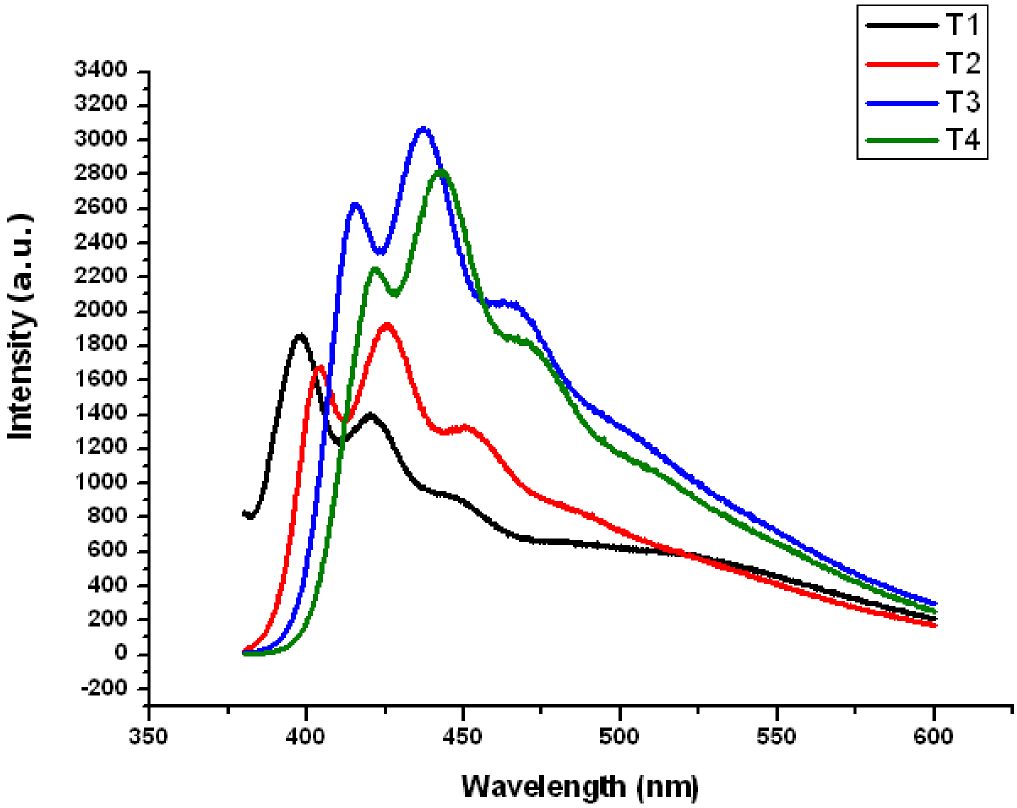

Figure 2.10: Emission spectra for the four truxene derivatives T1-T4 in solid films, showing the respective emission maxima and vibronic features.

2.2.2 Nanocrystal quantum dot emitters

Quantum dots are three dimensional semiconductor nanostructures where the length scale of the structure is below the exciton Bohr radius (the mean physical separation between the electron and the hole in the ground state). This causes the conduction and valence band structure of the semiconductor to form discrete energy levels mimicking an atom, hence quantum dots have been called 'artificial atoms'. This phenomenon is known as quantum confinement, which is also the principle behind quantum wells and quantum wires, in one and two dimensions, respectively. The gap between energy levels increases as the structure gets smaller, thus allowing for the engineering of the absorption and emission wavelengths.

Quantum dots can be produced epitaxially or via chemical methods in discrete nanocrystal (NC) form. In the following focus will be on the NCs. Because of their high quantum yield (typically 30–50%), environmental stability, high bleaching threshold, broadband absorption spectrum, and narrow and tuneable emission wavelength NCs have been used in various applications such as optoelectronics [20, 21], photovoltaics [22, 23] and colour conversion for white light generation [24, 25]. The QD NCs can also be surface modified [26] and be used in selective biological labelling [27].

Cadmium selenide/Zinc sulphide core-shell quantum dots: The material system used in this work is a II-IV compound that consists of a cadmium selenide (CdSe) core capped with a zinc sulphide (ZnS) shell. While NCs with only a CdSe core can be used the addition of a shell greatly enhances the stability and the quantum yield of the quantum dot by reducing surface traps [28]. A schematic representation of a CdSe/ZnS quantum dot is shown in figure 2.11.

A synthesis route for this type of quantum dots is described in [30]. First the CdSe NCs are synthesised by pyrolysis of organo-metallic precursors, containing cadmium and selenium, in a coordinating solvent, trioctylphosphine oxide (TOPO). The CdSe quantum dots are formed at a temperature between 290°C and 360°C. The temperature and time given for the growth determines the size of the nanocrystals. The dots are precipitated size-selectively using methanol and then redispersed in hexane. The ZnS shell is then added by heating the TOPO-capped CdSe nanocrystal solution to a temperature ranging from 140°C to 220°C,

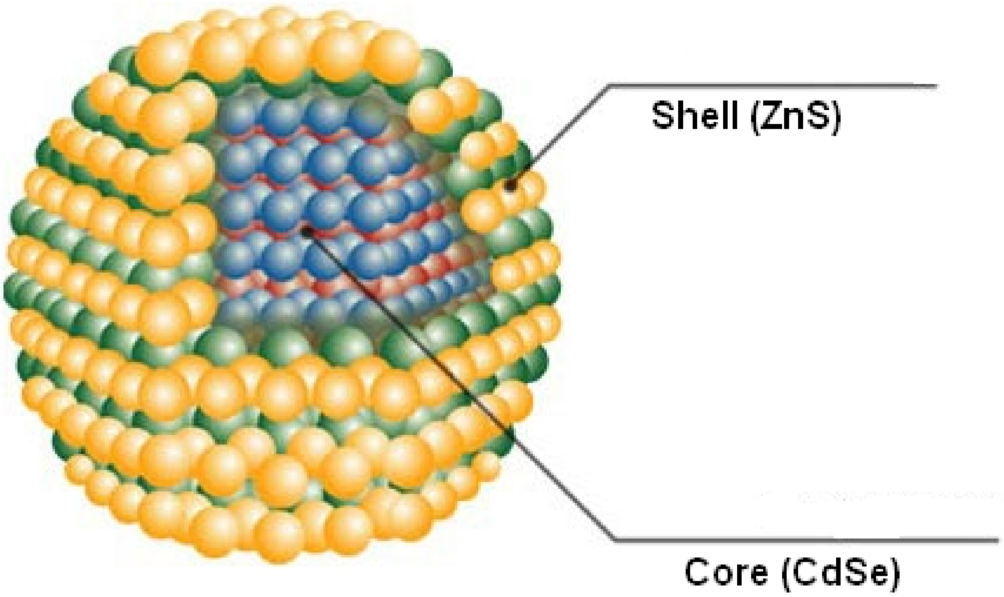

Figure 2.11: CdSe/ZnS quantum dot. Image from Evident Technologies Inc. [29].

depending on the size, and adding the zinc and sulphide precursors drop-wise in an inert atmosphere while rigorously stirring the mixture. The solution is then cooled down to 90°C and kept stirred for several hours. Before use, the core-shell quantum dots are percipitated using methanol and redispersed into the desired solvent.

The colloidal nanocrystals purchased from Evident Technologies are delivered monodispersed in toluene [29]. In addition to the ZnS shell, they have a capping of organic ligands to prevent aggregation and to maintain their beneficial photoluminescence properties. For some applications, the ligands can be modified so that the nanocrystals are miscible in other solvents, e.g., water. The ligands can also be functionalised with e.g., carboxyl or amine groups [31]. The spectra of the CdSe/ZnS quantum dots can be seen in figure 2.12 and some key characteristics

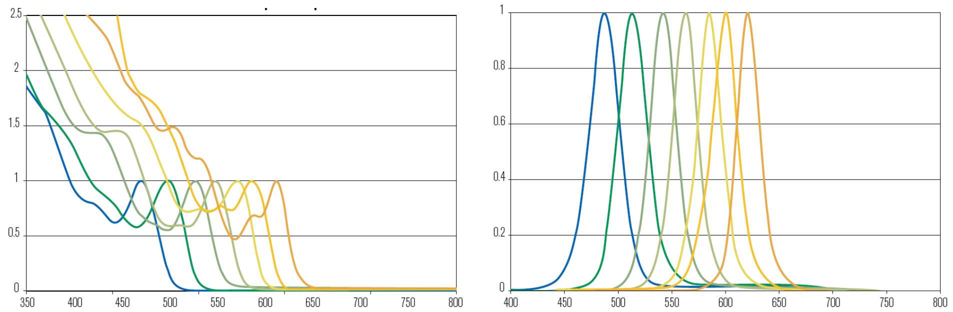

(a) Absoption spectra for CdSe/ZnS.

(b) Emission spectra CdSe/ZnS.

Figure 2.12: Spectra for colloidal CdSe/ZnS quantum dots of different sizes in toluene solution. From Evident Technologies Inc. [29].

are listed in table 2.2.

Table 2.2: Some key characteristics of EviDots. Ref. [29]

NC	λ_{abs} 1^{st} peak (nm)	λ_{emi} peak (nm)	FWHM (nm)	Conc. (mg/ml)
Lake Placid Blue	462	481	<40	0.29
Adirondack Green	513	526	<35	1.19
Hops Yellow	542	561	<30	1.3
Maple Red-Orange	591	610	<30	1.77

2.3 Composite materials

To provide processability and environmental protection, the approach taken is for the photoluminescing materials to be blended with photocurable (matrix or host) materials. The aim is to maintain the beneficial photo-characteristics of the luminescent materials described above, while adding the ability to photo-pattern the materials.

2.3.1 HTP3/Truxene

CHDV is a good candidate for mixing with oligofluorene truxenes, because truxene is, like PFO, completely miscible in CHDV [7, p.87] and since the CHDV lacks aromatic rings, there are no $\pi - \pi$ interactions that can otherwise cause solvatochromic shifts (shifts in emission and absorption spectra depending on the solvent the material is dispersed in) in conjugated light emitting materials [32].

The DAI-SbF6 PAG (figure 2.3(b)) normally has very low absorption in the *i*-line region, but a photo-induced electron transfer process between the truxene and PAG (figure 2.13) enables curing with near UV exposure. The process starts when a photon is absorbed by a truxene molecule and an electron is lifted from highest occupied molecular orbit (HOMO) to the lowest unoccupied molecular orbit (LUMO). Subsequently a photo-induced electron transfer (PET) to the PAG occurs and causes the release of a H^+-ion from the PAG [8, supplementary information].

The spectra for T4 in film, in toluene solution, and in a CHDV matrix (figure 2.14) show a slight broadening of the emission peak in the CHDV matrix compared to in toluene solution, indicating that the T4 molecules are pseudo-solvated and monodisperse in the matrix [8].

The CHDV matrix shows evidence of protecting the truxene molecules from photo-oxidation, which normally is a big problem for organic light emitting materials. In figure 2.15 the PL spectra of T4 in pure film and in a CHDV matrix are shown. Figure 2.15(a) shows the two initial spectra to be roughly the same. After 2 hours of UV illumination at 365 nm giving a dose of 187.2 J/cm^2 to both samples. The protection provided by the matrix can be seen clearly in the differ-

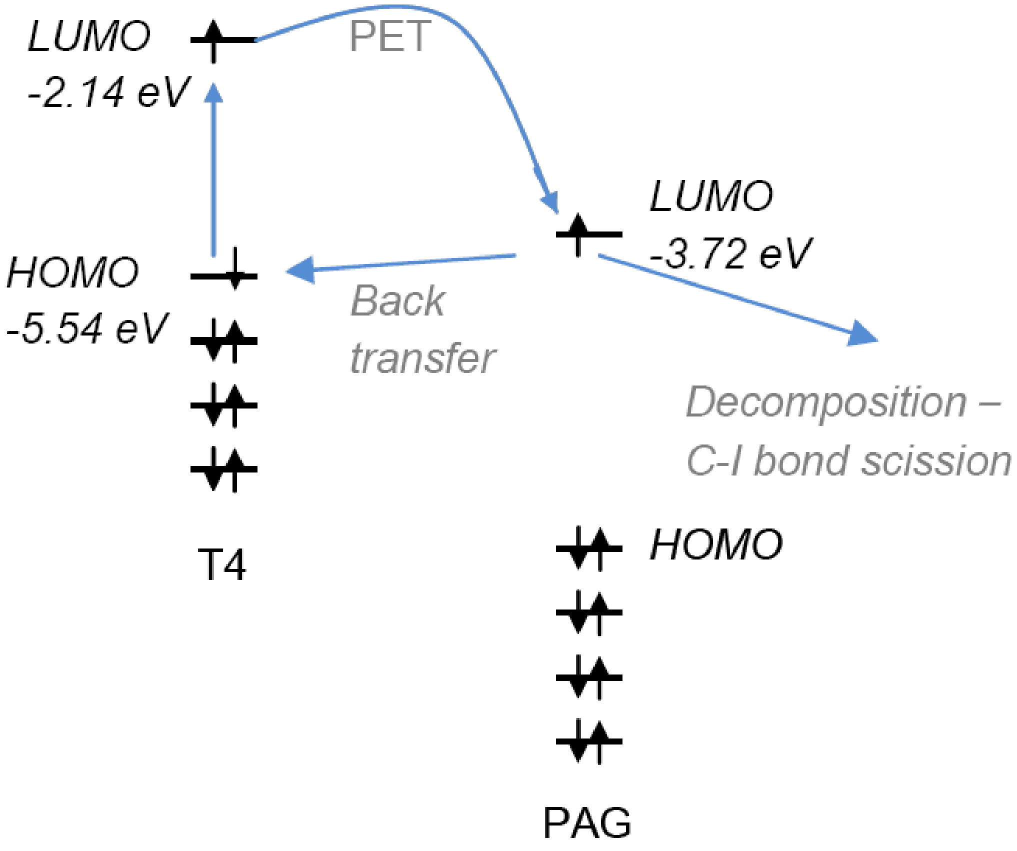

Figure 2.13: The energy transfer process from T4 to PAG. After [8, supplementary information].

ence between the two spectra in figure 2.15(b). The spectrum from the pure film is completely dominated by the oxidation peak in the green, while the CHDV protected structure remains dominated by the blue emission. The spectra are normalised with respect to the peak for clarity. The total emission intensity from the pure film is reduced by one to two orders of magnitude. The total emission intensity from the CHDV structures is also reduced by photo-bleaching, but to a much lower degree.

Experimental: To make the nanocomposite, the following recipe is used:

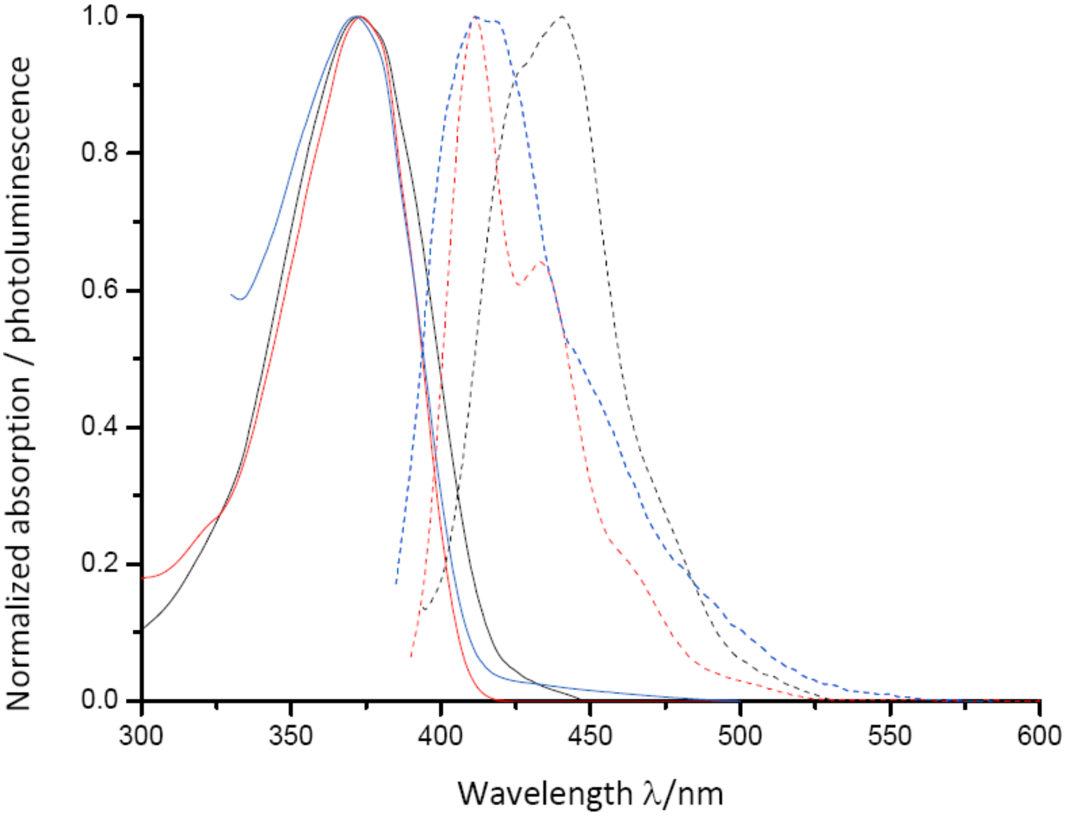

Figure 2.14: Absorption (solid lines) and emission (dotted lines) spectra for T4 in solid state (black), in toluene (red), and in CHDV matrix (blue). After [8].

1. The appropriate amount of dry truxene (powder) is measured with high precision scales (0.1 mg precision) in a small glass vial.
2. CHDV monomer is added to make up the desired weight ratio (0.1–10 wt-%).
3. The blend is mixed thoroughly to dissolve the truxene powder, with the assistance of an ultrasonic (US) bath. When no solid truxene can be seen it is assumed to be fully dissolved in the CHDV monomer.

The resulting solution is stable and can be stored in the dark and in a refrigerator (∼5°C) for months. Before use, the PAG is weighed and added to the blend at

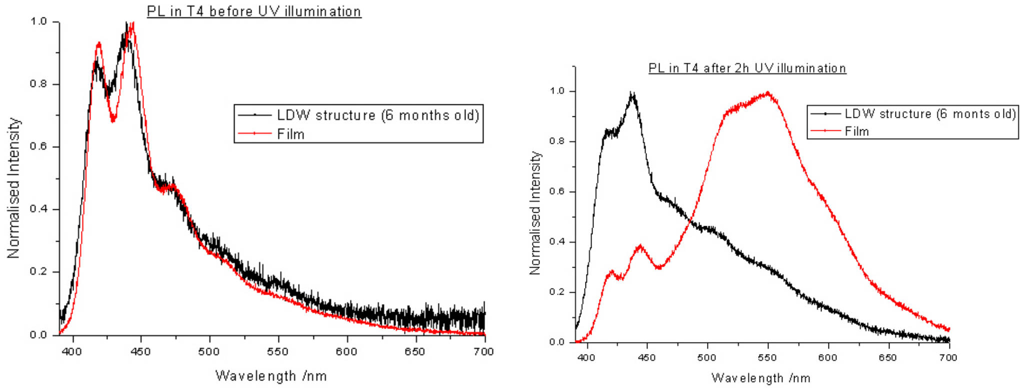

(a) Spectrum before exposure.

(b) Spectrum after exposure.

Figure 2.15: Spectra before and after the exposure dose of 187.2 J/cm^2 at 365 nm. Normalised to the peak intensity. After [8, supplementary information].

ratios of 0.1–1 wt-%.

For the exposure procedure see section 3.4.

After the exposure, development is done very gently in a toluene bath. The adhesion of the CHDV/truxene structures to the glass substrate is poor (the whole structure was transferred in an “adhesive-tape transfer test”, indicating good structural rigidity but poor adhesion) and can easily be washed off during the development if the substrate is moved around too vigorously. The toluene is subsequently washed off in a DI water bath.

Applications: These materials have been used for making waveguide type structures on glass substrates [8] (more on this in section 3.4) and for inkjet printing of colour converting structures on micro-pixel LEDs [33]. In a previous report a CHDV/PFO blend was used for colour down-conversion on a striped micro-LED by a self-aligned process [34].

2.3.2 NOA/QD

The CdSe/ZnS quantum dots are relatively environmentally stable and not as sensitive to oxidisation as the organic materials presented, but cannot be readily micro-patterned. There have been several suggested solutions for this, such as using peptides as molecular linkers to site-selectively attach to surfaces [35] and incorporating the nanocrystals in photocurable polymers [36, 37, 38, 39]. This is also the technique used here.

Experimental: Quantum dots with the provided surface ligands are not directly miscible in NOA81, therefore some measures had to be taken to enhance the miscibility.

The process used for blending quantum dots with NOA81 is as follows:

1. The quantum dots suspended in toluene are mixed with a small amount of CHDV and agitated in an ultrasonic bath for 30 minutes. The CHDV is believed to facilitate the dispersion of the quantum dots in the final composite.

2. The UV sensitive NOA polymer is weighed and added to the solution. The mixture is agitated for 1 hour in an ultrasonic bath. Due to the toluene in the solution, the viscosity is low and spin-coating is not possible.

3. To evaporate the solvent the blend is heated on a hotplate at 180°C for several hours with occasional application of a vacuum pump to increase the evaporation rate. After every full hour the solution is cooled under tap water to test the viscosity, more frequently when the viscosity starts to increase.

The resulting solution is a high viscosity nanocomposite with relatively good film-forming qualities. It can be photo-patterned by exposure with *i*-line light. The curing process seems to be ongoing while the nanocomposite is stored in the dark in a refrigerator and after one to two weeks it is gel-like and cannot be processed.

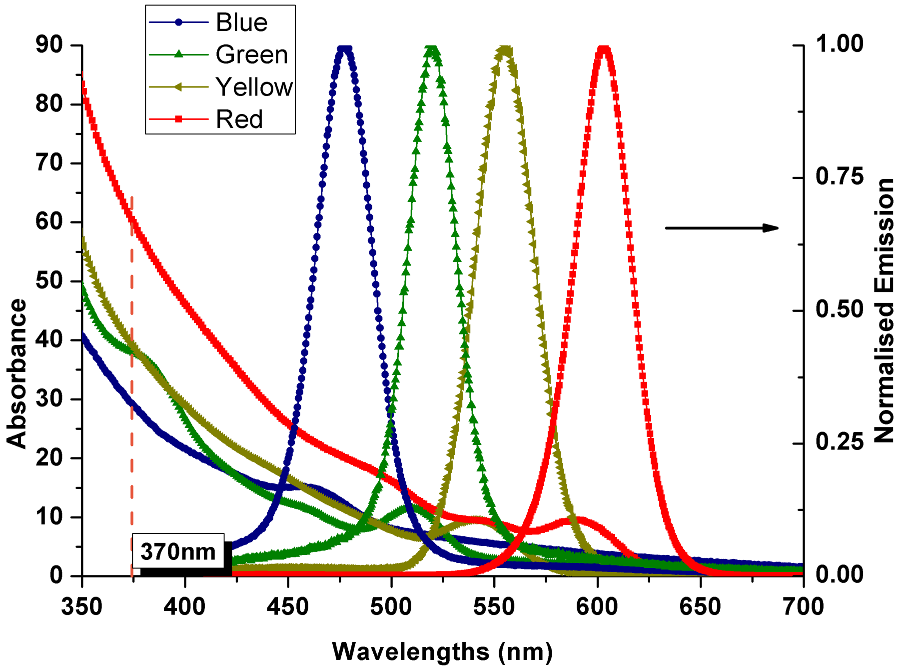

Figure 2.16: Absorption and emission spectra of nanocrystal composites in cured films.

By comparing the spectra from the nanocomposites in figure 2.16 with the spectra of nanocrystals in toluene solution in figure 2.12, it can be concluded that emission and absorption characteristics of the quantum dots are largely unchanged by incorporating them in the negative tone photoresist. The absorption spectra were taken with a UV-VIS Cary spectrophotometer on spun films. The film thicknesses were measured with a stylus profilometer. A Perkin Elmer LS

50B spectrometer was used for the emission spectra.

Applications: The quantum dot nanocomposites have been used for colour down conversion applications [40] that will be presented in Chapter 5.

2.4 Summary

The materials that are the basis of this thesis work have been presented.

The commercial negative and positive photoresist materials were first introduced and the principles by which they function explained. Negative photoresists become insoluble when exposed to the light of proper wavelength, while positive resists become soluble. Thus they form negative and positive images respectively. Two negative-type photoresists were focused on, namely NOA81 (an optical adhesive with beneficial mechanical and optical properties) and CHDV (a divinyl ether with for this work beneficial miscibility properties).

Luminescent materials, in particular organic light emitters based on polyfluorene and inorganic semiconductor nanocrystals (quantum dots), were introduced. Some main characteristics, spectral and quantum yeild data were given and their advantages and disadvantages were briefly discussed.

Methods used for producing custom blend materials based on negative-type photoresists and nanoluminophores were presented and their applications mentioned.

References

[1] Sudipta Roy. Fabrication of micro- and nano-structured materials using mask-less processes. *Journal of Physics D: Applied Physics*, 40(22):R413, 2007. vii, 46

[2] K. K. Tung, W. H. Wong, and E. Y. B. Pun. Polymeric optical waveguides using direct ultraviolet photolithography process. *Applied Physics A: Materials Science & Processing*, 80:621–626, February 2005. 45

[3] C.-H. Lin, G.-B. Lee, B.-W. Chang, and G.-L. Chang. A new fabrication process for ultra-thick microfluidic microstructures utilizing SU-8 photoresist. *Journal of Micromechanics and Microengineering*, 12:590–597, September 2002. 45

[4] Markus Deubel, Georg von Freymann, Martin Wegener, Suresh Pereira, Kurt Busch, and Costas M. Soukoulis. Direct laser writing of three-dimensional photonic-crystal templates for telecommunications. *Nat Mater*, 3(7):444–447, 2004. 10.1038/nmat1155. 45

[5] Norland Products Inc. *Norland Optical Adhesive 81*, 2007. vii, 47

[6] Christopher Harrison, Joao T Cabral, Christopher M Stafford, Alamgir

Karim, and Eric J Amis. A rapid prototyping technique for the fabrication of solvent-resistant structures. *Journal of Micromechanics and Microengineering*, 14(1):153–158, 2004. 47

[7] Alexander J.C. Kühne. *UV Transparent and Light Emitting Photo-Polymers for Optoelectronic Applications.* PhD thesis, University of Strathclyde, 2008. vii, 48, 49, 61

[8] Alexander J. C. Kuehne, David Elfström, Allan R. Mackintosh, Alexander L. Kanibolotsky, Benoit Guilhabert, Erdan Gu, Igor F. Perepichka, Peter J. Skabara, Martin D. Dawson, and Richard A. Pethrick. Fluorescent nanostructures: Direct laser writing of nanosized oligofluorene truxenes in uv-transparent photoresist microstructures (adv. mater. 7/2009). *Advanced Materials*, 21(7):781–785, 2009. vii, 49, 61, 62, 63, 64

[9] Shipley Company. *MICROPOSIT S1800 SERIES PHOTO RESISTS.* vii, 50, 51

[10] A Bernanose. Electroluminescence of organic compounds. *British Journal of Applied Physics*, 6(S4):S54, 1955. 52

[11] C. W. Ko and Y. T. Tao. Bright white organic light-emitting diode. *Applied Physics Letters*, 79:4234–4236, December 2001. 52

[12] Hirofumi Kubota, Satoshi Miyaguchi, Shinichi Ishizuka, Takeo Wakimoto, Jun Funaki, Yoshinori Fukuda, Teruichi Watanabe, Hideo Ochi, Tsuyoshi Sakamoto, Takako Miyake, Masami Tsuchida, Isamu Ohshita, and Teruo Tohma. Organic led full color passive-matrix display. *Journal of Luminescence*, 87-89:56 – 60, 2000. 52

[13] A. W. Grice, D. D. C. Bradley, M. T. Bernius, M. Inbasekaran, W. W. Wu, and E. P. Woo. High brightness and efficiency blue light-emitting polymer diodes. *Applied Physics Letters*, 73(5):629–631, 1998. 53

[14] Egbert Zojer, Alexander Pogantsch, Emmanuelle Hennebicq, David Beljonne, Jean-Luc Brédas, Patricia Scandiucci de Freitas, Ullrich Scherf, and Emil J. W. List. Green emission from poly(fluorene)s: The role of oxidation. *The Journal of Chemical Physics*, 117(14):6794–6802, 2002. 53

[15] Xiong Gong, Daniel Moses, Alan J. Heeger, and Steven Xiao. Excitation energy transfer from polyfluorene to fluorenone defects. *Synthetic Metals*, 141(1-2):17 – 20, 2004. Michael J. Rice Memorial Festschrift. 53

[16] J. Chappell, D. G. Lidzey, P. C. Jukes, A. M. Higgins, R. L. Thompson, S. O'Connor, I. Grizzi, R. Fletcher, J. O'Brien, M. Geoghegan, and R. A. L. Jones. Correlating structure with fluorescence emission in phase-separated conjugated-polymer blends. *Nature Materials*, 2:616–621, September 2003. vii, 54

[17] Alexander L. Kanibolotsky, Rory Berridge, Peter J. Skabara, Igor F. Perepichka, Donal D. C. Bradley, and Mattijs Koeberg. Synthesis and properties of monodisperse oligofluorene-functionalized truxenes: Highly fluorescent star-shaped architectures. *Journal of the American Chemical Society*, 126(42):13695–13702, 2004. doi: 10.1021/ja039228n. vii, xii, 54, 55, 56

[18] Maria Moreno Oliva, Juan Casado, Juan T. Lopez Navarrete, Rory Berridge, Peter J. Skabara, Alexander L. Kanibolotsky, and Igor F. Perepichka. Electronic and molecular structures of trigonal truxene-core systems conju-

gated to peripheral fluorene branches. spectroscopic and theoretical study. *The Journal of Physical Chemistry B*, 111(16):4026–4035, 2007. doi: 10.1021/jp065271w. 56

[19] Georgios Tsiminis, Yue Wang, Paul E. Shaw, Alexander L. Kanibolotsky, Igor F. Perepichka, Martin D. Dawson, Peter J. Skabara, Graham A. Turnbull, and Ifor D. W. Samuel. Low-threshold organic laser based on an oligofluorene truxene with low optical losses. *Applied Physics Letters*, 94(24):243304, 2009. 56

[20] Liang Yan, Jia-Yu Zhang, Yiping Cui, and Yi Qiao. Voltage-dependent electroluminescence from colloidal cdse/zns quantum dots. *Applied Physics Letters*, 91(24):243114, 2007. 58

[21] Qingjiang Sun, Y. Andrew Wang, Lin Song Li, Daoyuan Wang, Ting Zhu, Jian Xu, Chunhe Yang, and Yongfang Li. Bright, multicoloured light-emitting diodes based on quantum dots. *Nat Photon*, 1(12):717–722, 2007. 10.1038/nphoton.2007.226. 58

[22] A. J. Nozik. Quantum dot solar cells. *Physica E: Low-dimensional Systems and Nanostructures*, 14(1-2):115 – 120, 2002. 58

[23] Alexi C. Arango, David C. Oertel, Youfeng Xu, Moungi G. Bawendi, and Vladimir Bulovic. Heterojunction photovoltaics using printed colloidal quantum dots as a photosensitive layer. *Nano Letters*, 9(2):860–863, 2009. doi: 10.1021/nl803760j. 58

[24] Sedat Nizamoglu, Evren Mutlugun, Tuncay Özel, Hilmi Volkan Demir, Sameer Sapra, Nikolai Gaponik, and Alexander Eychmüller. Dual-color emit-

ting quantum-dot-quantum-well CdSe-ZnS heteronanocrystals hybridized on InGaN/GaN light emitting diodes for high-quality white light generation. *Applied Physics Letters*, 92(11):113110, 2008. 58

[25] Sedat Nizamoglu, Gülis Zengin, and Hilmi Volkan Demir. Color-converting combinations of nanocrystal emitters for warm-white light generation with high color rendering index. *Applied Physics Letters*, 92(3):031102, 2008. 58

[26] Ming-Qiang Zhu, Emmanuel Chang, Jiantang Sun, and Rebekah A. Drezek. Surface modification and functionalization of semiconductor quantum dots through reactive coating of silanes in toluene. *Journal of Materials Chemistry*, 17(8):800–805, 2007. 58

[27] W. J. Parak, T. Pellegrino, and C. Plank. TOPICAL REVIEW: Labelling of cells with quantum dots. *Nanotechnology*, 16:9–25, February 2005. 58

[28] Margaret A. Hines and Philippe Guyot-Sionnest. Synthesis and characterization of strongly luminescing ZnS-capped CdSe nanocrystals. *The Journal of Physical Chemistry*, 100(2):468–471, 1996. doi: 10.1021/jp9530562. 58

[29] Evident technologies Inc. *EviDot datasheet*, 2007. vii, xii, 59, 60

[30] B. O. Dabbousi, J. Rodriguez-Viejo, F. V. Mikulec, J. R. Heine, H. Mattoussi, R. Ober, K. F. Jensen, and M. G. Bawendi. (CdSe)ZnS coreshell quantum dots: Synthesis and characterization of a size series of highly luminescent nanocrystallites. *The Journal of Physical Chemistry B*, 101(46):9463–9475, 1997. doi: 10.1021/jp971091y. 58

[31] Daniel R. Larson, Warren R. Zipfel, Rebecca M. Williams, Stephen W.

Clark, Marcel P. Bruchez, Frank W. Wise, and Watt W. Webb. Water-soluble quantum dots for multiphoton fluorescence imaging in vivo. *Science*, 300(5624):1434–1436, 2003. 10.1126/science.1083780. 59

[32] Mihalis Fakis, Dimitris Anestopoulos, Vassilis Giannetas, and Peter Persephonis. Influence of aggregates and solvent aromaticity on the emission of conjugated polymers. *The Journal of Physical Chemistry B*, 110(49):24897–24902, 2006. doi: 10.1021/jp0619033. 61

[33] M. Wu, Z. Gong, A. J. Kuehne, A. L. Kanibolotsky, Y. J. Chen, I. F. Perepichka, A. R. Mackintosh, E. Gu, P. J. Skabara, R. A. Pethrick, and M. D. Dawson. Hybrid GaN/organic microstructured light-emitting devices via ink-jet printing. *Opt. Express*, 17(19):16436–16443, 2009. 64

[34] E. Gu, H. X. Zhang, H. D. Sun, M. D. Dawson, A. R. Mackintosh, A. J. C. Kuehne, R. A. Pethrick, C. Belton, and D. D. C. Bradley. Hybrid inorganic/organic microstructured light-emitting diodes produced using photocurable polymer blends. *Applied Physics Letters*, 90(3):031116, 2007. 64

[35] Turgay Kacar, John Ray, Mustafa Gungormus, Ersin Emre Oren, Candan Tamerler, and Mehmet Sarikaya. Quartz binding peptides as molecular linkers towards fabricating multifunctional micropatterned substrates. *Advanced Materials*, 21(3):295–299, 2009. 65

[36] Z.-B. Sun, X.-Z. Dong, W.-Q. Chen, S. Nakanishi, X.-M. Duan, and S. Kawata. Multicolor polymer nanocomposites: In situ synthesis and fabrication of 3d microstructures. *Advanced Materials*, 20(5):914–919, 2008. 65

[37] Lin Pang, Kevin Tetz, Yaoming Shen, Chyong-Hua Chen, and Yeshaiahu Fainman. Photosensitive quantum dot composites and their applications in optical structures. *Journal of Vacuum Science & Technology B: Microelectronics and Nanometer Structures*, 23(6):2413–2418, 2005. 65

[38] Anna C. Balazs, Todd Emrick, and Thomas P. Russell. Nanoparticle polymer composites: Where two small worlds meet. *Science*, 314(5802):1107–1110, 2006. 10.1126/science.1130557. 65

[39] C. Ingrosso, V. Fakhfouri, M. Striccoli, A. Agostiano, A. Voigt, G. Gruetzner, M. L. Curri, and J. Brugger. An epoxy photoresist modified by luminescent nanocrystals for the fabrication of 3d high-aspect-ratio microstructures. *Advanced Functional Materials*, 17(13):2009–2017, 2007. 65

[40] B. Guilhabert, D. Elfström, A. Kuehne, D. Massoubre, H. X. Zhang, S. R. Jin, A. R. Mackintosh, E. Gu, R. Pethrick, and M. D. Dawson. Integration by self-aligned writing of nanocrystal/epoxy composites on InGaN micro-pixelated light-emitting diodes. *Opt. Express*, 16(23):18933–18941, 2008. 67

Chapter 3

Laser Direct Writing

This chapter will introduce the basic principles of laser writing with a Gaussian beam and present results achieved with a home-built laser-direct writing setup. First the setup will be presented and characterisation measurements given, then writing results for some different photoresist based material systems will be given.

Laser direct writing has been used for a long time to rapidly prototype and to produce e.g., waveguides [1], conductive copper patterns [2], and photonic crystals [3].

The objective in this work was to build a relatively inexpensive laser writing setup capable of patterning novel material systems developed by the Department of Pure and Applied Chemistry at Strathclyde University. The goal for the resolution was a few μm and computer control of the writing was required. Sample scanning rather than beam scanning was chosen because of simplicity and the larger writeable area available with this technique, the main disadvantage being lower writing speed. A semiconductor laser operating at 375nm (close to the Hg i-line at 368nm commonly used in photolithography) was chosen for low cost and sufficient power. With custom circularising and collimating optics the output beam can be approximated to a Gaussian beam (see figure 3.1(a)).

3.1 Laser direct writing theory

Laser light can cause a change in photosensitive materials if an energy density dose over a certain material specific threshold is delivered to the material. By directing the laser beam in a controlled manner on the sample, a pattern can be produced. There are two ways of controlling where the laser beam hits the sample, either the beam is directed or the sample is moved during the exposure. The first approach is more complicated but allows for fast scanning and very precise control. The most common way to achieve this is to use movable mirrors, which the laser beam is reflected from. When using a microscope objective (something that is advantageous for various reasons, which will be discussed later) to focus the laser beam this technique can only pattern an area the size of the field of view of the objective. As there is a trade-off between the field of view and the resolution (or numerical aperture) of objectives this is a problem. The alternative is to move the sample under the static laser beam. With this technique the resolution and patternable area are mainly decided by the translation stages used for the movement. The scanning speed is generally lower with this approach, but for this work this is not an important factor and this is the technique chosen.

The shape of the laser beam will affect the resulting structures in laser direct writing. Throughout this chapter a Gaussian beam profile will be assumed and beam profile measurements support this assumption. The two dimensional intensity profile of a Gaussian beam is described by the equation $f(x, y) = e^{-(x^2+y^2)}$,

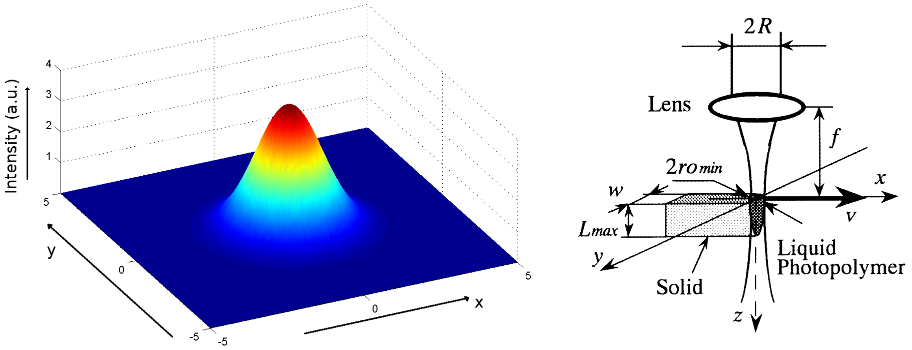

(a) Gaussian beam in two dimensions.

(b) Theoretical model of laser writing in negative type photoresist. From [4].

Figure 3.1: Images showing schematics of laser writing with a Gaussian beam.

a graphical representation of which can be seen in figure 3.1(a).

When a Gaussian beam illuminates a photosensitive polymer through a transparent substrate, the profile of the cured polymer can be modelled in accordance with figure 3.1(b), if the beam is focused at the interface between the substrate and the polymer. The calculations are based on the theory for the profile of cured photo-polymer presented in [5] and the theory of focusing a Gaussian beam presented in [6], but adapted for use of a microscope objective instead of a single lens. Apart from the laser beam being Gaussian, it is also assumed that the polymer obeys the Beer-Lambert Law of absorption ($T = \frac{I}{I_0} = e^{-\alpha l}$, where T is the transmission, I is the intensity after the travelled distance l in the material, I_0 is the initial intensity, and α is the absorption coefficient of the material) and that there is a threshold exposure dose above which the resist material cures.

The intensity distribution in a focused Gaussian beam, with total power P and $1/e^2$-Gaussian halfwidth r_0, is described by

$$I_g(x, y, z) = \frac{2P}{\pi r_0^2} exp\Big[-\frac{2(x^2 + y^2)}{r_0^2(z)}\Big] \tag{3.1}$$

where

$$r_0(z) = r_{0,min}\sqrt{1 + \Big(\frac{\lambda z}{\pi r_{0,min}^2}\Big)^2} \tag{3.2}$$

where $r_{0,min}$ is the smallest spot size (at z = 0) for a beam propagating in the z-direction. There are many ways of estimating the smallest possible (diffraction limited) spot size. Here we assume the smallest spot size to be given by the resolution limit of the optical system, i.e., the Rayleigh criterion stating that two points can be resolved if their distance is larger than the radius of the Airy disk's first minimum given by $d = \frac{0.61\lambda}{N.A.}$, where λ is the laser operating wavelength and N.A. is the numerical aperture (= $n\sin(\theta)$, where n is the refractive index of the propagating medium (≈1 for air) and θ half the acceptance angle to the objective used) of the microscope objective used.

Further, the intensity at the depth z is given by

$$I(x, y, z) = I_g(x, y, z)exp[-\alpha z] \tag{3.3}$$

The dose given at each point when the sample is scanned under the laser beam along the x-axis at a velocity, v, is expressed as

$$E(x, y, z) = \int_{-\infty}^{\infty} I(x - vt, y, z)\mathrm{d}t \tag{3.4}$$

Solving the integral for z = 0 gives

$$E(x,y,0)=\frac{\sqrt{2}P}{\sqrt{\pi}r_{0,min}v}e^{2(y/r_{0,min})^2} \tag{3.5}$$

This is the energy dose delivered at the interface between the resist material and the transparent substrate.

When $E(x,y,z)$ is over a threshold value, E_0, the polymer is solidified and the profile of the resulting cured polymer can be described by

$$y(z)=\frac{r_{0,min}}{\sqrt{2}}\sqrt{\ln\Big(\sqrt{\frac{2}{\pi}}\frac{P}{E_0 r_{0,min}v}\Big)-\alpha z} \tag{3.6}$$

or

$$z(y)=\frac{1}{\alpha}\Big(\ln\Big(\sqrt{\frac{2}{\pi}}\frac{P}{E_0 r_{0,min}v}\Big)-\Big(\frac{\sqrt{2}y}{r_{0,min}}\Big)^2\Big) \tag{3.7}$$

α and E_0 are material specific constants and can be experimentally determined.

The general shape of the solidified polymer according to the above can be seen in figure 3.2. The polymer is exposed from above and moved in the x-direction.

The z-resolution or depth of focus is defined by the Rayleigh range, $\pm z_R$, at which distance from $z=0$ (where the width is minimum) the beam area is twice that of the minimum or equivalently the beam radius, $r_0=\sqrt{2}\times r_{0,min}$. Put into equation 3.2 this gives the Rayleigh range

$$2z_R=2\frac{\pi r_{0,min}^2}{\lambda} \tag{3.8}$$

The spot size and the Rayleigh range define the smallest possible dimensions

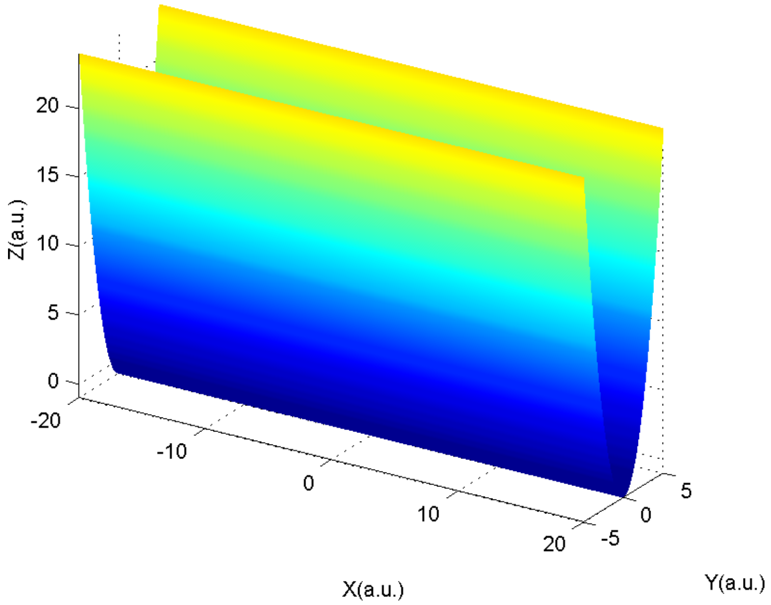

Figure 3.2: The theoretical profile of cured polymer. The laser beam is exposing the polymer from above and the sample is moved in the x-direction.

for the cured volume element (voxel) when curing a photosensitive polymer with a Gaussian beam by direct laser writing.

3.2 The laser direct writing setup

Images of the laser direct writing (LDW) setup are shown in figure 3.3.

The setup consist of:

- An InGaN based diode laser operating at 375 nm (Laser2000 Ltd). It has an output power of ∼15 mW in continuous wave (CW) operation and is fitted with circularising and collimating optics.
- A variable neutral density filter (from Thorlabs), with optical density ranging from 0 to 100, to attenuate the laser power and thus control the exposure dose for a given exposure duration.

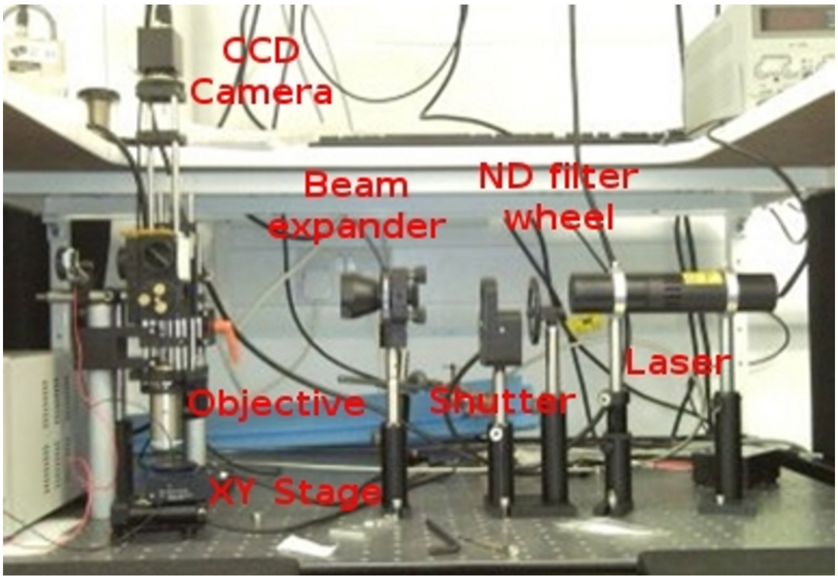

(a) Photograph of the laser writing setup.

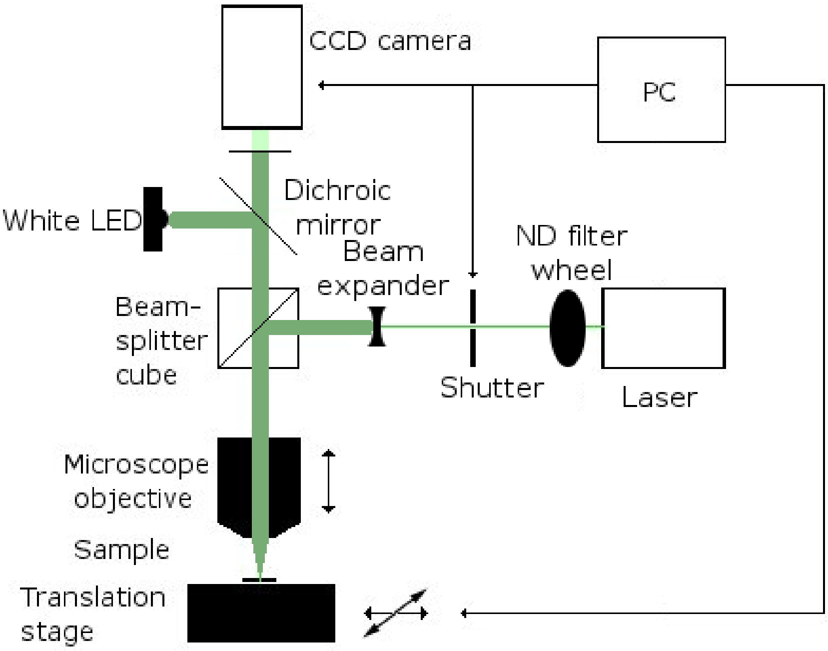

(b) Schematic image of the laser writing setup.

Figure 3.3: Laser writing setup

- A mechanical shutter (SH05 from Thorlabs), with a minimum open time of 10ms.
- A beam expander (from Thorlabs) to expand the laser beam diameter three times and fill the back aperture of the microscope objective.
- An interchangeable microscope objective (Nikon infinity corrected), mounted on a piezo translation stage (P-725.4CD with E-665 controler from Physik Instrumente (PI)) with a sub-nanometer movement resolution and a manual stage for coarse translation to focus the laser beam onto the sample.
- XY translation stage (2 x M-112.1DG from PI), with repeatability (effective resolution) of ~0.1 μm in each direction and maximum velocity of 1.5 mm/s in any direction.
- A CCD camera (JVC TK-C721EG) and UV-filtered white light illumination to image the sample.
- A computer with LabView^{TM} software to control the shutter and the stages.

3.2.1 Software control

LabView^{TM} control of the stages and the shutter provides the ability to create two-dimensional patterns with automation. Several different LabView^{TM} vi-programs were written for the control of the stages. The most basic program (screen shots in appendix A) draws a straight line between the origin and a given point at a constant given velocity. The program first reads the end point (input position) and the start point (current position), then calculates the distance between the two points in X and Y direction then sets the speed for the travel in each direction such that they will add up to the given velocity and reach the destination at the same time. The program also has an option for synchronising the shutter with the movement. When enabled this will open the shutter a few tens of milliseconds before the movement starts and closes it just after the movement stops.

3.2.2 Characterisation

The theoretical resolution limit of the system is given by $d = \frac{0.61\lambda}{N.A.}$, as discussed in section 3.1. The numerical aperture ($N.A.$) of the Nikon Plan 20X microscope is 0.40 and the laser wavelength is 375 nm, hence the smallest spot size is $d = \frac{0.61\times 375nm}{0.40} = 572nm$ and the Rayleigh range is $2z_R = 2\frac{\pi\times(572nm)^2}{375nm} = 5.48\mu m$. However since the laser beam is not truly single mode the actual spot size will be bigger.

The setup was characterised regarding e.g., spot size and optical power delivered.

The power was measured with a calibrated powermeter (Coherent FieldMax) with the sensor placed at the sample position. The neutral density filter wheel is graded in degrees with the maximum optical density at 360° and the 0–90° sector being transparent. Figure 3.4 shows the optical power as measured at the sample position. The values range from 285 μW to 3.3 μW. With the shutter minimum open time being 10 ms, this means the minimum energy in one exposure is 33 nJ.

To measure the spot size, a knife-edge type technique was applied. A grating with alternating transparent and reflective areas was used. The pitch of the grating is 25 μm divided evenly between reflective and transparent areas. The laser beam was focused on the grating, which was slowly translated in a direction

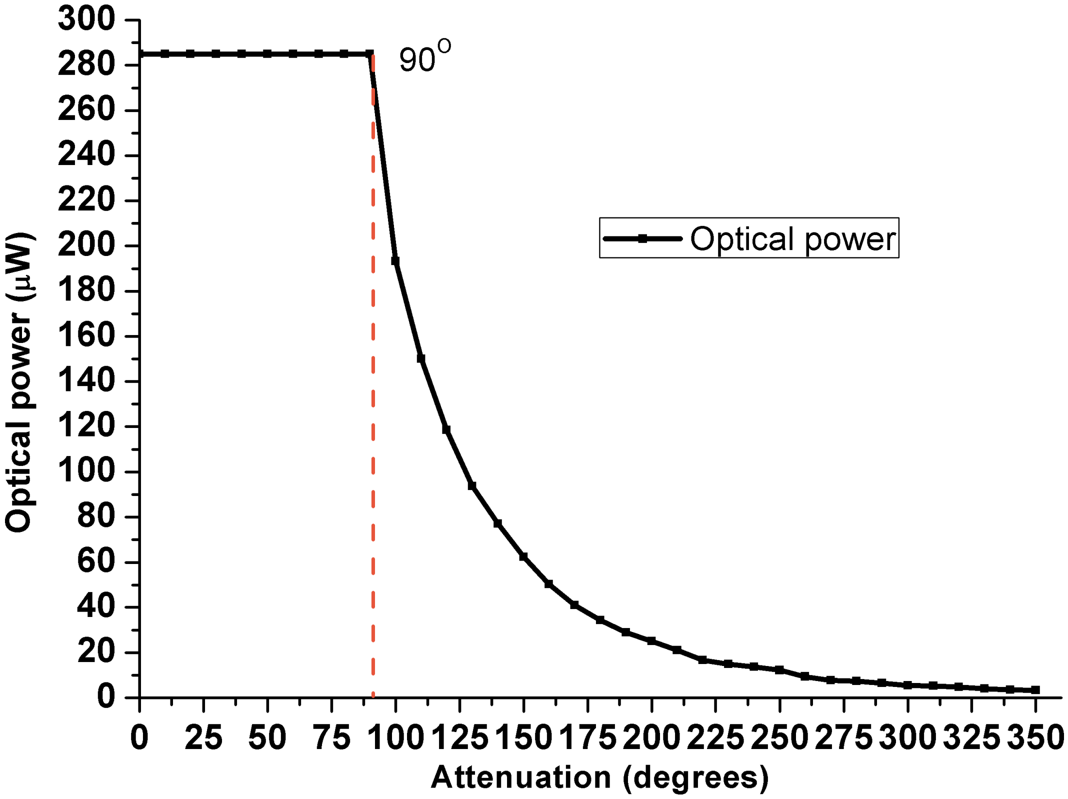

Figure 3.4: The optical power measured at the sample position dependence on the position of the neutral density filter wheel.

perpendicular to the grating alignment (figure 3.5). The transmitted optical power was measured with the powermeter. The resulting plot can be seen in figure 3.6(a). Because the edge of the grating is well defined, the spot size is given by differentiating the rise and falls of the plot. The resulting envelope can with reasonable accuracy be fitted to a Gaussian curve (as can be seen in figure 3.6(c)) and by doing this the $1/e^2$-half width of the focused spot can be calculated. The curve fitting and the calculations were done with Origin$^{\mathrm{TM}}$ software. By rotating the grating and the translation direction 90°, the spot size in the perpendicular direction was also measured. In one direction the average value was 0.8 μm and in a perpendicular direction the average was 0.9 μm. This indicates as expected

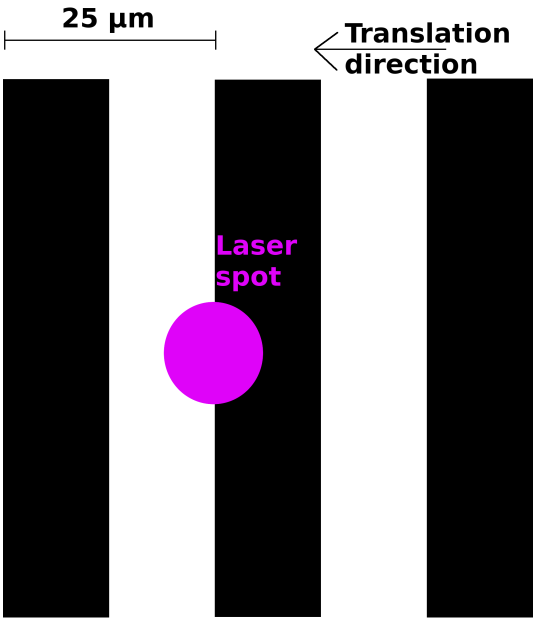

Figure 3.5: Schematic of the focused laser beam on the grating.

that the beam was not symmetrically Gaussian. The measured spot size is in reasonable agreement with the theoretical diffraction-limited spot size of 0.57 μm. Reasons for this discrepancy include the beam quality from a laser diode (see section sec:laserdiode), which can not be fully corrected for with lenses, and minor misalignment in the setup.

By combining the optical power and spot size measurements, the intensity at the focus can be expressed (cf. equation 3.5)as:

$$I_g(r) = \frac{2P}{\pi r_{min}^2} exp\Big[-\frac{2(r^2)}{r_{min}^2}\Big] \tag{3.9}$$

With $r_{min} = 0.8$ μm and $P = 285$ μW, the maximum value of the intensity is:

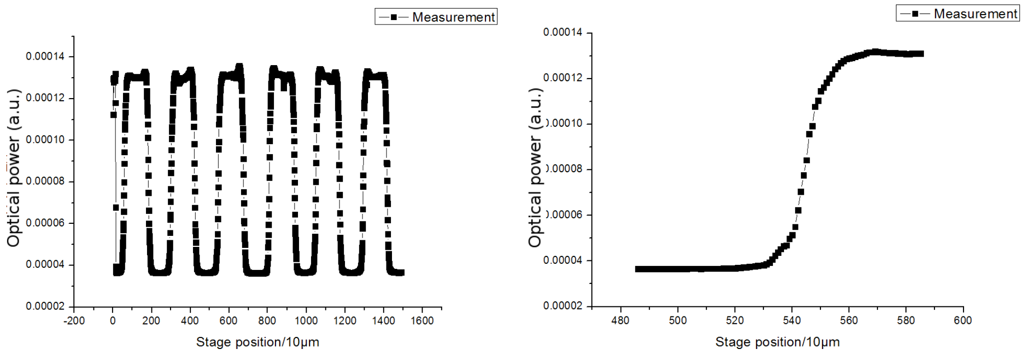

(a) Raw data from the beamprofile measurement. Transmitted optical power (Y-axis) is measured while a grating is scanned through the laser beam at the focal plane.

(b) One slope extracted from the transmitted power measurement.

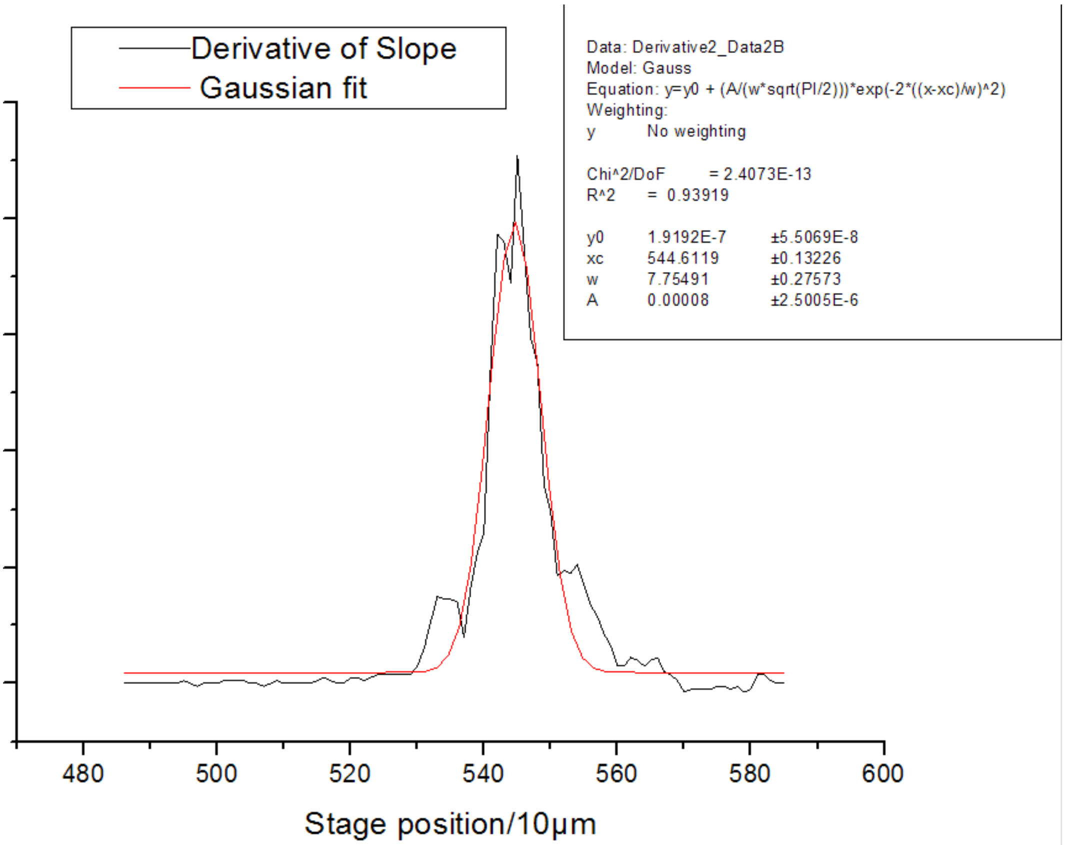

```
Data: Derivative2_Data2B
Model: Gauss
Equation: y=y0 + (A/(w*sqrt(PI/2)))*exp(-2*((x-xc)/w)^2)
Weighting:
y        No weighting

Chi^2/DoF      = 2.4073E-13
R^2    = 0.93919

y0      1.9192E-7       ±5.5069E-8
xc      544.6119        ±0.13226
w       7.75491         ±0.27573
A       0.00008         ±2.5005E-6
```

(c) The data from the slope in plot 3.6(b) was differentiated using Origin 7.5$^{\mathrm{TM}}$ and a Gaussian curve was fitted to the differentiated plot.

Figure 3.6: Beam profile and spot size measurements. X-axis is the sample position given in 1/10 μm.

$$I_g(0) = \frac{2 \times 285\mu W}{\pi(0.8\mu m)^2} = 283\mu W/\mu m^2 = 28.3kW/cm^2$$

To calculate the average intensity in the $1/e^2$-radius the power inside the radius is first calculated as

$$\int_0^{2\pi} \int_0^{r_{min}} I(r) r \, \mathrm{d}r \mathrm{d}\theta = \frac{2P}{\pi r_{min}^2} \int_0^{2\pi} \int_0^{r_{min}} exp\Big[- \frac{2r^2}{r_{min}^2} \Big] r \, \mathrm{d}r \mathrm{d}\theta$$

$$\Big[s = -\frac{2r^2}{r_{min}^2}, \frac{\mathrm{d}s}{\mathrm{d}r} = -\frac{4r}{r_{min}^2} \Rightarrow \mathrm{d}r = -\frac{r_{min}^2}{4r} \mathrm{d}s \Big]$$

$$= \frac{2P}{\pi r_{min}^2} \left(-\frac{r_{min}^2}{4} \right) \int_0^{2\pi} \int_{-2}^{0} exp\Big[- \frac{2r^2}{r_{min}^2} \Big] \mathrm{d}r \mathrm{d}\theta$$

$$= \frac{2\pi P}{2\pi} \left[e^0 - e^{-2} \right] = P(1 - e^{-2})$$

i.e., 86.5% of the total power is within the $1/e^2$-radius (see figure 3.7) and the average power inside the radius is

$$P_{avg} = \frac{0.865 \times 285\mu W}{\pi(0.8\mu m)^2} = 122\mu W/\mu m^2 = 12.2kW/cm^2$$

This means that the required dose for curing e.g., Norland Optical Adhesive 81 (NOA81, section 2.1.1) is reached in just 0.33 ms, which is shorter than the minimum open time of the shutter. This explains the need for the ability to attenuate the laser power.

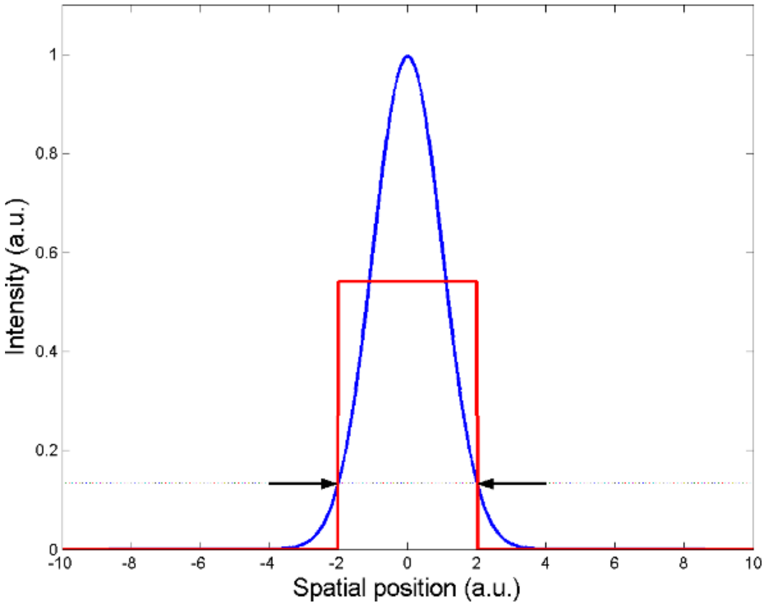

Figure 3.7: Schematic showing the Gaussian intensity distribution (blue) approximated to a 'flat top' (red) intensity profile. Arrows show the $1/e^2$-radius.

3.3 Norland optical adhesive writing

Initial testing of the system was done using a Norland Optical Adhesives negative tone photoresist (presented in detail in section 2.1.1) on borosilicate glass substrates. The good spinning properties, fast cure, and excellent adhesion once cured, makes NOA ideal for testing the laser writing system.

3.3.1 Experimental

Laser writing patterns in NOA on glass substrates were made by the following experimental process:

1. The borosilicate glass cover slide was thoroughly cleaned in an ultrasonicated acetone and methanol bath, and rinsed in deionised (DI) water. The substrate was then spun dry and was put on a hotplate at 120°C for 15

minutes to evaporate solvent residues.

2. The substrate was placed on the chuck of the spin coater and NOA was carefully dropped on the substrate, with care taken to avoid air bubbles.
3. Spin coating was performed at speeds ranging from 4000 to 8000 rpm for 30–60 seconds to give different thicknesses of the NOA film.
4. The NOA-film-covered substrate was placed directly onto the translation stage.
5. Laser exposure was done by opening the shutter for a determined duration and/or by moving the stage in a determined pattern.
6. Development was done by immersing the substrate in acetone and moving it gently for approximately 30 seconds and subsequently rinsing in first methanol then DI water.
7. The substrate was dried gently with a flow of air or nitrogen.

Solvents were used as bought from Sigma-Aldrich without further purification. The cleaning process is critical for the adhesion of the cured structures. Dust and other contaminations on the substrate surface not only compromise the quality of the spun film but may also cause the pattern to release from the substrate during the development process. The film thickness after the spin coating is primarily dependent on the viscosity of the photopolymer, but also on the spinning speed used. 8000 rpm is the highest speed of the spin coater and the speed most commonly used for thin films. For the exposure the sample is placed directly on the translation stage, which is then slid under the microscope objective. To find the optimal focus the laser beam at maximum attenuation is directed to a corner of the sample and the microscope objective is translated first with the coarse manual stage and then finely tuned with the high precision piezo stage until the reflected spot imaged by the camera is as small as possible. The writing was mostly done with help of the LabView^{TM} vi-programs described earlier in this section. The opening and closing of the shutter is synchronised with the movement of the motorised translation stages. The development process was done in a small glass beaker filled with acetone, as this is the solvent recommended for removing uncured residue by Norland products [7]. It was the solvent which gave the best results when compared to methanol and toluene. After ∼30 seconds development in acetone, the substrate is rinsed with methanol and deionised water. After being dried in a flow of air or nitrogen the sample is ready for characterisation. Before performing stylus profilometry (where a pointed stylus is moved over the surface of the substrate and the LDW structures) the pattern is allowed to set for 24 hours or is postbaked on a hotplate at ∼100°C for one hour to reach maximum bond strength.

3.3.2 Results

Characterisation of the produced patterns was performed with optical microscopy, stylus profilometry (Dektak), and atomic force microscopy (AFM).

The lines in NOA63 in figure 3.8 were produced with a delivered average optical laser power of 56.7 μW and a stage velocity of 1.5 mm/s. This gives a maximum exposure dose in the centre of the line (calculated by putting $y = 0$ in equation 3.5) of:

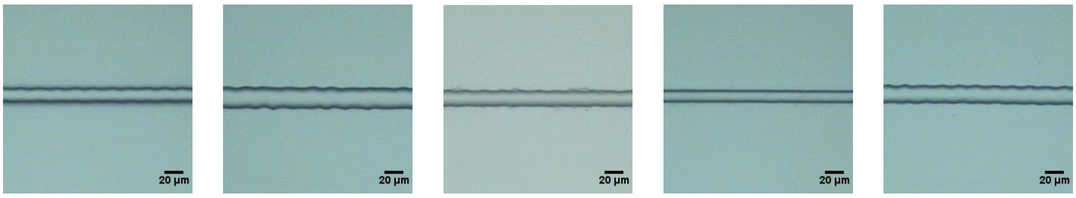

(a) 4000 rpm. (b) 5000 rpm. (c) 6000 rpm. (d) 7000 rpm. (e) 8000 rpm.

Figure 3.8: LDW lines in NOA63, as a function of film thickness (defined by spin speed).

$$E = \frac{\sqrt{2}P}{\sqrt{\pi}r_{min}v} = \times\frac{\sqrt{2}\times 56.7\mu W}{\sqrt{\pi}\times 0.8\mu m\times 1500\mu m/s}$$
$$= 37.7nWs/\mu m^2 = 3.77J/cm^2$$

The spinning speed was varied for the substrates for each line from 8000 rpm to 4000 rpm in figure 3.8(e) to 3.8(a), respectively. The height and the width of the LDW line structures are given in table 3.1. The heights were measured by Dektak profilometer and the widths were determined from optical micrographs with ImageJ$^{\text{TM}}$ software and using a graticule for calibration.

Table 3.1: Some characteristics of the lines written in NOA63 shown in figure 3.8.

	4000 rpm	5000 rpm	6000 rpm	7000 rpm	8000 rpm
Height	4.0 μm	3.6 μm	3.2 μm	2.8 μm	2.2 μm
Width	16 μm	22 μm	17 μm	14 μm	18 μm

While the height of the laser written structures has a clear dependence on the spinning speed, the width is decided by the z-position of the laser beam focus. As calculated earlier, the Rayleigh range is 5.48 μm, meaning that if the focus is misaligned with the substrate surface by 2.74 μm, the spot diameter and hence the cured structure will be ~1.41 times bigger. The structures in figure 3.8 were written before the acquisition of the piezo driven Z-translation stage and the difficulty in manually adjusting the focus accounts for the variations in width for the lines.

As an attempt to write narrow lines, NOA61, which has a lower viscosity than NOA63, was used. The film was spun at 8000 rpm on borosilicate glass giving an approximate film thickness of 800 nm. In figure 3.9, an AFM image of the resulting line is shown when using a writing speed of 1.5 mm/s and a total power of 27 μW, corresponding to a maximum dose of 1.6 J/cm^2.

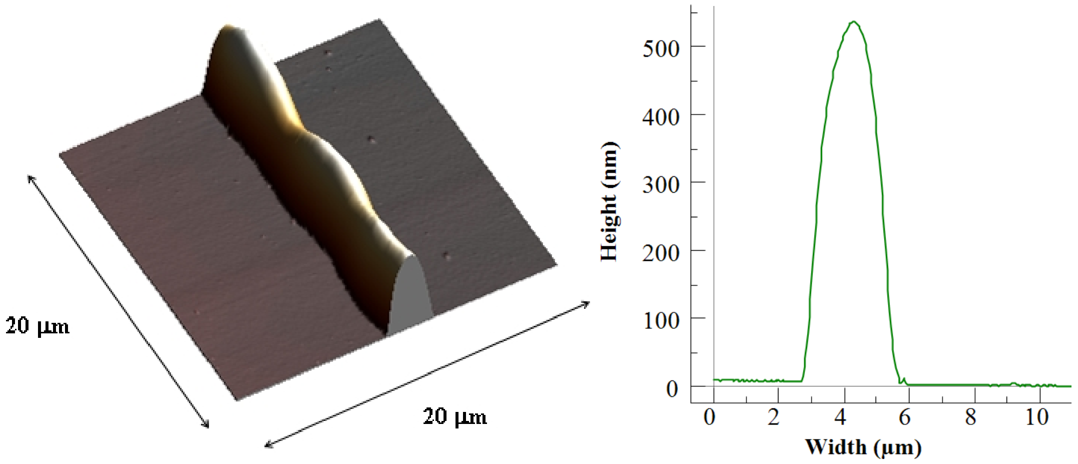

Figure 3.9: Atomic force microscope image of a LDW line in NOA61 on a glass substrate and the surface profile from the narrow region.

The line width of the laser written structure in the imaged 20 μm × 20 μm region ranges from 1.6 μm to 3.0 μm and the height of the line structure is 550–800 nm.

Figure 3.10 shows a test pattern of dots in NOA81 aligned with a micro-LED array. The LabView$^{\text{TM}}$ program used for this pattern is described in section A.2 in the appendix. NOA81 was spun directly on the device with a spinning speed of 4000 rpm. Exposure was done for 20 ms with a total laser optical power of 120

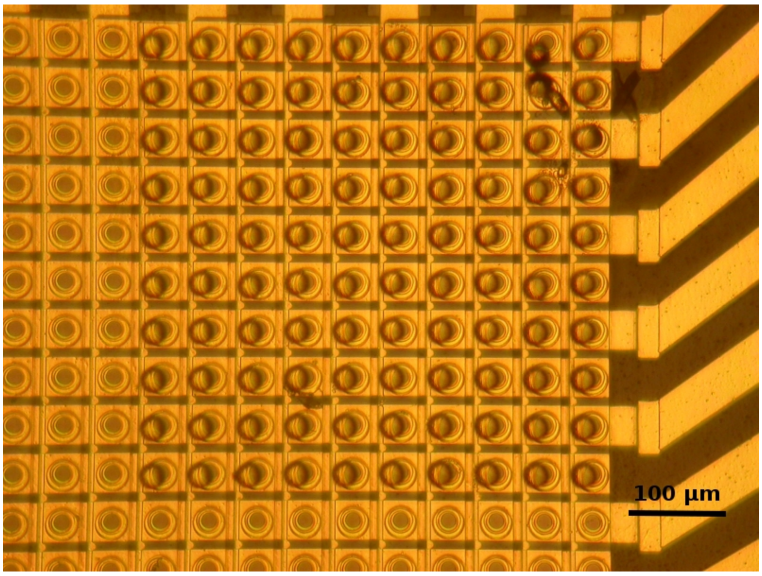

Figure 3.10: Test pattern of dots in NOA81 aligned with a micro-LED array.

μW, the spot diameter was defocused to approximately match the pixel diameter, which is 20 μm, giving an exposure dose of 1.5 J/cm^1.

3.4 Truxene nanocomposite writing

The ability to accurately pattern light-emitting materials is important for many applications, such as single photon sources [8, 9], waveguides, and lasers. There have been reports on incorporating nanoscaled inorganic materials into organic photoresists [10, 11, 12], and here we extend such studies to include the oligofluorene-functionalised truxenes.

Fabricating waveguide structures in truxene blends can play an important role in realising functioning lasers from these materials. Current organic lasers often use only a grating to provide the feedback, a waveguide structure in addition to this could reduce laser threshold and increase efficiency.

Another application is for truxene blend structures to work as colour down-converting structures on micro-LED arrays [13].

3.4.1 Experimental

As organic light emitting materials are generally not compatible with standard photolithographic processes [14], patterning them constitutes a major technical challenge. In this section nanoscaled organic light emitters, oligofluorene truxenes (presented in detail in section 2.2.1), are blended with a negative tone photoresist material, CHDV (section 2.1.1), as described in section 2.3.1.

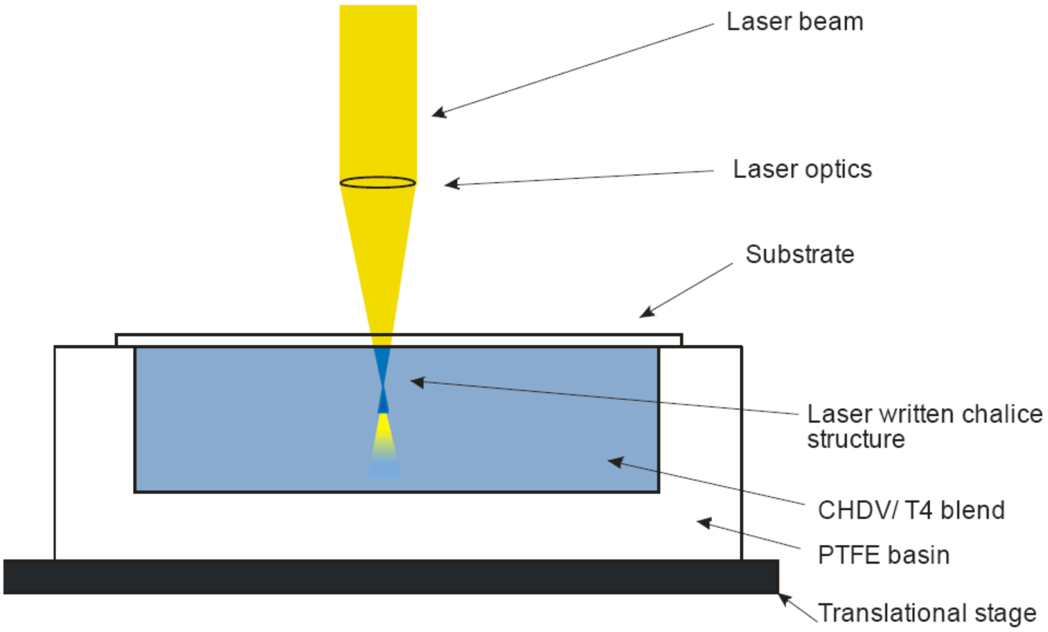

Figure 3.11: The sample setup when writing through the substrate.

The CHDV material is highly transparent in the UV spectral region (see figure 2.5), a desirable property when photopumping the light emitting material with an UV source. The truxene materials are also miscible in CHDV. The reason for this is the absence of aromatic rings (present in most negative type photoresists) and $\pi - \pi$ interactions. However, this also causes low viscosity (5.62 cP [15]), which is detrimental to the film-forming properties. When CHDV is spun onto a glass substrate it is immediately dewetted and therefore an alternative method had to be used to pattern the CHDV/T4 blend on glass substrates. In the method chosen, the exposure is made through the transparent substrate into a liquid basin of the nanocomposite material. The setup can be seen in figure 3.11. The polytetrafluoroethylene (PTFE) block contains a shallow basin where the nanocomposite is pipetted, with care taken to avoid air bubbles. The borosilicate glass coverslip is then carefully placed over the basin, again with care taken not to trap any air under the substrate. The PTFE block is then placed on the translation stage and the exposure is performed. Because of the photoinduced electron transfer (PET) discussed in section 2.3.1, the curing of the nanocomposite occurs very rapidly.

3.4.2 Results

For comparison, three different concentrations of T4 in CHDV were tried, being 0.5 wt%, 1.0 wt%, and 5.0 wt%, respectively. 1.0 wt% of photo acid generator (PAG) was used throughout these experiments, unless stated otherwise. Four lines written at 40 μW, 80 μW, 120 μW, and 160 μW optical laser power (as measured at the sample position), respectively, were written on each substrate. Associated micrographs of the sample with 1.0 wt% T4 can be seen in figure 3.12. The writing speed was 1 mm/s throughout. The micrographs were taken using a Nikon Eclipse TE2000-U inverted microscope with a 20X/0.5 N.A. Plan

Fluor objective. The fluorescence mode microscopy images were taken under illumination from a mercury lamp with peak emission at 365 nm and a UV-2A filter cube is used to filter out the excitation source. They show uniformly distributed blue photoluminescence from the T4 truxene.

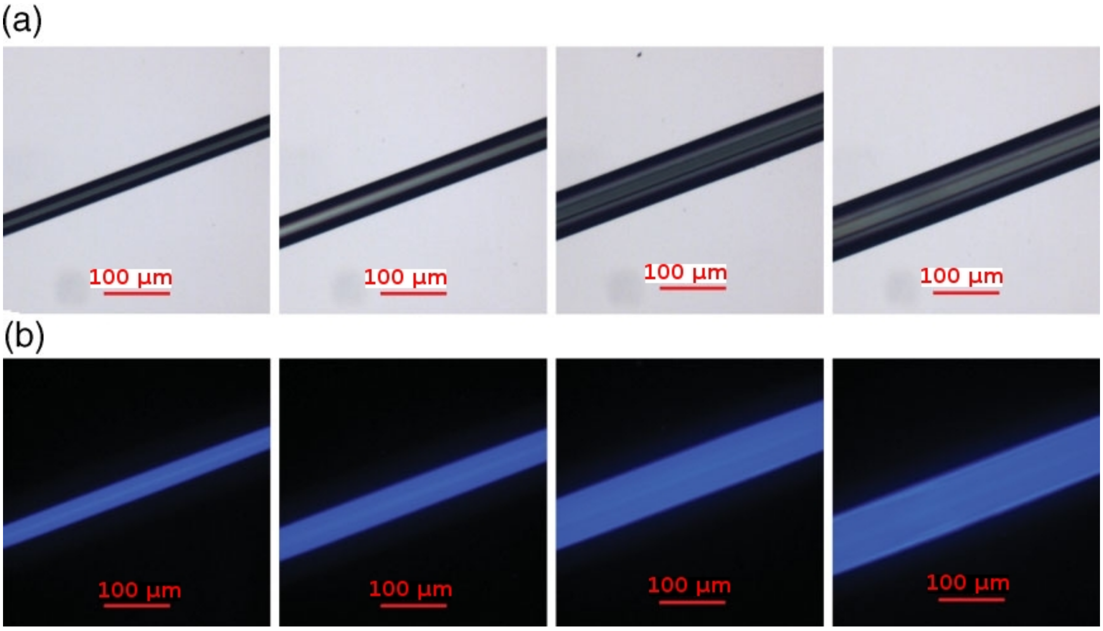

Figure 3.12: Micrographs of LDW lines in normal (a) and fluorescence (b) mode. 1.0 wt% T4 and 1.0 wt% PAG concentration. The laser is power is varied, from 40 μW, 80 μW, 120 μW, to 160 μW going from left to right.

The dimensions of the laser direct written structures at different T4 concentrations and laser powers can be seen in table 3.2. The widths are measured from micrographs with ImageJ$^{\mathrm{TM}}$ software using a graticule as reference.

The scanning electron micrographs (SEM), which can be seen in figure 3.13, were taken by first evaporating carbon on the laser written structures and the substrate with a BAL-TEC CED 200 carbon evaporator. This was done to add a conductive layer to the insulating laser written structure and substrate to avoid charging the substrate with the electron beam. This would otherwise distort the

Table 3.2: Line widths for different laser powers and concentrations of T4 in CHDV.

Laser power	0.5 wt% T4	1 wt% T4	5 wt% T4
40 mW	35 μm	35 μm	50 μm
80 mW	45 μm	50 μm	80 μm
120 mW	70 μm	70 μm	100 μm
160 mW	90 μm	95 μm	120 μm

images by deflecting the e-beam. The images in figure 3.13 were then taken with a FEI Sirion field emission SEM. The SEM images show “three dimensional” images of the written structures. As can be seen the shape of the structures do not follow the outline suggested by the theoretical calculations in figure 3.2. The reason for this is hinted at in figure 3.11, as the focal point actually occurs well inside the CHDV/T4 blend, instead of at the interface between the blend and the substrate. This together with the beam shape and the absorption causes the 'chalice shape'. Predicting the exact shape of the cured structure is however difficult as it depends on other factors than the laser beam, such as migrating behaviour of polymerisation centres (diffusion of low molecular weight molecules with ongoing polymerisation) from the illuminated area. Also the development can affect the final shape of the structures. However the structures are well defined and have smooth side walls with high aspect ratios.

The thin patches seen for instance in figure 3.13(c) and 3.13(d) are residues of the CHDV/T4 composite due to incomplete wash-off. The slightly larger features at the end of some of the lines are due to a time lag between the stopping of the motion and the shutting of the computer-controlled mechanical shutter.

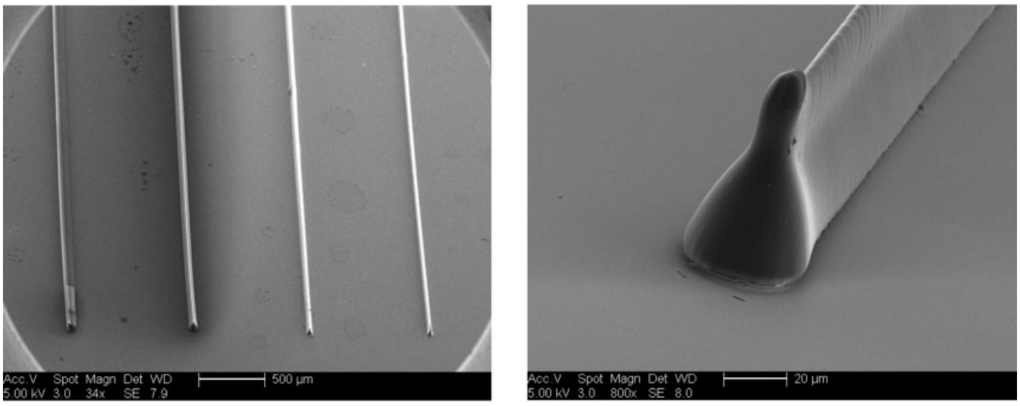

(a) Image showing the 0.5 wt% T4 sample with four lines written at 160 μW, 140 μW, 80 μW, and 40 μW from left to right.

(b) Image showing a close up of the line written at 40 μW with 0.5 wt% T4 in CHDV blend.

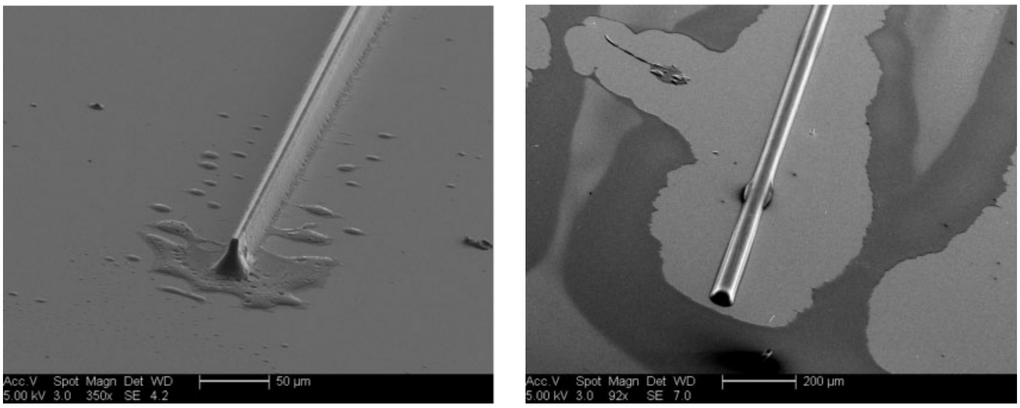

(c) Image of the line written at 40 μW with 1.0 wt% T4 in CHDV blend.

(d) Image showing the line written at 40 μW with 5.0 wt% T4 in CHDV blend.

Figure 3.13: Scanning electron micrographs of laser written lines in CHDV/T4 blends.

A Lissajous pattern, defined by

$$x = A \sin at + \delta, y = B \cos bt \tag{3.10}$$

with A=B, a=5, b=4, and δ=0, laser written in the nanocomposite can be seen in figure 3.14. It was used because it contains many intersections so that the behaviour of the curing can be studied when exposing areas which have already

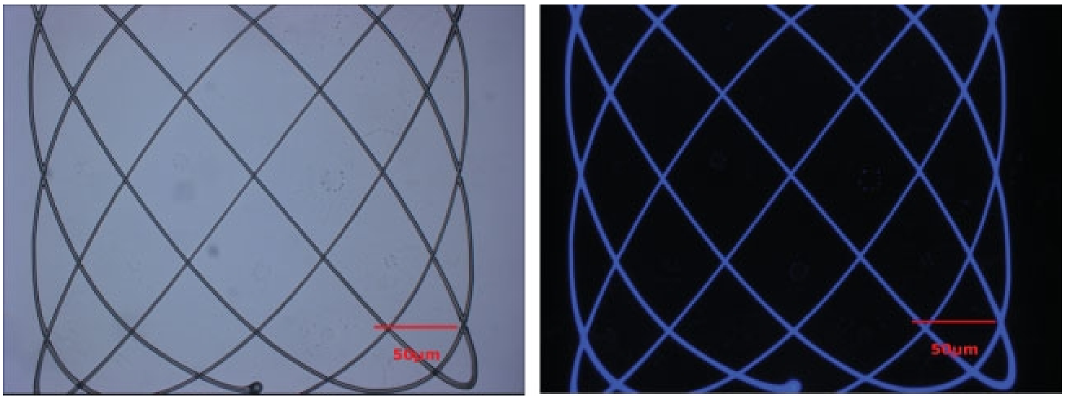

Figure 3.14: Micrographs of LDW Lissajous patterns in normal and fluorescence mode.

been exposed. By adding PAG at a lower ratio than the standard 1.0 wt% a slower and more controlled curing was achieved. The pattern in figure 3.14 was written with a laser power of 0.4 μW in a blend with 1.0 wt% T4 and 0.1 wt% PAG. The resulting line width is 2.5 μm, approaching the resolution limit of the writing system.

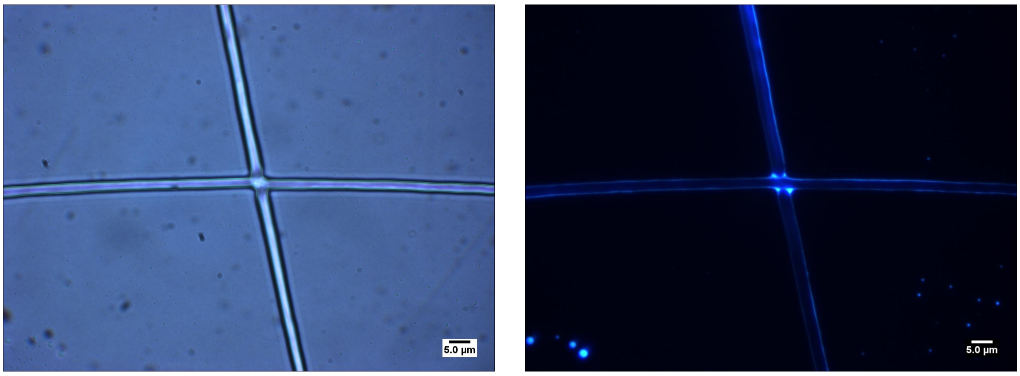

(a) Normal illumination micrograph.

(b) UV illumination fluorescence micrograph.

Figure 3.15: Close up of one intersection in figure 3.14 using a high resolution oil immersion 100X/1.3 N.A. objective.

The images in figure 3.15 were taken using a high resolution oil immersion objective (CFI Plan Fluor 100X/1.3 N.A.), they further confirm the uniform distribution of the T4 molecules in the CHDV matrix. The brighter spots on the edges in the intersection also seem to indicate that light is guided along the structure (it is, in effect, a waveguide).

3.5 Summary

In this chapter, the theory of laser writing with a Gaussian beam has been presented. Resolution limits have been defined and calculated.

The laser writing setup built as part of this thesis work was introduced and its performance characterised.

Results for laser writing in negative type photoresists were given. Optical adhesives from Norland products were used to test the setup and feature sizes down to 1.6 μm was achieved in NOA61.

Nanocomposites consisting of truxene light emitting molecules and CHDV negative photoresist were made and used to make fluorescing microstructures on glass substrates with feature sizes down to 2.5 μm.

References

[1] Robert R. Krchnavek, Gail R. Lalk, and Davis H. Hartman. Laser direct writing of channel waveguides using spin-on polymers. *Journal of Applied Physics*, 66(11):5156–5160, 1989. 75

[2] K. Kords, K. Bali, S. Leppvuori, A. Uusimki, and L. Nnai. Laser direct writing of copper on polyimide surfaces from solution. *Applied Surface Science*, 154-155:399 – 404, 2000. 75

[3] Markus Deubel, Georg von Freymann, Martin Wegener, Suresh Pereira, Kurt Busch, and Costas M. Soukoulis. Direct laser writing of three-dimensional photonic-crystal templates for telecommunications. *Nat Mater*, 3(7):444–447, 2004. 10.1038/nmat1155. 75

[4] Takeshi Nakamoto, Katsumi Yamaguchi, Petros A Abraha, and Kunihiro Mishima. Manufacturing of three-dimensional micro-parts by UV laser induced polymerization. *Journal of Micromechanics and Microengineering*, 6(2):240, 1996. 77

[5] Paul F. Jacobs. *Rapid Prototyping and Manufacturing: Fundamentals of StereoLithography.* McGraw-Hill, Inc., New York, NY, USA, 1993. 77

[6] J. D. Zook and T. C. Lee. Geometrical interpretation of gaussian beam optics. *Appl. Opt.*, 11(10):2140–2145, 1972. 77

[7] Norland Products Inc. *Norland Optical Adhesive 81*, 2007. 90

[8] Brahim Lounis and Michel Orrit. Single-photon sources. *Reports on Progress in Physics*, 68(5):1129, 2005. 93

[9] Mark Oxborrow and Alastair G. Sinclair. Single-photon sources. *Contemporary Physics*, 46(3):173 – 206, 2005. 93

[10] Lin Pang, Kevin Tetz, Yaoming Shen, Chyong-Hua Chen, and Yeshaiahu Fainman. Photosensitive quantum dot composites and their applications in optical structures. *Journal of Vacuum Science & Technology B: Microelectronics and Nanometer Structures*, 23(6):2413–2418, 2005. 93

[11] C. Ingrosso, V. Fakhfouri, M. Striccoli, A. Agostiano, A. Voigt, G. Gruetzner, M. L. Curri, and J. Brugger. An epoxy photoresist modified by luminescent nanocrystals for the fabrication of 3D high-aspect-ratio microstructures. *Advanced Functional Materials*, 17(13):2009–2017, 2007. 93

[12] Anna C. Balazs, Todd Emrick, and Thomas P. Russell. Nanoparticle Polymer Composites: Where Two Small Worlds Meet. *Science*, 314(5802):1107–1110, 2006. 93

[13] M. Wu, Z. Gong, A. J. Kuehne, A. L. Kanibolotsky, Y. J. Chen, I. F. Perepichka, A. R. Mackintosh, E. Gu, P. J. Skabara, R. A. Pethrick, and M. D. Dawson. Hybrid gan/organic microstructured light-emitting devices via ink-jet printing. *Opt. Express*, 17(19):16436–16443, 2009. 94

[14] John A. DeFranco, Bradley S. Schmidt, Michal Lipson, and George G. Malliaras. Photolithographic patterning of organic electronic materials. *Organic Electronics*, 7(1):22 – 28, 2006. 94

[15] Alexander J.C. Kühne. *UV Transparent and Light Emitting Photo-Polymers for Optoelectronic Applications.* PhD thesis, University of Strathclyde, 2008. 95

Chapter 4

Micro-LED Direct Writing

This chapter will present a capability for mask-less photolithography based on a complementary metal-oxide semiconductor (CMOS) driven micro-LED device operating in the near UV spectral region. The setup will be introduced and characterisation measurements of it will be given. Results achieved in writing structures with positive- and negative-type photoresist will be presented.

Photolithography (as described in section 1.2) is the standard method for patterning in the semiconductor industry and in such emerging technologies as micro-fluidics, Lab-on-a-Chip, microelectromechanical systems (MEMS), opto-genetics, etc. Standard photolithographic methods require a custom photomask for each process. Manufacturing this mask is often expensive and time consuming, hence limiting researchers' ability to quickly put their ideas into practice. There have been several proposed solutions for this; laser direct writing was presented in the previous chapter and several others will be presented below.

4.1 Maskless photolithography tools

Maskless photolithography is a big area of research and there are many different systems with capabilities ranging from tens of nanometer resolution to hundreds of micrometers and with very varying throughput, cost, and complexity.

Laser direct writing is the most mature of the maskless lithography tools [1, 2, 3] and is commonly used in rapid prototyping, however it has limitations in being a single beam technique, hence reducing throughput. The cost of high quality coherent sources is still high and their use requires special safety precautions, hence adding to cost and complexity of such systems.

A low cost method proposed is projection writing using a single spatially filtered light emitting diode (LED) [4]. The light from a standard 365 nm LED, mounted in a plastic tube, is filtered through a pinhole aperture of 3 mm and then focused down to a spot with a microscope objective (50X and 0.55 N.A.). This resulted in feature sizes down to $\sim$35 μm with a writing speed of 80 μm/s. By reducing the pinhole aperture to 1 mm and increasing the speed to 250 μm/s line widths of 17 μm were achieved. The movement was done using a syringe pump.

A Digital Micromirror Device (DMD) can be used to create an image to be projected onto a sample [5]. Images showing the setup used are shown in figure 4.1. The light from a ultrahigh pressure (UHP) lamp from a video projector is used instead of a (in lithography) more commonly used mercury arc lamp. The light from the lamp is focused and projected onto a DMD type spatial light modulator (SLM), which consists of 768 000 tiltable mirrors each of $\sim 17.5 \times 17.5$ μm^2 size. The SLM is placed in the image plane of an infinity corrected

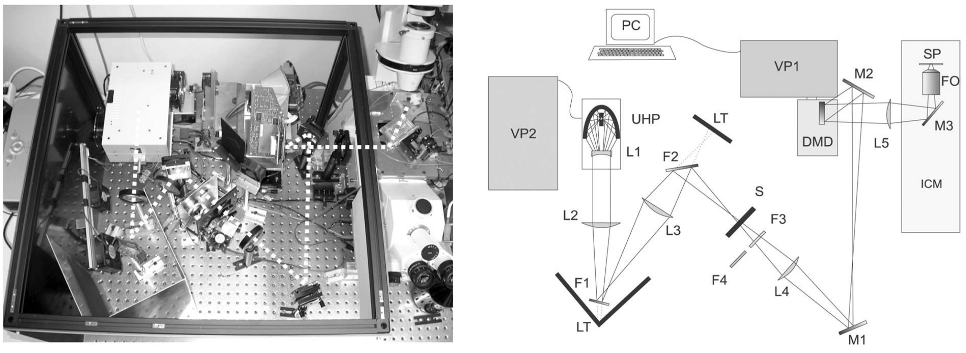

(a) Photograph of the setup. (b) Schematic of the setup.

Figure 4.1: The setup used in [5]. The light from an UHP lamp is filtered and projected onto a DMD to form an image, which is then demagnified through a microscope objective.

microscope objective (5X and 0.25 N.A.) by using an extra lens and the sample to be patterned is placed in the focal plane. The resolution achieved with this system is 3.5 μm with a high aspect ratio (1:10 in a 40 μm thick SU-8 film). By replacing the 5X objective with a 20X microscope objective submicron resolution was shown on UV sensitive photochromic films. The system was primarily developed for light-directed in situ synthesis of DNA microarrays [6, 7]. The system based on a commercial DMD works well in the visible and the near UV, but for even higher resolution writing, lower wavelengths are required and the appropriate mirrors have to be custom made. A micro-mirror device for deeper UV is presented in [8]. These systems have an impressive resolution and versatility, but are rather complex and bulky and all require an external high-power light source.

An example of a low cost, low resolution technique is to use a standard photocopier to define a pattern on a transparency, which is then used as a master to pattern polydimethylsiloxane (PDMS) micro-fluidic channels [9]. The resolution is limited to $\sim$50 μm with this low cost method. A simple, fast, and inexpensive masking technology for fabricating etch patterns on glass is proposed by Coltro et al. in [10]. The standard office laser printer is used to write the pattern on wax paper. The toner layer is then thermally transferred to a glass slide and used as an etch mask. When using a 600 dpi printer, channels down to 200 μm wide could be manufactured. Another method with similar limits in resolution is the use of a cutter plotter to define the etching mask [11]. Although these techniques are remarkable in simplicity and low cost, the resolution is not enough for many applications.

Focused ion beam (FIB) based techniques have been used to achieve impressive resolutions (30 nm) for more than 20 years [12]. A beam of ions (most commonly Ga^+) hits the substrate and sputters material from the surface. As the beam is scanned over the substrate a pattern is produced. Electron beam lithography (EBL) is, along with LDW, the most common method of producing the photomasks for conventional lithography. The basic principle is that an electron beam is focused on a substrate covered with a thin film of specialised e-beam resist, such as Poly(methyl methacrylate) (PMMA). Both these techniques are well established commercial techniques with a resolution of a few tens of nm, but they are complex, expensive, and suffer from low throughput.

A technique suitable for periodic patterns such as gratings is interference lithography or holographic lithography. In the simplest form a coherent beam is divided in two (e.g., with a beam splitter) and then allowed to interfere with itself thus forming a pattern with a period $p = \frac{\lambda}{2\sin(\theta)}$ where λ is the wavelength and θ is half the angle between the two beams as they recombine. By passing a laser beam through a grating and allowing the 1^{st}-order diffracted beams (while blocking the zero-order beam) to propagate through a second and third grating, then allowing the beams to interfere, an interference pattern with a period of half that of the gratings used is produced. With this technique, gratings with a period of 100 nm have been created on areas as big as 10 cm^2, by using an ArF laser ($\lambda = 193$ nm) and gratings with 200 nm period [13, 14]. While this technique has high resolution and good throughput, creating patterns other than regular gratings is difficult and requires a very complex holographic template, a process that is considerably more complex than the manufacturing of a photomask.

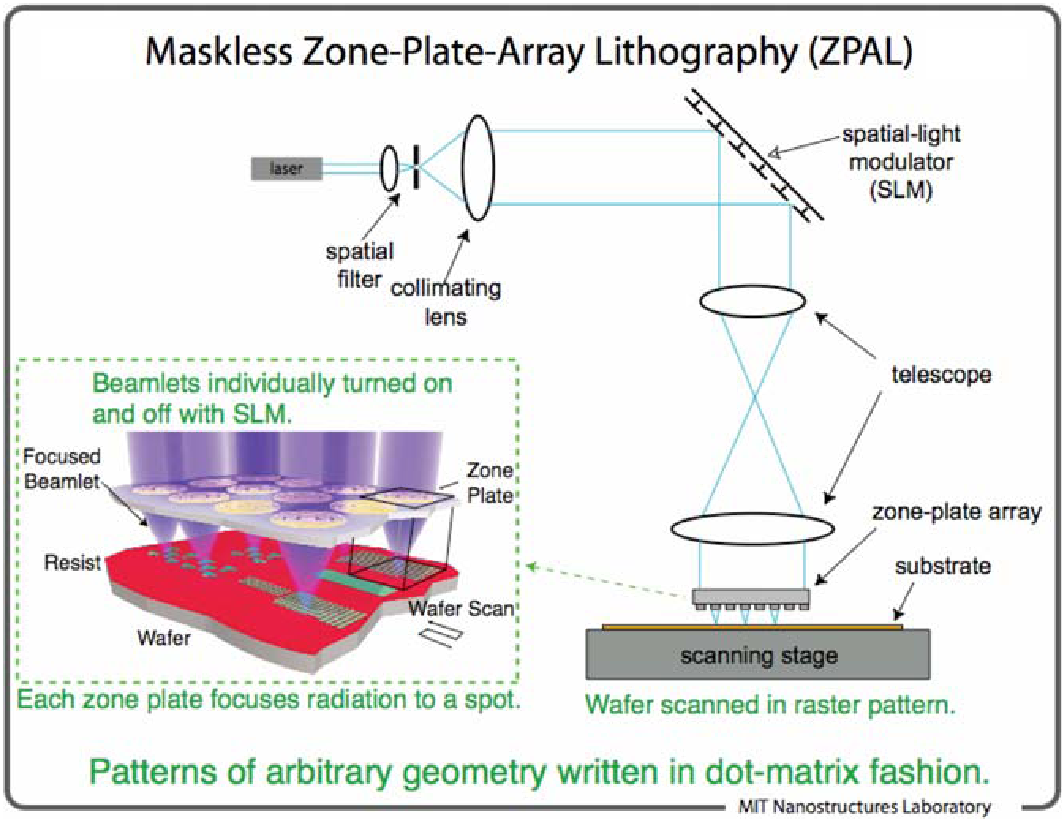

Figure 4.2: Schematic image of a ZPAL system. After [15].

Zone-plate-array lithography (ZPAL) is a technique that promises high resolution and large area patterning [16]. Figure 4.2 shows a schematic of the ZPAL system used in [15]. The laser used is a GaN based semiconductor laser operating at 400 nm, the SLM used is a commercial array of 1024 grating light valves, the zone plates of the array are phase zone plates fabricated using EBL and hydrogen silsesquioxane (HSQ) resist. The N.A. of the zone plates is 0.85. The SLM is used to turn off and on the light to each individual zone plate and as the substrate is scanned a pattern is produced. Without the use of water immersion this system has been shown to produce gratings with 135 nm spacing and with water immersion 115 nm. However promising it is, the ZPAL system is a complex tool.

4.2 CMOS driven micro-LED device

CMOS is the preferred technology for large scale semiconductor manufacturing, e.g., microprocessors and computer memory. Gallium nitride LEDs cannot be made directly by CMOS processes, but making LEDs compatible with a CMOS driver is important for commercialisation and adds functionality, such as pulsed driving, to the device. By integrating an array of single photon avalanche diodes (SPADs), functionality for on-chip sensing in time resolved fluorescence measurements can be added to the chip[17, 18]. The CMOS-driver, which was used in this early work, was originally developed for electro-wetting. This led to a number of disadvantages when adapting it and the LED device to be compatible.

The CMOS driver used herein was custom-designed (by colleagues at the University of Edinburgh) to work with a micro-pixellated LED [19]. It was fabricated using a standard 0.35 μm CMOS process by Austria Microsystems. It consists of 64 individual drivers in an 8×8-array. Each driver measures 200 μm × 200 μm on the chip of which one quadrant (100 μm × 100 μm) is a full metal bond stack (figure 4.3), where the LED p-pads will be bump bonded. The CMOS driver

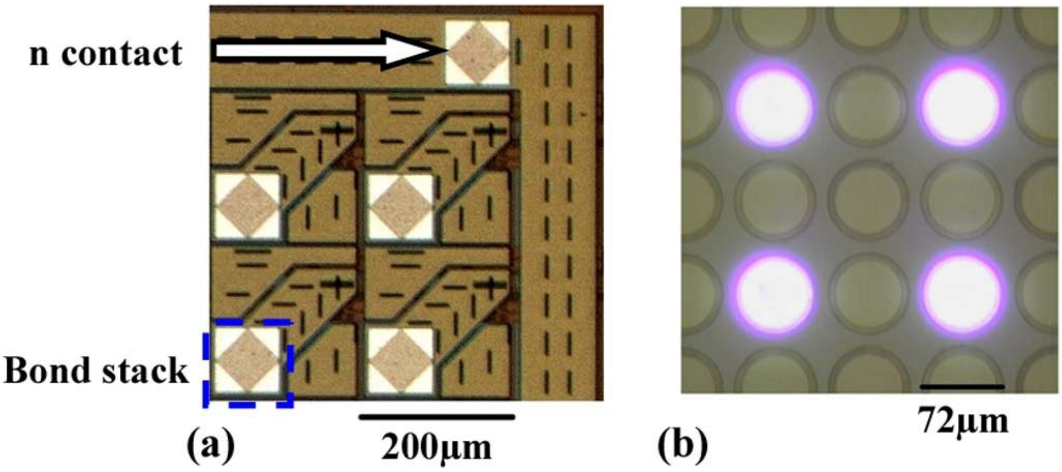

Figure 4.3: Optical micrograph of the CMOS driver (a) and the bonded micro-LED device with four pixels turned on (b).

supplies a maximum voltage of 5 V and a maximum current of 100 mA to each pixel. However the ground level of the LED connection is not connected to the ”global” ground. Therefore it is possible to connect an external power supply and apply a negative bias to the ground, hence increasing the effective voltage applied to the LED. The driver is also designed to be able to deliver short pulses of controlled duration and frequency. The pulses can be as short as 300 ps full-width at half-maximum (FWHM) and the frequency can be set with the on-chip voltage-controlled oscillator (VCO) from 6MHz to 800MHz. There is also the capability of connecting an external oscillator, in which case any frequency can be applied.

The micro-LED devices used here were presented in section 1.1. For the work of this chapter they are in a flip-chip configuration, meaning that the light is extracted through the sapphire substrate which the GaN layers are grown on. The device used is a 16×16-array with each light emitting pixel being 72 μm in diameter and the pitch is 100 μm, as can be seen in figure 4.3(b). Alternating

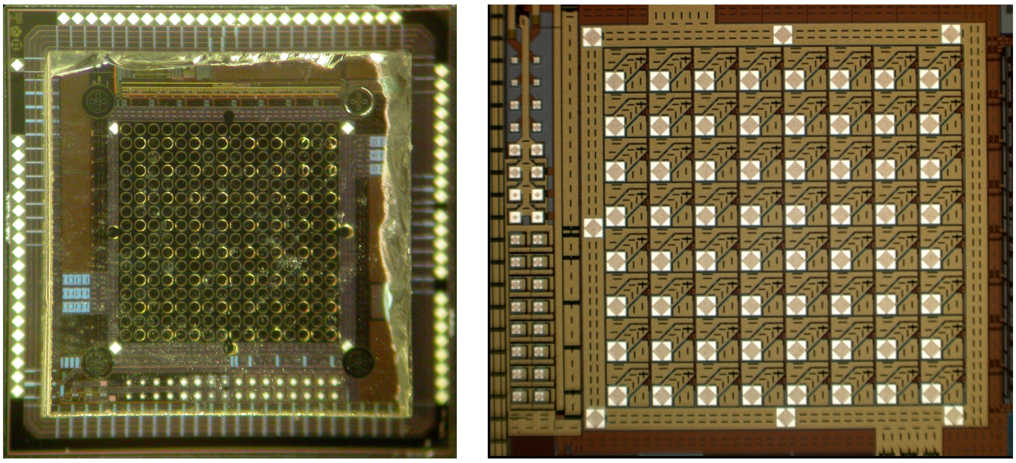

(a) Optical micrograph of the micro-LED device bonded to the CMOS driver.

(b) Optical micrograph of the bare CMOS chip before bonding the micro-LED.

Figure 4.4: Images of the CMOS driver chip. Alternating pixels in (a) are bump-bonded to the CMOS chip in (b).

pixels are bonded to the CMOS driver by a bump-bonding process, where a Au bump provides the electrical and physical contact between the LED and the CMOS driver. The bump bond is also believed to increase the thermal dissipation from the LED and hence improving the performance compared to wire bonded devices. A micrograph of the LED bonded to the CMOS driver can be seen in figure 4.4(a). In figure 4.4(b) the CMOS chip is shown before the micro-LED device is bump bonded.

The optical output power is measured by a calibrated power meter (Coherent FieldMax Top) in close proximity to the device. The ouput from one LED pixel under direct current (DC) driving was measured to be 604 μW at a driving current of 80.0 mA and a voltage of 6.18 V and 340 μW at 20 mA at a driving voltage of 4.50 V. I-V and L-I charactersitics are presented in figure 4.5.

The CMOS control device was attached to a printed circuit board (PCB),

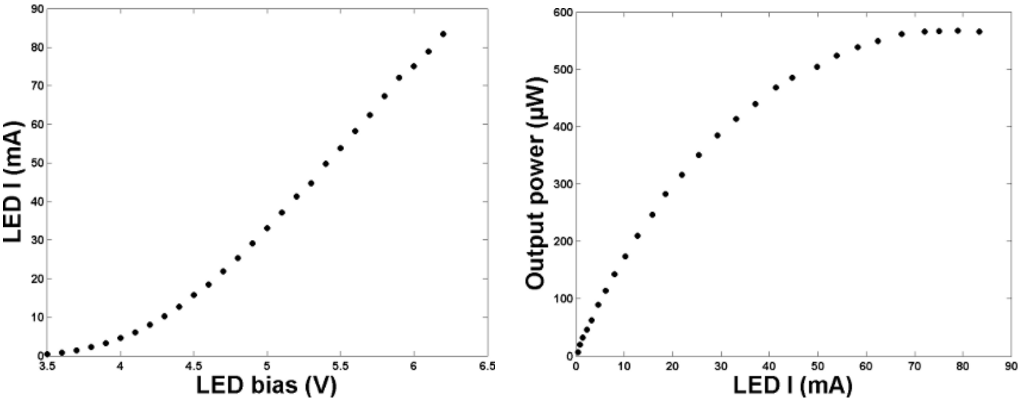

(a) The I-V plot.

(b) The L-I plot.

Figure 4.5: Data plots of injection current vs. voltage and optic power output vs. injection current in a CMOS-driven UV micro-LED.

which is computer controlled via a field programmable gate array (FPGA) board (XEM3010-1000 from Opal Kelly). The voltage delivered to the pixels, the pulse duration, and the VCO frequency are all set by voltage controls on the PCB.

4.3 The micro-LED writing setup

The maskless photolithography system was built to be flexible, inexpensive, and precise. The setup consists of

- Mounting rods and cages for optical components (Linos Microbench).
- A PCB with the CMOS driven LED device and the FPGA board.
- A manual XYZ-translation stage on which the PCB is mounted.
- Two infinity corrected microscope objectives (Nikon CFI Plan Fluor-series) (collection and projection objective).
- A mirror.

- A 50/50 UV beamsplitter cube.
- A piezo Z-translation stage for the projection objective (PI P-725.4CD).
- A motorised XY-translation stage (2 x PI M-112.1DG) for the sample.
- A CCD camera (Prosilica EC650C) with a zoom lens (Navitar, 11-110mm) attached.
- A computer for the control of the sample translation stage, the LED device, and the camera.

For the optical mounts a cage system (Microbench) from Linos was used. It is easy to use and the alignment is simplified by keeping the optic axis in the centre of the cage. A photograph and a schematic image of the setup can be seen in figure 4.6. The mirror mount and the beamsplitter mount are used as bought, while custom mounts for the microscope objectives were produced in-house. The board for the CMOS driver and LED device is mounted on XYZ manual translation stage, which is bolted onto a solid metal plate, which is in turn bolted to the optical breadboard that provides the base of the setup. The collection objective can be slid on the mounting rods but is otherwise static. The mirror is mounted on a platform with adjustment screws for fine alignment. The beamsplitter can be rotated freely in the cage and fine tuned with adjustment screws. The projection objective is mounted on a piezo-electric translation stage to provide very precise focusing, and with the driver used, the measurement feedback gives a precision of 0.1 μm. The sample to be patterned is placed on the motorised XY-translation stage, which is computer controlled and has a repeatability of $\sim$0.1 μm (effective resolution). The minimum incremental motion achievable is 50 nm.

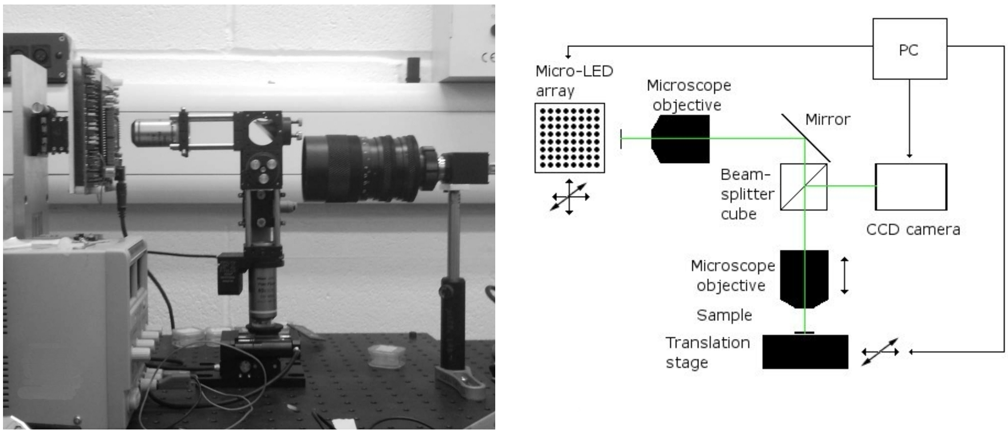

(a) Photograph. (b) Schematic.

Figure 4.6: The CMOS-driven, micro-LED based maskless lithography tool.

The light from the CMOS-driven UV micro-LED array is collected by one microscope objective, which is infinity-corrected, meaning that the output is collimated when the emitting area of the LED is in the focal plane. A second infinity-corrected objective is used to project the light onto the sample. By matching the magnification of the two objectives, magnification or demagnification of the pixel spot can be achieved. The setup also contained a rotatable beamsplitter cube in the path between the two objectives. With a CCD camera equipped with a zoom lens adjusted to focus at infinity, this enables monitoring of the writing in real time and control of the focus. Since the zoom lens is set to focus at infinity and the microscope objectives are infinity corrected, the image displayed on the camera is optically conjugate to the focal plane of each of the objectives.

4.3.1 Software control

The software control for the CMOS-driven micro-LED array device was developed in LabWindows^{TM} by Dr. Gareth Valentine (Institute of Photonics, University of

Strathclyde). A screenshot of the graphical user interface (GUI) for this software can be seen in figure 4.7(b) and the corresponding pattern shown on the LED array can be seen in figure 4.7(a). The panel on the upper left represents the LED array and is used to address the pixels, either by clicking in the panel or by choosing the pixels in the controls to the right of the panel. When the 'Mode', just below the panel, is switched to 'CW' the 'ON' button will switch on the addressed pixels in continuous wave (CW) operation until the button is pressed again. If instead the 'Mode' is switched to 'Pulsed' the controls to the right of it are used. 'Pulse count' sets the number of pulses, for the duration set in the 'Pulse ON-time' and with the interval set in 'Pulse OFF-time'. The pulse time is accurate down to ~100 ms, due to hardware and software limitations. 'Clear' will clear the pixel addressing panel.

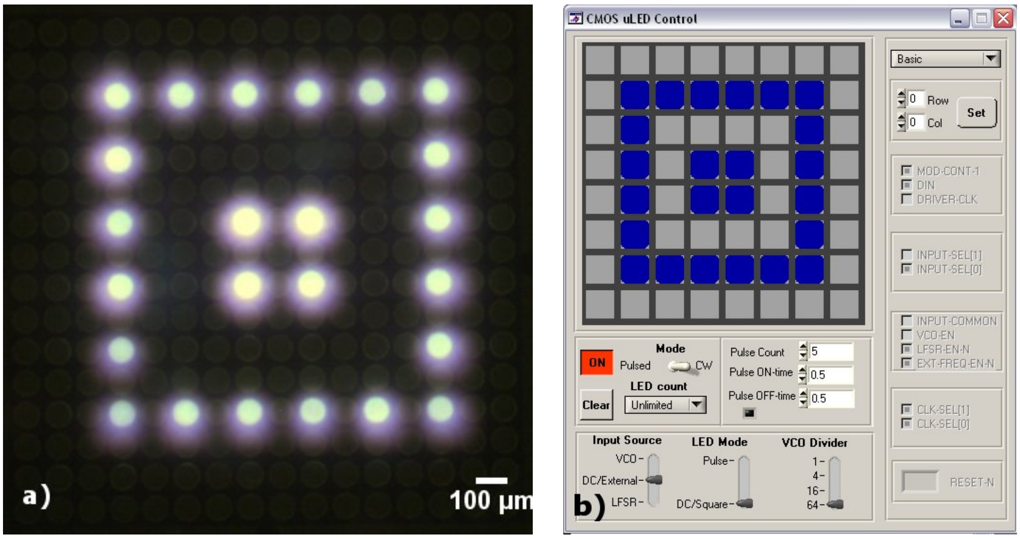

Basic
Row: 0
Col: 0
LED count: Unlimited
Pulse Count: 5
Pulse ON-time: 0.5
Pulse OFF-time: 0.5
☑ MOD-CONT-1
☑ DIN
☐ DRIVER-CLK
☐ INPUT-SEL[1]
☑ INPUT-SEL[0]
☐ INPUT-COMMON
☐ VCO-EN
☑ LFSR-EN-N
☑ EXT-FREQ-EN-N
☑ CLK-SEL[1]
☑ CLK-SEL[0]

(a) Optical micrograph of micro-LED. (b) Screenshot of the software control.

Figure 4.7: Images showing a pattern being addressed with the software control and being displayed on the micro-LED device.

The controls at the bottom of the screen set the operational modes of the

CMOS driver. The first slider, 'Input Source', sets whether (i) the CMOS control uses the on-chip VCO to define a frequency ('VCO'), (ii) an external frequency generator if no external source is present this gives CW operation ('DC/External'), or (iii) use of on-chip linear feedback shift registers (LFSRs) to output a pseudo-random binary sequence. The middle slider, 'LED Mode', has two positions 'Pulsed' and 'DC/Square'. The former gives an output in non-CW mode of a pulse on the rising edge of the input wave (external, VCO, or LFSR) the duration of this pulse is set on the CMOS driver PCB. The latter gives the output of a square wave at the same frequency as the input source or CW if no AC signal is present. The 'VCO Divider' slide sets a value (1, 4, 16, or 64) by which the on-chip VCO frequency is divided before it is used.

To view the image on the camera and to take snapshots, the software delivered with the camera is used. It has controls to set the exposure time, which can be used to compensate when a weak reflection of a sample is viewed, as opposed to when the LED device is imaged directly.

For sample scanning with the motorised stages, the same software as described in 3.2.1 is used.

4.3.2 Characterisation

The system was characterised in terms of spot size, spectrum, and optical power delivered at the sample as a function of pulse duration.

The average optical power was measured by placing the sensor of a calibrated power meter at the sample position. As can be seen in figure 4.8(a) the average optical power has a linear relationship with the pulse duration for pulses longer than ∼4 ns. Below this, the rise time and fall time becomes significant in relation to the pulse duration and reduces the average power. These measurements were taken using a 40X microscope objective as collection objective and a 4X as the projection objective to focus the light onto the sample. The maximum optical power measured in CW operation in this configuration is 140 μW at a driving current of 27 mA. The device delivers 370 μW at this driving current and the beam splitter deflects 50% of the power, meaning that the ∼24% of the power is not collected by the collection objective or lost in the transmission. The collection efficiency for a 0.75 N.A. objective cannot be expected to be higher than 80%, hence the transmission losses are estimated to be less than 5%.

The spectrum (figure 4.8(b)) was measured with an Ocean Optics USB2000 fibre coupled spectrometer with the fibre end placed at the sample position of the setup. As expected, the spectrum is not changed by the optical system. It has a centre wavelength of 370 nm and a FWHM of 15 nm at a driving current of 27 mA. Higher driving currents mean higher working temperature and hence longer wavelength. This is due to the thermal energy added to the system.

To determine the spot size with different microscope objective combinations, a mirror was placed at the sample position and the CCD camera was used to image the reflected spot. In figure 4.9 the intensity profile of one micro-LED pixel can be seen. The micrograph, from which the plot was calculated, was taken using a 40X/40X combination. The edges have higher intensity than the rest of the surface. This is attributed to side wall scattering in the mesa structure of the emitting pixels, and the intensity falls quickly outside the pixel area. This feature, although unintended, is actually beneficial when exposing photoresist as it gives better defined feature edges compared to the case with a Gaussian

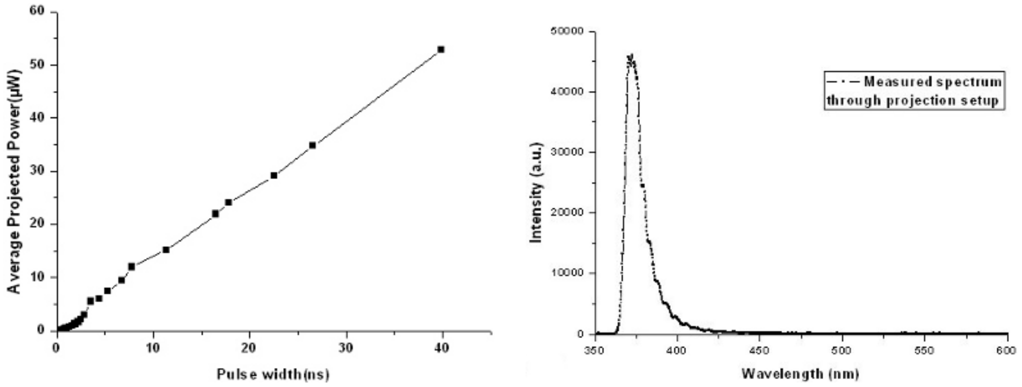

(a) The optical power through the setup plotted against the pulse duration.

(b) Spectrum of the light from the LED as measured at the sample position. Drive current was 27 mA.

Figure 4.8: Graphs showing some key characteristics of the tool.

intensity profile. The ideal is a 'flat-top' intensity profile.

The images in figure 4.10 are thresholded at a value approximately half of the maximum intensity (white pixels above this value and black below). The spot sizes were measured from these images by fitting a circle to the spot. The scales of the images were determined from micrographs of a graticule with each of the different objectives. This was done using ImageJ^{TM} software.

In table 4.1 spot sizes and corresponding optical intensities are presented. The total collected optical power was 4.40 μW when using the 4X objective and 138 μW for the 40X objective. The projected power is assumed to be independent of the projecting objective.

When calculating the intensities, the total power is assumed to be projected inside the spot diameter, i.e., a "flat top" beam profile is assumed. The 4X collection objective has a larger field of view (4mm), but it also has a lower N.A. which means it has a lower collection angle. This allows for the whole micro-LED array (1.6 mm × 1.6 mm) to be imaged, but with the trade-off of lower

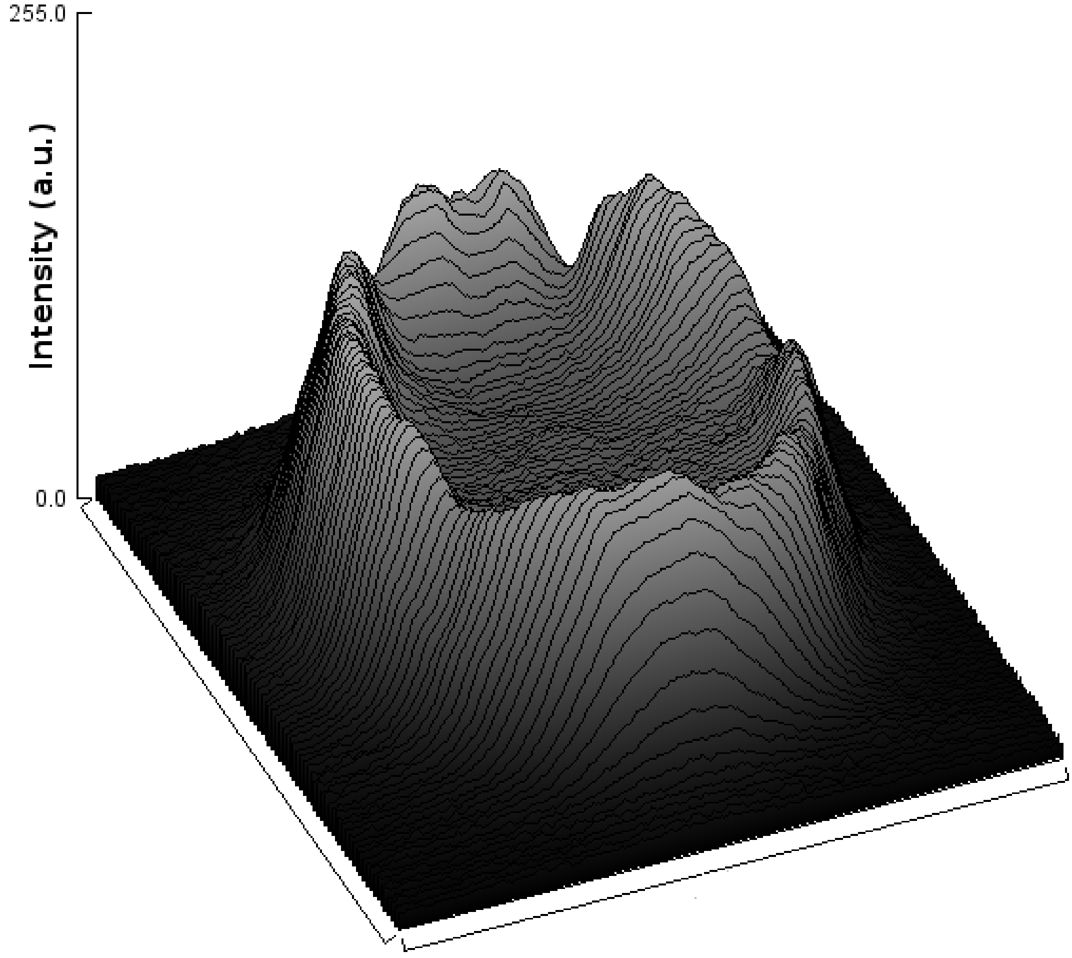

Figure 4.9: Intensity plot for one imaged micro-LED pixel, using a 40X/40X objective combination.

light collection. Despite this, the highest optical power density is achieved using the 4X collection/40X projection objective combination. The 4X microscope objective has large enough field of view to image the whole micro-LED emitting area, but the projected optical power will depend on the distance from the centre of the imaged area simply because less light will hit the lens of the objective from the edges compared to the centre. A map showing how much projected optical power each pixel of the device delivers at the sample position is shown in figure

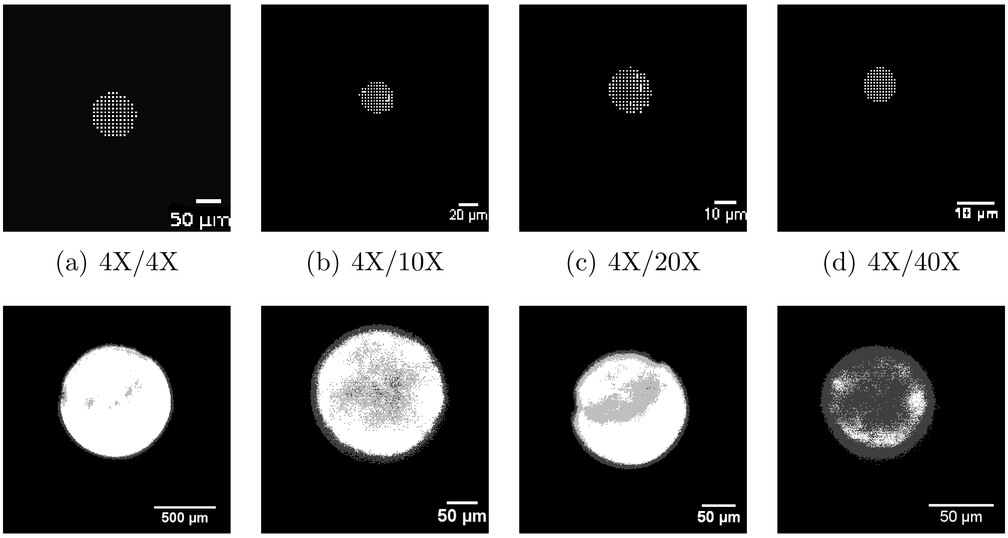

(a) 4X/4X (b) 4X/10X (c) 4X/20X (d) 4X/40X

(e) 40X/4X (f) 40X/10X (g) 40X/20X (h) 40X/40X

Figure 4.10: Thresholded micrographs of reflections off a mirror placed at the sample position with different collection/projection objectives.

Table 4.1: Spotsizes and optical power intensities for different collection and projection objective combinations.

Projection Collection	4X	10X	20X	40X
4X	93 μm 65 mW/cm^2	30 μm 0.62 W/cm^2	20 μm 1.4 W/cm^2	8.5 μm 7.7 W/cm^2
40X	900 μm 22 mW/cm^2	340 μm 0.15 W/cm^2	170 μm 0.61 W/cm^2	82 μm 2.6 W/cm^2

4.11.

If the sample is static while exposing, the exposure dose is simply given by multiplying the intensity with the exposure time. When the sample is moving a 'flat-top' uniform illumination pattern is assumed and the exposure dose is calculated with the equation (cf. equation 3.4):

$$E = \frac{2P}{\pi R^2 v}\sqrt{R^2 - y^2} \tag{4.1}$$

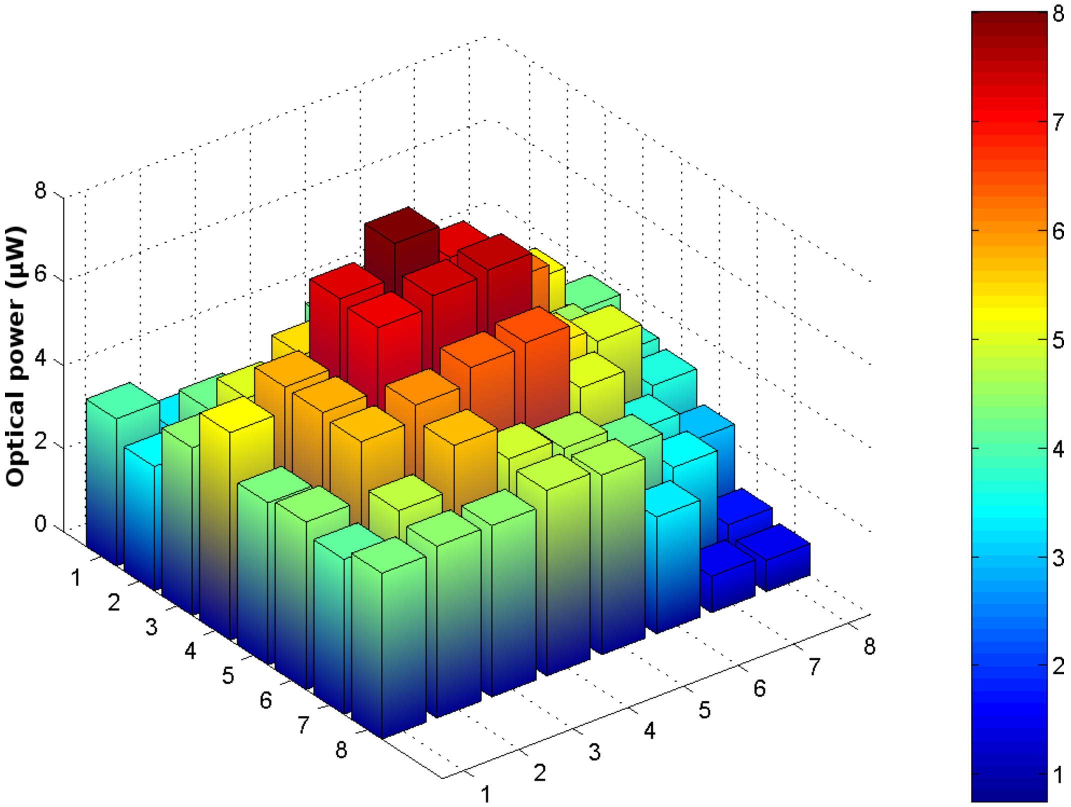

Figure 4.11: A map of the projected optical power from each pixel on the micro-LED device.

where P is the total power, R the pixel radius, v the velocity , and y ($\leq$R) the coordinate perpendicular to the velocity. The dosage profile forms a half-circle.

4.4 Writing results

A number of different patterns were written into negative and positive photoresists under different exposure conditions to test the system. Details about the photoresist materials can be found in section 2.1.

4.4.1 Negative photoresist

The negative resist used for the test patterns was Norland Optical Adhesive 81. It was chosen because of its excellent adhesion to glass and relatively low viscosity, allowing thin films to be spun on substrates and hence offering the possibility of features a few μm in size.

Experimental: The following recipe was used for the exposure of NOA81 on borosilicate glass slides:

1. A glass cover slide was thoroughly cleaned in an ultrasonicated acetone bath. Subsequently the procedure was repeated in methanol instead of acetone, and then the substrate was rinsed in deionised (DI) water. The substrate was then spun dry and was put on a hotplate at 120°C for 15 minutes.

2. The substrate was placed on the chuck of the spin coater. Norland optical adhesive 81 (NOA81) was carefully dropped on the substrate with care taken to avoid bubbles.

3. Spinning was performed at 8000 rpm for a film thickness of 1.8 μm.

4. The film covered substrate was placed directly onto the XY-translation stage in the writing setup.

5. Exposure was done by turning on desired pixels for a predetermined length of time, while the stage remains static or is moved to produce lines.

6. Development was done by immersing the substrate in acetone and moving

it gently around for approximately 30 seconds and subsequently rinsing in first methanol then DI water.

7. The substrate is dried gently with a flow of air or nitrogen.

After the development the written patterns were characterised in terms of width and height, by optical microscopy and stylus profilometry, respectively.

Results: The results presented are all done with the combination of a 4X collection objective and a 40X projection objective, as this gives the smallest features and has the highest optical power intensity and hence the shortest curing times.

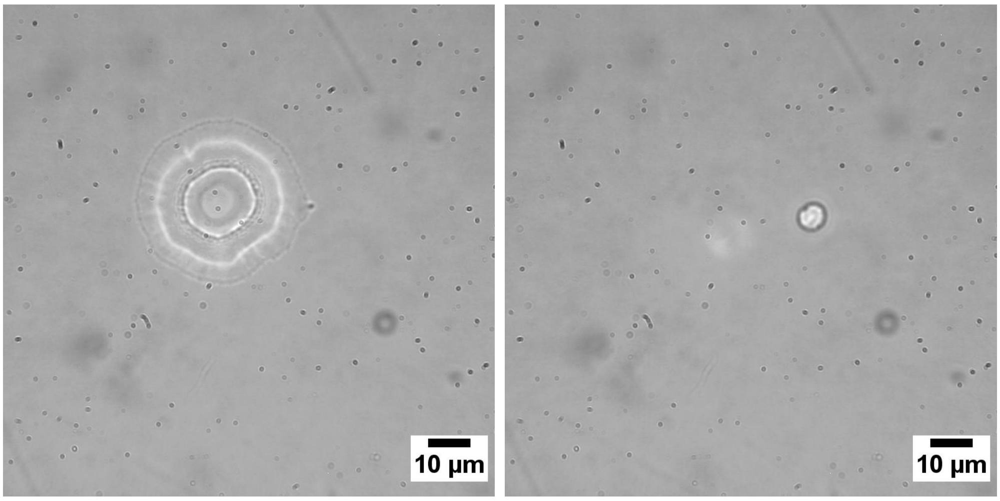

Figure 4.12: Optical micrographs taken with a high resolution oil immersion 100X objective of dots cured under pulsed operation. The dots 100 s (left) and 1 s (right) with pulse durations of 40 ns a repetition rate of 9.75 MHz.

To examine how short pulses affect the curing behaviour, exposures with the same pixel under the same conditions, but with different pulse lengths, were performed. Optical micrographs of two of the resulting dots are shown in figure 4.12 and the corresponding dot diameters and exposure doses of all the exposed dots are shown in table 4.2. Comparing the similar sized dots exposed for 1 s with 40 ns pulse duration, for 2 s with 30 ns pulse duration, and for 10 s with 10 ns pulse duration, the required dose seems to increase with shorter pulses. The dot exposed for 100 s with 1 ns pulse duration does not follow this pattern and appears to be an outlier, possibly due to an experimental mistake.

Table 4.2: Sizes of the dots in figure 4.12 as measured by circle fitting in ImageJ$^{\mathrm{TM}}$ software. The dot size are given in μm followed by the exposure dose in J/cm^2.

Pulse Exposure	40 ns	30 ns	20 ns	10 ns	5 ns	1 ns
100 s	39 μm 270	29 μm 200	24 μm 150	17 μm 72	15 μm 36	14 μm 3.3
40 s	24 μm 108	19 μm 80	17 μm 60	15 μm 29	11 μm 14	- 1.3
10 s	14 μm 27	12 μm 20	12 μm 15	8 μm 7.2	- 3.6	- 0.33
5 s	12 μm 14	11 μm 10	9.7 μm 7.5	- 3.6	- 1.8	- 0.17
2 s	8.7 μm 5.4	7.4 μm 4.0	(6.0 μm) 3.0	- 1.4	- 0.72	- 0.066
1 s	8.3 μm 2.7	- 2.0	- 1.5	- 0.72	- 0.36	- 0.033

Patterns were also written while moving the sample. The three lines in figure 4.13(a) were exposed while moving the sample at 5 μm/s. From left to right in the image the lines where exposed using 40 ns and 50 ns pulse durations at a repetition rate of 9.75 MHz and at CW operation. This gives maximum doses, in the middle of the line, of 4.4 J/cm^2, 5.1 J/cm^2, and 12.2 J/cm^2, respectively, as calculated by equation 4.1. The widths are 8 μm, 8 μm and 11 μm, respectively. The heights were measured by stylus profilometry to be 0.9 μm, 0.9 μm, and 1.8 μm, respectively. The height profiles can be seen in the graph in figure 4.13(b).

The 'IoP' pattern seen in the micrograph of figure 4.14 was exposed while

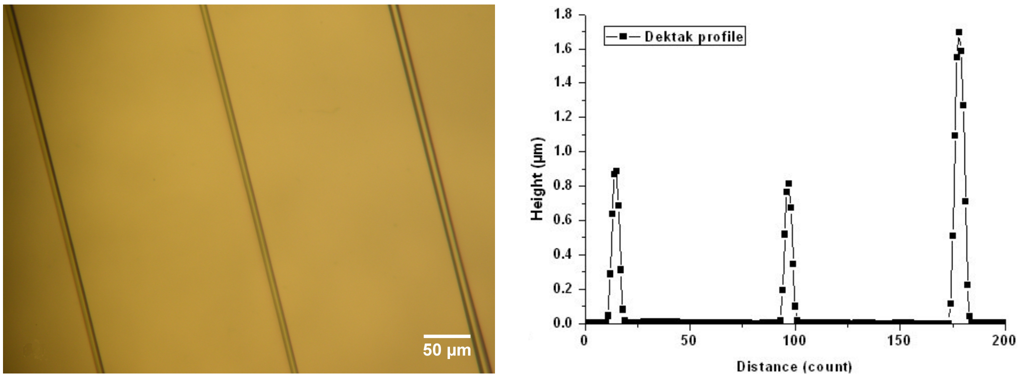

(a) Optical micrograph of three lines in negative photoresist.

(b) Dektak profile of the three lines.

Figure 4.13: The lines written in NOA81 negative photoresist with 40 ns and 50 ns pulse widths and CW mode going from left to right and a speed of 5 μm/s. Widths are 8 μm, 8 μm and 11 μm and heights are 0.9 μm, 0.9 μm and 1.8 μm respectively.

keeping the sample static. First the 'I' and the 'P' of the pattern were exposed for 8 s under square wave operation and the 'o' was exposed for 4 s. Since the pixels forming the 'o' are in the centre of the field of view the collection is more effective compared to the pixels forming the 'I' and the 'P' (cf. figure 4.11). The average exposure for each dot was 10 J/cm^2.

4.4.2 Positive photoresist

Test patterns were written into standard positive tone photoresist.

Experimental: The photoresists used for the pattern were from the Microposit S1800-series from Shipley, for which more details can be found in section 2.1.2. The process used for the Microposit resists is as follows:

1. The silicon substrates are thoroughly cleaned. Water and solvents are evaporated by placing them on a hotplate at 110°C for at least 20 minutes.

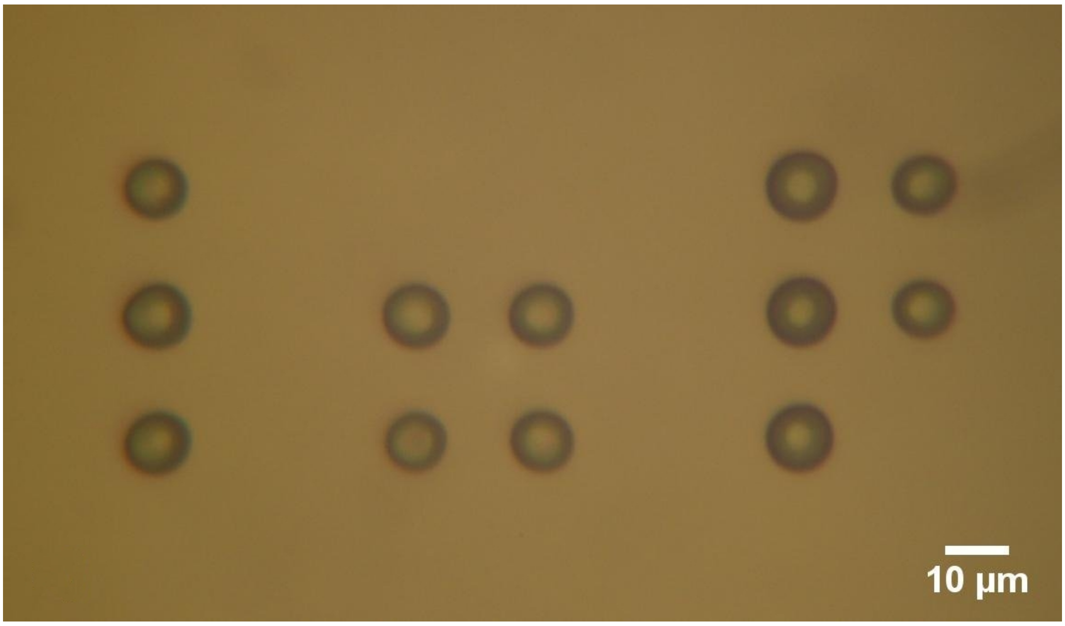

Figure 4.14: Optical micrograph of 'IoP' pattern.

2. The resist is spun at 2000 rpm for 30 seconds.
3. Soft bake is performed on a hotplate at 120°C for 60 seconds.
4. The sample is placed on the XY-translation stage and is exposed by light from the UV micro-LED device.
5. Development is performed in Microposit Micro-Dev solution at 1:1 volume ratio with DI water for 60 seconds while moving the sample gently.
6. The sample is rinsed in DI water.

As can be seen in figure 2.6, the film thickness for S1818 is approximately 2.7 μm and 0.7 μm for S1805 at the spinning speed of 2000 rpm.

Results: An example of a static written pattern can be seen in figure 4.15. The array was written by exposure with four pixels for a duration of 2 s, giving an exposure dose of 1.1 J/cm^2. Subsequently, the sample was moved 40 μm and the exposure repeated. This was repeated four times to form the array. The scanning electron microscope (SEM) image in figure 4.15(b) was taken with a Hitachi S4700 in ultra high resolution mode. The sample was tilted to clearly show the side walls. The images confirms that we have well defined patterns with close-to-vertical side walls.

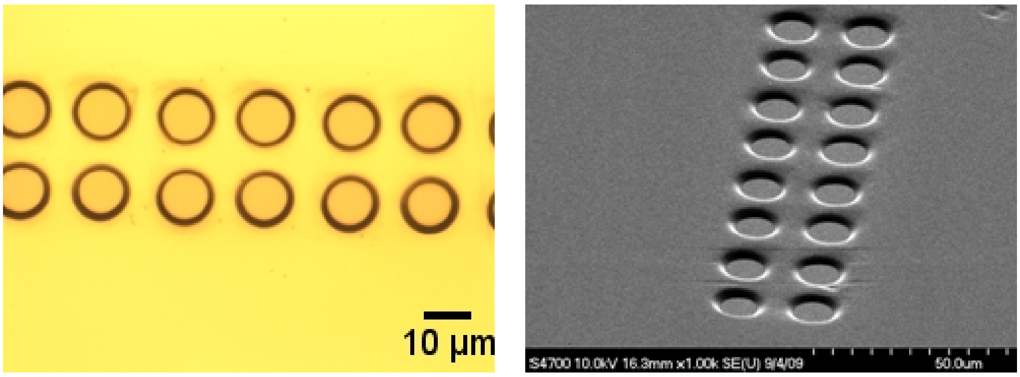

(a) Optical micrograph of an array of holes.

(b) SEM image of an array of holes.

Figure 4.15: Images showing an array of holes written into positive photoresist. The images show that the holes are uniform and the SEM reveals well defined and close-to-vertical side walls. Each hole has a diameter of ~9 μm.

The four parallel “channels” in figure 4.16 were patterned in the less viscous photoresist, Microposit S1805. Four pixels in one column of the CMOS driven micro-LED device were turned on simultaneously while the sample was translated at a speed of 100 μm/s. The exposure was done in CW operation and each pixel delivers ~2.5 μW to the sample giving an exposure dose of ~0.4 J/cm^2 in the centre lines, slightly less on the outer lines. The channels are each 10 μm wide.

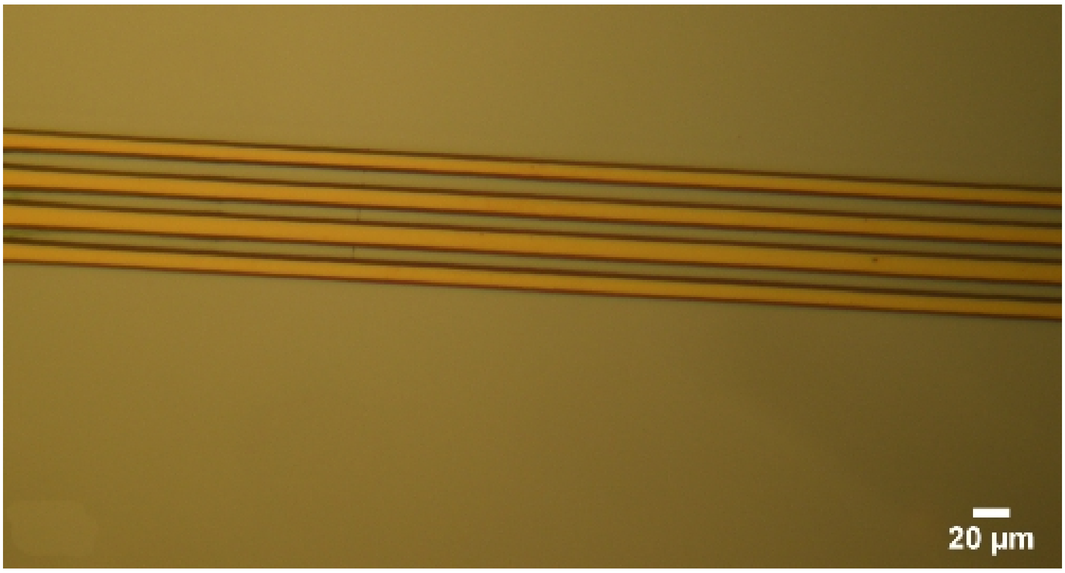

Figure 4.16: Optical micrographs of four parallel lines in S1805 positive photoresist. The lines were written by moving the sample at a linear speed of 100 μm/s giving a maximum exposure dose of 400 mJ/cm^2 in the middle of each line.

4.5 Summary

In this chapter, examples of maskless lithography techniques for high and low resolution micro- and nano-fabrication have been presented. Examples of techniques representing the forefront of research, such as ZPAL, as well as well established commercial techniques, e.g., EBL, were given.

A tool based on a CMOS driven micro-LED array where the light from the device is projected through an optical system consisting of two back-to-back microscope objectives, has been introduced and characterised. Spot sizes and optical intensities for different configurations of the setup have been given. A maximum intensity of 7.7 W/cm^2 in a spot with a diameter of 8.5 μm was achieved.

Patterns in both negative and positive tone photoresists was presented showing the capability of static and dynamic writing. In both materials features down to $\sim$8 μm were shown. Developments of the CMOS-driver and the micro-LED array has improved the resolution of the maskless photolithography setup, more on this in section 6.1.

The maskless lithography system based on a UV emitting micro-LED represents a low-cost prototyping tool which can be used to directly test pattern design in e.g., micro-fluidics, MEMS, and opto-genetics [20].

References

[1] Clemens Rensch, Stefan Hell, Manfred v. Schickfus, and Siegfried Hunklinger. Laser scanner for direct writing lithography. *Appl. Opt.*, 28(17):3754–3758, 1989. 105

[2] Ji-Yen Cheng, Meng-Hua Yen, Cheng-Wey Wei, Yung-Chuan Chuang, and Tai-Horng Young. Crack-free direct-writing on glass using a low-power UV laser in the manufacture of a microfluidic chip. *Journal of Micromechanics and Microengineering*, 15(6):1147–1156, 2005. 105

[3] Paul F. Jacobs. *Rapid Prototyping and Manufacturing: Fundamentals of StereoLithography.* McGraw-Hill, Inc., New York, NY, USA, 1993. 105

[4] Rosanne M. Guijt and Michael C. Breadmore. Maskless photolithography using UV LEDs. *Lab on a Chip*, 8(8):1402–1404, 2008. 105

[5] Thomas Naiser, Timo Mai, Wolfgang Michel, and Albrecht Ott. Versatile maskless microscope projection photolithography system and its application in light-directed fabrication of DNA microarrays. *Review of Scientific Instruments*, 77(6):063711, 2006. ix, 105, 106

[6] S. P. A. Fodor, J. Leighton Read, M. C. Pirrung, L. Stryer, A. Tsai Lu, and

D. Solas. Light-Directed, Spatially Addressable Parallel Chemical Synthesis. *Science*, 251:767–773, February 1991. 106

[7] Sangeet Singh-Gasson, Roland D. Green, Yongjian Yue, Clark Nelson, Fred Blattner, Michael R. Sussman, and Franco Cerrina. Maskless fabrication of light-directed oligonucleotide microarrays using a digital micromirror array. *Nat Biotech*, 17(10):974–978, 1999. 10.1038/13664. 106

[8] G. P. Watson, V. Aksyuk, M. E. Simon, D. M. Tennant, R. A. Cirelli, W. M. Mansfield, F. Pardo, D. O. Lopez, C. A. Bolle, A. R. Papazian, N. Basavanhally, J. Lee, R. Fullowan, F. Klemens, J. Miner, A. Kornblit, T. Sorsch, L. Fetter, M. Peabody, J. E. Bower, J. S. Weiner, and Y. L. Low. Spatial light modulator for maskless optical projection lithography. *Journal of Vacuum Science Technology B: Microelectronics and Nanometer Structures*, 24:2852–+, 2006. 106

[9] Aimin Tan, Kenneth Rodgers, John P. Murrihy, rsquo, Cian Mathuna, and Jeremy D. Glennon. Rapid fabrication of microfluidic devices in poly(dimethylsiloxane) by photocopying. *Lab on a Chip*, 1(1):7–9, 2001. 106

[10] Wendell Karlos Tomazelli Coltro, Evandro Piccin, Jose Alberto Fracassi da Silva, Claudimir Lucio do Lago, and Emanuel Carrilho. A toner-mediated lithographic technology for rapid prototyping of glass microchannels. *Lab on a Chip*, 7(7):931–934, 2007. 107

[11] Mohammad H. Sorouraddin, Mohammad Amjadi, and Mohammad Safi-Shalamzari. Simple and rapid methods for the fabrication of polymeric

and glass chips for using in analytical chemistry. *Analytica Chimica Acta*, 589(1):84–88, 2007. 107

[12] G. M. Atkinson, F. P. Stratton, R. L. Kubena, and J. C. Wolfe. 30 nm resolution zero proximity lithography on high-Z substrates. *Journal of Vacuum Science Technology B: Microelectronics and Nanometer Structures*, 10:3104–3108, November 1992. 107

[13] Anthony Yen, Erik H. Anderson, R. A. Ghanbari, M. L. Schattenburg, and Henry I. Smith. Achromatic holographic configuration for 100-nm-period lithography. *Appl. Opt.*, 31(22):4540–4545, 1992. 108

[14] T. A. Savas, M. L. Schattenburg, J. M. Carter, and H. I. Smith. Large-area achromatic interferometric lithography for 100 nm period gratings and grids. *Journal of Vacuum Science Technology B: Microelectronics and Nanometer Structures*, 14:4167–4170, November 1996. 108

[15] Henry I. Smith, Rajesh Menon, Amil Patel, David Chao, Michael Walsh, and G. Barbastathis. Zone-plate-array lithography: A low-cost complement or competitor to scanning-electron-beam lithography. *Microelectronic Engineering*, 83(4-9):956 – 961, 2006. Micro- and Nano-Engineering MNE 2005. ix, 108

[16] Dario Gil, Rajesh Menon, and Henry I. Smith. The case for diffractive optics in maskless lithography. *Journal of Vacuum Science Technology B: Microelectronics and Nanometer Structures*, 21(6):2810–2814, 2003. 108

[17] C. Griffin, J. McKendry, H.X. Zhang, E. Gu, B.R. Rae, R. Henderson, D. Renshaw, J.M. Girkin, and M.D. Dawson. CMOS-integrated flip-chip,

micro-pixel InGaN LED arrays for on-chip microfluorimetry. In *Lasers and Electro-Optics Society, 2007. LEOS 2007. The 20th Annual Meeting of the IEEE*, pages 588–589, Oct. 2007. 109

[18] B R Rae, C Griffin, J McKendry, J M Girkin, H X Zhang, E Gu, D Renshaw, E Charbon, M D Dawson, and R K Henderson. CMOS driven micro-pixel LEDs integrated with single photon avalanche diodes for time resolved fluorescence measurements. *Journal of Physics D: Applied Physics*, 41(9):094011, 2008. 109

[19] J. McKendry, B.R. Rae, Zheng Gong, K.R. Muir, B. Guilhabert, D. Massoubre, E. Gu, D. Renshaw, M.D. Dawson, and R.K. Henderson. Individually addressable AlInGaN micro-LED arrays with CMOS control and subnanosecond output pulses. *Photonics Technology Letters, IEEE*, 21(12):811–813, June15, 2009. 109

[20] Nir Grossman, Vincent Poher, Matthew S Grubb, Gordon T Kennedy, Konstantin Nikolic, Brian McGovern, Rolando Berlinguer Palmini, Zheng Gong, Emmanuel M Drakakis, Mark A A Neil, Martin D Dawson, Juan Burrone, and Patrick Degenaar. Multi-site optical excitation using chr2 and micro-led array. *Journal of Neural Engineering*, 7(1):016004, 2010. 129

Chapter 5

Colour Conversion

In this chapter multicolour devices based on the pixel-wise down-conversion of light from UV emitting micro-pixellated LEDs will be presented. Applications and competing methods will be discussed in brief.

While the micro-LEDs, previously described (section 1.1.3), have been utilised in instrumentation [1] and for biological applications [2], for some applications their use is limited by having monochromatic emission. By adding multi-wavelength capability, the devices could be more versatilely used as excitation sources and, for example, structured white light illumination sources for sectioned microscopy is a possibility. To achieve such colour conversion, nanocrystal quantum dots have been added on top of the light emitting devices. Two alternative methods of integrating quantum dot nanocomposites on micro-striped UV emitting LEDs will be introduced and results and device performance achieved with each method will be presented.

5.1 Multi-coloured/White LEDs

The emission wavelength of light emitting diodes is determined by the materials and the active layer configuration, e.g., the quantum well thickness and placement within the epitaxial layers (c.f. section 1.1) in inorganic LEDs. A device based on a single epitaxial growth run will hence have one narrow emission peak (although there is some variation across a wafer due to growth nonuniformities). Multi-wavelength capability needs to be added by post processing.

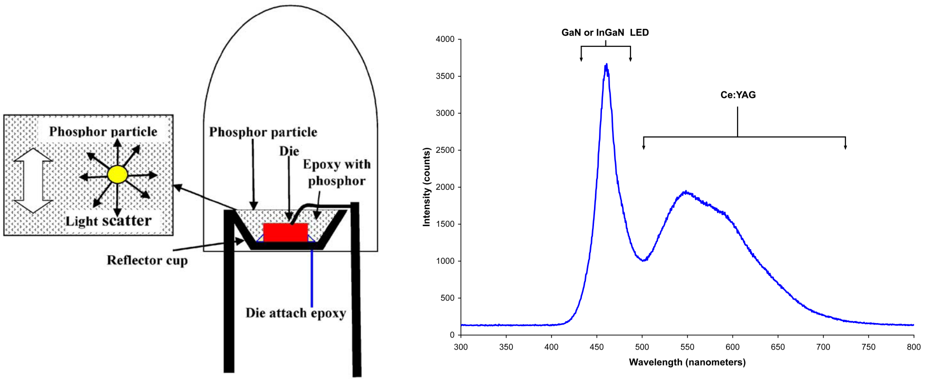

(a) Schematic of a phosphor-converted LED.

(b) Spectrum from a typical white emitting pc-LED.

Figure 5.1: Commercial white emitting LED. After [3].

Commercial white LEDs are most commonly based on blue emitting GaN diodes with a colour down-converting phosphor, which has a broad emission centred in the yellow, added. Figure 5.1 shows a schematic and a typical spectrum of such an phosphor-converted light emitting diode (pc-LED). Cerium-doped yttrium aluminium garnet (Ce3+:YAG) is often used for this, however new material systems are also being tested [4].

The performance of LEDs is often measured by their external quantum efficiency, the ratio between the number of photons extracted from the device and the number of electrons injected (equation 5.1), and the power efficiency (informally "wall plug efficiency"), the ratio between the output optical power and the input electrical power (equation 5.2).

$$\eta_{ext} = \frac{P/(h\nu)}{I/e} \tag{5.1}$$

$$\eta_{power} = \frac{P}{IV} \tag{5.2}$$

For illumination applications, another measure is more important, namely the luminous efficiency, which is the ratio of luminous flux to the input electrical power, measured in lumen per watt. The lumen (lm) is a photometric unit, i.e., it takes into account the human eye's spectral sensitivity (see figure 5.2(a)), hence it measures how bright a light source is perceived to be.

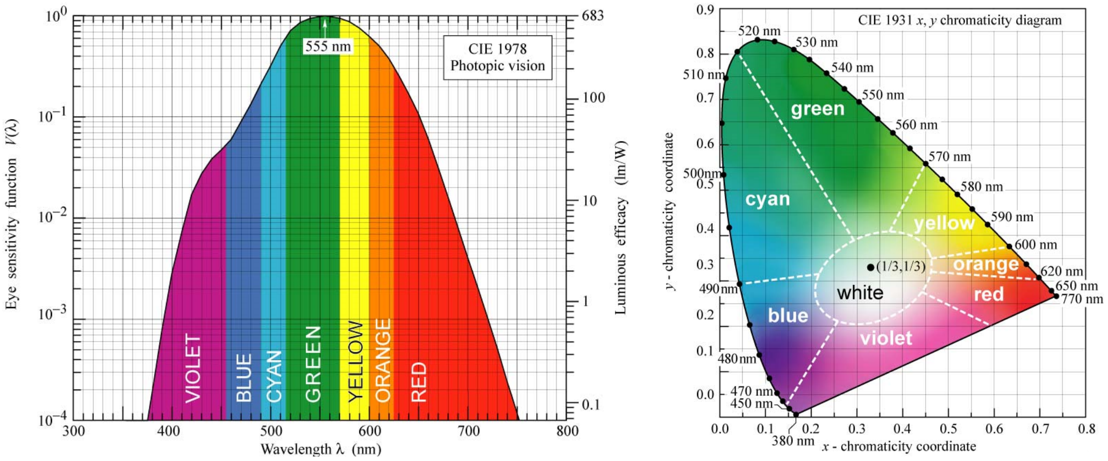

(a) Eye sensitivity function.

(b) CIE 1931 diagram.

Figure 5.2: Human eye spectral sensitivity and CIE 1931 chromaticity diagram.

The colour of a light source is often given as coordinates in the Commission internationale de l'clairage (CIE) 1931 colour space (see figure 5.2(b)). White light falls in the area around (0.33 , 0.33). An important performance figure for white light illumination is the colour rendering index (CRI), which measure how close an illumination source mimics the sun in terms of colour rendering (the sun and incandescent bulbs with tungsten filament have CRI of 100). White-LEDs with yellow phosphor converters have poor colour rendering index, typically ∼70. For this reason quantum dots have been suggested as alternative colour converters [5, 6] for better colour rendering and 'warmer' light.

Organic materials have also been used as colour converters [7] and as the direct electrically injected light emitting material [8].

It has been proposed to use white light LED illumination for communication [9]. For this purpose the long radiative lifetimes of phosphorescing materials are a problem, because they can compromise the modulation bandwidth.

5.2 Self-aligned writing

The nanocomposite material described in section 2.3.2 was used to create colour converting films on a micro-striped UV LED [10]. The technique was previously employed to integrate a PFO based blend on a micro-LED for UV → blue colour conversion [11].

5.2.1 Experimental

To produce aligned patterns on micro-striped UV LEDs, which have been produced in-house at the Insitute of Photonics, the quantum dot nanocomposite is spun to a thin film directly on the cleaned device, using a spinning speed of 4000 rpm for 40 seconds, achieving 20 to 25 μm thick films. A special holder was produced in PTFE plastic to fit the device onto the chuck of the spincoater. The exposure of the photosensitive nanocomposite was then done by the device itself by turning on the desired pixel for a determined length of time. The curing was done while driving the pixel at a current of 0.5 mA delivering an optical intensity at the surface of the pixel of 4.4 mW/cm^2. Each of the nanocomposites used has a concentration of quantum dots of 0.2%-wt. The curing photo-sensitivity of the nanocomposite depends on the size and amount of quantum dots, and some batch to batch variations exist as well. The red QD nanocomposite requires a dose as high as ~93 mJ/cm^2 (21 s exposure time) while the blue QD blend requires only ~9 mJ/cm^2 (2 s exposure). The reason for this is believed to be mainly the higher absorption of the red QD at 370 nm (see figure 2.16). The QDs compete with the photocuring initiator in the matrix material for photon harvesting, hence increased absorption in the QDs leads to slower curing of the nanocomposite. The absorption spectra of the nanocrystal composites can be seen in figure 2.16. The absorption for the red nanocomposite film is 65 at 370 nm, while the yellow, green and blue blends have lower absorbance of about 42, 39, and 32 in arbitary units, respectively. Measurements were described in section 2.3.2.

The driving current and hence the optical intensity can be considerably higher, than was the case while doing the curing. The intensity was intentionally kept low when curing for the purpose of controlling the dose delivered more accurately, since there was no accurate enough timing control of the ON-time.

After the exposure, uncured residue nanocomposite is washed-off in a toluene bath for 20 s. The device is subsequently rinsed in DI water. The procedure is repeated several times to layer by layer build a thicker colour converting film over the pixel.

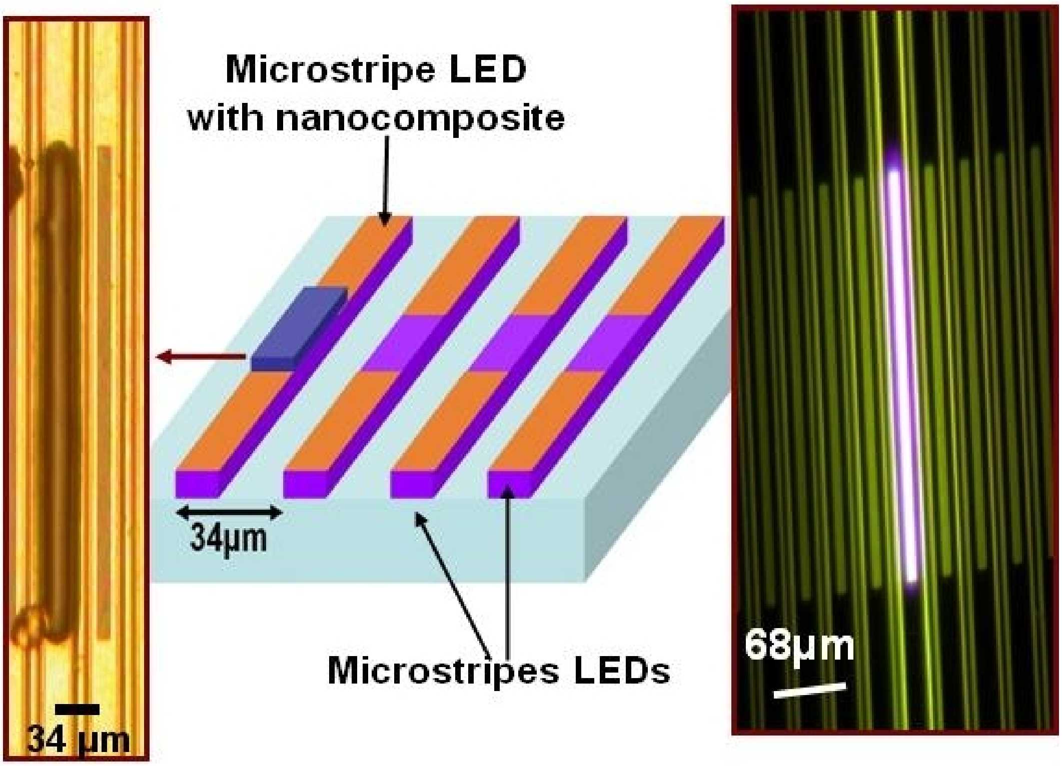

Figure 5.3: Optical micrographs of a pixel with integrated nanocomposite (left) and bare pixels (right). In the middle a schematic of the micro-striped device is shown.

In figure 5.3 micrographs of the device with and without nanocomposite integrated can be seen.

5.2.2 Characterisation

After the integration of the colour converting nanocomposites on the UV emitting micro-LED device, the device was characterised with regards to emission spectra and conversion efficiency.

The spectra in figure 5.4 were taken with a UV-visible fibre-coupled calibrated optical spectrometer (Ocean Optics USB4000). The fibre tip was aligned with the emission direction of the pixel. The spectra were normalised with regards to

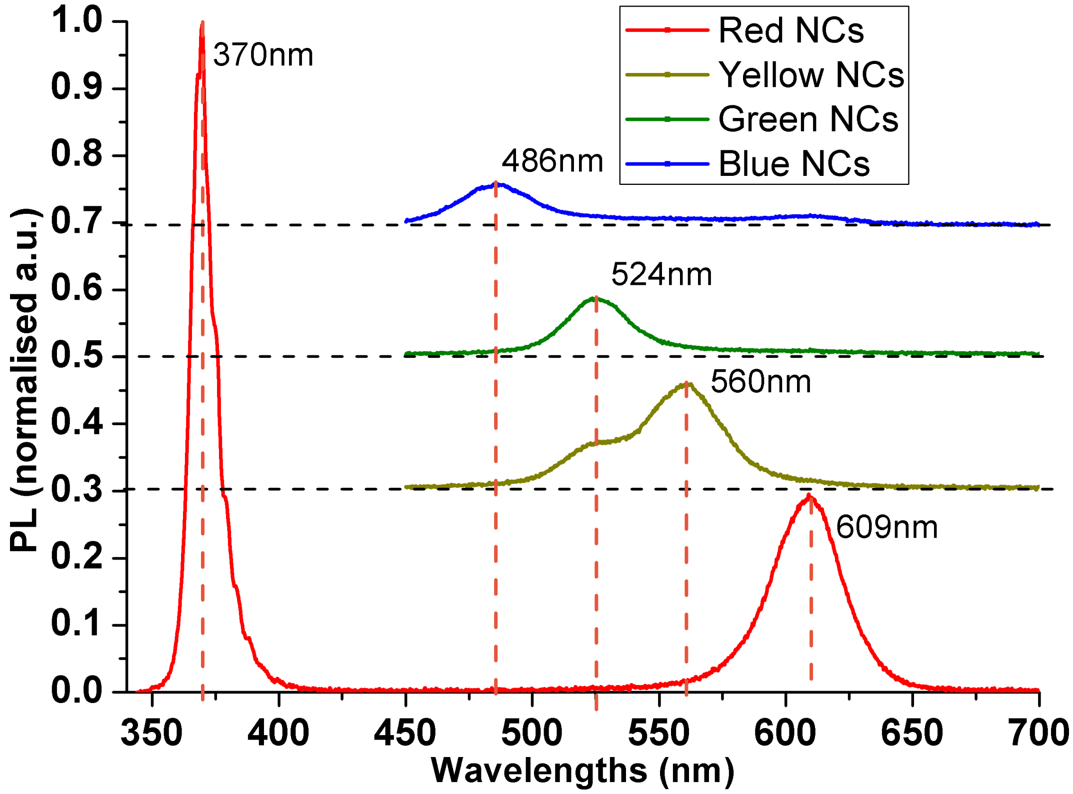

Figure 5.4: Spectra for pixels with red, yellow, green, and blue nanocomposite colour converters. For clarity, the blue, green, and yellow spectra are offset vertically and 370 nm component removed.

the UV peak, but the peak was cut off in the yellow, green, and blue case for presentation clarity. The base level was also shifted in the graph to more clearly display the plots. The pixels were driven at 3.6 mA while the spectra were taken. The peak at each colour converted wavelength, at 609 nm, 560 nm, 524 nm, and 486 nm, respectively, is clearly visible in each spectrum. The yellow spectrum has a “shoulder” in the green. This is due to UV light leakage (light emitted from the side walls rather than top of the mesa structure), which is being converted by the adjacent green pixel. It can also be seen that there are elevations from the background level at longer wavelength from the main peak. This is due to the fact that the larger quantum dots are excited by the light emitted from the shorter wavelength (smaller) QDs.

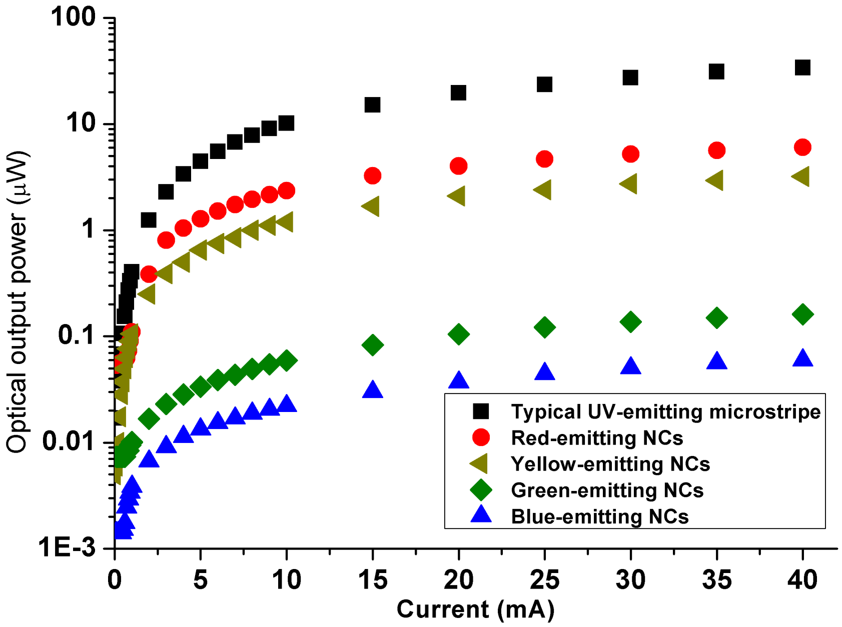

Figure 5.5: Optical output powers for four pixels with different integrated nanocomposites plotted against driving current.

Optical power measurements were performed with a UV Si photodetector placed in close proximity (~2 mm) to each emitting pixel. A bare microstripe with dimensions of 300 μm × 12 μm gives a measured optical output power as high as 34 μW at a driving current of 40 mA (~944 mW/cm^2 optical power density at a driving current density of 55 A/cm^2; current injected over the full length of the mesa structure, 3600 μm × 20 μm). The black squares in figure 5.5 correspond to this measurement. The power measurements on pixels with nanocomposite integrated on them were done with a filter placed in-between the detector and the device to remove the contribution from unconverted light. For the red QD integrated pixel, a filter with a cut-off at 520 nm and a 95% transmission at 610 nm was used. The red circles in figure 5.5 correspond to this measurement. The output power collected at 609 nm reaches a maximum of about 6 μW at a driving current of 40 mA (∼166 mW/cm^2 optical output power at 55 A/cm^2 current density). If the losses of the filter are compensated for, the approximate colour conversion efficiency at 40mA driving current is calculated for the red-emitting quantum dot nanocomposite to be ∼17.7% (∼18.2% at 30mA). The yellow, green, and blue pixels were characterised in an equivalent fashion. The measurements are also plotted in figure 5.5. Optical output powers achieved were respectively 3 μW, 0.15 μW, and 0.05 μW at 40 mA driving current (∼83 mW/cm^2, ∼4 mW/cm^2 and ∼1.3 mW/cm^2 at 55 A/cm^2). The respective estimated colour conversion efficiencies are 9%, 0.5%, and 0.2%, filter losses having been allowed for when calculating these figures.

To investigate the saturation behaviour of the QD nanocomposites, the driving current was increased while the spectrum was being measured (as plotted in figure 5.6). By comparing the area under the UV peak (350 nm to 409 nm) and the converted peak - in the case of figure 5.6 red peak centred at 609 nm (590 nm to 630 nm) - a figure corresponding to the colour conversion efficiency is obtained. As can be seen in the inset in figure 5.6 the ratio (S$_{NC}$/S$_{UV}$) is linearly decreasing and not consistent with saturation behaviour. Indeed a focused laser beam with a 500 μm FWHM spotsize and with an optical power ranging from 0 mW to 15 mW does not saturate a 20 μm thick nanocomposite film at a concentration of 0.2%-wt neither with blue, green, yellow, nor red QDs. There are several possible explanations for the decrease in conversion efficiency with increased output. A higher proportion of the output power is believed come from the side walls of the

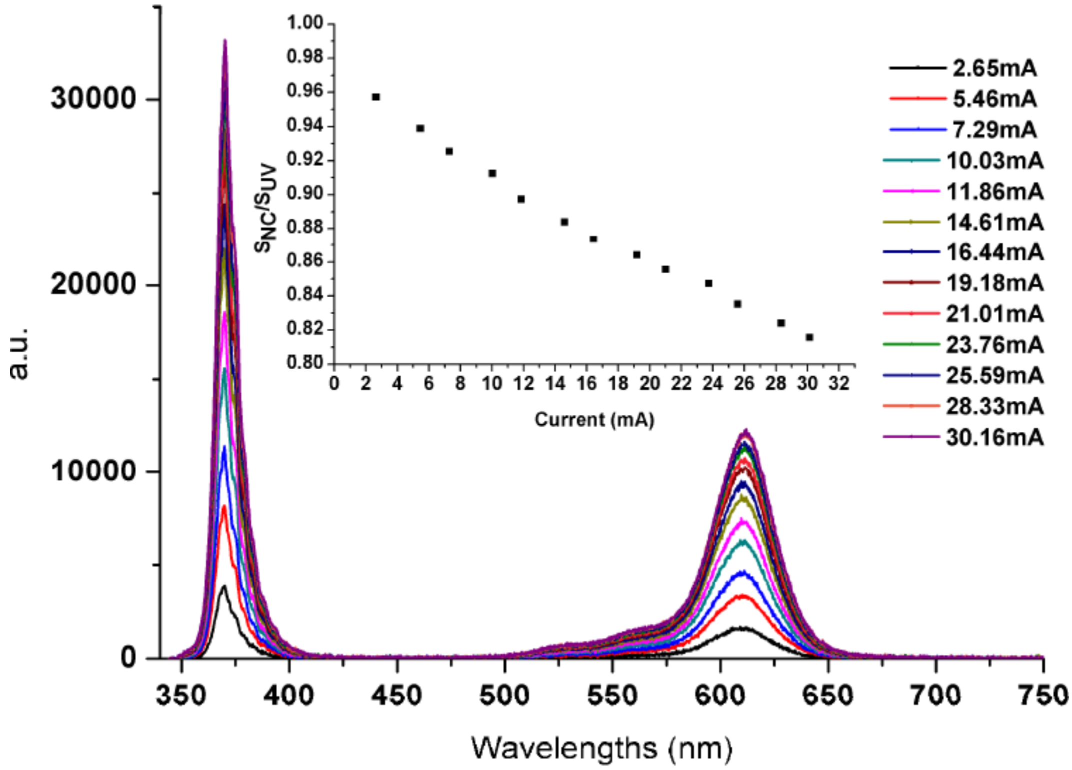

Figure 5.6: Spectra for different driving currents of a red converted pixel. Inset show the ratio between the areas of each peak as the current increase.

LED mesa structure as the injection current increases. As the injection current increases the temperature in the quantum well increases as well. This causes a redshift in the emission spectrum, and the QDs have a decreasing absorption at longer wavelengths (this probably is a minor contribution as the observed redshift in the spectrum is small). It could also be attributed to different spectral broadening of the micro-LED and the NC emissions. A combination of these effects is the most likely explanation.

In conclusion, QD/photoresist nanocomposite micro-structures were fabricated on micro-LEDs with a self-aligned technique. The nanocomposite was spun directly on the device and the desired pixel was turned on, thus curing

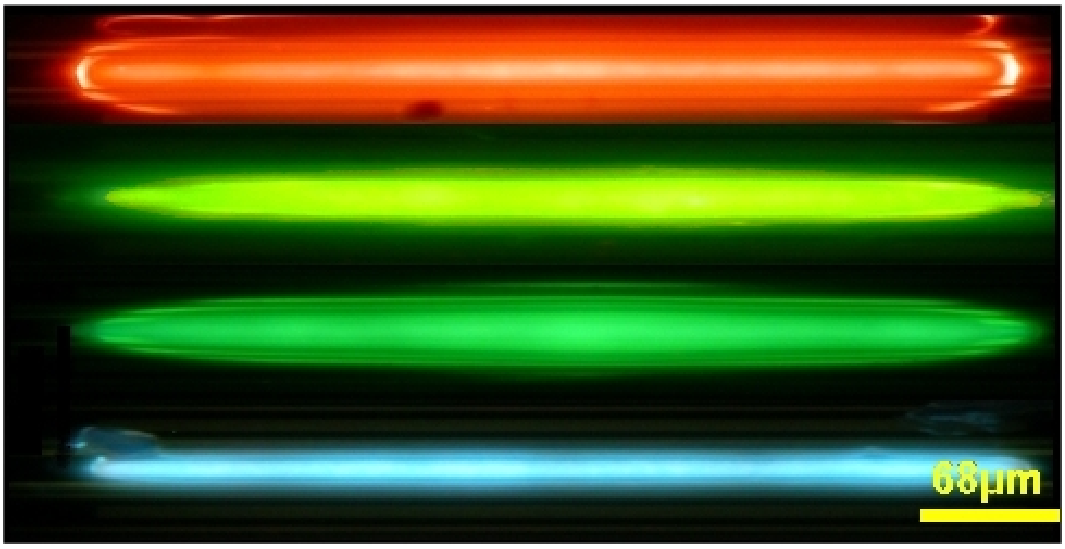

Figure 5.7: Optical micrographs of blue (486 nm), green(524 nm), yellow(560 nm), and red(609 nm) emitting pixels put together.

the composite locally on top of the light emitting pixel. The quantum dots immersed in the matrix photoresist act as colour converters for the UV emission from the LED. By integrating several different nanocomposites, incorporating different sized quantum dots, a multi-wavelength emitting micro-LED was realised. The estimated colour conversion efficiencies were 17.7%, 9%, 0.5%, and 0.2% for the red, yellow, green, and blue NCs respectively. However as can be seen the in figure 5.7 the colour converting structures usually cover more than one light emitting pixel, making it impossible to have adjacent pixel emitting at different wavelengths.

5.3 Laser direct writing

As an attempt to create structures covering only one pixel for each colour converting nanocomposite, laser direct writing, as described in chapter 3, was employed.

5.3.1 Experimental

The quantum dot nanocomposites were prepared in a similar manner as before, but at higher concentration to increase the absorption and hence the conversion efficiency. Some key properties of the nanocomposites can be seen in table 5.1.

Table 5.1: Properties of the quantum dot nanocomposites.

Prop. Comp.	Conc.(%-wt)	Conc. (nmol/mg)	Peak Em.
Red	1.2%-wt	0.039 nmol/mg	617 nm
Green	0.26%-wt	0.14 nmol/mg	543 nm
Blue	0.96%-wt	0.12 nmol/mg	488 nm

The device was prepared by cleaning it first in an acetone bath, then in a methanol bath and then it was rinsed in DI water and left to dry on a hotplate at 110 °C for at least 20 minutes. The nanocomposite was then spun directly on the device as previously described in the case of self-aligned writing. The device was then placed on the translation stage in the LDW setup.

Figure 5.8 shows a close up of the setup while writing. The device would be placed where the cover slip is in the image. The coordinates of the end points of the stripe, that was to be covered with the nanocomposite, was found by moving the stages and observing the position of the device, on a monitor, with the CCD camera. The coordinates were noted and a motion forming a straight line between the two sets of coordinates was programmed with the control software. The exposure was done with a linear velocity of 1 mm/s and total laser power of 5.5 μW for the red QD nanocomposite and 12.2 μW for the green and the blue. The spot size was adapted to the stripe width, $\sim$15 μm FWHM (12.7 μm $1/e^2$-radius). This gave maximum exposure doses of 35 mJ/cm^2 for the red and 77 mJ/cm^2 for the green and the blue nanocomposite.

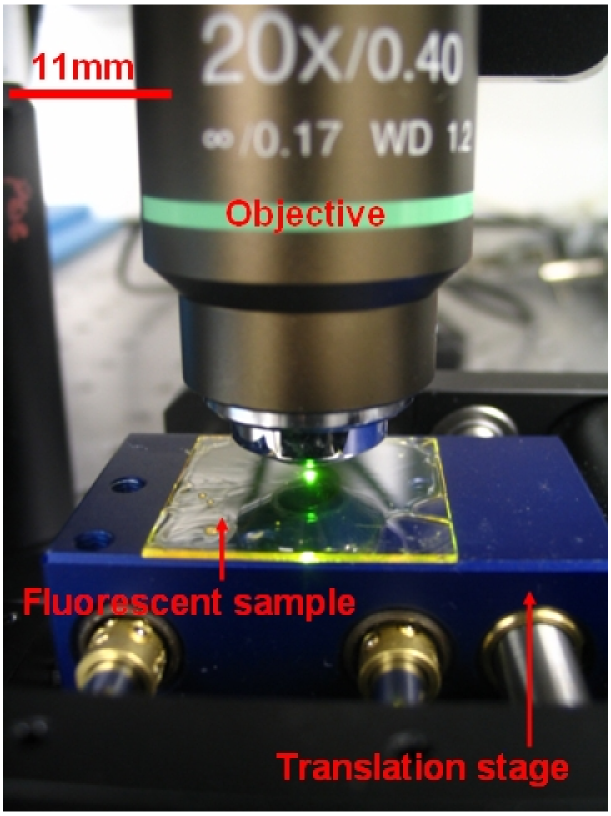

Figure 5.8: Photograph of the LDW setup while exposing a cover slip with a film of green nanocomposite.

After exposure of the desired stripes, the residue nanocomposite was washed off in an acetone bath, similarly to the self-aligned case. The procedure was then repeated for each different nanocomposite.

The adhesion of the nanocomposites to the bare device surface was however poor and it was easy to wash-off written lines, as can be seen in figure 5.9(a). This issue was helped by adding thin Norland lines on the device stripes before integrating the nanocomposite lines. The NOA lines were laser written in the same way as described in section 3.3. The NOA 81 was spun at 8000 rpm directly on the device and laser written at a total laser power of 5.5 μW in a small spot size of approximately 1 μm $1/e^2$-radius. With a writing velocity of 1 mm/s, this

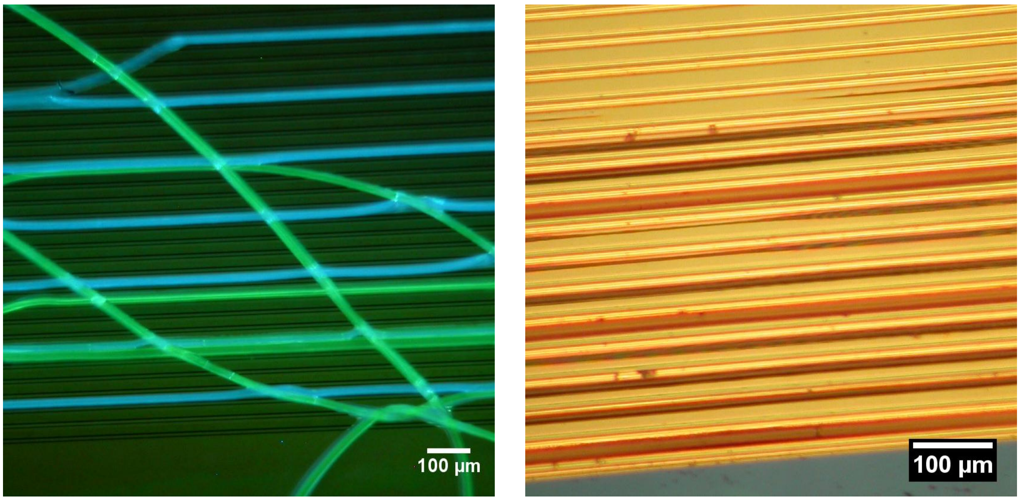

(a) Optical micrograph of fluorescing detached nanocomposite lines due to wash-off. With UV flood illumination.

(b) Optical micrograph of device with thin NOA lines aligned with the stripes of the micro-LED. The thicker line on every fourth stripe is the integrated red nanocomposite. With white light illumination.

Figure 5.9: Optical micrographs of stripe LED device with and without thin NOA attachment enhancing lines.

gave a maximum dose of ~0.44 J/cm^2. The resulting NOA lines are less than 2 μm high and 4–7 μm wide. These lines, together with lines of red nanocomposite, on a device can be seen in figure 5.9(b). This approach seemed to greatly enhance the adhesion of the nanocomposite lines on the device surface.

5.3.2 Characterisation

The micro-striped device after sequential integration with three nanocomposites, giving red, green, and blue emission can be seen in figure 5.10. The fourth stripe in the sequence is bare and hence emits only in the UV. The devices have been characterised with regards to the structures and the spectral properties of the device. The lines cover the full light emitting area of each stripe and are approximately 25 μm wide. The height of the structures was determined by stylus profilometry to be $\sim$9 μm.

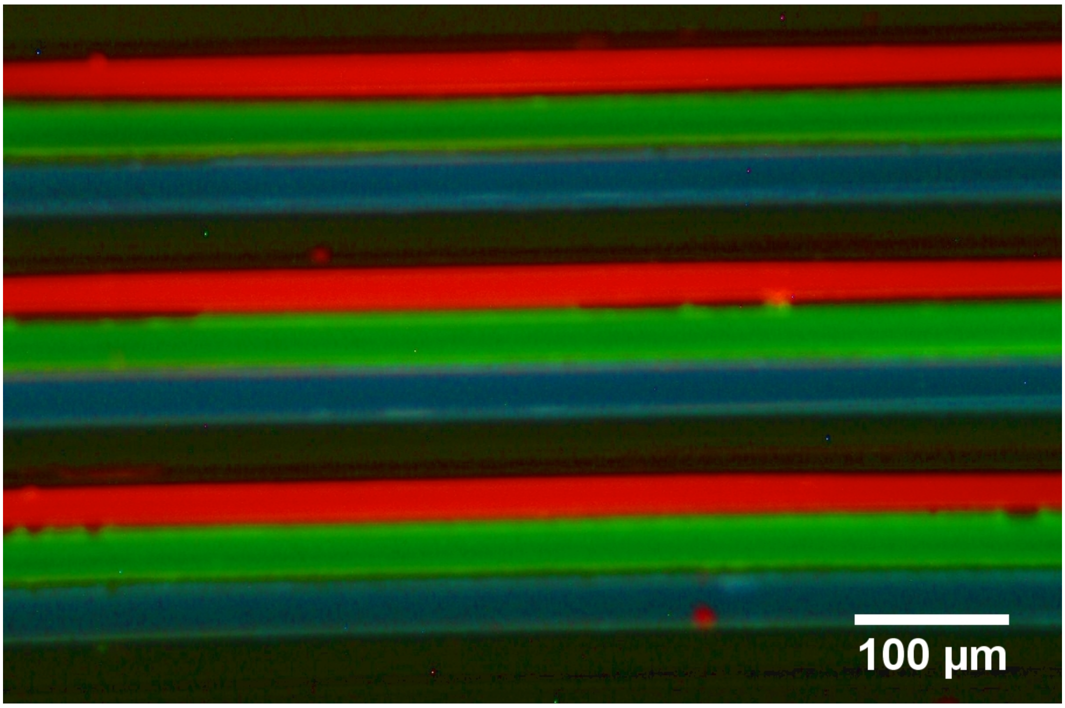

Figure 5.10: Optical micrograph of device with adjacent stripes covered with red, green, and blue nanocomposites, and the fourth stripe in sequence left bare, under external UV illumination.

In figure 5.11 the emitting device with laser written integrated quantum dot nanocomposites can be seen with adjacent stripes emitting at red, green, and blue and all three at once. The nanocomposites are excited by the UV emitting micro-stripes below them. The 'tail' appearence of the emission is due to UV power variation along each stripe. As can be seen in the images the stripes do not to any significant degree excite the structures on adjacent stripes.

The above was confirmed by the spectral measurements of the three different pixels, which can be seen in figure 5.11. The conversion efficiency is not improved compared to the self-aligned case (except for the green and the blue case), but

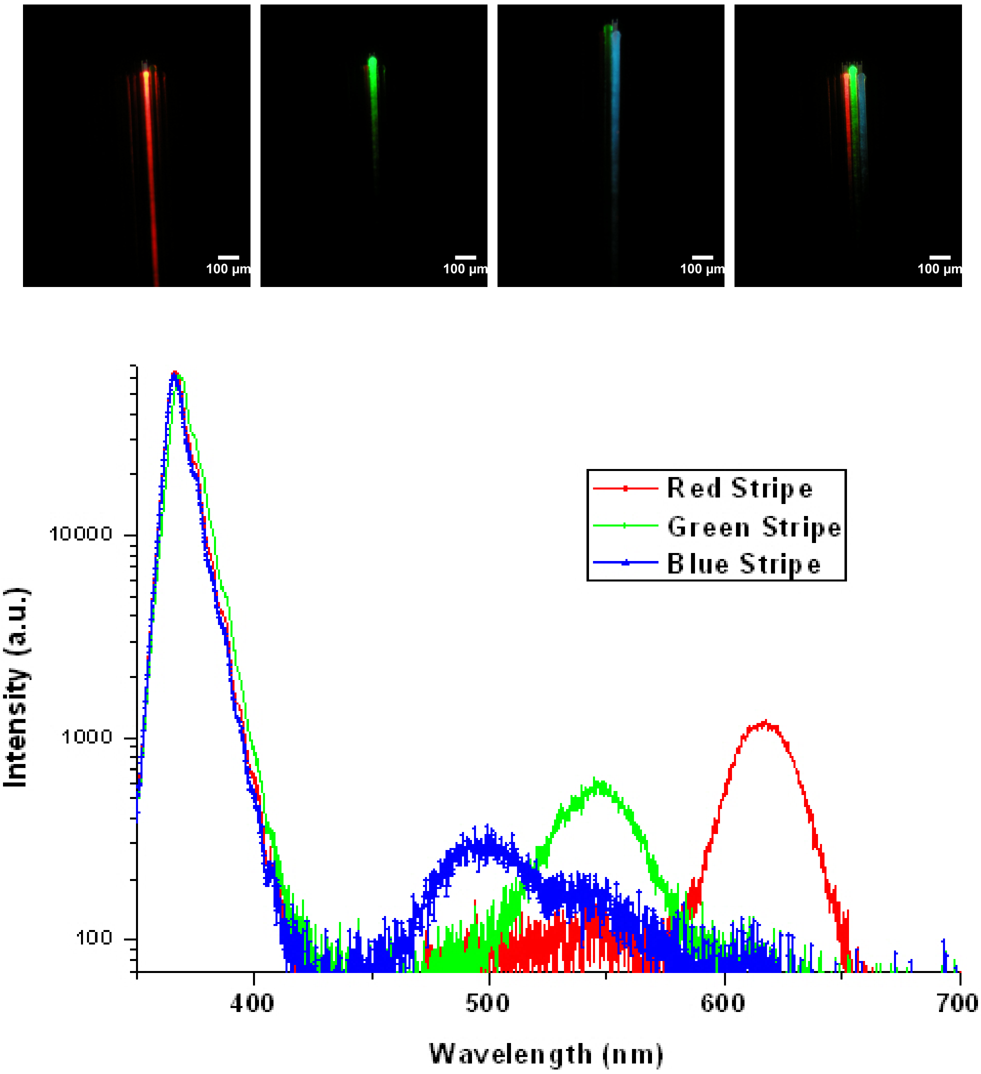

Figure 5.11: Device with laser written integrated quantum dot nanocomposites. From left to right: red pixel turned on, green pixel, blue pixel, and all three pixels turned on. The corresponding spectral data is given below.

the spectral contribution from non-addressed nanocomposite lines is considerably lower. The conversion efficiency is estimated (by comparing the area under the peaks) to be ~5%, ~3%, and ~2% for the red, green, and blue, respectively.

Unfortunately this device was damaged in the processing and full optical power measurements were not possible. The integration did not damage the device directly, but when it was wire bonded, residue polymer on the bonding pads caused problems. Too much force had to be used, causing damage to the device and a leakage current to flow.

To investigate how much the light escaping from the side walls of the mesa structure decreases the conversion efficiency, a novel type of planar, mesaless, device was tested. This device was patterned with a plasma treatment to deactivate the semiconductor material, instead of using etching to define mesa structures which in turn define the light emitting area. The nanocomposite was integrated on the device by laser writing, as before and the resulting device can be seen in figure 5.12. The conversion efficiency is considerably better for the green nanocomposite at ∼14% compared with ∼3% for the conventional device. However, the conversion efficiency decreases with increased voltage also with this device. The maximum efficiency of 14.4% was achieved at 5–6 V and reduced to 12.6% at 10 V.

5.4 Summary

In this chapter, techniques for producing multicoloured and white light LEDs and in particular colour conversion methods for micro-LED arrays have been described. Two methods for integrating quantum dot/negative photoresist nanocomposites on micro-LED devices have been introduced and tested. The first method is a self-aligned technique where the UV light emitted from the device itself defines the patterned structure. The second method utilises laser writing. While the second is more complicated and requires an external writing setup, it enables the manufacturing of colour converting structures which are smaller than the light emitting pixel. It also makes it possible to have two adjacent stripes converting light to different wavelengths.

The conversion efficiencies achieved with the two methods do not differ in a significant way. The estimated colour conversion efficiencies were 17.7%, 9%, 0.5%, and 0.2% for the red, yellow, green, and blue NCs respectively for the self-aligned method and ∼5%, ∼3%, and ∼2% for the red, green, and blue respectively in the laser writing case.

With a device without a mesa structure, hence less side scattering, the conversion efficiency was estimated to be ∼14% with a green colour converting structure.

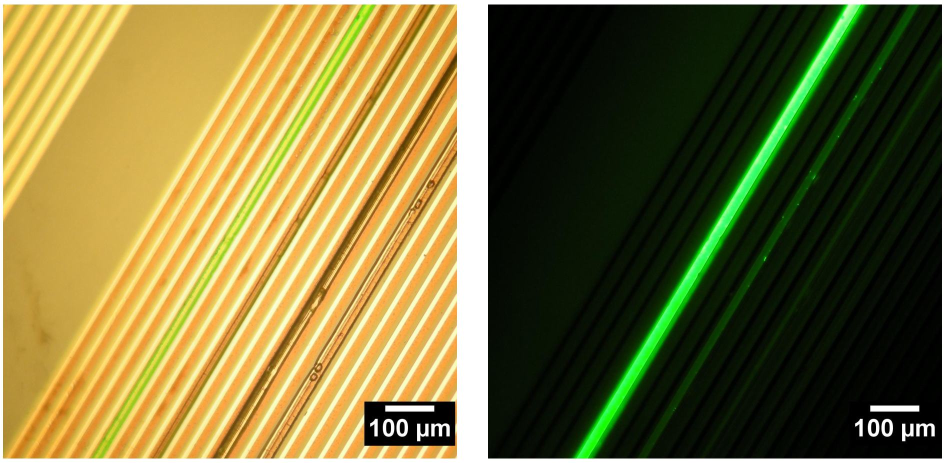

(a) Optical micrograph of planar micro-striped LED with a green nanocomposite line being addressed. With microscope illumination turned on.

(b) Optical micrograph of planar micro-striped LED with a green nanocomposite line being addressed. With microscope illumination turned off.

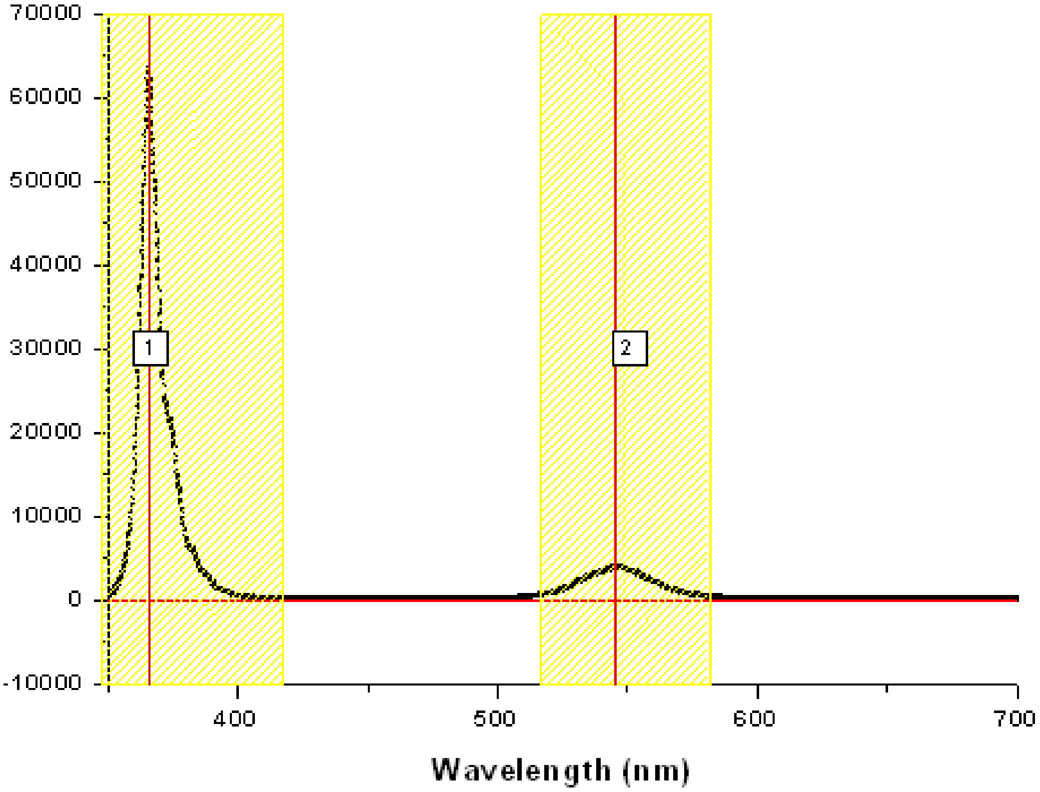

(c) Spectrum of the green nanocomposite covered micro-LED pixel. The area of the two peaks are marked as 1 (UV LED peak) and 2 (green converted peak).

Figure 5.12: Planar micro-LED device with integrated green nanocomposite. Approximately 14% of the light from LED is converted to green light.

References

[1] V. Poher, H. X. Zhang, G. T. Kennedy, C. Griffin, S. Oddos, E. Gu, D. S. Elson, M. Girkin, P. M. W. French, M. D. Dawson, and M. A. Neil. Optical sectioning microscopes with no moving parts using a micro-stripe array light emitting diode. *Opt. Express*, 15(18):11196–11206, 2007. 134

[2] V Poher, N Grossman, G T Kennedy, K Nikolic, H X Zhang, Z Gong, E M Drakakis, E Gu, M D Dawson, P M W French, P Degenaar, and M A A Neil. Micro-LED arrays: a tool for two-dimensional neuron stimulation. *Journal of Physics D: Applied Physics*, 41(9):094014 (9pp), 2008. 134

[3] N. Narendran, Y. Gu, J. P. Freyssinier, H. Yu, and L. Deng. Solid-state lighting: failure analysis of white LEDs. *Journal of Crystal Growth*, 268(3-4):449–456, 2004. x, 135

[4] Rong-Jun Xie, Naoto Hirosaki, Mamoru Mitomo, Kosei Takahashi, and Ken Sakuma. Highly efficient white-light-emitting diodes fabricated with short-wavelength yellow oxynitride phosphors. *Applied Physics Letters*, 88(10):101104, 2006. 135

[5] Sedat Nizamoglu, Gülis Zengin, and Hilmi Volkan Demir. Color-converting

combinations of nanocrystal emitters for warm-white light generation with high color rendering index. *Applied Physics Letters*, 92(3):031102, 2008. 137

[6] Sedat Nizamoglu, Evren Mutlugun, Tuncay Özel, Hilmi Volkan Demir, Sameer Sapra, Nikolai Gaponik, and Alexander Eychmüller. Dual-color emitting quantum-dot-quantum-well CdSe-ZnS heteronanocrystals hybridized on InGaN/GaN light emitting diodes for high-quality white light generation. *Applied Physics Letters*, 92(11):113110, 2008. 137

[7] S. Guha, R. A. Haight, N. A. Bojarczuk, and D. W. Kisker. Hybrid organic–inorganic semiconductor-based light-emitting diodes. *Journal of Applied Physics*, 82(8):4126–4128, 1997. 137

[8] Shiyong Liu, Jingsong Huang, Zhiyuan Xie, Yu Wang, and Baijun Chen. Organic white light electroluminescent devices. *Thin Solid Films*, 363(1-2):294–297, 2000. 137

[9] T. Komine and M. Nakagawa. Integrated system of white LED visible-light communication and power-line communication. In *Personal, Indoor and Mobile Radio Communications, 2002. The 13th IEEE International Symposium on*, volume 4, pages 1762–1766 vol.4, Sept. 2002. 137

[10] B. Guilhabert, D. Elfström, A. Kuehne, D. Massoubre, H. X. Zhang, S. R. Jin, A. R. Mackintosh, E. Gu, R. Pethrick, and M. D. Dawson. Integration by self-aligned writing of nanocrystal/epoxy composites on InGaN micro-pixelated light-emitting diodes. *Opt. Express*, 16(23):18933–18941, 2008. 137

[11] E. Gu, H. X. Zhang, H. D. Sun, M. D. Dawson, A. R. Mackintosh, A. J. C. Kuehne, R. A. Pethrick, C. Belton, and D. D. C. Bradley. Hybrid inorganic/organic microstructured light-emitting diodes produced using photocurable polymer blends. *Applied Physics Letters*, 90(3):031116, 2007. 137

Chapter 6

Conclusions

Micro-patterning of functional materials is increasing in importance. Low-cost, accurate, and flexible methods for patterning of sensitive organic and inorganic materials will have a wide range of applications in various fields, such as microfluidics, micro-electro mechanical systems, optogenetics, and organic lasers.

In this thesis maskless micro-patterning techniques, suitable for sensitive organic materials, have been presented. The aim was to develop photo-based techniques for patterning of functional materials, for which conventional patterning techniques are unsuitable.

In Chapter 1 basic principles and devices, such as light emission in LEDs, lasers, micro-patterning techniques, and photoresist systems, were introduced. Special emphasis was put on GaN alloy based light emitting devices, as they form the basis of much of the further work. Conventional photolitography was briefly explained and general resolution limits were introduced. Nanoluminophores, including organic nanoengineered materials and semiconductor nanocrystals, were introduced and some concepts in photoluminescence were also presented.

The material systems which form the basis of the thesis work were introduced in chapter 2. Positive and negative photoresist systems were presented. The difference between the two, in that they form positive and negative images of a photomask respectively, was explained. Luminecent materials used in this work, i.e., organic flourescent molecules and inorganic nanocrystal quantum dots, were also presented. Key characteristics of these materials, including absorption and emission spectra, were given. Blended materials based on negative-type photoresists and nanoluminophores were presented and the routes used to make these materials were described. Important characteristics, including spectral data, of the blended systems were also presented. For organic light-emitting materials the matrix material, i.e., the negative photoresist, not only provide photolithographic patterning capability, but also give environmental protection. This was shown by exposing two samples, one bare and one in a matrix, to the same dosage of UV light, which is known to cause photooxidisation in the luminescent organic material. While the spectra for the bare material was dominated by the peak in the green emanating from oxidised flourene moieties, while the blended materials were still emitting blue light.

In Chapter 3 the principles of laser direct writing was introduced and the resolution limit discussed. A laser writing system suitable for producing patterns in nanocomposite materials based on negative-type photoresists was described. In particular the optical power delivered at the sample position as a dependence of the attenuation of a neutral density filter wheel and the minimum spot size was measured. The latter was measured with a "knife edge"-type method. The average value of the spot diameter ($1/e^2$-diameter) was 0.8 μm and 0.9 μm in the perpendicular direction, respectively. The LDW system was used to produce test patterns in different types of the negative-type photoresist Norland optical adhesive. The smallest feature size produced was ∼2 μm in the negative-type photoresist NOA61. Optical measurements as well as atomic force micrographs of the structures were presented. Test patterns in NOA81 was written on micro-disc LED arrays as a test of the capabilities of the setup. The system was also used to pattern oligofluorene functionalised truxene blended with a divinyl based monomer (CHDV) based negative-type photoresist (HTP3) in waveguide-type structures. A range of different feature sizes, from ∼2.5 μm to 120 μm, were produced. This work was published in Advanced Materials in 2009 [1]. The laser writing system represents a low cost photopatterning system with good resolution.

In Chapter 4 a novel maskless photopatterning system based on a CMOS driven micro-LED array emitting in the UV and a combination of microscope objectives was introduced. First a brief review of some relevant maskless lithography techniques was given. The CMOS-driven UV micro-LED device was then presented. Characteristics and performance figures, including modulation features and I-V and L-I plots, for this device were given. The device consists of 8×8 pixels with a diameter of 72 μm, each capable of delivering ∼600 μW of optical power. This device was put into a maskless photolithography setup consisting of back-to-back infinity-corrected microscope objectives. By changing the objectives magnification or demagnefication of the micro-LED array was achieved at the sample position. The writing can be monitored with a CCD camera by deflecting some light with a beam splitter placed between the microscope objectives. The setup was characterised with regards to e.g., spot size and optical power delivered at the sample position. The spot size was measured in optical micrographs of reflected images of one micro-LED pixel taken by the CCD. The minimum spot diameter achieved was measured to be 8.5 μm and the maximum optical power density was 7.7 W/cm^2. The setup was tested by writing test patterns in postive- and negative-type photoresists. Writing under CW as well as under pulsed driving was tested. The minimum feature size in NOA81 achieved was ∼7.4 μm with 30 ns-pulsed driving for 2 s giving an exposure dose of 4.0 J/cm^2. Line patterns with widths from ∼8.0 μm to ∼10 μm in negative photoresist ("waveguide structures") and positive photoresist ("channels") were also produced. The work on the maskless photolithography system was published in Optics Express in 2009 [2].

In Chapter 5 micro-LED arrays with integrated nanocrystal composite structures were presented. First a brief review of multi-coloured and white LEDs was given and the need for colour conversion was discussed. Some different techniques for achieving colour down-conversion on LEDs was also introduced. The material system chosen for the colour conversion was nanocomposites based on a negative-type photoresist (NOA81) and semiconductor nanocrystals (quantum dots). Two different methods of aligning the photopatternable nanocomposites on micro-striped LEDs were presented. The first method is a self-aligned technique where the patterned area is defined by the LED itself. The stripe, which is to be covered by the luminescent material, is turned on and the UV emission from the LED pixel cures the nanocomposite. By this method a device capable of converting UV light output to red (609 nm), yellow (560 nm), green (524 nm), and blue (486 nm), with conversion efficiencies of 17.7%, 9%, 0.5%, and 0.2%, respectively, was produced. The conversion efficiency was found to decrease as the injection current current increased. The work on self-aligned nanocomposite structures for colour conversion on micro-striped LED devices was published in

Optics Express in 2008 [3]. Due to the strongly divergent output beam of the striped LED device structures cured by the self-aligned technique tend to cover several micro-stripes. To address this issue the LDW system described in chapter 3 was utilised to write aligned structures on the micro-LED device. Due to adhesion problems a thin line of pure NOA81 was written on the device before the nanocomposite integration. With this technique a micro-stripe device with red, green and blue nanocomposites on adjecent stripes was produced. The conversion efficiency achieved with this technique was ∼5%, ∼3%, and ∼2% for the red, green, and blue, respectively. The optical "cross-talk" was greatly reduced by this technique compared to the self-aligned method as confirmed by spectral data. Colour converting nanocomposite structures were also integrated on a novel "mesa-less" (planar) device. The conversion efficiency achieved with green quantum dot nanocomposite was ∼14% on this device. This was attributed to less UV light escaping from the mesa side-walls and not getting converted.

6.1 Future work

A new generation of CMOS driven micro-LED device with circular light emitting pixel diameters from 14 μm to 84 μm has been developed. When fitted into the lithography tool described in chapter 4, features down to 1.4 μm are theoretically feasible. Figure 6.1 shows an optical micrograph of the new generation device with five pixels turned on.

Figure 6.2 presents the I-V and L-I characteristics of the new generation device.

In initial test the maskless photolithography tool with the new generation

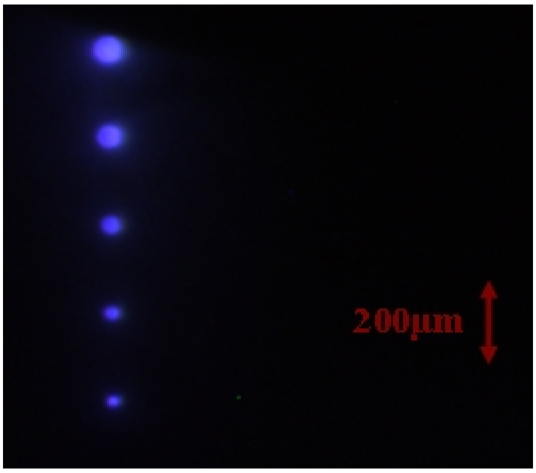

Figure 6.1: Optical micrograph showing a range of different size pixels of the new generation of CMOS driven micro-LED.

LED device (using the 14 μm diameter pixel) was able to produce structures in the positive-type photoresist S1805 with features $\sim$2 μm in size, by writing at a velocity of 65 μm/s and a delivered total optical power of 0.3 μW and an exposure dose of 100 mJ/cm^2.

Other possible uses for similar setups include neural stimulation and optogenetics [4] or photopumping of organic lasers.

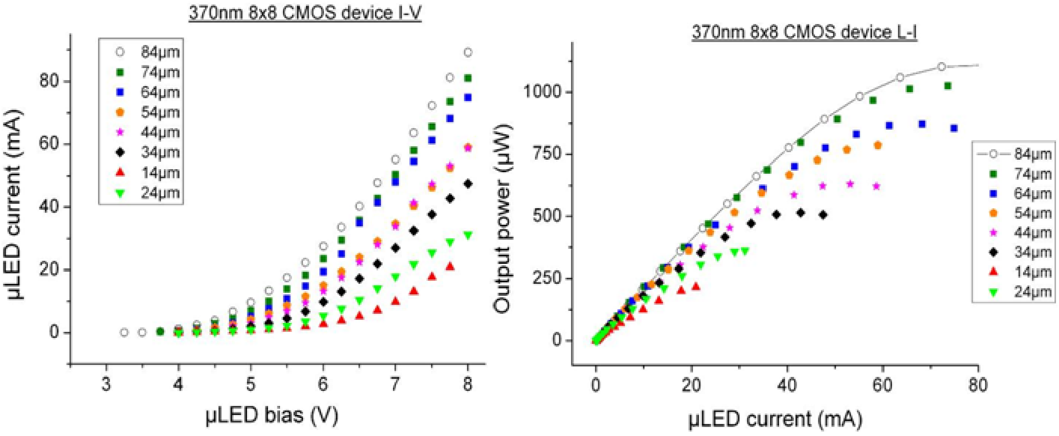

Figure 6.2: Electrical and optical performance of the new generation micro-LED device.

References

[1] Alexander J. C. Kuehne, David Elfström, Allan R. Mackintosh, Alexander L. Kanibolotsky, Benoit Guilhabert, Erdan Gu, Igor F. Perepichka, Peter J. Skabara, Martin D. Dawson, and Richard A. Pethrick. Fluorescent nanostructures: Direct laser writing of nanosized oligofluorene truxenes in UV-transparent photoresist microstructures (adv. mater. 7/2009). *Advanced Materials*, 21(7):781–785, 2009. 158

[2] D. Elfström, B. Guilhabert, J. McKendry, S. Poland, Z. Gong, D. Massoubre, E. Richardson, B. R. Rae, G. Valentine, G. Blanco-Gomez, E. Gu, J. M. Cooper, R. K. Henderson, and M. D. Dawson. Mask-less ultraviolet photolithography based on CMOS-driven micro-pixel light emitting diodes. *Opt. Express*, 17(26):23522–23529, 2009. 159

[3] B. Guilhabert, D. Elfström, A. Kuehne, D. Massoubre, H. X. Zhang, S. R. Jin, A. R. Mackintosh, E. Gu, R. Pethrick, and M. D. Dawson. Integration by self-aligned writing of nanocrystal/epoxy composites on InGaN micro-pixelated light-emitting diodes. *Opt. Express*, 16(23):18933–18941, 2008. 160

[4] Nir Grossman, Vincent Poher, Matthew S Grubb, Gordon T Kennedy, Konstantin Nikolic, Brian McGovern, Rolando Berlinguer Palmini, Zheng Gong,

Emmanuel M Drakakis, Mark A A Neil, Martin D Dawson, Juan Burrone, and Patrick Degenaar. Multi-site optical excitation using chr2 and micro-led array. *Journal of Neural Engineering*, 7(1):016004, 2010. 161

Appendix A

LabView$^{\mathrm{TM}}$ virtual instruments

A.1 Program for line writing

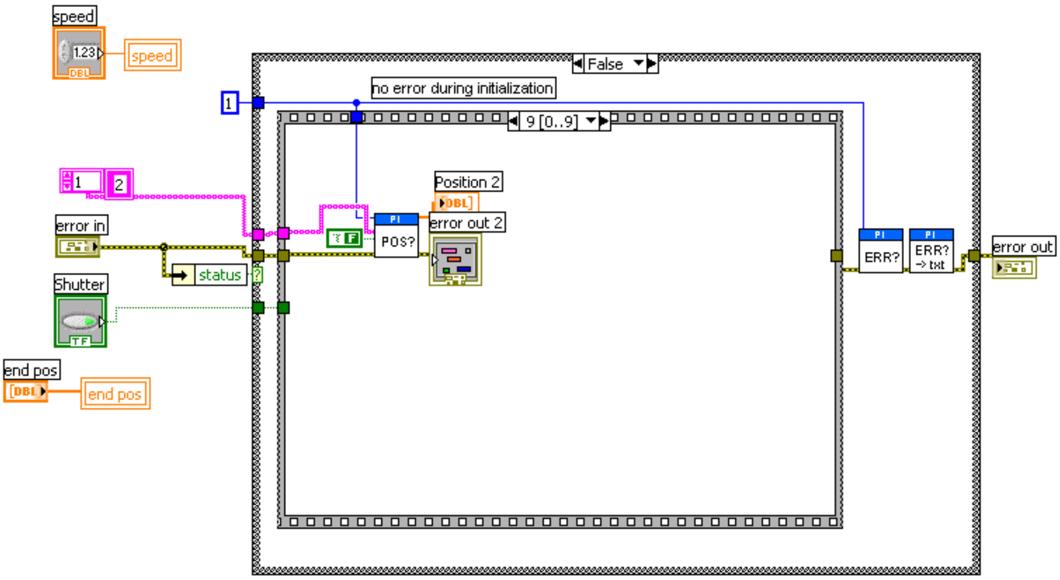

Figure A.1: LabView$^{\mathrm{TM}}$ screen shot showing the first panel of a movement control program.

The program progresses in sequence as follows:

1. The ’speed’, the ’end pos’ and the ’Shutter’ (’T’/’F’) is read from the user interface.
2. The ’start pos’ (current position) is read from the stages.
3. The distance and the vector between the ’start pos’ and ’end pos’ is calculated and saved.
4. The ’time’ is calculated, by dividing the distance with the speed, and saved.
5. The velocity for each axis is calculated and saved.
6. The velocity is written to the stage control.
7. If the ’shutter’ is ’T’, the shutter is opened.
8. The movement is initialised with the ’end pos’ as destination.
9. The stage is asked if it is on target. This is looped until the stage is on target.
10. If the ’shutter’ is ’T’, the shutter is closed.
11. The position of the stage is read as a control.

Each pane in the sequence is depicted in figures A.2 through to A.5.

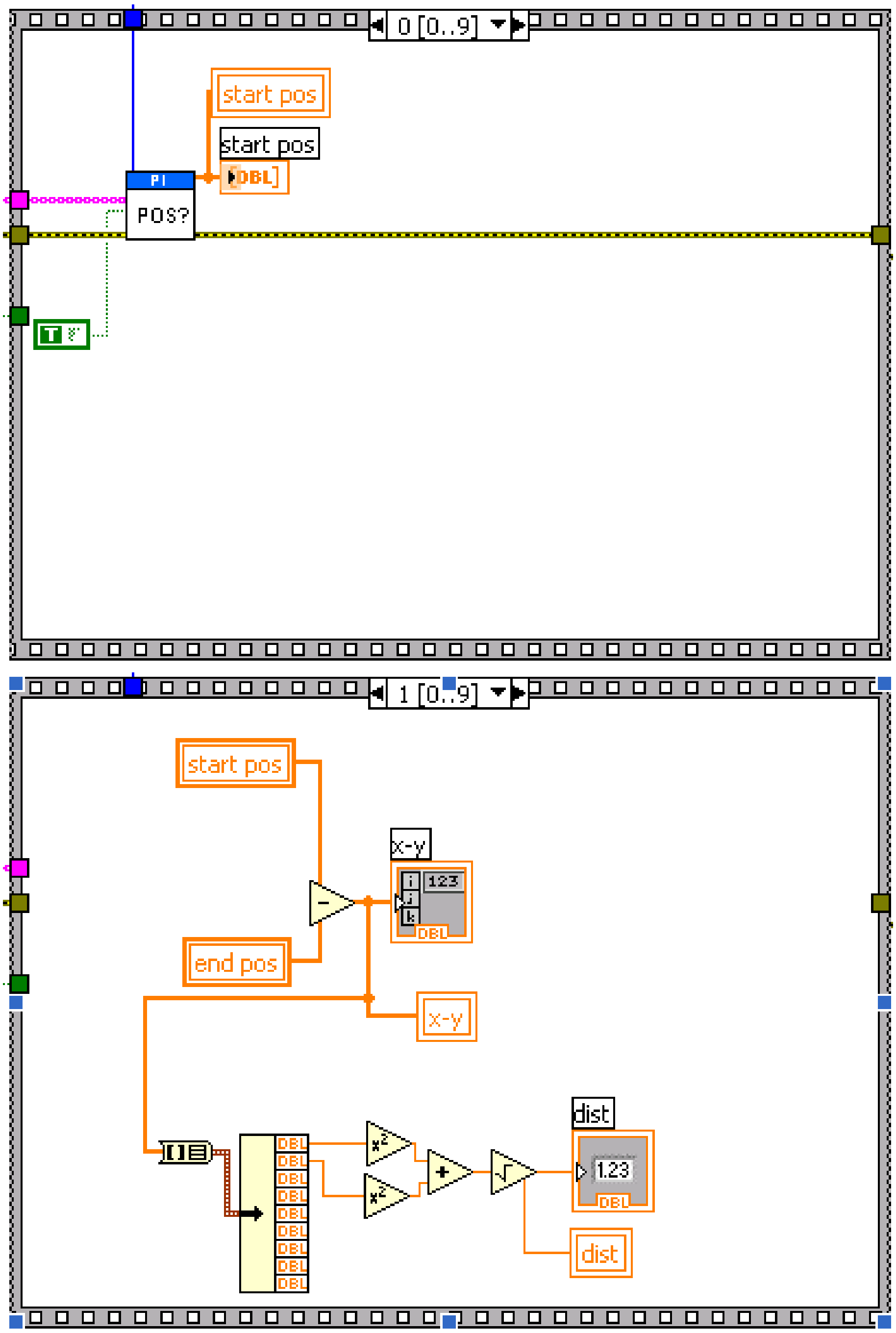

Figure A.2: Sequence 0–1.

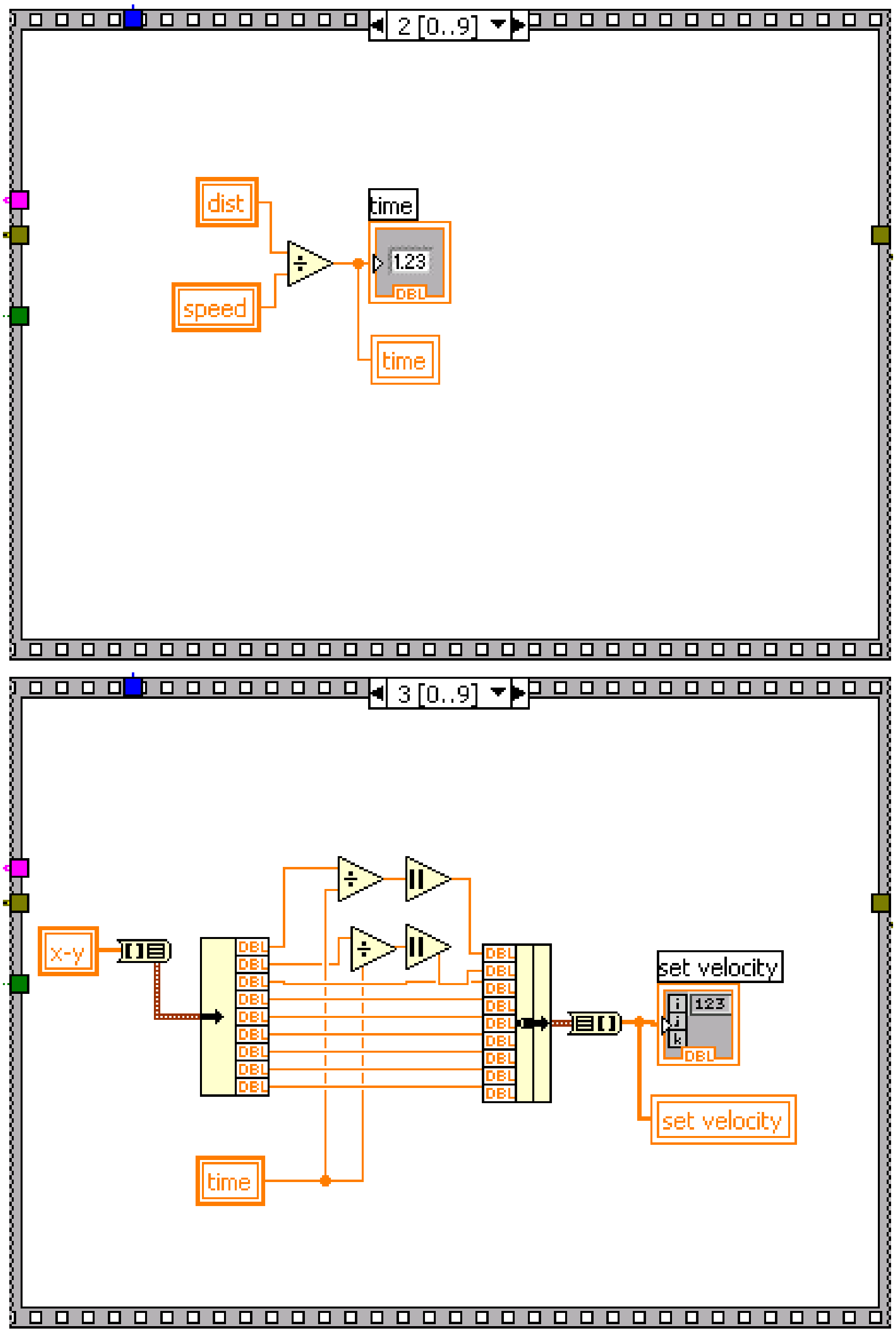

Figure A.3: Sequence 2–3.

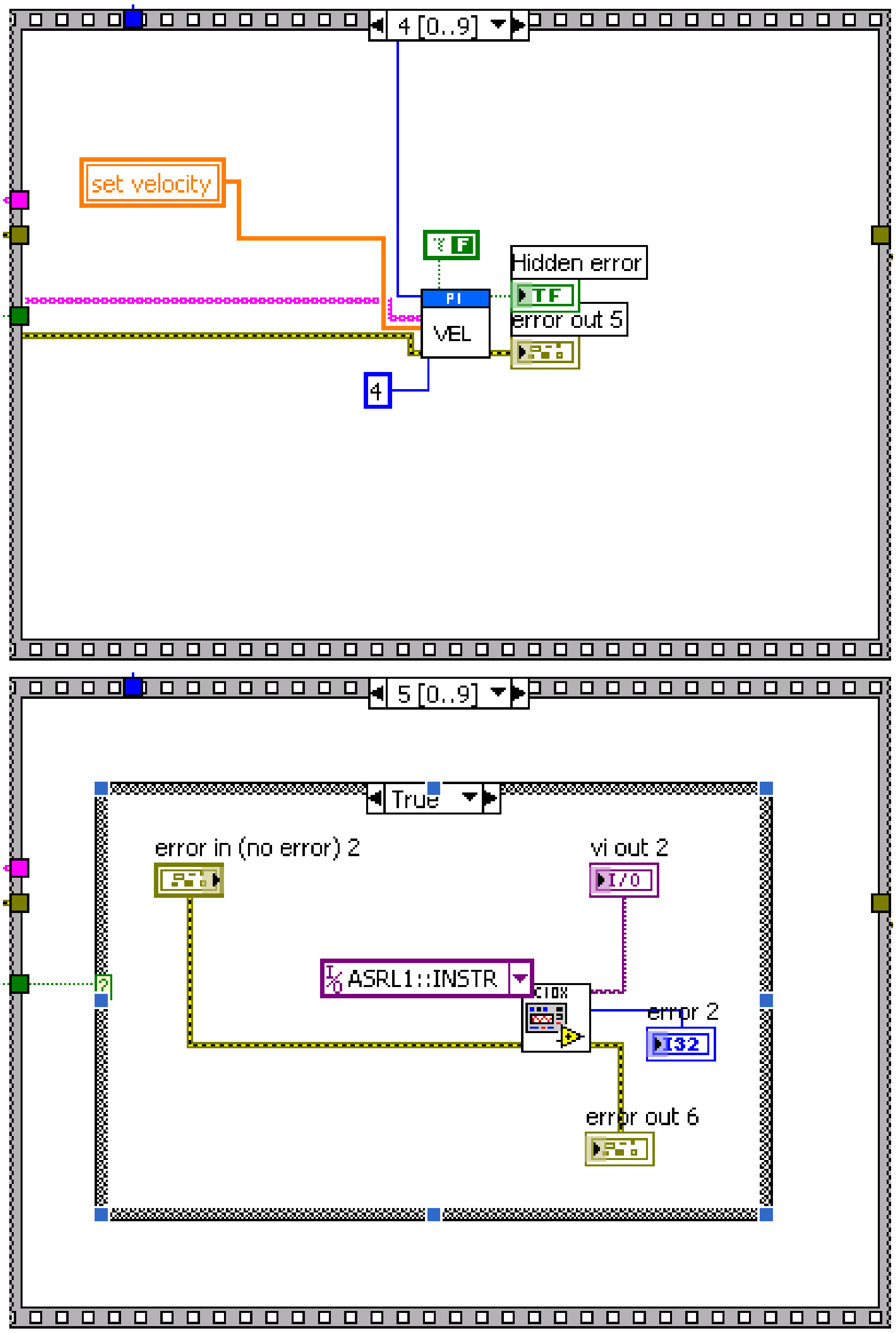

Figure A.4: Sequence 4–5.

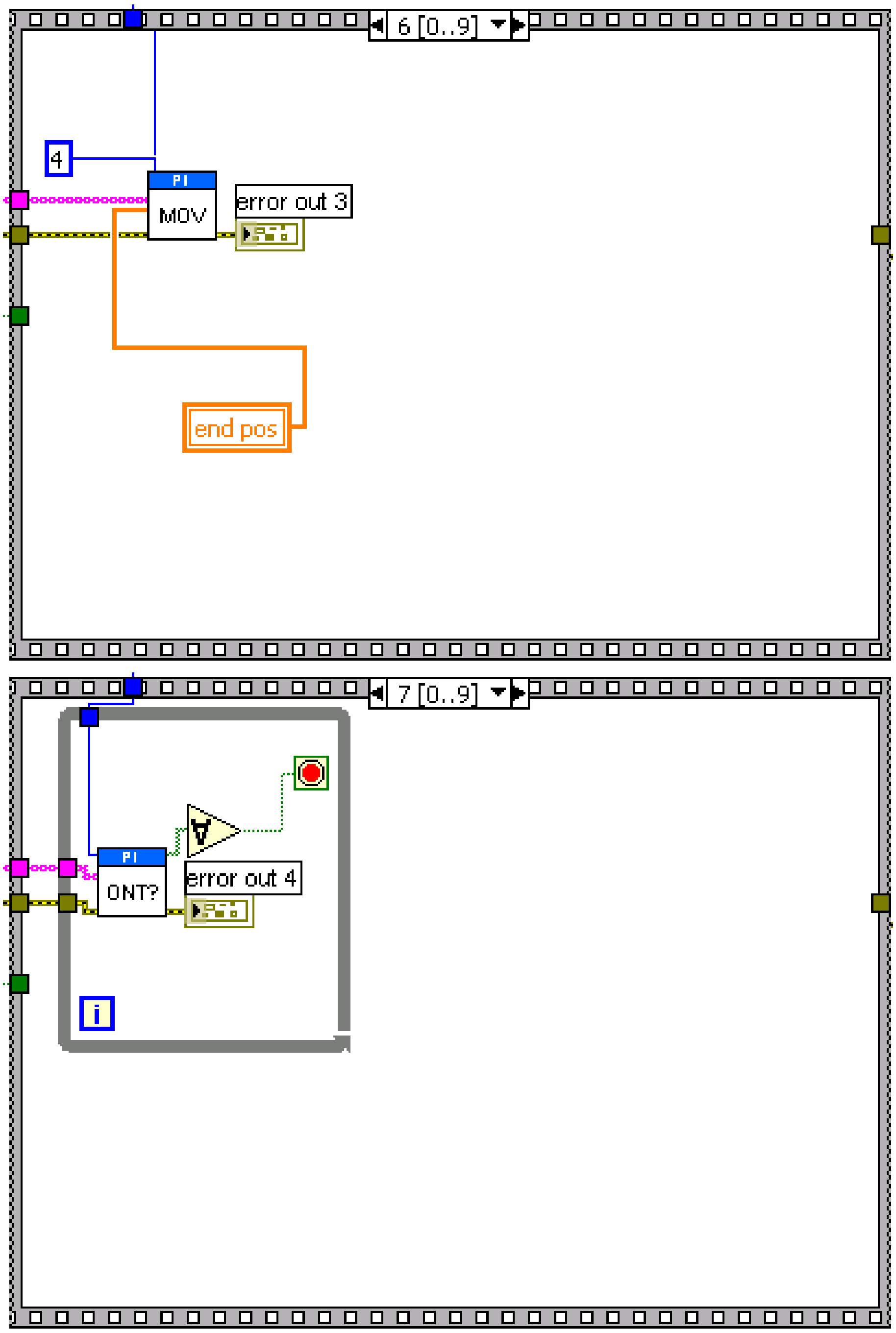

Figure A.5: Sequence 6–7.

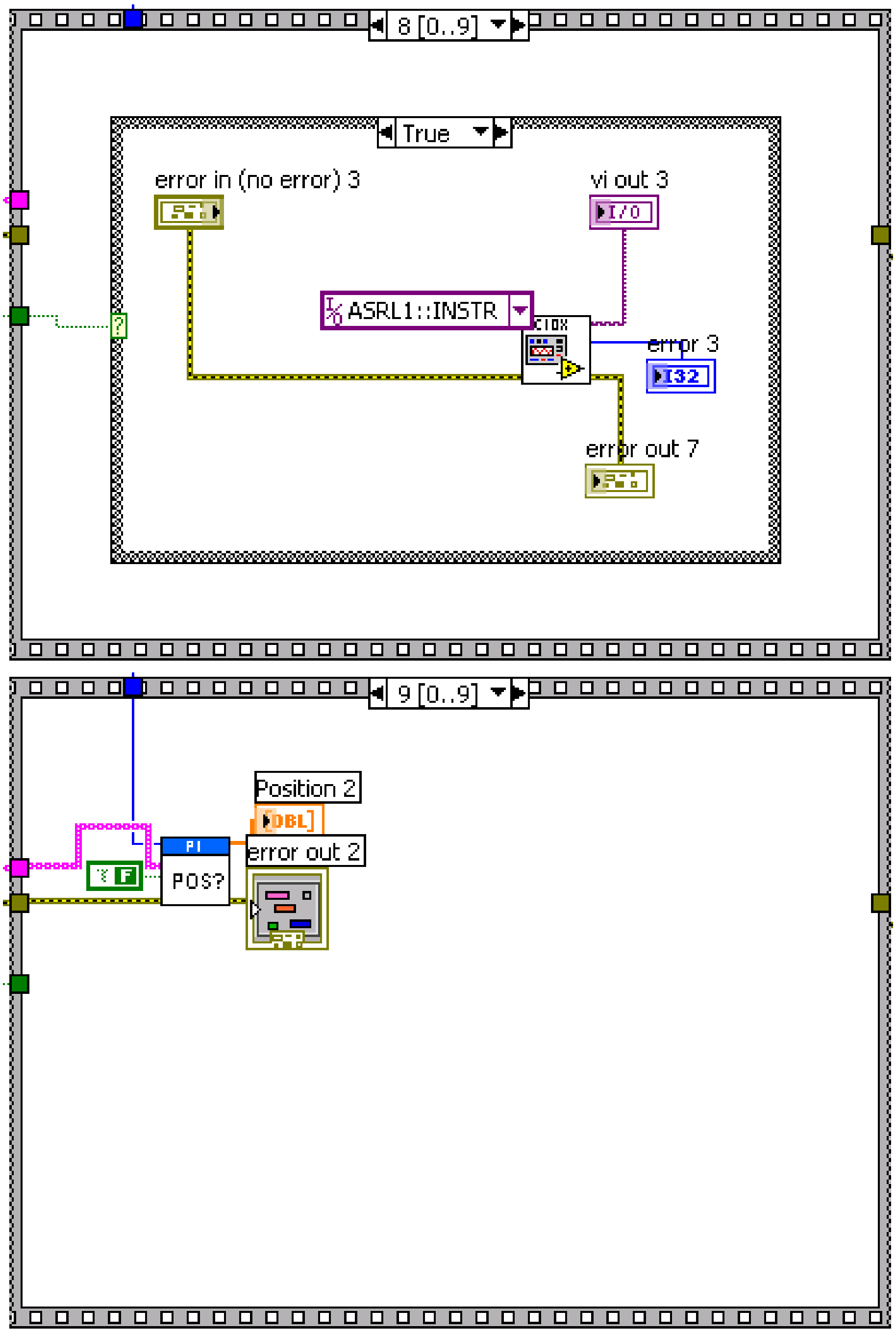

Figure A.6: Sequence 8–9.

A.2 Program for micro-disk array writing

A program for writing $n \times n$ locations (i.e., a square area with $n \times n$ discrete locations) on a micro-pixelated device has the following flow sequence:

1. n (the desired number of locations to be written on in each row and column) is read from the user interface.
2. The stage position ((x_n, y_n)-coordinates) of the (n,n)-position is read from the user interface. (The position is first located with help of the microscope imaging.)
3. The current stage position ((x_1, y_1)-coordinates) is read as the (1,1)-position.
4. The diagonal vector is calculated as $\vec{d} = (x_n, y_n) - (x_1, y_1)$.
5. Two vectors $\vec{v1}$ and $\vec{v2}$ are defined as $\vec{v1} = \vec{d}/2 + \left[\begin{smallmatrix} 0 & 1 \\ -1 & 0 \end{smallmatrix}\right] \vec{d}/2$ and $\vec{v2} = \vec{d}/2 - \left[\begin{smallmatrix} 0 & 1 \\ -1 & 0 \end{smallmatrix}\right] \vec{d}/2$. These two vectors now defines the movement directions of the stages.
6. The open time for shutter and hence the exposure dose for each location is written to the shutter.
7. The writing is started and the expsure is performed at the first location $(1, 1)$ (see figure A.7).
8. The stage is moved $\vec{v1}/(n-1)$ and the next exposure is performed at location $(2, 1)$. The step is repeated (n-1) times.
9. The stage is moved $\vec{v2}/(n - 1)$ and performed at location $(n, 2)$.
10. Steps are repeated to cover the designated $n \times n$ area.

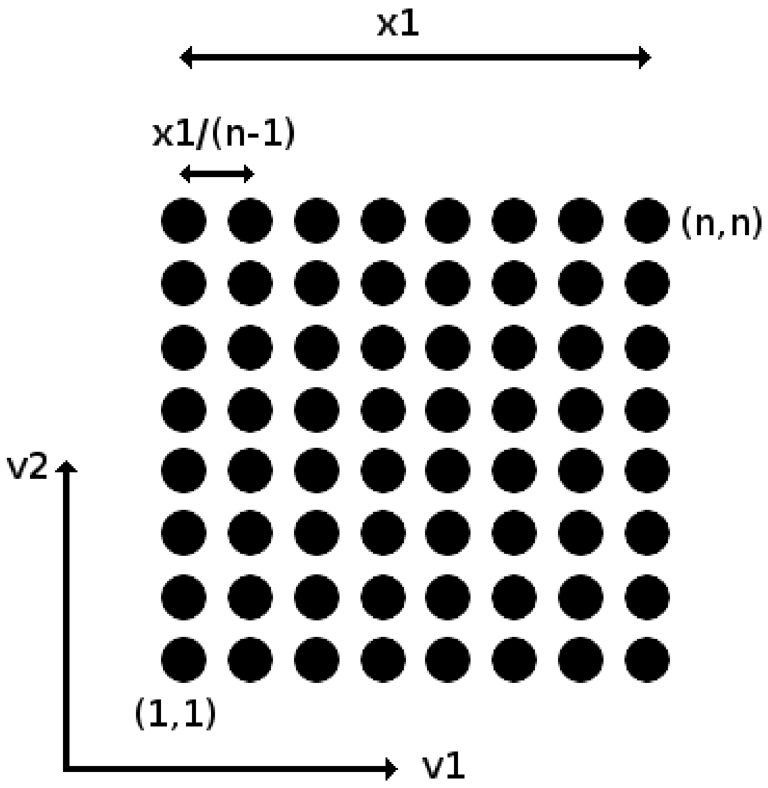

Figure A.7: Schematic image showing a $n \times n$ area on a device. v1 and v2 denotes two vectors defined in the LabView^{TM} code.

Appendix B

Publications

Journal publications

D. Elfström, B. Guilhabert, J. McKendry, S. Poland, Z. Gong, D. Massoubre, E. Richardson, B.R. Rae, G. Valentine, G. Blanco-Gomez, E. Gu, J.M. Cooper, R.K. Henderson, and M.D. Dawson, *Mask-less ultraviolet photolithography based on CMOS-driven micro-pixel light emitting diodes*, Opt. Express, 17(26):23522–23529, 2009.

A.J.C. Kuehne, **D. Elfström**, A.R. Mackintosh, A.L. Kanibolotsky, B. Guilhabert, E. Gu, I.F. Perepichka, P.J. Skabara, M.D. Dawson, and R.A. Pethrick, *Direct Laser Writing of Nanosized Oligofluorene Truxenes in UV-Transparent Photoresist Microstructures*, Advanced Materials, **21**, 7, 781–785, 2009. Featured on the front cover.

B. Guilhabert, **D. Elfström**, A. Kuehne, D. Massoubre, H.X. Zhang, S.R. Jin, A.R. Mackintosh, E. Gu, R. Pethrick, and M.D. Dawson, *Integration by self-aligned writing of nanocrystal/epoxy composites on InGaN micro-*

pixelated light-emitting diodes, Opt. Express **16**, 18933–18941, 2008.

Conference Publication

D. Elfström, B. Guilhabert, C. Griffin, D. Massoubre, H.X. Zhang, J. McKendry, Z. Gong, E. Gu, M.D. Dawson, *Quantum dot nano-composites as colour-converters for micro-pixellated gallium nitride light-emitting diodes*, IEEE Lasers and Electro-Optics Society annual meeting 2008.

M. Wu, **D. Elfström**, Z. Gong, B. Guilhabert, A. Zarowna, E. Gu, M. D. Dawson, A.L. Kanibolotsky, P.J. Skabara, A.J.C. Kuehne, A.R. Mackintosh, R.A. Pethrick, P.R. Edwards, R.W. Martin, O.J. Rolinski, D.J.S. Birch, I.F. Perepichka, *Controlled micro-patterning of highly-fluorescent truxene-oligofluorene nanostructured blends*, IEEE Lasers and Electro-Optics Society annual meeting 2008.

M. Wu, A. Zarowna, **D. Elfström**, B. Guilhabert, C.L. Lee, E. Gu, M.D. Dawson, A.L. Kanibolotsky, P.J. Skabara, A.J.C. Kuehne, A.R. Mackintosh, R.A. Pethrick, P.R. Edwards, O.J. Rolinski, R.W. Martin, D.J.S. Birch and I.F. Perepichka, *Drop-on-demand inkjet printing of organic and inorganic fluorescent nano-particles*, 3rd International colloquium on integrated manufacture by printing, 2007.

M. Wu, **D. Elfström**, B. Guilhabert, E. Gu, M.D. Dawson, P.J. Skabara, A.L. Kanibolotsky, A.R. Mackintosh and R.A. Pethrick, *Photoluminescence and micro-patterning of the star-shaped truxene-core oligofluorenes*, SID organic electronics for displays UK 2007.

Oral Presentations

D. Elfström, B. Guilhabert, C. Griffin, D. Massoubre, H.X. Zhang, J. McKendry, Z. Gong, E. Gu, M.D. Dawson, *Quantum dot nano-composites as colour-converters for micro-pixellated gallium nitride light-emitting diodes*, IEEE Lasers and Electro-Optics Society annual meeting 2008.

D. Elfström, M. Wu, B. Guilhabert, A. Zarowna, E. Gu, M.D. Dawson, A.J.C. Kuhne, A.R. Mackintosh, R.A. Pethrick, A.L. Kanibolotsky, P.J. Skabara, P.R. Edwards, R.W. Martin, O.J. Rolinski, and D.J.S. Birch, *Micro-patterning and applications of organic and inorganic fluorescent nano-particles*, Strathclyde University Research Day 2008.

D. Elfström, *Light-directed micro-patterning of polymers and electrodes for applications in biomedicine and instrumentation*, Strathclyde University Physics Department Postgraduate Conference 2007.

Direct Laser Writing of Nanosized Oligofluorene Truxenes in UV-Transparent Photoresist Microstructures

By *Alexander J. C. Kuehne,* David Elfström, Allan R. Mackintosh, Alexander L. Kanibolotsky, Benoit Guilhabert, Erdan Gu, Igor F. Perepichka, Peter J. Skabara,* Martin D. Dawson,** and *Richard A. Pethrick**

Recently, the incorporation of nanoscaled inorganic components into organic photoresist hosts to produce photocurable composite materials, has been reported.[1] Combining highly processable photoresists with nanoscaled inorganic quantum dots or nanocrystals in this way creates an attractive method for the production of photonic-device structures, including single-photon sources, waveguides, and lasers.

Due to the recognized incompatibilities between functional organic light-emitting molecules and conventional photolithography materials, the fabrication of all-organic microstructures presents a significant technological challenge.[2] In this paper, we report the incorporation of nanosized oligofluorene truxenes into a novel UV-transparent organic photoresist material, as an alternative approach to fluorescent nanocomposites. Oligofluorene truxenes are a new class of monodisperse organic light-emitting molecules.[3] The blending of oligofluorene truxenes and a UV-transparent photoresist enables photoprocessing of individually dispersed nanoscopic organic light-emitting molecules within a microstructured UV-transparent matrix. These blends will allow the creation of all-organic optical-device structures for a wide range of photonic applications.

It is well known that the incorporation of inorganic quantum dots into photoresists reduces the speed of polymerization relative to the pure resist.[1a] The reduction in rate is partially attributed to the effects of the competing absorption of the quantum dots with the photoacid generator (PAG) that initiates the polymerization process. In sharp contrast, the incorporation of the organic oligofluorene truxene into the UV photoresist leads to large increases in the rate of polymerization. The observed increase in rate is due to a photoinduced electron transfer (PET) from the photon harvested by the oligofluorene truxenes to the PAG.[4]

In the ideal matrix, the spectral properties of the oligofluorene truxene should be unaltered by the nature of the photoresist matrix. It should also act as an encapsulant, to inhibit photo-oxidation of the organic light-emitting molecules and allow the creation of appropriate optical structures for device fabrication.

Here, we examine the spectral properties of novel oligofluorene truxene photoresist composites, and show easy processability of the composite by direct laser writing (DLW) of waveguide-type structures. The laser-written structures are characterized using optical microscopy and scanning electron microscopy (SEM).

Most commercial negative-photoresist materials are based on aromatic entities, which impart to the resist desirable properties for semiconductor processing, but are not ideal as a matrix for light-emitting materials. The π–π interaction between aromatic units generates the desired high viscosity for spin-coating. However, these aromatic units limit the transparency of the matrix, and provide a possible source of energy transfer and quenching. A resist such as SU-8 has acceptable transparency above 360 nm. However, below this wavelength it absorbs almost all of the energy. In addition, aromatic groups can induce solvatochromic shifts in π-conjugated light-emitting molecules.[5] In a previous paper, we reported the development of an epoxy-based photoresist that achieves transparency down to 300 nm in a film 20 μm thick.[6] However, as a result of the polarity of the glycidyl ether groups in the cyclohexyldiglycidyl ether (CHDG) photoresist, it is difficult to achieve miscibility of the fluorene molecules, which tend to form large aggregates and are less effective photoemitters.

In this paper, we report on a novel UV-transparent negative photoresist system based on 1,4-cyclohexyldimethanol divinyl ether (CHDV, see Fig. 1). Cross-linking in this system is achieved via the vinyl ether moieties instead of using glycidyl ether groups. CHDV is less polar than CHDG, and more readily solvates fluorene light-emitting molecules. When a proton is produced from the decomposition of the PAG, the vinyl ether moieties polymerize, to produce a carbon-based backbone with pending vinyl ether groups (see Fig. 1, structure 4), and extended polymerization leads to the creation of a cross-linked network. The absence of aromatic groups in CHDV creates a matrix that is passive, and allows transmission of light down to about 240 nm. The PAG of choice was a *para*-octyloxy-functionalized diphenyliodonium hexafluoroantimonate. The *para*-octyloxy chain pro-

---

[*] Dr. A. J. C. Kuehne, Prof. P. J. Skabara, Prof. R. A. Pethrick, Dr. A. R. Mackintosh, Dr. A. L. Kanibolotsky
WestCHEM, Department of Pure and Applied Chemistry
University of Strathclyde
295 Cathedral Street, Glasgow G1 1XL (UK)
E-mail: alexander.kuhne@strath.ac.uk; peter.skabara@strath.ac.uk; r.a.pethrick@strath.ac.uk

Prof. M. D. Dawson, D. Elfström, B. Guilhabert, Dr. E. Gu
Institute of Photonics, University of Strathclyde
106 Rottenrow, Glasgow G4 0NW (UK)
E-mail: m.d.dawson@strath.ac.uk

Dr. I. F. Perepichka
Centre for Materials Science
Faculty of Science and Technology
University of Central Lancashire
Preston PR1 2HE (UK)

DOI: 10.1002/adma.200802656

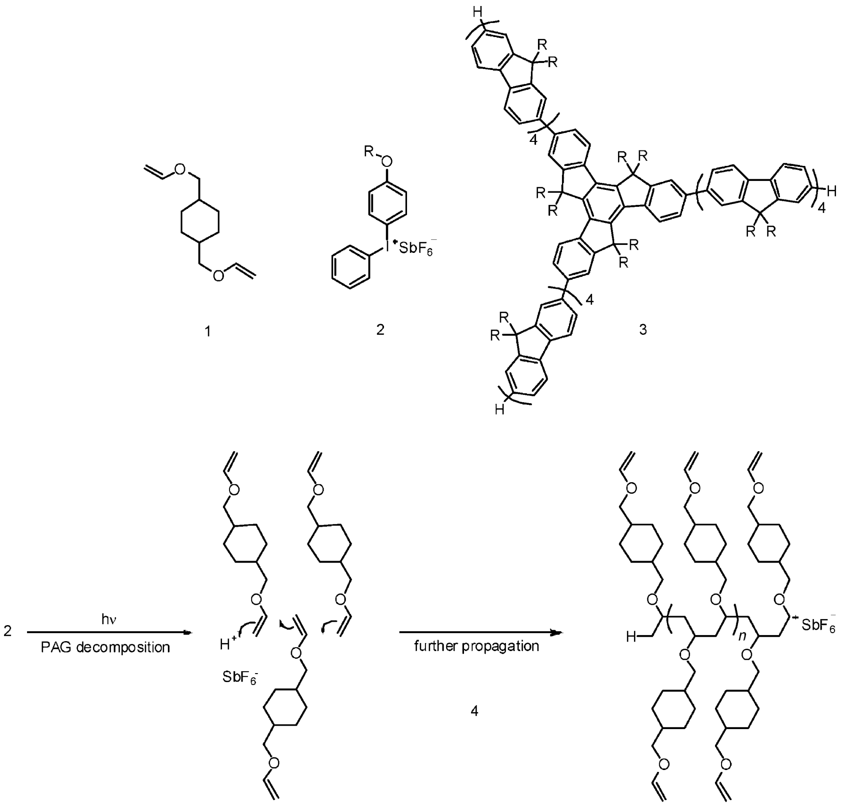

Figure 1. 1) 1,4-Cyclohexanedimethanol divinyl ether, 2) 4-octyloxy diphenyliodonium hexafluoroantimonite (PAG), with R as an octyl chain, 3) oligofluorene truxenes T4, with R as a hexyl chain, and 4) photoinduced cationic polymerization mechanism for CHDV.

vides improved solubility in the nonpolar CHDV photoresist matrix. The peak absorption for PAG is at ~250 nm, as determined from a solution in acetonitrile (see Fig. 2a). The absorption at 225 nm is due to $\pi \rightarrow \pi^*$ transitions in the conjugated phenyl rings of the PAG. Photocuring pure CHDV with PAG requires a deep UV wavelength for initiation. After cure, the CHDV photoresist has over 90% transparency at 250 nm for a 2.6 μm thick film (see Fig. 2a). The high transparency of the photoresist material in the UV spectrum enables complete photoexcitation of the incorporated fluorescing molecules.

The light-emitting molecules used in this study were the oligofluorene truxene designated T4.[3] The molecules consist of a truxene core with three pendant quaterfluorene units (see Fig. 1, structure 3). The CHDV photoresist system is miscible with these oligofluorene truxenes, which are approximately 4 nm in radius, and exerts little or no solvatochromic shift on the spectra of these molecules. The lack of a solvatochromic shift is in contrast to that observed when the oligofluorene truxene is dispersed in toluene. The T4 oligofluorene truxenes show very efficient blue photoluminescence with a high fluorescence quantum yields in both solution and the solid state (86% and 60% respectively).[3a] Figure 2b compares the absorption spectra for T4 as a solid film, in solution, and in the cured CHDV matrix, demonstrating similarity of the T4 in cured CHDV spectrum with that of the solution spectrum. The absorption maxima for T4 are at 372 nm in the solid state, 373 nm in toluene, and 371 nm in the polymerized CHDV, respectively. However, the emission spectra in the various states exhibit significant differences (see Fig. 2b). The emission maximum of the T4 toluene solution peaks at 413 nm, and for T4 incorporated in the polymerized CHDV matrix the maximum is at 411 nm. The maximum of the solid T4 film is red-shifted by ~30 nm, at 440 nm. Blending the T4 molecules into the CHDV photoresist system and curing the film produces an emission spectrum for the oligofluorene truxenes, which is comparable to that in toluene solution. The spectrum of T4 in the CHDV matrix is broadened with respect to its solution spectrum, due to greater vibronic interactions of the fluorescing molecules with the polymer matrix, indicating that the T4 molecules are monodisperse and "pseudo-solvated" within the solid CHDV matrix. Larger aggregates of oligofluorene truxenes would produce a red-shifted spectrum of shape similar to that of the solid-state spectrum.[5,7]

When oligofluorene truxenes are incorporated into the CHDV photoresist system, PAG can be activated at the absorption wavelengths of the truxenes, which are at much lower energies than its own absorption maximum. PET from the light-emitting molecule to the PAG leads to photolysis of the PAG at lower energies than its usual absorption wavelength. Here, an electron is excited to the LUMO of the T4 at a value of −2.14 eV, and is transferred into the LUMO of the PAG, which has a value of −3.72 eV. The iodonium initiator, hence, gets reduced from a cation to a radical. To relax, the radical electron can now return to the ground state of the T4, or relax through a follow-up reaction that involves scission of the C–I bond, and hence the decomposition of the PAG (an energy diagram of the process is available in the Supporting Information).[4] The LUMO of the PAG was determined by cyclic voltametry against ferrocene as internal standard. The HOMO and LUMO levels of T4 were taken from reference [3a].

This transfer mechanism as a result of the incorporation of the oligofluorene truxenes is very effective in enhancing the rate of cure, and allows irradiation at 368 nm, whereas the neat photoresist material requires irradiation at 254 nm. If neat CHDV with PAG is irradiated at 368 nm, no cure of the resin is observed. The observed high rate of reaction when the oligofluorene truxenes are present is consistent with their photon harvesting ability, activating all the PAG molecules at essentially the same time.[8]

The essentially low-polarity CHDV matrix appears to effectively protect the T4 molecules from photo-oxidation. Normally, fluorene molecules, when exposed to atmospheric oxygen, are subject to photo-oxidation, and form fluorenone moieties that shift the fluorescence spectrum towards the green.[9] Recent work in our laboratories suggests that the encapsulation of fluorene-based molecules within a polymer matrix reduces the diffusion of oxygen and suppresses photo-oxidation.[10]

A sample with a direct-laser-written structure of T4 in a CHDV blend did not show any change in its emission spectrum after 6 months of exposure to air and ambient light. A neat T4 film

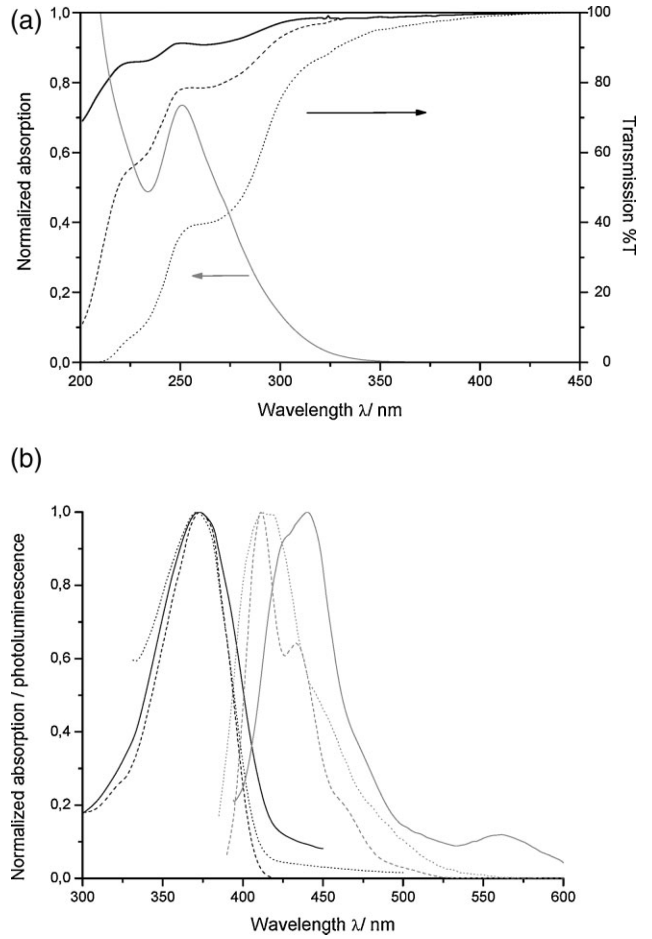

Figure 2. a) Transmission spectra of different thicknesses of CHDV with 1 wt% of PAG: 2.6 μm (solid black), 7.0 μm (dashed black), 11.0 μm (dotted black), and normalized absorption spectrum of PAG in acetonitrile (gray). b) Normalized absorption and photoluminescence spectra of a solid T4 film (solid black and gray), T4 in a toluene solution (dashed black and gray), and T4 pseudosolvated within a CHDV polymer matrix (dotted black and gray).

spin-coated from toluene and the laser-written T4/CHDV structure were exposed to radiation from a 368 nm UV lamp. After a radiation dose of 187.2 J cm^{-2}, the spectrum of the neat T4 film was dominated by a broad peak with a maximum at ~550 nm, which can be attributed to fluorenone formation due to photo-oxidation of the fluorene moiety.[9] The spectrum of the laser-written T4/CHDV structure, however, shows only minor changes (spectra are supplied in the Supporting Information). We can hence conclude that CHDV films containing the fluorene molecules exhibit very good stability and color retention compared to neat T4 films.

In this study, cure of the T4/CHDV mixture was achieved using a standard amount of 1.0 wt% PAG. The photoinitiator was first dissolved in the same amount of toluene wt/wt for compatibilization and to improve solubility in the CHDV photoresist. Use of more than 1.0 wt% of PAG leads to a reduction in the resolution of the pattern, and does not shorten the cure time significantly. The photopatterned structures adhered well to the substrate during and after the wash-off process. However, the full pattern was transferred in an "adhesive-tape transfer test". In this study, no surface treatment of the substrate was applied. The adhesion of the structures could be further increased by use of an adhesion promoter before DLW. The full pattern was transferred onto the tape, and was intact after transfer, which implicates good mechanical properties of the cured T4/CHDV composites in terms of structural rigidity (a microscopy image of the transferred pattern can be found in the Supporting Information).

Due to the low viscosity (5.62 cP) of the CHDV, the creation of spin-cast films is not possible, because the CHDV is dewetting the substrate, and an alternative approach to pattern generation was carried out. For direct laser writing, a borosilicate glass substrate used for its near UV transparency was brought into contact with the T4/CHDV photoresist mixture, which had been placed in a polytetrafluoroethylene (PTFE) basin (a schematic of the setup can be found in the Supporting Information). The structures were written face down through the substrate, with the sample stage translated under a fixed optical beam position by computer-controlled *X*–*Y*–*Z* translation stages. Using this direct laser writing approach, patterns were created with 0.5 wt%, 1.0 wt%, and 5.0 wt% of T4 in CHDV. Because of the PET from T4 to the photoacid, the polymerization of CHDV occurs very rapidly, and writing was carried out at very high speeds. In this study, the writing speed was maintained at a constant rate of 1.5 mm s^{-1}, and the output power of the 375 nm gallium nitride diode laser source was varied between 40 μW, 80 μW, 120 μW, and 160 μW, in order to study the effect on the feature size and resolution that could be achieved. After laser writing, the borosilicate glass slide was lifted from the basin, and excess photoresist removed by washing in toluene. The dimensions achieved were extracted from microscope images, and hence represent the width at the bottom. The values are listed in Table 1. It can be seen that increasing the laser intensity produces a broader line, whilst a change in the T4 concentration from 0.5 wt% to 1.0 wt% produces only a small increase in line width. The resolution, however, is reduced with a 5.0 wt% content of T4. Changing the concentration of T4 will influence the light-harvesting characteristics of the resist, and allow for more PAG molecules to be activated and, hence, a greater chance of 'dark'-polymerization, where reaction occurs outside the illuminated region as a consequence of proton migration from the illuminated zone. When more PAG molecules are initiated, there is a greater chance of active polymerization centres propagating beyond the illuminated zone, and reduced overall resolution.[11] Figure 3 shows optical microscopy images of the 1.0 wt% T4 series in the CHDV photoresist system under ambient and UV illumination. The images show a uniform blue fluorescence throughout the laser-written lines, indicating that a homogeneous dispersion of

Table 1. Line-widths of T4/CHDV microstructures.

Laser output power	0.5 wt % T4 in CHDV	1 wt % T4 in CHDV	5 wt % T4 in CHDV
40 μW	35 μm	35 μm	50 μm
80 μW	45 μm	50 μm	80 μm
120 μW	70 μm	70 μm	100 μm
160 μW	90 μm	95 μm	120 μm

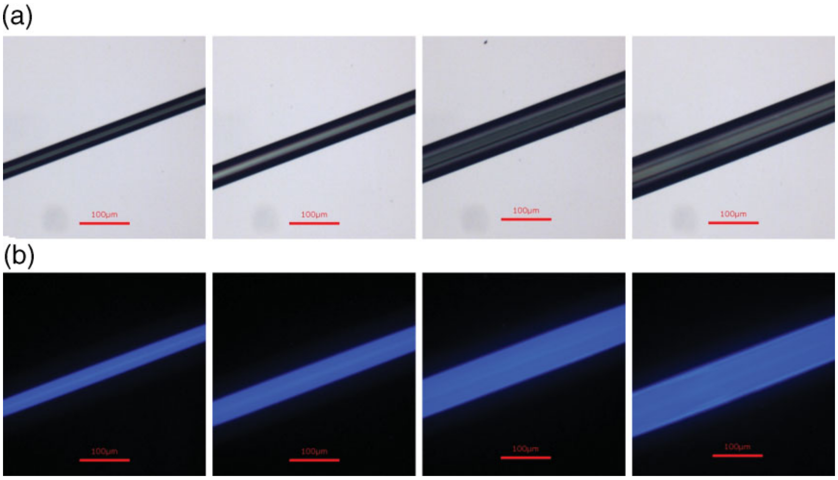

Figure 3. Microscopy images of fluorescing microstructures with 1 wt% T4 and 1 wt% PAG, written with a laser, observed using optical microscopy with a) white-light illumination and b) 368 nm illumination, written at 40 µW, 80 µW, 140 µW, and 160 µW (from left to right).

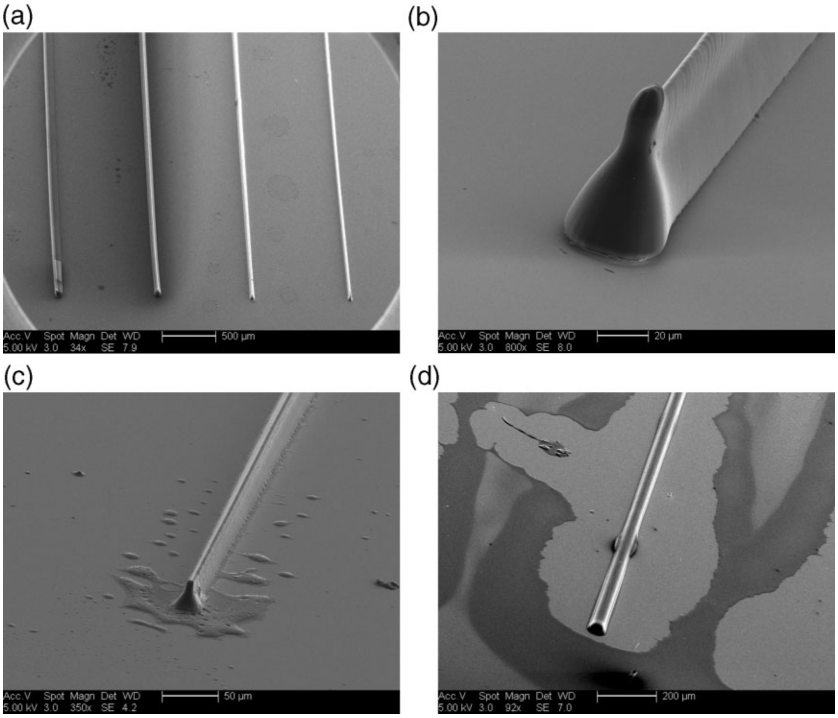

Figure 4. Scanning electron microscopy images of different percentages of T4 in CHDV: a) image of the 0.5 wt% T4 sample with four lines written at 160 µW, 140 µW, 80 µW, and 40 µW from left to right; b) close up image of the line written at 40 µW into the 0.5 wt% T4 in CHDV blend; c) image of the line written at 40 µW into the 1.0 wt% T4 in CHDV blend; d) image of the line written at 40 µW into the 5.0 wt% T4 in CHDV blend.

the T4 in the CHDV was achieved, consistent with the spectroscopic characteristics.

The SEM images of the laser-written structures (Fig. 4) show in more detail the structure of the T4/CHDV series written at 40 µW. The thin-film patches in the images of Figure 4c and d are due to residues of the composite, from incomplete wash-off. Examination of the structure of the line produced with the lowest T4 concentration (i.e., 0.5 wt%) indicates a good aspect ratio and smooth walls. The thicker features that can be seen at the end of the structure are due to an exposure time lag when starting and stopping the stage and opening and closing the laser-beam shutter. The shape of the feature reflects as much the shape of the optical beam as the effects of the polymerization process on the feature structure. The 'upside-down chalice' shape of the structures in the blends of 0.5 and 1.0 wt% is assumed to be a result of the high sensitivity of the resist material, due to the light-harvesting character of the T4. When writing into the resist, face down through the substrate, the focal point of the laser beam lies beyond the substrate. After the focal point, convergence of the beam occurs, and combined with the high sensitivity of the resist, the observed shape in the material represents the profile of the laser beam. This is not apparent in the 5.0 wt% T4/CHDV blend. With the higher loading of the photon-harvesting T4, the composite absorbs more strongly, and limits the extent to which the laser beam penetrates into the resist composite in the PTFE basin. Hence, in the 5.0 wt% T4/CHDV blend, no activation of the PAG occurs beyond the focal point of the laser, leading to a half-cylindrical shape of the written line. In conclusion, a higher content in photon-harvesting T4 leads to greater absorption, and hence structures that have a lower aspect ratio. With lower T4 contents, the laser beam can penetrate deeper into CHDV/T4 blend, and hence produce structures that have a higher aspect ratio. This effect defines the shape of the structure, whereas dark-polymerization, which occurs after the direct-laser-writing step, reduces the overall resolution of the structures.

Figure 5 shows a more complicated pattern created, under computer control of the translation stages, as a 4:5 Lissajous structure using 1 wt% of T4 in the CHDV resist. When the laser power was limited to 0.4 µW, and PAG content was reduced to 0.1 wt%, a line width of 2.5 µm was achieved.

This paper presents the cure characteristics of a photoresist material, which contains fluorene-based light-emitting molecules. The absorption and fluorescence spectra of the oligofluorene derivative indicate that a homogeneous dispersion of the T4 molecules is achieved throughout the CHDV matrix. Apparent environmental protection of the T4 molecules from oxygen, combined with the short cure time, render these novel photo-cross-linkable composites of CHDV and T4 highly attractive for applications in organic optoelectronics.

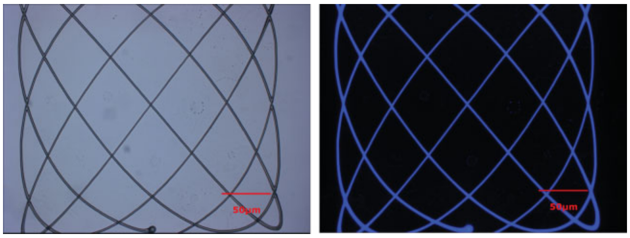

Figure 5. 4:5 Lissajous structure written in CHDV with 1 wt% T4 and low laser intensity 0.4 μW, resulting in a line width of 2.5 μm.

We have shown facile processability of the composite by direct laser writing, resulting in structures with tunable size down to 2.5 μm, smooth side walls, and high aspect ratios.

Experimental

Materials and Instruments: The oligofluorene truxene T4 was synthesized by A. L. K., I. F. P., and P. J. S., and the synthetic route can be found elsewhere [3]. CHDV and solvents were purchased from Sigma–Aldrich and used without further purification. *Para*-octyloxy-functionalized diphenyliodonium hexafluoroantimonate was purchased from ABCR.

UV-vis Absorption Spectroscopy: Spectra were taken using a Perkin Elmer Lambda 20 UV/Vis spectrophotometer. Deposited T4 films were recorded on a 1 mm thick quartz wafer spin-coated from a 20 mg mL^{-1} toluene solution at 1000 rpm. CHDV and T4/CHDV composites with 1 wt% PAG were drop-cast onto quartz wafers. Solutions were taken in toluene in a quartz cuvette of 10 mm path length.

Photoluminescence Spectroscopy: Spectra were recorded using a Perkin Elmer LS 50B fluorescence spectrometer in a quartz cuvette of 10 mm path length, and for the solid films from a quartz wafer. The same samples as for the UV-vis absorption analysis were used.

Microscopy Images: Microscopy images were taken using a CCD camera (Q-imaging Inc.) mounted onto an inverted fluorescent microscope (Nikon Eclipse TE2000-U) with a set of 10×/0.25NA, 20×/0.5NA Plan Flour objectives. Fluorescent images were taken using a UV-2A filter cube, to filter out the excitation source.

Scanning Electron Microscopy: For SEM imaging, carbon was evaporated onto the laser-written structures using a BAL-TEC CED 200 carbon evaporator, and the structures were examined using a FEI Sirion field-emission SEM.

Direct Laser Writing: The setup consisted of a GaN diode laser (15 mW @ 374 nm, circularized and collimated output beam with a spot size of 1 μm in diameter in the focal point) with a variable neutral density filter wheel, a mechanical shutter (minimum open time 10 ms), and a beam expander. A microscope objective (N.A. 0.4) was controlled by a piezo objective-translational stage (400 μm range, sub-nanometer precision). The sample was placed onto a *X*–*Y* sample-translation stage (25 mm × 25 mm range, $\sim$1 μm precision, 1.5 mm s^{-1} max speed). The system was controlled through a CCD camera imaging system and a control PC operating the shutter and stages.

Sample Preparation: Direct Laser Writing: For sample preparation, the borosilicate cover slides (near UV transparent) were thoroughly cleaned in a standard procedure using an ultrasonic bath in acetone and then methanol (3–5 min each). The cover glasses were then rinsed with deionized water, and subsequently treated in an isopropanol ultrasonic bath and rinsed again, dried with a spinner at 8 000 rpm for 30 s, and then left on a hotplate at $\sim$100 °C for at least 20 min. The composite is prepared by carefully weighing desired ratios of CHDV, PAG, and oligofluorene truxenes, and ultrasound is used to facilitate mixing and dispersion of the T4. The composite is pipetted into a shallow ($\sim$500 μm deep) 10 mm × 10 mm basin in a block of PTFE plastic. The clean cover glass is placed over the basin with care taken not to capture any air bubbles. The sample is placed under the objective. The writing was carried out by moving the sample while the shutter was open. The laser beam is static. After direct laser writing, the structures were developed by taking the cover slide from the plastic block and washing off in toluene for 5–10 s.

Acknowledgements

The authors gratefully acknowledge support by the EPSRC through a research grant (GR/T28379), a Basic Technology Programme grant (GR/S85764) and a Science & Innovation award. We thank Chang Xiong, Dr. P.R. Edwards and Prof. R.W. Martin for support with scanning electron microscopy. Supporting Information is available online from Wiley InterScience or from the author.

Received: September 8, 2008
Revised: October 28, 2008

---

[1] a) L. Pang, K. Tetz, Y. Shen, C.-H. Chen, Y. Fainman, *J. Vac. Sci. Technol. B* **2005**, *23*, 2413. b) A. C. Balazs, T. Emrick, T. P. Russell, *Science* **2006**, *314*, 1107. c) C. Ingrosso, V. Fakhfouri, M. Striccoli, A. Agostiano, A. Voigt, G. Gruetzner, M. L. Curri, J. Brugger, *Adv. Funct. Mater.* **2007**, *17*, 2009.

[2] J. A. DeFranco, B. S. Schmidt, M. Lipson, G. G. Malliaras, *Org. Electron.* **2006**, *7*, 22.

[3] a) A. L. Kanibolotsky, R. Berridge, P. J. Skabara, I. F. Perepichka, D. D. C. Bradley, M. Koeberg, *J. Am. Chem. Soc.* **2004**, *126*, 13695. b) M. M. Olivia, J. Casado, J. T. L. Navarrete, P. J. Skabara, A. L. Kanibolotsky, I. F. Perepichka, *J. Phys. Chem. B* **2007**, *111*, 4026.

[4] a) S. Fung, S. C. Moratti, S. C. Graham, R. H. Friend, *Synth. Met.* **1999**, *102*, 1167. b) D. Rehm, A. Weller, *Isr. J. Chem.* **1970**, *8*, 259. c) K. Meerholz, C.-D. Müller, O. Nuyken, in *Organic Light-Emitting Devices – Synthesis, Properties, and Applications*, (Eds: K. Müllen, U. Scherf), Wiley-VCH, Weinheim, Germany **2006**, Ch. 9.

[5] M Fakis,, D. Anestopoulos, V. Giannetas, P. Persephonis, *J. Phys. Chem. B* **2006**, *110*, 24897.

[6] a) A. R. Mackintosh, A. J. C. Kuehne, R. A. Pethrick, B. Guihabert, E. Gu, C. L. Lee, M. D. Dawson, G. Heliotis, D. D. C. Bradley, *J. Phys. D* **2008**, *41*, 094007. b) R. A. Pethrick, A. R. Mackintosh, A. J. C. Kuehne, E. Gu, M. D. Dawson, *British Patent* GB0623936.2, **2006**.

[7] T.-Q. Nguyen, V. Doan, B. J. Schwartz, *J. Chem. Phys.* **1999**, *110*, 4068.

[8] a) R. de Bettignies, Y. Nicholas, P. Blanchard, E. Levillain, J.-M. Nunzi, J. Roncali, *Adv. Mater.* **2003**, *15*, 1939. b) A. Petrella, J. Cremer, L. De Cola, P. Bäuerle, R. M. Williams, *J. Phys. Chem. A* **2005**, *109*, 11687. c) J. Cremer, P. Bäuerle, *J. Mater. Chem.* **2006**, *16*, 874.

[9] a) E. Zojer, A. Pogantsch, E. Hennebicq, D. Beljonne, J. L. Bredas, P. S. de Freitas, U. Scherf, E. J. W. List, *J. Chem. Phys.* **2002**, *117*, 6794. b) X. Gong, D. Moses, A. J. Heeger, S. Xiao, *Synth. Met.* **2004**, *141*, 17.

[10] E. Gu, H. X. Zhang, H. D. Sun, M. D. Dawson, A. R. Mackintosh, A. J. C. Kuehne, R. A. Pethrick, C. Belton, D. D. C. Bradley, *Appl. Phys. Lett.* **2007**, *90*, 031116.

[11] C. Decker, C. Bianchi, D. Decker, F. Morel, *Prog. Org. Coat.* **2001**, *42*, 253.

Mask-less ultraviolet photolithography based on CMOS-driven micro-pixel light emitting diodes

D. Elfström[1], B. Guilhabert[1], J. McKendry[1], S. Poland[1], Z. Gong[1], D. Massoubre[1], E. Richardson[1], B. R. Rae[2], G. Valentine[1],G. Blanco-Gomez[3], E. Gu[1*], J.M. Cooper[3], R.K. Henderson[2], and M.D. Dawson[1]

[1]*Institute of Photonics, University of Strathclyde, Glasgow G4 0NW, UK*
[2]*Institute for Integrated Micro and Nano Systems, University of Edinburgh, Edinburgh EH9 3JL, UK*
[3]*Dept. of Electronics and Electrical Engineering, University of Glasgow, Glasgow G12 8LT, UK*
**erdan.gu@strath.ac.uk*

Abstract: We report on an approach to ultraviolet (UV) photolithography and direct writing where both the exposure pattern and dose are determined by a complementary metal oxide semiconductor (CMOS) controlled micro-pixellated light emitting diode array. The 370nm UV light from a demonstrator 8 x 8 gallium nitride micro-pixel LED is projected onto photoresist covered substrates using two back-to-back microscope objectives, allowing controlled demagnification. In the present setup, the system is capable of delivering up to 8.8W/cm^2 per imaged pixel in circular spots of diameter ~8μm. We show example structures written in positive as well as in negative photoresist.

OCIS codes: (110.3960) Microlithography; (230.3670) Light-emitting diodes; (220.4000) Microstructure fabrication

References and links

1. S. P. A. Fodor, J. L. Read, M. C. Pirrung, L. Stryer, A. T. Lu, and D. Solas, “Light-directed, spatially addressable parallel chemical synthesis,” Science **251**(4995), 767–773 (1991).
2. C. Rensch, S. Hell, M. Schickfus, and S. Hunklinger, “Laser scanner for direct writing lithography,” Appl. Opt. **28**(17), 3754 (1989).
3. R. M. Guijt, and M. C. Breadmore, “Maskless photolithography using UV LEDs,” Lab Chip **8**(8), 1402–1404 (2008).
4. T. Naiser, T. Mai, W. Michel, and A. Ott, “Versatile maskless microscope projection photolithography system and its application in light-directed fabrication of DNA microarrays,” Rev. Sci. Instrum. **77**(6), 063711 (2006).
5. G. P. Watson, V. Aksyuk, M. E. Simon, D. M. Tennant, R. A. Cirelli, W. M. Mansfield, F. Pardo, D. O. Lopez, C. A. Bolle, A. R. Papazian, N. Basavanhally, J. Lee, R. Fullowan, F. Klemens, J. Miner, A. Kornblit, T. Sorsch, L. Fetter, M. Peabody, J. E. Bower, J. S. Weiner, and Y. L. Low, “Spatial light modulator for maskless optical projection lithography,” J. Vac. Sci. Technol. B **24**(6), 2852 (2006).
6. C. W. Jeon, E. Gu, and M. D. Dawson, “Mask-free photolithographic exposure using a matrix-addressable micropixellated AlInGaN ultraviolet light-emitting diode,” Appl. Phys. Lett. **86**(22), 221105 (2005).
7. H. X. Zhang, D. Massoubre, J. McKendry, Z. Gong, B. Guilhabert, C. Griffin, E. Gu, P. E. Jessop, J. M. Girkin, and M. D. Dawson, “Individually-addressable flip-chip AlInGaN micropixelated light emitting diode arrays with high continuous and nanosecond output power,” Opt. Express **16**(13), 9918–9926 (2008).
8. J. McKendry, B. R. Rae, Z. Gong, K. R. Muir, B. Guilhabert, D. Massoubre, E. Gu, D. Renshaw, M. D. Dawson, and R. K. Henderson, “Individually-Addressable AlInGaN Micro-LED Arrays with CMOS Control and Sub-Nanosecond Output Pulses,” IEEE Photon. Technol. Lett. **21**(12), 811–813 (2009).
9. A. Tan, K. Rodgers, J. P. Murrihy, C. O?Mathuna, and J. D. Glennon, “Rapid fabrication of microfluidic devices in poly(dimethylsiloxane) by photocopyingPresented at the 14th International Symposium on Microscale Separations and Analysis, Boston, January 13?18, 2001,” Lab Chip **1**(1), 7 (2001).
10. W. K. T. Coltro, E. Piccin, J. A. Fracassi da Silva, C. Lucio do Lago, and E. Carrilho, “A toner-mediated lithographic technology for rapid prototyping of glass microchannels,” Lab Chip **7**(7), 931–934 (2007).
11. M. H. Sorouraddin, M. Amjadi, and M. Safi-Shalamzari, “Simple and rapid methods for the fabrication of polymeric and glass chips for using in analytical chemistry,” Anal. Chim. Acta **589**(1), 84–88 (2007).
12. G. M. Atkinson, F. P. Stratton, R. L. Kubena, and J. C. Wolfe, “30 nm resolution zero proximity lithography on high-Z substrates,” J. Vac. Sci. Technol. B **10**(6), 3104–3108 (1992).
13. T. A. Savas, M. L. Schattenburg, J. M. Carter, and I. Henry, “Smith, “Large-area achromatic interferometric lithography for 100 nm period gratings and grids,” J. Vac. Sci. Technol. B **14**(6), 4167–4170 (1996).
14. T. Sandstrom, A. Bleeker, J. Hintersteiner, K. Troost, J. Freyer, and K. van der Mast, “OML: optical maskless lithography for economic design prototyping and small-volume production,” Proc. SPIE **5377**, 777 (2004).

15. N. Choksi, D. S. Pickard, M. McCord, R. F. W. Pease, Y. Shroff, Y. Chen, W. Oldham, and D. Markle, "Maskless extreme ultraviolet lithography," J. Vac. Sci. Technol. B **17**(6), 3047–3051 (1999).
16. D. Gil, R. Menon, and H. I. Smith, "The case for diffractive optics in maskless lithography," J. Vac. Sci. Technol. B **21**(6), 2810–2814 (2003).
17. X. Sun, D. Yin, H. Dai, J. Liu, R. Lu, and S. T. Wu, "Intermittent curing and its effect on pulsed laser-induced photopolymerization," Appl. Phys. B **92**(1), 93–98 (2008).
18. H. Xu, J. Zhang, K. M. Davitt, Y.-K. Song, and A. V. Nurmikko, "Applications of blue-green and ultraviolet micro-LEDs to biological imaging and detection," J. Phys. D Appl. Phys. **41**(9), 094013 (2008).

1. Introduction

Photolithography is the preferred method of micro-patterning, not only in electronics manufacturing but also in such emerging areas as micro-electromechanical systems (MEMS), micro-fluidics and 'digital optical chemistry' [1]. The process normally requires a custom-produced hard photo-mask to be manufactured, which is expensive, time consuming, and often limits flexibility. Much research has therefore gone into developing mask-less photolithographic methods for rapid prototyping, e.g. laser direct writing [2] which is now a commercial technique. Other mask-less approaches also under development include projection writing using a single spatially filtered light emitting diode (LED) [3], and various spatial light modulator (SLM) and digital light projector (DLP) based methods [4,5].

Micro-pixelated gallium nitride LED's ('micro-LEDs'), consisting of arrays of individually addressable micrometer-sized light emitting pixels, are being investigated by several groups for applications in areas including micro-displays, bioscience and instrumentation. These devices offer spatio-temporal control of the emission pattern, and also spectrally selective excitation because the emission bandwidth is typically narrow (~15nm full-width at half maximum (FWHM)), with the central wavelength being defined by the semiconductor epitaxy of the light-emitting quantum wells. Indeed, in a preliminary demonstration [6] we were able to show some simple micrometer-sized exposure patterns in photoresist achieved by a 'first generation' array designed to operate at an approximately *i*-line photolithography wavelength (365nm). More recently, the technology has advanced to the point where much higher powers are available per pixel through flip-chip bonding of the devices [7] and independent element addressing by custom CMOS control circuitry is possible [8].

Here we explore the implications for mask-free photolithography and other forms of optical direct-write patterning engendered by these recent developments. A CMOS-controlled 8 x 8 flip-chip 370nm gallium nitride-based micro-LED array demonstrator is de-magnified through various combinations of back-to-back microscope objectives. The CMOS is shown to be capable not only of controlling the emission pattern, but also the exposure dose. We show example structures written in positive as well as in negative photoresist. The system can be used to directly reproduce the pattern on the micro-LED array and/or lines can be written by moving the sample while one or several LED pixels are turned on. Our system can be considered to bridge the gap between low cost, but low resolution, mask-less prototyping techniques, such as the use of a photocopier [9], toner mediated lithography [10], or etching through a mask made using a cutter plotter [11] (feature size limited to over 200µm) and high cost methods competing with traditional optical projection lithography (OPL) in terms of resolution, such as scanning electron-beam lithography (SEBL), focused ion-beam (FIB) lithography [12], interference lithography (IL) [13], maskless optical-projection lithography (MOPL) [14,15], and zone-plate-array lithography (ZPAL) [16].

2. CMOS-bonded flip-chip micro-LED array

The AlInGaN quantum well micro-LED devices are based on 370nm-emitting epitaxial wafers and are designed for flip-chip bonding. They consist of a 16 x 16 array of individually-addressable micro-disk pixels, each 72µm in diameter on a 100µm center-to-center pitch. The sapphire (epitaxial substrate) side was polished and the substrate was diced into individual device chips of approximately 3x3mm^2, of which the active area is 1.6x1.6mm^2. A bump bonding process was used to electrically and physically contact these chips to a custom-designed CMOS control device in the manner reported recently [8], such that alternate pixels were operable, thus giving a light-emitting 8 x 8 array [Fig. 1(a)]. This was done due to the bump bonding process, which currently limits the pixel to pixel pitch to ~200µm.

The CMOS device permits continuous wave (CW) operation of the individual micro-pixels, square wave and pulsed operation [8]. In CW operation, we measured a single bare pixel to deliver an optical power of up to 604µW at a driving current of 80.0mA (340µW at 20mA) at 370nm. The frequency of the square wave (the repetition rate in pulsed mode) can be set by the on-chip voltage-controlled oscillator (VCO) from 6MHz to 800MHz. With the external clock facility any frequency can be chosen. In pulsed mode the duration of the pulses can be controlled, ranging from 300ps to 40ns.

The spectral characteristic in CW operation at 27mA, measured after the imaging, confirms that it is close to Hg *i*-line operation (peak at 370nm with a FWHM of 15nm).

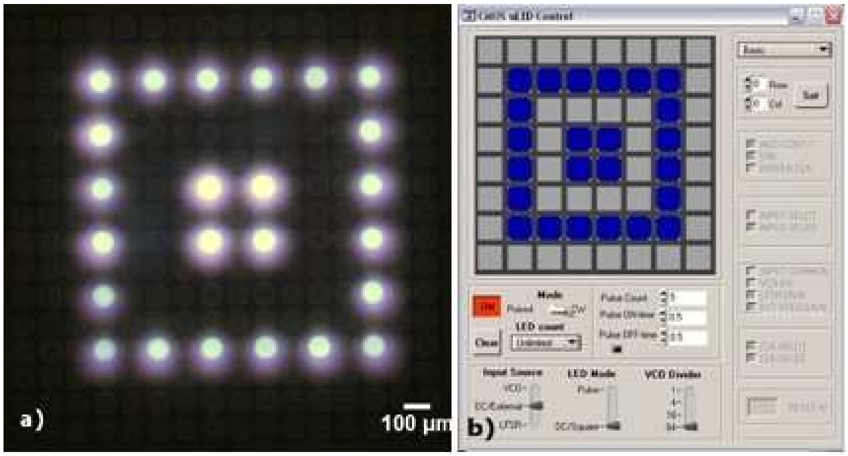

Fig. 1. (a) CMOS driven micro-LED device with pixels turned on to show a representative double square pattern, and (b) the computer control interface as the pattern in (a) is addressed.

The CMOS control device was attached to a printed circuit board (PCB), which is computer controlled via a field programmable gate array (FPGA) board (XEM3010-1000 from Opal Kelly). In the custom-made software interface, shown in Fig. 1(b), the mode of operation of the CMOS chip can be set to linear feedback shift register (LFSR, not used in this work), DC/External (if no external clock is present this is CW operation), or VCO. The LED mode can be set to either DC/Square (CW operation or a square wave clocked to the external or VCO frequency) or Pulse (pulse at a controllable duration with the repetition rate set by external or VCO frequency). The VCO divider sets a value (1, 4, 16, or 64) with which the VCO frequency is divided before it is used. A pixel or a pattern consisting of a set of pixels can be chosen either by setting the row and column [upper right corner in Fig. 1 (b)] or by highlighting the desired pixels in the grid pattern of the software interface. With the timing control the LED on-time can be set accurately down to ~100ms

3. The setup

A photographic image and a corresponding schematic of the setup for mask-less photolithography can be seen in Fig. 2. The setup consists of the CMOS driven computer controlled micro-LED device mounted vertically on a manual XYZ stage, a horizontally-mounted infinity-corrected microscope objective (Nikon CFI Plan Fluor Series) for light collection (collection objective), a mirror to direct the light downwards, a 50-50 UV beam-splitter cube, and a second (vertical) infinity-corrected microscope objective (projection objective), mounted on a Z-translation stage, to project the LED array image onto the sample. A CCD camera (Prosilica EC650C) with zoom lens attachment (Navitar, 11-110mm) adjusted to focus at infinity is used to monitor the position of the sample or the LED array depending on the orientation of the beam-splitter. Infinity-corrected objectives give collimated (or parallel) output beams of the object in the focal plane, hence when the camera objective is set to focus at infinity, the image displayed on the camera is optically conjugate to the focal plane of each objective.

A piezo-driven stage (PI P-725.4CD) for the Z-translation of the projection microscope objective gives a very accurate (100nm resolution with current driver and feedback measuring system) control of the focus on the sample. The sample is placed on an XY stage (2 x PI M-112.1DG) allowing for large areas (up to 25x25mm^2) to be patterned. The computer control allows for movement of the sample in any pre-defined pattern at a maximum velocity of 1.5mm/s and with a repeatability of ~1µm.

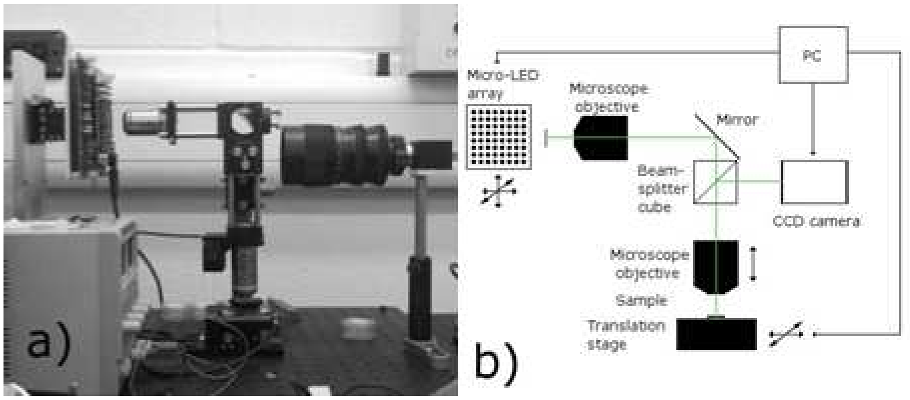

Fig. 2. A photograph of the micro-projection setup (a) and schematic of the same (b).

The two objectives can be changed to give the capability of magnifying or de-magnifying the projected spots from the LED pixels. A range of microscope objectives with magnifications from 4X to 40X gives theoretical spot-sizes from 7.2µm (4X collection objective and 40X projection objective) to 720µm (40X collection objective and 4X projection objective) when projecting the 72µm diameter pixels of the micro-LED device. In Fig. 3, four pixels can be seen through the 4X collection objective [Fig. 3(a)] and reflected off a mirror placed at the sample position through the 40X collection objective [Fig. 3(b)], showing how the system can demagnify the illuminated spot.

4. Characterization of the system

To characterize the performance of the system, the optical power *per pixel* delivered at the sample was measured by placing a calibrated UV optical power meter (Coherent FieldMax Top) at the sample position. The total projected power was measured to be 140µW with the 40X collection objective and 4.4µW with the 4X collection objective, all obtained at a CMOS drive current of ~27mA. The projected powers are independent of the projection objective as the transmission losses are low and very similar for this type of objective. The measurements also indicate that there are only small transmission losses in the overall system (approximately less than 4%), except for the beam-splitter where ~50% of the power is lost.

Projected spot-sizes are determined by imaging a reflection off a mirror placed at the sample position. By using the high precision Z-translation stage the projection objective was translated to match the focal plane to the reflective surface of the mirror. From the thus acquired images, intensity profiles were taken of the projected spots and the FWHM values were measured of the profiles. An example image, of the reflection from a mirror at the sample position, is shown in Fig. 3(b). The intensity profile through the centre of the two top spots in Fig. 3(b), is shown in Fig. 3(c). In this particular case, the 4X collection objective and the 40X projection objective were used, giving spot sizes of approximately 8µm FWHM. The form of the intensity profile is determined by the emission pattern from the light emitting pixel and typically has brighter edges, attributed to sidewall scatter in the emitting pixels. This feature, although unintended, is actually beneficial when exposing photoresist as it gives better defined feature edges compared to the case with a Gaussian intensity profile.

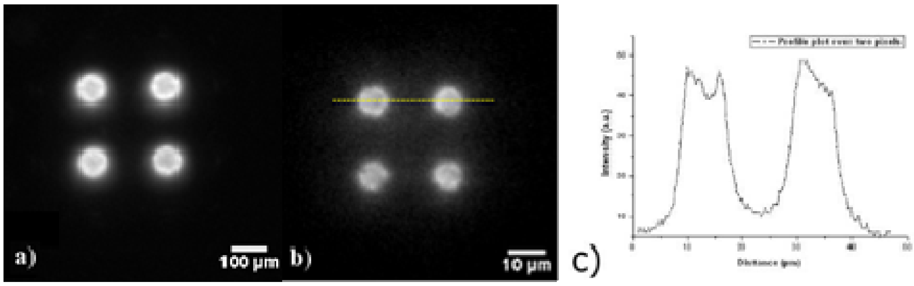

Fig. 3. Four LED pixels turned on., (a) on the device itself and (b) reflection off a mirror at the sample position, showing the focal spot size at the applications plane. The dashed line corresponds to the trace of the intensity profile plotted in (c).

By combining the spot-size measurements with the power measurements for various combinations of objectives, the intensity values presented in Table 1 were obtained. The maximum power density value of 8.8W/cm^2 permits the required exposure dose for most photoresist types to be reached in fractions of a second (e.g. 46ms for an exposure dose of 400mJ/cm^2).

Table 1. Intensities delivered by different collection and projection objectives. Image plane spot sizes measured in FWHM are in parentheses. Spot sizes have also been established by measurements in exposed photoresist and the errors in the measurements below are determined to be less than ± 10% throughout.

Collection objective\ Projection objective	4X	10X	20X	40X
4X	88mW/cm^2 (80µm)	0.51W/cm^2 (33µm)	1.7W/cm^2 (18µm)	8.8W/cm^2 (8.0µm)
40X	25mW/cm^2 (850µm)	0.16W/cm^2 (330µm)	0.61W/cm^2 (170µm)	3.3W/cm^2 (73µm)

The 4X collection objective has a larger field of view (~4mm), but it also has a lower N.A. which means it has a lower collection angle. This allows for the whole micro-LED device (1.6x1.6mm^2) to be imaged at once, but with the trade-off of lower light collection. Despite this, the highest optical power density is achieved using the 4X collection/40X projection objective combination. When calculating the power densities, all power was assumed to be uniformly distributed within the spot diameter [c.f. ‘flat top’ beam profiles in Fig. 3(c)]. Dosage energy is given by multiplying the optical power by the exposure time. When the sample is moving the dosage curve is given by

$$E = \frac{2P}{\pi R^2 v}\sqrt{R^2 - y^2},$$

where P is the total power, R the pixel radius, v the velocity, and y (≤R) the coordinate perpendicular to the velocity, i.e. a half-circular dosage curve.

The measurements presented above are all made under CW (DC driven) operation, however the CMOS driver provides the capability to use pulses for exposure. By adjusting the length of each pulse at a given repetition rate, effectively changing the duty cycle to the LED pixel, the projected optical output can be accurately controlled. Figure 4 shows how the average projected optical power varies with pulse duration from 0.5ns to 40ns at an example fixed repetition rate of 9.75MHz. The power scales linearly, but the pulsed driving of the LED allows us to explore the intermittent curing behaviour of photoresists [17]. This feature of the CMOS driver can also, in principle, be used to correct differences in output power between pixels and to compensate for collection efficiency variations over the field of view.

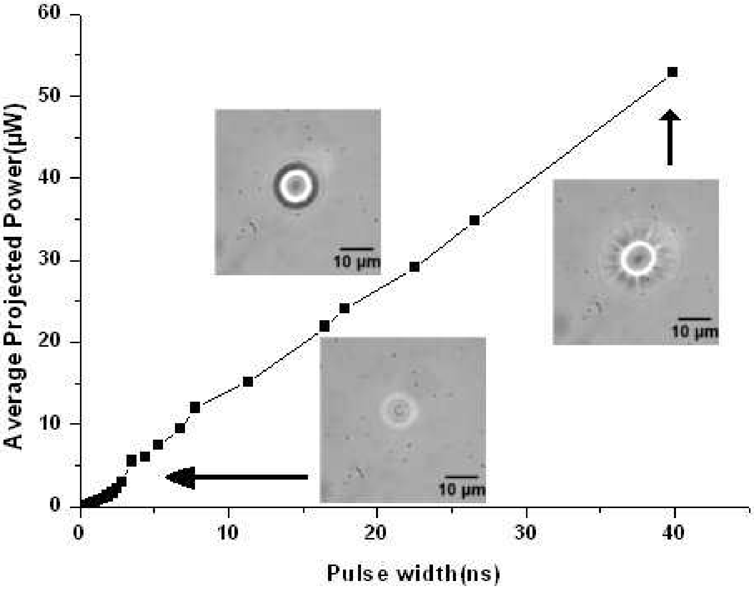

Fig. 4. The relationship between average projected power and pulse width is linear for long enough pulses. Repetition rate = 9.75 MHz throughout. The insets are optical micrographs of exposed dots in NOA81 negative photoresist on glass substrates exposed for 40s at 5ns, 20ns and 40ns pulse width. The spot diameters are 11µm, 17µm and 24µm, respectively.

5. Patterning experiments

To test the micro-lithography system, a number of different ‘demonstrator’ patterns were produced in positive as well as in negative photoresist. An optical adhesive from Norland (NOA81) was chosen for the negative type photoresist because of its excellent adhesion to glass and relatively low viscosity, allowing thin films to be spun on substrates and hence offering the possibility of feature a few µm in size. The optical adhesive has a spectral peak sensitivity at 365nm and the manufacturer’s recommended dose for full cure is 2J/cm^2. In preparation, substrates of borosilicate glass were cleaned thoroughly in an ultrasonic bath with acetone and subsequently methanol. They were then rinsed in deionised (DI) water and dried on a hotplate at 110°C for at least 20 minutes. NOA81 was then spin-coated at 8000 rpm for 40s, resulting in a film thickness of 1.7µm as measured by a stylus (DekTak) profilometer on cured structures. The substrate with the Norland film was placed on the XY stage and then exposed by the UV light from the micro-LED device projected through the setup. Directly after the exposure, the development was done by immersing the substrate in acetone for 1 minute. The substrate was cleaned of acetone and polymer residue in running methanol and subsequently in running DI water. The ‘IoP’ logo in Fig. 6(a) is used as a demonstrator pattern. The ‘I’ and the ‘P’ were exposed with square wave addressing for 8s while the ‘o’ was exposed for 4s, giving an average exposure dose of 10J/cm^2 for each dot. This variation is due to the collection efficiency decreasing as the distance from the centre of the imaging area increases, which we note can be corrected for directly by the CMOS control. Small variations in exposure dose exist because pixel to pixel uniformity is not perfect. These issues can also, however, in principle be compensated for by adjusting the CMOS control duty cycle for each individual pixel.

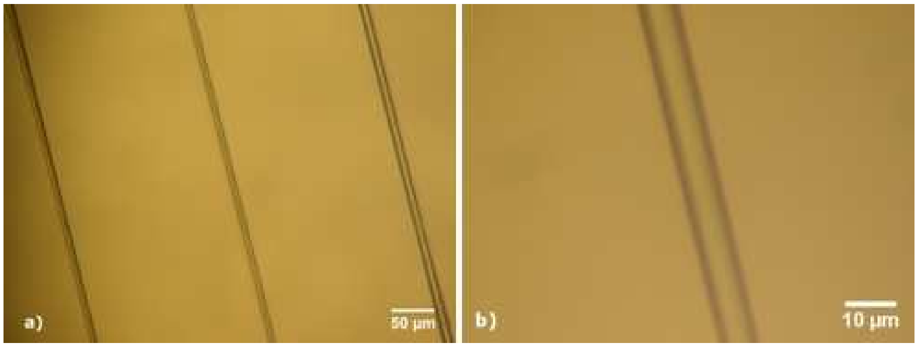

Fig. 5. (a) Three lines in NOA81 written in, respectively, CW mode, with 50ns pulses and with 40ns pulses at a velocity of 5µm/s. Widths are 11µm, 8µm and 8µm respectively. (b) Close up on the middle line showing good uniformity of the line width.

Further curing experiments in NOA81 were performed under pulsed operation of the LED device. By varying the pulse width from 5ns to 40ns, and hence the exposure dose from 16.4J/cm^2 to 120J/cm^2, spot-sizes ranging from 11µm to 24µm diameter were written with an exposure time of 40s. A selection of these written dots is shown as insets in Fig. 4. Lines in NOA81 were also written under pulsed operation, as well as in CW. The lines shown in Fig. 5(a) were exposed with a maximum dose, in the middle of the line, of 14.7J/cm^2, 6.0J/cm^2, and 5.4J/cm^2 going from right to left, corresponding to line widths of 11µm, 8µm, and 8µm respectively. The height of the lines was determined to be 1.7µm (i.e. curing the full thickness of the film), 0.9µm, and 0.9µm, by a stylus (Dektak) profilometer. The uniformity of the cured lines is good and shows no bulging or other variations.

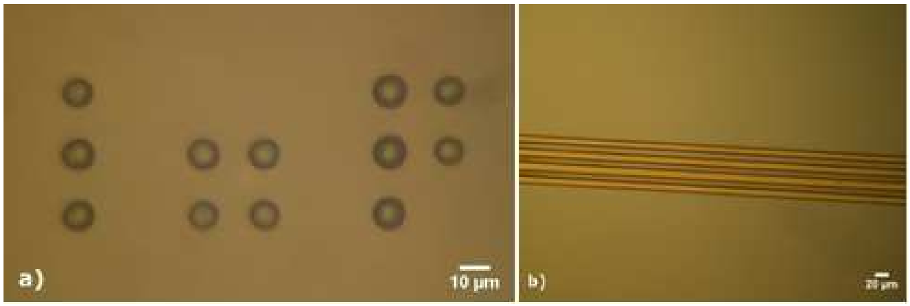

Fig. 6. (a)'IoP' (Institute of Photonics) pattern in NOA81. The exposed dots are 8-9µm in diameter. (b) Four parallel channels written in Microposit S1805 photoresist at a velocity of 100µm/s. Lines are 9-11µm wide. The two different patterns were chosen to show the static and dynamic writing capability of the system.

For the positive photoresist features as shown in Fig. 6(b), a standard photoresist, Microposit S1805 from Shipley, was used. It is optimized for *g*-line (436nm) exposure, but works well for exposure wavelengths down to 350nm. Recommended exposure dose at the *g*-line is 150mJ/cm^2. Silicon substrates were cleaned thoroughly in an ultrasonic bath with acetone and subsequently methanol. They were then rinsed in DI water and dried on a hotplate at 110°C for at least 20 minutes. The photoresist was spun at 2000 rpm for 30s. The substrate with the 0.7µm thick film was then placed on a hotplate at 120°C for 1 minute to soft-bake the photoresist prior to being exposed. After the exposure, development was completed using a micro-developer solution (Microposit 1:1 volume ratio with deionised water). The substrate was immersed and gently moved around in the solution for a duration of 1 minute. Residue developer was washed off with DI water. The four "channels" seen in Fig. 6(b) are written by turning on four individual pixels (each delivering an optical power of ~2.5µW to the sample) in one column of the micro-LED array while moving the sample at a velocity of 100µm/s. This corresponds to a maximum exposure dose, in the middle of each channel, of ~400mJ/cm^2.

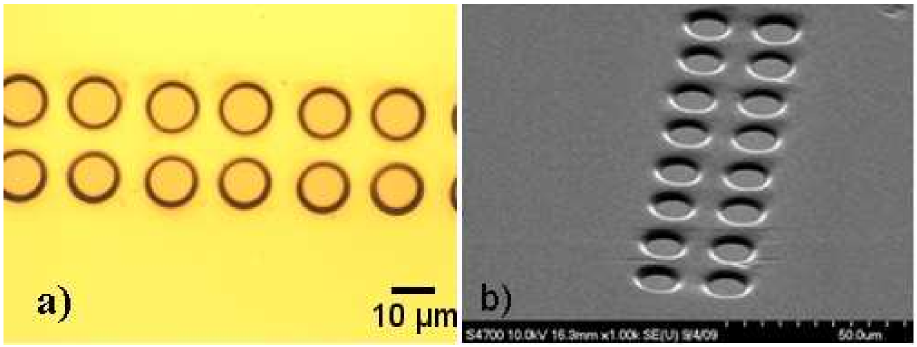

Fig. 7. (a) Micrograph showing an array of exposed dots in S1818, each with a diameter of ~9µm. (b) Oblique SEM image of the same array, showing well defined sidewalls and good dot to dot uniformity.

As a further demonstration patterns were written in a thicker positive type photoresist, Microposit S1818 from Shipley. Glass substrates were cleaned in a similar manner to previous samples and were subsequently covered with a ~2.0µm thick layer photoresist by spincoating. The samples were then exposed simultaneously by four pixels for the duration of 2s in pulsed mode, giving an exposure dose of 1.1J/cm^2. The sample was then translated 40µm and an other exposure was performed. This was repeated four times and followed by a development step as described above. The resulting pattern is shown in Fig. 7. The scanning electron microscope (SEM) image in Fig. 7(b) was taken by a Hitachi S4700 in ultra high resolution mode and confirms that we have well defined patterns with close to vertical sidewalls.

6. Conclusion

By combining novel CMOS driven micro-LED arrays with a projection system, we have built a versatile computer-controlled micro-photolithography tool capable of writing features down to ~8µm in positive and negative photoresist. It is capable of simultaneously exposing multiple spots and has, through the CMOS driving mechanism, facility to precisely control the dose delivered during a determined period of time as well as capability to correct for non-uniform exposure across the field of view. This type of system offers attractive prospects for many areas of direct write photo-patterning and patterned photo-stimulation, including polymer microstructuring, mask-less photolithography, digital optical chemistry, microfluidic systems and optogenetics [18]. Our demonstrator establishes a baseline capability, but offers considerable scope for further scaling and refinement. Wavelengths from deep ultraviolet to violet can readily be chosen for spectrally selective excitation and we have developed flip-chip devices of pixel diameter 5-10µm, where there is a separate bond-pad for each pixel for “off-pixel” bump bonding to CMOS. When incorporated into the system at 10:1 de-magnification, we anticipate being able to create 8 x 8 arrays capable of writing features down to ~1um. There is the prospect of further scaling of the number of CMOS controlled pixels.

Acknowledgements

We acknowledge support under an EPSRC Science and Innovation programme on “Molecular Nanometrology”, the EPSRC “HYPIX” programme, from the EU (PHOTOLYSIS - LSHM-CT-2007-037765) and the Scottish Consortium in Integrated Microphotonic Systems.

Integration by self-aligned writing of nanocrystal/epoxy composites on InGaN micro-pixelated light-emitting diodes

B. Guilhabert[1*], D. Elfström[1], A. J. C. Kuehne[2], D. Massoubre[1], H. X. Zhang[1], S. R. Jin[1], A. R. Mackintosh[2], E. Gu[1], R. A. Pethrick[2] and M. D. Dawson[1]

[1] *Institute of Photonics, University of Strathclyde, Glasgow G4 0NW, UK*
[2] *WestCHEM, Department of Pure and Applied Chemistry, University of Strathclyde, Glasgow G1 1XL, UK*
[*] Corresponding author: benoit.guilhabert@strath.ac.uk

Abstract: We report on the integration of monodisperse semiconductor nanocrystal (NC) color converters onto gallium nitride ultraviolet micro-pixelated light-emitting diodes ('micro-LEDs'). Integration is achieved in a 'self-aligned' process by forming a nanocomposite of the respective NCs in a photocurable epoxy polymer. Blue, green, yellow and red NC/epoxy blend microstructures have been successfully integrated onto micro-pixelated LEDs by this technique and utilised for color conversion, resulting in a five color emission single chip. Optical output power density of up to about 166mW/cm^2 is measured; spectral emission at 609nm gives an estimated optical-to-optical conversion as high as 18.2% at 30mA driving current.

OCIS codes: (250.5590) Quantum-well, -wire and -dot devices; (230.3670) Light-emitting diodes; (230.3990) Micro-optical devices; (220.4000) Microstructure fabrication; (160.5470) Polymers.

References and links

1. W. J. Parak, T. Pellegrino, and C. Plank, "Labelling of cells with quantum dots," Nanotechnol. **16**, 9-25 (2005).
2. L. Yan, J. Y. Zhang, Y. Cui, and Y. Qiao, "Voltage-dependent electroluminescence from colloidal CdSe/ZnS quantum dots," Appl. Phys. Lett. **91**, 243114 (2007).
3. Q. Sun, Y. A. Wang, L. S. Li, D. Wang, T. Zhu, J. Xu, C. Yang, and Y. Li, "Bright, multicoloured light-emitting diodes based on quantum dots," Nature Photon. **1**, 717-722 (2007).
4. D. R. Larson, W. R. Zipfel, R. M. Williams, S. W. Clark, M. P. Bruchez, F. W. Wise, and W. W. Webb, "Water-soluble quantum dots for multiphoton fluorescence imaging in vivo," Science **300**, 1434-1436 (2003).
5. M. Q. Zhu, E. Chang, J. Sun, and R. A. Drezek, "Surface modification and functionalization of semiconductor quantum dots through reactive coating of silanes in toluene," J. Mater. Chem. **17**, 800-805 (2007).
6. L. Pang, K. Tetz, Y. Shen, C. H. Chen, and Y. Fainman, "Photosensitive quantum dot composites and their applications in optical structures," J. Vac. Sci. Technol. B **23**, 2413-2418 (2005).
7. L. Pang, Y. Shen, K. Tetz, and Y. Fainman, "PMMA quantum dots composites fabricated via use of pre-polymerisation," Opt. Express. **13,** 44-49 (2005).
8. Y. M. Shen, L. Pang, Y. Fainman, M. Griswold, S. Yang, L. V. Butov, and L. J. Sham, "Photoluminescence spectral switching of single CdSe/ZnS colloidal nanocrystals in poly(methyl methacrylate)," Phys. Rev. B. **76**, 085312 (2007).
9. H. Wang, K. S. Lee, J- H. Ryu, C. H. Hong, and Y. H. Cho, "White light emitting diodes realized by using an active packaging method with CdSe/ZnS quantum dots dispersed in photosensitive epoxy resins," Nanotechnol. **19**, 145202 (2008).
10. K. N. Hui, P. T. Lai, and H. W. Choi, "Spectral conversion with fluorescent microspheres for light-emitting diodes," Opt. Express. **16**, 13-18 (2008).
11. E. Gu, H. X. Zhang, H. D. Sun, M. D. Dawson, A. R. Mackintosh, A. J. C. Kuehne, R. A. Pethrick, C. Belton, and D. D. C. Bradley, "Hybrid inorganic/organic microstructured light-emitting diodes produced using photocurable polymer blends," Appl. Phys. Lett. **90**, 031116 (2007).
12. S. X. Jin, J. Li, J.Z. Li, J. Y. Lin, and H. X. Jiang, "GaN microdisk light-emitting diodes," Appl. Phys. Lett. **76**, 631 (2000).

#100149 - $15.00 USD Received 14 Aug 2008; revised 9 Oct 2008; accepted 14 Oct 2008; published 3 Nov 2008

13. M. D. Dawson and M. A. A. Neil, eds., "Cluster issue on 'Micro-pixellated LED's for science and instrumentation'" J. Phys.D: Appl. Phys. **41**, (2008).
14. H. X. Zhang, D. Massoubre, J. McKendry, Z. Gong, B. Guilhabert, C. Griffin, E. Gu, P. E. Jessop, J. M. Girkin, and M. D. Dawson, "Individually-addressable flip-chip AlInGaN micropixelated light emitting diode arrays with high continuous and nanosecond output power," Opt. Express **16**, 9918-9926 (2008).
15. L. G. Krzewina and M. K. Kim, "Single-exposure optical sectioning by color structured illumination microscopy," Opt. Lett. **31**, 477-479 (2006).
16. V. Poher, H. X. Zhang, G. T. Kennedy, C. Griffin, S. Oddos, E. Gu, D. S. Elson, J. M. Girkin, P. M. W. French, M. D. Dawson, and M. A. A. Neil, "Optical sectioning microscopes with no moving parts using a microstripe array light-emitting diode," Opt. Express **15**, 11196-11206 (2007).
17. H. X. Zhang, E. Gu, C. W. Jeon, Z. Gong, M. D. Dawson, M. A. A. Neil, and P. M. W. French, "Microstripe array InGaN light-emitting diodes with indicidually addressable elements," IEEE Photon. Technol. Lett. **18**, 1681-1683 (2006).
18. X. Sun, D. Yin, H. Dai, J. Liu, R. Lu, and S- T. Wu, "Intermittent curing and its effect on pulsed laser-induced photopolymerisation," Appl. Phys. B **92**, 93-98 (2008).

1. Introduction

Colloidal semiconductor nanocrystals (NCs) have been widely reported in recent years for applications including selective biological labeling [1] and optoelectronics [2,3]. The most-studied NCs have been those with a CdSe core and a ZnS shell, which can be surface-functionalised, and tailored by varying their mean size to give narrow photoluminescence (PL), sharp excitonic absorption and high quantum yields across the visible spectrum. Usually they are dispersed in a solvent such as toluene, chloroform or water [4]; however, for many applications such as optoelectronics the NCs are required in solid film phase. Polymers are attractive candidates to be blended with NCs for such applications as they are easily processable materials and are readily transparent in the near UV and visible region provided they do not quench the NC luminescence and keep them in a uniform distribution. Surface modification can be applied to make the NCs compatible with most relevant organic materials [5], but poly(methyl methacrylate) (PMMA) was first reported as a matrix for as-received NCs [6]. Spectral shifting in the photoluminescence was a major drawback in the latter case which has subsequently been addressed using a pre-polymerized polymer [7,8]. In recent developments, epoxy resins have also been used as matrices with single-wavelength or mixed NCs to realise encapsulating color converters for light-emitting diodes (LEDs) [9]. Spectral conversion of light-emitting diodes emission has also been achieved using fluorescent microspheres [10].

We report here a further step in the integration of NCs with LEDs by developing a 'self-aligned' technique [11] capable of controllably micro-forming NC/epoxy resin nanocomposites on micro-pixellated AlInGaN LEDs ('micro-LEDs') [12]. Micro-LED arrays are very attractive pattern-programmable optoelectronic micro-projection sources being explored for a wide range of display and instrumentation applications [13,14]. They come in many formats, but typically consist of a few hundred to a few thousand individually-addressable micro-pixel LED elements in a device active area of a few square millimetres, emitting at *one given wavelength* defined by the particular nitride epitaxial structure used. By utilizing devices operating at 370nm, we show that one can selectively fabricate nanocomposite microstructures aligned to the underlying active device structures, thus opening up the benefits of quantum dot color converters and potentially integrated quantum dot laser structures with these sources.

The UV micro-stripe AlInGaN LEDs used as demonstrators in this work are chosen for convenience and for their relevance to producing multi-color versions [15] of the structured illumination microscopy we have explored previously [16]. They involve a similar epitaxial structure and fabrication process to those reported earlier [17]. Rectangular parallel mesa structures, 3600x20μm^2, are dry-etched down to the n-GaN underlayer using inductively coupled plasma (ICP) etching, creating 120 side-by-side micro-stripe pixels in the LED

#100149 - $15.00 USD Received 14 Aug 2008; revised 9 Oct 2008; accepted 14 Oct 2008; published 3 Nov 2008

epilayer with a 34µm centre-to-centre spacing. As a result, all the mesas share a common n-electrode. A p-metallization layer runs on each pixel with an independent connection pad for individual current injection. The emitting area of each pixel is defined by an aperture in the p-metal layer 300µm long and 12µm wide. The NCs used in these experiments are commercially available CdSe/ZnS samples (Evident Technologies Inc.) dispersed in toluene with emission from blue (481nm) to red (610nm). The epoxy resin used is a cross-linkable polymer photosensitive at 370nm.

2. Nanocomposite preparation

The nanocomposites are blends of three components comprising the colloidal NCs in toluene, an epoxy matrix in a pre-polymerised form with photo-initiator which acts as a host matrix and a vinyl ether monomer which is believed to help the dispersion of the NCs in the epoxy matrix. The nanocomposite preparation aims to achieve a solution of 0.2% weight percentage (w/w) of NCs in the epoxy matrix. First, the NCs are mixed with a fixed weight of vinyl monomer for all the NCs in toluene. The solution is then agitated in an ultrasonic bath at room temperature for 30 minutes. The UV-sensitive epoxy pre-polymer is then weighed on a high precision scale and added to the NCs/vinyl solution to achieve the designated concentration. Further agitation in an ultrasonic bath is then carried out for 1 hour. As a consequence, the solution has a uniform dispersion of NCs with a low viscosity due to the dilution of the epoxy pre-polymer by toluene. In addition, at this stage this inorganic/organic blend is UV-curable due to the epoxy pre-polymer but it has no particular sensitivity to temperature. The last step of the nanocomposite preparation is then the evaporation of the toluene and other solvents contained in the epoxy pre-polymer to produce a more viscous solution while preventing the latter from curing. To achieve this, magnetic stirring on a hot plate at 180ºC (the toluene boiling point is around 110ºC) in air for several hours is performed, with rapid cool down under tap water every hour to stop evaporation and determine the viscosity of the solutions. The solvent evaporation time varies with the type of NCs used in the blend. The evaporation time increases for NCs emitting at shorter wavelengths. Table 1 lists the NCs used to make the respective solutions, along with their concentrations in toluene. As the NC concentration decreases when their emission goes to the blue region of the spectrum, a larger volume of NCs in toluene has to be mixed with the epoxy pre-polymer, for example in the case of the blue emitting NCs compared to the red emitting ones, in order to achieve the same concentration. As a consequence, the red NC solution has less added solvent to evaporate and takes about 5h30 while this time increases to 7h30 in the case of blue emitting NCs. These evaporation times are empirical values and do not result from viscosity measurements; as a consequence, the viscosities of the solutions are all different and are the result of almost complete evaporation of the solvents. The solutions are usually kept in a refrigerator and they are left at room temperature for 30 minutes prior to any processing. No apparent degradation of the nanocomposites has been noticed while samples are kept in these conditions for several months.

3. Integration experiments

Four solutions of 0.2% w/w were prepared with the NCs summarised in table 1. The self-alignment technique uses individual micro-LED elements emitting around (in this case) 370nm to locally photocure the nanocomposite deposited on top which then provides an appropriate aligned micro/nanostructure to color convert the output of the same element. To achieve this, the nanocomposite is initially spin-coated onto the device. The packaged micropixelated LED is loaded in a spin coater and a film of NCs/vinyl/epoxy solution is deposited using a spinning speed of 4000 rpm for 40 seconds achieving 20 to 25µm thick films. The micropixels to be covered are then switched on at a specific driving current for a certain amount of time to give the correct exposure dose to the polymer film that triggers curing and cross-linking. The uncured nanocomposite is then washed off using a toluene bath

Received 14 Aug 2008; revised 9 Oct 2008; accepted 14 Oct 2008; published 3 Nov 2008

for 20 seconds followed by rinsing in deionised water. These steps can be repeated several times on the same pixel to build up a thicker encapsulation. The devices have been electrically characterised and they have a typical turn-on voltage of 3.6V. All the self-alignment curing has been done at a driving current of 0.5mA giving an optical power density of 4.4mW/cm^2 in the spin-coated film. Depending on the nanocomposite considered, different exposure doses are required; the red NCs nanocomposite needs a dose as high as 93mJ/cm^2 while the blue NCs blend requires only 9mJ/cm^2.

Table 1. Commercial CdSe/ZnS core/shell NC absorption, fluorescence characteristics, FWHM and concentrations in toluene (from datasheet). Fluorescence peaks are given with an error margin of +/-10nm.

NCs	**1st absorption peak (nm)**	**Emission peak (nm)**	**Typical FWHM (nm)**	**Concentration (mg/mL)**
Lake Placid Blue	**462**	**481**	**<40**	**0.29**
Adirondack Green	**513**	**526**	**<35**	**1.19**
Hops Yellow	**542**	**561**	**<30**	**1.3**
Maple Red-Orange	**591**	**610**	**<30**	**1.77**

This difference could be attributed to a photon harvesting competition between the photosensitive initiator of the epoxy pre-polymer and the NCs but also to a modification in the curing kinetics within the matrix itself due to possible polymer chains propagation alteration by the NCs. The difference of exposure doses is directly related to the typical absorption curves of the corresponding NCs. With an excitation wavelength near 370nm, as in our case, red NCs absorb much more strongly than the blue NCs as shown in fig. 1. To separately characterize absorption and emission properties, each nanocomposite was spin-coated on clean glass substrates and spectrally analysed with a UV-VIS Cary spectrophotometer for the absorption and a Perkin Elmer LS 50B for the fluorescence spectra. The film thicknesses were then measured with a stylus profilometer. A reference baseline of a clean glass substrate with a corresponding spin coated and cured vinyl ether/epoxy polymer was also measured in both instruments. The resulting absorbance spectra confirm the assumption of differing absorbance for different types of NC used in the nanocomposite fixed at the same concentration (0.2% w/w). For instance, the red nanocomposite has an absorbance at 370nm of about 65cm^{-1} while the yellow, green and blue nanocomposites have lower absorbance of about 42cm^{-1}, 39cm^{-1} and 32cm^{-1}, respectively. The fluorescence spectra of the different nanocomposites also included in fig. 1 show peaks at respectively 604nm, 555nm, 518nm and 477nm. All the peaks are slightly blue-shifted in comparison with the centred values from the datasheet given in table 1 but within the error margin for sample variability. The measured full widths at half maxima (FWHM) are very similar to the manufacturer’s values: 30.5nm for the red and yellow nanocomposites and 32.5nm for the green and 35.5nm for the blue nanocomposites.

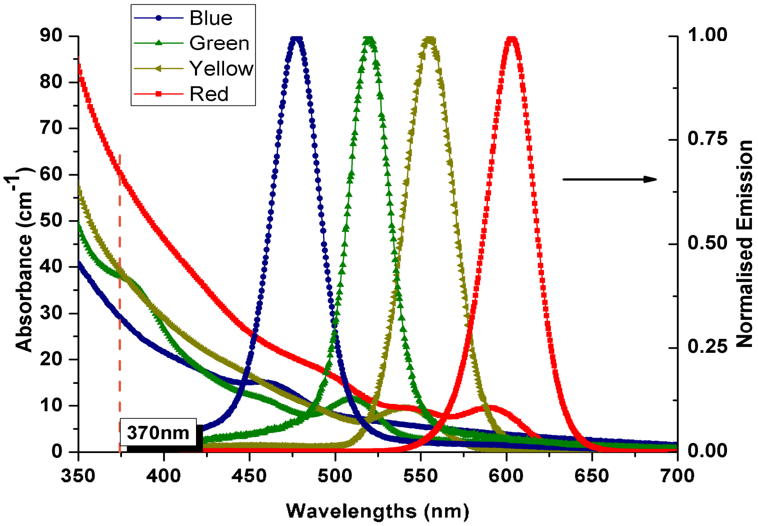

Fig. 1. Absorbance and emission spectra of the NC nanocomposite films after photocuring

Figure 2(a) is an optical micrograph under white light illumination of an integrated nanocomposite (left) produced by the self-aligned direct writing technique. The patterned nanocomposite covers the entire emitting area of the micro-pixel and only that micro-pixel. A schematic of the integration (centre) and a typical micro-pixel in operation before self-aligned writing are also represented (right).

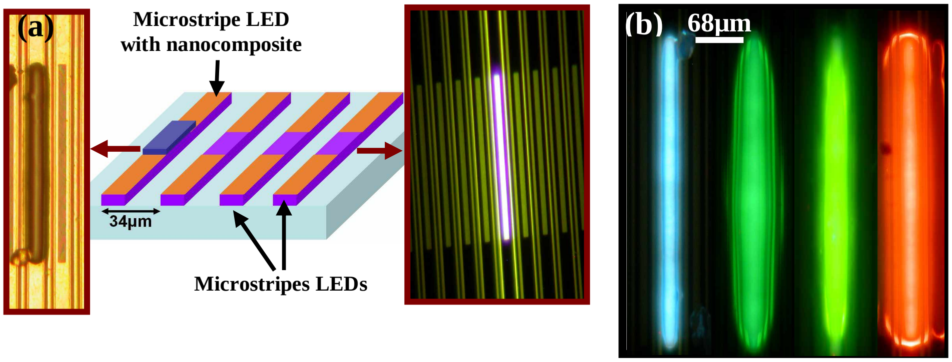

Fig. 2. Optical micrographs of respectively, (a) an integrated nanocomposite microstructure under white light illumination (left), a schematic of the integration (centre) and a representative single operating UV pixel (right) and (b) encapsulated micro-LEDs turned-on showing efficient blue, green, yellow and red colour conversion from the UV-emitting micro-pixels by the NCs nanocomposites.

Figure 2(b) shows the full range of nanocomposites microstructures integrated onto one micro-LED array. As a consequence, a full visible range of colours is enabled on a same micro-LED array chip with up to five different colour emitters (including UV). However, a broadening of the microstructures is noticeable while considering the nanocomposites emitting to longer wavelengths. This effect is attributed to the increase of the exposure doses for some blends while the microstripes LEDs are driven at constant injection current (constant optical output power). With a constant optical output power, a longer exposure time is needed for achieving a high exposure dose, which results in active cationic polymerization centres to diffuse out of the illumination area. A simple way to address this issue would be to keep the exposure time constant while changing the micro-LED output to meet the requirement for the exposure dose. A pulsed mode operation for curing could also be employed to achieve uniform polymerisation [17] and is under investigation with our devices.

4. Results

The spectral analysis of these hybrid devices is employed to characterize the colour conversion. Blue, green, yellow and red nanocomposites have been integrated by the self-alignment writing method. The PL spectra of the integrated NCs nanocomposites are measured with a UV-visible fibre-coupled calibrated optical spectrometer (Ocean Optics USB4000) with 800ms integration time and aligned with the considered micro-emitter through a 200µm wide slit placed aligned perpendicularly to the micro-pixel and approximately in the middle so emission from about 50µm on both sides of the micro-pixel is not collected by the set-up. Fig. 3 gives the spectral analysis of the emission of particular pixels driven at an injection current of 3.6mA and normalised in respect to the unconverted UV peak intensity. For clarity, and to display all the results together, only the UV emission corresponding to the optical pumping of the red-emitting nanocomposite is shown on this graph, but it was common to all. In addition, the emission spectra for the yellow, green and blue nanocomposites are vertically offset for clarity. While the micro-LED emission peaks at 370nm is clearly noticeable, peaks at 609nm, 560nm, 524nm and 486nm demonstrate the successful optical pumping by the micro-pixel directly underneath and the colour conversion by the NCs nanocomposites from UV to different colours in the visible, from blue to red.

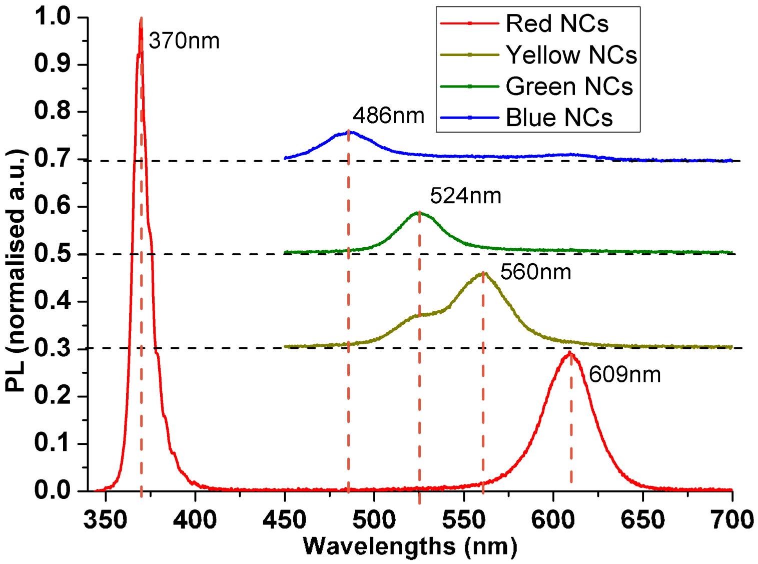

Fig. 3. Emission spectroscopy of a device with blue, green, yellow and red NCs nanocomposites encapsulating single micro-pixel driven at the same injection current of 3.6mA

The emission spectrum of the yellow nanocomposite in fig. 3 shows an extra peak at 524nm along with the expected peak at 560nm, which is attributed to an adjacent integrated green-emitting nanocomposite which is optically pumped by scattered UV light from the mesas of the micro-emitters. The absorption properties of these NCs nanocomposites allow a radiative energy transfer of the yellow emission to red-emitting NCs nanocomposites and, generally, from high energy emitting to lower energy emitting nanocomposites (fig. 1). The red-emitting nanocomposite is susceptible to absorbing the emission of all the others but as it was spaced several micro-LEDs elements away on the array from the blue, green and yellow-emitting NCs, only a very weak red-contribution is noticeable in the fluorescence spectra concerned.

The optical output power was then characterised to determine the colour conversion efficiency of such devices. First a bare micro-LED was characterised using a UV-enhanced Si photodetetector placed in close proximity (~2mm) to the emitting pixel. The pixel is turned on and the light output power is collected for different driving current. Fig. 4 plots these results with an emission at 370nm. A bare microstripe with dimensions of 300µm x 12µm gives an optical output power as high as 34µW at a driving current of 40mA (~944mW/cm^2 optical power density at a driving current density of 55A/cm^2, current injected over the full length of the mesa structure, 3600x20µm^2). Subsequent measurements are carried out after the nanocomposite integration on similar microstripes. The same measurement method is used through coloured glass long-pass filters to remove the unconverted UV. For the red-emitting nanocomposite, a cut-off frequency at 520nm and 95% transmission at 610nm is chosen. The results are also plotted in fig. 4; the output power collected at 609nm reaches a maximum of about 6µW at a driving current of 40mA (~166mW/cm^2 optical output power at 55A/cm^2 current density). The approximate colour conversion efficiency at 40mA driving current can be estimated for the red-emitting NCs nanocomposite to be about 17.7% (with compensated loss from the filter) (18.2% at 30mA). Yellow (560nm), green (524nm) and blue-emitting (486nm) nanocomposites optical output powers are also plotted in fig. 4 and achieve respectively about 3µW, 0.15µW and 0.05µW at 40mA driving current (~83mW/cm^2, ~4mW/cm^2 and ~1.3mW/cm^2 at 55A/cm^2). The respective estimated colour conversion efficiencies are 9%, 0.5% and 0.2% (with compensation from filter loss).

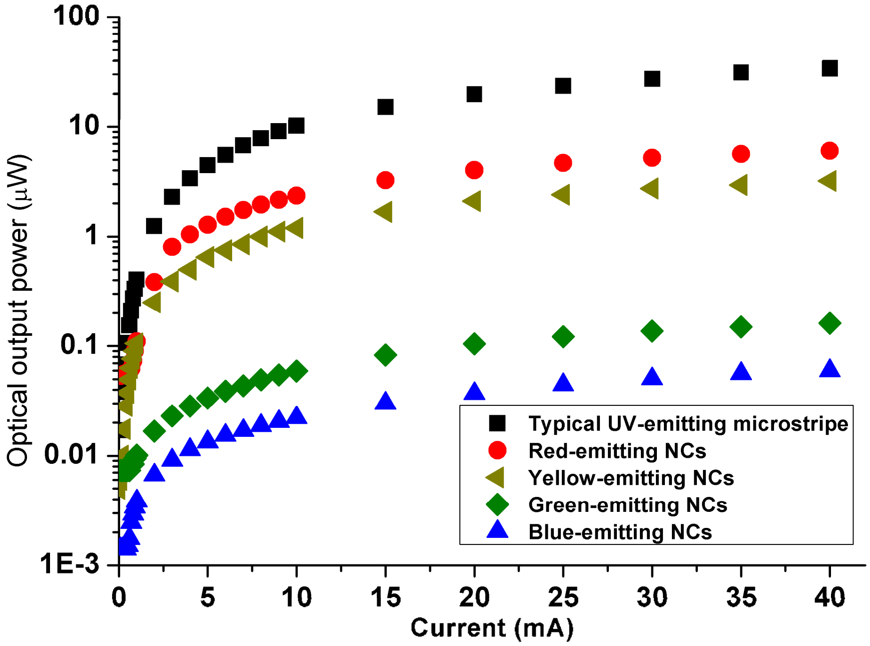

Fig. 4. Typical optical powers versus injection current for UV microstripe LED and integrated NC nanocomposites by self-alignment writing.

#100149 - $15.00 USD Received 14 Aug 2008; revised 9 Oct 2008; accepted 14 Oct 2008; published 3 Nov 2008

The characterisation of the eventual saturation of the emission of these NCs nanocomposites is an interesting feature to inspect. Figure 5 shows the experimental spectral data relevant to this experiment. Spectra are taken with increase of the driving current in the device. Although only the pixel with the NCs nanocomposite emitting at 609nm is turned on, shoulders emitting at 526nm and 561nm are noticeable, although no radiative transfer is possible in this situation, these peaks are attributed to UV light scattering out from the microstripe mesa structure optically pumping these adjacent nanocomposites. The spectral evolution shows no wavelength shift in the case of the nanocomposite; however, the peaks – both UV and red - broaden. The evolution of the peaks at 370nm and 610 nm were then recorded and the area underneath each was integrated to take into account this broadening effect. The UV peak is integrated on the 350nm to 409nm range and the peak at 610nm from 590nm to 630nm. The ratio of the integrated values of the 610nm peak over the UV emission peak at 370nm (S_{NC}/S_{UV}) is then plotted versus the driving current in inset of fig. 5. A linear law could fit this evolution meaning that no saturation of the nanocomposite was observed; however, the conversion coefficient is not constant over the driving current which could be attributed to different spectral broadening of the micro-LED and the NC emissions. The conversion efficiency is approximated to be 18% at a driving current of 30mA. This value reasonably matches the estimation obtained with the optical output power. Further saturation study shows that a focussed laser beam down to a 500µm diameter spot with optical power ranging from 0mW to 15mW does not saturate a 20µm thick nanocomposite film at a concentration of 0.2%w/w with either blue, green, yellow or red NCs. Saturation and lifetime characterisation of these nanocomposites are in progress and will be reported later.

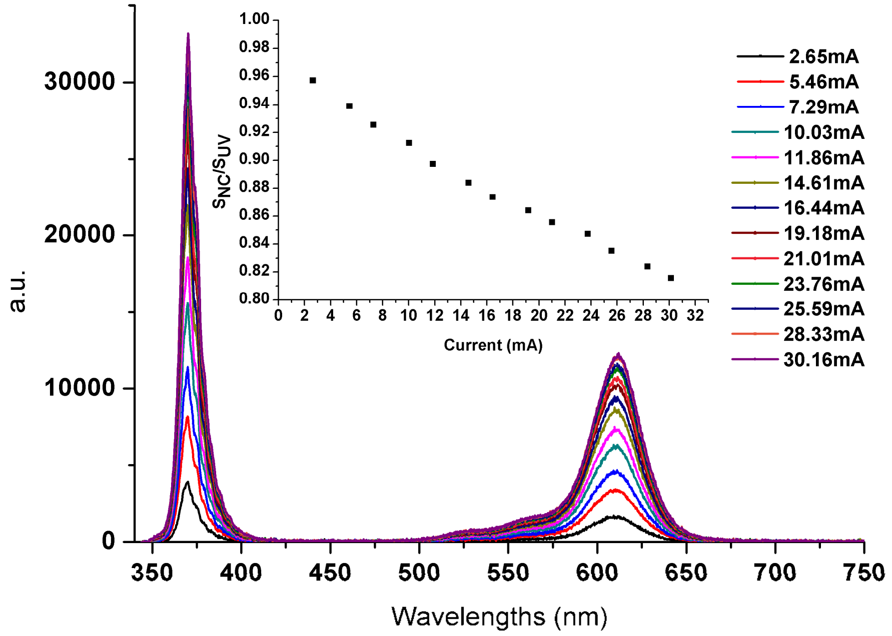

Fig. 5. Red-emitting NCs nanocomposite emission spectrum optically pumped by the micro-LED underneath over the driving current. Inset, peak area ratio of the emissions at 370nm and 609nm.

4. Conclusion

We have reported the successful use of a self-alignment technique to integrate NC nanocomposites onto micro-scale LEDs, as a means of producing multi-color programmable microstuctured sources for a range of applications in displays, microscopy and optoelectronics. The NC nanocomposites are a mix of the NCs in toluene, a vinyl ether monomer and an epoxy polymer. After solvent evaporation, the solutions present themselves as a viscous, spin-coatable and UV-sensitive solution with NC densities ranging from 64x10^{14} cm^{-3} to 525x10^{14} cm^{-3} respectively for the red to blue nanocomposites. The measurements of the absorbance and fluorescence spectra of cured nanocomposites spin-coated onto glass show the successful creation of NC nanocomposites with typical characteristics similar to the colloidal NCs in toluene. The integration of the nanocomposites covering emitting area of single microstripe LEDs shows good color conversion characteristics. Color conversion up to 18.2% is thus achieved in the case of the red-emitting NCs for an injection current of 30mA. Converted optical power density up to 166mW/cm^2 at 609nm is achieved at a driving current density of 55A/cm^2 in a micron scale format. This technique and the advantage of using UV devices allow the fast creation of multi-colour micro-LED chips with emission ranging from the UV to the red making this sort of device particularly attractive for lab-on-chip and other instrumentation applications.

Acknowledgment

This research work was supported by the UK Basic Technology Research Programme “A Thousand Micro-Emitters Per Square Millimetre: New Light on Organic Material & Structures”, by a Science and Innovation Award on “Molecular Nanometrology” and by the Scottish Consortium on Integrated Micro-photonic Systems.